POLSKA AKADEMIA NAUK
KOMITET ELEKTRONIKI I TELEKOMUNIKACJI

KWARTALNIK ELEKTRONIKI I TELEKOMUNIKACJI

ELECTRONICS AND TELECOMMUNICATIONS QUARTERLY

TOM 51 — ZESZYT SPECJALNY

WARSZAWA 2005

ADRES REDAKCJI
00-665 Warszawa, ul. Nowowiejska 15/19 Politechnika, pok. 470
Instytut Telekomunikacji, Gmach im. prof. JANUSZA GROSZKOWSKIEGO

Dyżury Redakcji: środy i piątki, godz. 14–16
4tel/fax (022) 660 77 37

Telefony domowe: Redaktora Naczelnego: 812 17 65
Zast. Red. Naczelnego: 826 83 41
Sekretarza Odpowiedzialnego: 633 92 52

Ark. wyd. 15 Ark. druk. 11,75	Podpisano do druku we wrześniu 2005 r.
Papier offset. kl. III 80 g. B-1	Druk ukończono we wrześniu 2005 r.

Skład, druk i oprawa: Warszawska Drukarnia Naukowa PAN
00-656 Warszawa, ul. Śniadeckich 8
Tel./fax: 628-87-77

Szanowni Autorzy

„Kwartalnik Elektroniki i Telekomunikacji" — Electronics and Telecommunications Quartery jest kontynuatorem tradycji powstałego 51 lat temu kwartalnika p.t. „Rozprawy Elektrotechniczne".

Kwartalnik jest czasopismem Komitetu Elektroniki i Telekomunikacji Polskij Akademii Nauk. Wydawany jest przez Wydawnictwo Naukowe PWN SA w Warszawie. Kwartalnik jest czasopismem naukowym, na którego łamach są publikowane artykuły i komunikaty prezentujące wyniki oryginalnych prac teoretycznych i doświadczalnych, a także przeglądowych. Związane są one z szeroko rozumianymi dziedzinami współczesnej elektroniki, telekomunikacji, mikroelektroniki, oproelektroniki, radiotechniki i elektroniki medycznej.

Autorami publikacji są wybitni naukowcy, znani specjaliści o wieloletnim doświadczeniu, a także młodzi badacze — głównie doktoranci.

Artykuły charakteryzują się oryginalnym ujęciem zagadnienia, interesującymi wynikami badań, krytyczną oceną teorii lub metod, omówieniem aktualnego stanu, lub postępu danej gałęzi techniki oraz omówieniem perspektyw rozwojowych. Sposób pisania matematycznej części artykułów zgodny jest z wytycznymi IEC (International Electronics Commision) oraz ISO (International Organization of Standarization).

Wszystkie publikowane w Kwartalniku artykuły są recenzowane przez znanych krajowych specjalistów, co zapewnia że publikacje te są uznawane jako autorski dorobek naukowy. Opublikowane w kwartalniku wyników prac naukowych zrealizowanych w ramach „GRANTów" Komitetu Badań Naukowych spełnia więc jeden z wymogów stawianych tym pracom.

Czasopismo dociera do wszystkich zajmujących się elektroniką i telekomunikacją krajowych ośrodków naukowych oraz technicznych, a także szeregu instytucji zagranicznych. Jest ponadto prenumerowane przez liczne grono specjalistów i biblioteki.

Każdy Autor otrzymuje bezpłatnie 20 egzemplarzy nadbitek swojego artykułu, co ułatwia przesłanie go do indywidualnych wybranych przez Autora osób i instytucji w kraju lub za granicą. Ułatwia to dodatkowo fakt, że w Kwartalniku są publikowane artykuły w języku angielskim.

Nadesłane do redakcji artykuły są publikowane w termini około pół roku, w przypadku sprawnj współpracy Autora z Redakcją. Wytyczne dla Autorów dotycząc formy publikacji są zamieszczone w zeszytach Kwartalnika, można je także otrzymać w siedzibie Redakcji.

Artykuły można dostarczać osobiście, lub pocztą pod adresem zamieszczanym na stronie redakcyjnej w każdym zeszycie.

Redakcja

Preface

The Institute of Radioelectronics was established in 1970 on the basis of four Departments: Radio Engineering Equipment (founded in 1946), lead by prof. S. Ryżko, Radiology (founded in 1946), headed by prof. C.Pawłowski and subsequently by prof. W. Rotkiewicz, Radiolocation (founded in 1948), headed by prof. P.Szulkin and prof. S.Sławiński, Electroacoustics (founded in 1949), headed by prof. I. Malecki and Television (founded in 1955), lead by prof. L.Kędzierski. Research in the area the Institute focused on had been already pursued in the prewar period in the Department of Radio Engineering headed by Professor J. Groszkowski (founded in 1929).

As a result of the recently conducted reorganization, the Institute is presently organized into five divisions: Electroacoustic, Microwave and Radiolocation Engineering, Nuclear and Medical Electronics, Radiocommunications and Television. Research and teaching activities in the Institute, previously embracing numerous fields, presently concentrate on the following areas, which do fall into latest world research trends: radiocommunications, multimedia technologies and biomedical engineering.

The most valuable asset of the Institute of Radioelectronics, the way I see it, is our staff. We cherish a legacy of innovative research dating back a few decades. This has always been combined with class leading dedication to technical teaching as well as education in its broader sense. Over the past few years several personnel changes and valuable extensions have taken place, and I am pleased to say that we have grown in rank as well as in number of young, brilliant scientists. Our day-to-day work as well as strategic planning are presently driven by 14 professors (including 9 with state professorial titles) and 44 assistant professors. From this perspective, I am also pleased to mention our team of over 40 Ph.D. students already exhibiting many brilliant skills. Several of them have already gained valuable distinctions at scientific conferences and are expressing deep interest in further University career.

Some of our teams have gained worldwide recognition, e.g. in the area of intelligent multimedia systems, electromagnetic simulators, antenna techniques, theory of multi-dimensional analytic signals, digital processing of measurement signals and construction of equipment for elementary particles physics experiments.

Besides people, another important asset of the Institute resides in our strong laboratory base comprising a range of high profile measurement and control equipment, which has recently been further upgraded and can be said to have met European standards. Our well equipped laboratories include the new antenna laboratory, radiocommunications laboratory with a GSM system, anechoic chamber and a sound studio, microwave laboratory and tomography laboratories.

Another proof of our commitment to ensure that our research results are integrated into industrial practice is through the participation in design projects for and together with industrial and commercial companies from Poland, Europe, Asia and US. Presently, we also mainly participate in European Union project activities – currently, we are involved in

6 projects within the Sixth Framework initiatives: VISNET, TARGET, WISE, RESOLUTION, SAFESPOT, CODMUCA. Moreover, we are continuing the long-term collaboration with CERN.

This special issue comprises 11 papers, which are aimed to indicate some of the research works, currently conducted in the Institute. Those interested in the research subject area of the Institute are advised to refer to the Institute Annual Reports as well as proceedings of some conferences, coorganized by the Institute, e.g. the *International Conference on Microwaves, Radar and Wireless Communications* MIKON and the *National Conference on Radiocommunications and Broadcasting* KKRRiT.

I would like to thank all the paper Authors for their valuable contributions and all Reviewers for their constructive comments. It is my hope that the papers contained herein will prove of interest and usefulness to the Readers.

prof. dr hab. inż. Józef Modelski
Director of the Institute of Radioelectronics
Guest Editor

CONTENTS

SPIS TREŚCI

KWARTALNIK ELEKTRONIKI I TELEKOMUNIKACJI, 2005, 51, ZESZYT SPECJALNY, ss. 9–21

Pseudo-Wigner and double-dimensional pseudo-Wigner distributions with extension for 2-D signals

KAJETANA M. SNOPEK

Institute of Radioelectronics,
Warsaw University of Technology
E-mail: K.Snopek@ire.pw.edu.pl

The paper summarizes the theory of pseudo-Wigner (PWDs) and double-dimensional pseudo-Wigner distributions (DDPWDs). Both are members of the Cohen's class and respectively, the double-dimensional Cohen's class. The relations between the PWDs, the Short-Time Fourier Transform and the Narrow-Band Inverse Fourier Transform are described in detail. The extension of the theory for 2-D signals is presented. The paper is illustrated with examples of PWDs and DDPWDs of test signals.

Keywords: Time-frequency distributions, double-dimensional distributions, Cohen's class.

1. INTRODUCTION

1.1. COHEN'S CLASS OF TIME-FREQUENCY DISTRIBUTIONS

Consider the complex signal $\psi(t)$. Its Fourier spectrum is denoted $\Gamma(f)$ and the Fourier relation is $\psi(t) \overset{F}{\Leftrightarrow} \Gamma(f)$. Let us define the shift variables in time- and frequency domain respectively. The variable τ represents a time-lag and μ a shift in the frequency domain. The Cohen's class of time-frequency distributions of 1-D signals has been defined in [1]. Each distribution $C_\psi(t,f)$ belonging to this class is defined as

$$C_\psi(t,f) = \iiint \phi_{ft}(\mu,\tau)\ \psi(u+\tau/2)\ \psi^*(u-\tau/2)\ e^{j2\pi\mu(u-t)} e^{-j2\pi f\tau} du d\tau\ d\mu \qquad (1)$$

where the form of the kernel $\phi_{ft}(\mu,\tau)$ is different for each distribution. Note that all integrals presented in this paper are indefinite integrals (with limits changing from $-\infty$

to $+\infty$). From (1) the following four equivalent forms of the Cohen's class are derived [2]

$$\text{"frequency-time"} \qquad C_\psi(t,f) = \iint \phi_{ft}(\mu,\tau) A_\psi(\mu,\tau)\, e^{-j2\pi(f\tau+\mu t)} d\mu d\tau \tag{2}$$

where A_ψ is the Woodward's ambiguity function defined in [3],

$$\text{"time - time"} \qquad C_\psi(t,f) = \iint \phi_{tt}(t'-t,\tau)\, \psi(t'+\tau/2)\, \psi^*(t'-\tau/2)\, e^{-j2\pi f\tau} dt' d\tau, \tag{3}$$

$$\text{"time - frequency"} \qquad C_\psi(t,f) = \iint \phi_{tf}(t'-t,\mu-f) W_\psi(t',\mu) dt d\mu \tag{4}$$

where W_ψ is the Wigner distribution defined in [4] ($W_\psi(t,f) = \int \psi(t+\tau/2)\psi^*(t-\tau/2)e^{-j2\pi/f\tau} d\tau$),

$$\text{"frequency-frequency"} \qquad C_\psi(t,f) = \iint \phi_{ff}(\mu,f'-f)\Gamma(f'+\mu/2)\Gamma(f-\mu/2)e^{j2\pi\mu t} d\mu df'. \tag{5}$$

The kernels of the Cohen's class are interrelated by Fourier and inverse Fourier transformations w.r.t. t, f, τ and μ as shown in Fig.1(a).

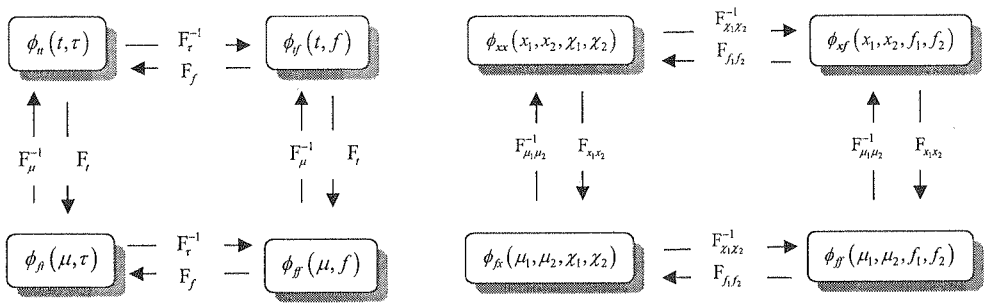

Fig. 1. Fourier relations between the kernels of the Cohen's class (a) time-frequency distributions, (b) spatial-frequency distributions

1.2. COHEN'S CLASS OF SPATIAL-FREQUENCY DISTRIBUTIONS

Consider the 2-D complex signal $\psi(x_1, x_2)$ with the Fourier spectrum $\Gamma(f_1, f_2)$, $\psi(x_1,x_2) \overset{F}{\Leftrightarrow} \Gamma(f_1,f_2)$. The 2-D shift variables in spatial- and frequency-domains

will be denoted respectively as $\chi = (\chi_1, \chi_2)$ and $\mu = (\mu_1, \mu_2)$. The Cohen's class of spatial-frequency distributions of 2-D signals has been firstly defined in [5]. Note that all kernels of this class are 4-D functions of spatial-, frequency-, spatial shift- and frequency shift variables. In analogy to Eqs. (2)÷(5), the four equivalent forms of the Cohen's class of spatial-frequency distributions are classified as:

$$\text{"}frequency - spatial\text{"} \quad C_\psi(\mathbf{x},\mathbf{f}) = \iint\limits_{\mu} \iint\limits_{\chi} \phi_{fx}(\mu,\chi) A_\psi(\mu,\chi) e^{-j2\pi(f_1 X_1 + f_2 X_2 + \mu_1 x_1 + \mu_2 x_2)} \mathrm{d}\mu_1 d\mu_2 \mathrm{d}\chi_1 \mathrm{d}\chi_2, \tag{6}$$

$$\text{"}spatial - spatial\text{"} \quad C_\psi(\mathbf{x},\mathbf{f}) = \iint\limits_{\mu} \iint\limits_{\chi} \phi_{xx}(\mathbf{x}' - \mathbf{x}, \chi) \psi(\mathbf{x}' + \chi/2) \psi^* (\mathbf{x}' - \chi/2) \mathrm{e}^{-j2\pi(f_1 X_1 + f_2 X_2)} dx_1' dx_2' d\chi_1 d\chi_2, \tag{7}$$

$$\text{"}spatial - frequency\text{"} \quad C_\psi(\mathbf{x},\mathbf{f}) = \iint\limits_{\mu} \iint\limits_{\chi} \phi_{xf}(\mathbf{x}' - \mathbf{x}, \mu - \mathbf{f}) W_\psi(\mathbf{x}', \mu) dx_1' dx_2' d\mu_1 d\mu_2 \tag{8}$$

$$\text{and "}frequency - frequency\text{"} \quad C_\psi(\mathbf{x},\mathbf{f}) = \iint\limits_{\mu} \iint\limits_{\chi} \phi_{ff}(\mu, \mathbf{f}' - \mathbf{f}) \Gamma(f' + \mu/2) \Gamma^*(f' - \mu/2) \mathrm{e}^{j2\pi(\mu_1 X_1 + \mu_2 X_2)} d\mu_1 d\mu_2 df_1' df_1'. \tag{9}$$

All kernel functions are interrelated by 2-D Fourier or inverse Fourier transformations w.r.t. $\mathbf{x} = (x_1, x_2), \mathbf{f} = (f_1, f_2), \chi = (\chi_1, \chi_2)$ or $\mu = (\mu_1, \mu_2)$ [see Fig.1(b)], [5].

1.3. COHEN'S CLASS OF DOUBLE-DIMENSIONAL DISTRIBUTIONS

The theory of double-dimensional distributions (DDDs) has been presented in detail in [6]. The definition of the 4-D Cohen's class double-dimensional distributions has been introduced in [5] basing on spatial-frequency and frequency-spatial forms of the 4-D Cohen's class of spatial-frequency distributions [see (8), (6)]. Let us remind that the double-dimensional Wigner distribution (DDWD) is defined as the 4-D Wigner distribution of the 2-D Wigner distribution $W_\psi(t, f)$. So, the Wigner distribution $W_\psi(t, f)$ plays the role of a 2-D real signal. Analogously, the double- dimensional ambiguity function (DDAF) has been defined as the 4-D ambiguity function of the 2-D ambiguity function $A_\psi(\mu, \tau)$. In this paper we propose to apply for $W_\psi(t, f)$ the name "*first-order* WD" and for the DDWD the name "*second-order* WD". Similarly, the ambiguity function will be named "*first-order* AF" and DDAF – "*second-order* AF". Of course, it is possible to derive the WDs and AFs of higher orders. This topic is not

considered here because of the limited volume of this paper. The "spatial-frequency" and "frequency-spatial" forms of the double-dimensional Cohen's class respectively are

$$C^{(2)}(t,f,f_1,t_1) = \iint\limits_{t'} \iint\limits_{f'} \phi_{xf}(t'-t,f'-f,f_2-f_1,t_2-t_1)W^{(2)}(t',f',f_2,t_2)dt'df'df_2dt_2, \tag{10}$$

$$C^{(2)}(t,f,f_1,t_1) = \iint\limits_{f_2} \iint\limits_{t_2} \phi_{fx}f_2,t_2,t_{12},f_{12})A^{(2)}(f_2,t_2,t_{12},f_{12}) \\ \mathrm{e}^{-j2\pi(F_1t_{12}+t_1f_{12}+f_2t+t_2f)}df_2dt_2dt_{12}df_{12} \tag{11}$$

where $W^{(2)}$ is the second-order WD and $A^{(2)}$ the second-order ambiguity function [5], [6]. In (10) and (11) the new notation of variables has been introduced. We denote by $t_{subscript}$ the time shifts of various orders and by $f_{subscript}$ the frequency-shifts of various orders. So that, t_1 is the first-order time shift variable (equal τ in (1)), f_1 is the first-order frequency shift variable (equal μ in (2)) and t_2, t_{12}, f_2 , f_{12} are second-order shifts.

2. PSEUDO-WIGNER DISTRIBUTIONS

2.1. PSEUDO-WIGNER DISTRIBUTIONS OF ONE-DIMENSIONAL SIGNALS

The *time-domain pseudo-Wigner distribution* PW_t of the complex signal $\psi(t)$ has been defined in [7] in the form

$$PW_t(t,f) = \int h(\tau)\psi(t+\tau/2)\psi^*(t-\tau/2)\mathrm{e}^{j2\pi f\tau}\mathrm{d}\tau. \tag{12}$$

The adjective "*pseudo*" has a pure historical meaning and has been introduced by authors of [7] to point out the difference with the Wigner distribution of the complex signal $\psi(t)$. In (12), $h(\tau)$ is a specific time-window function. It can be shown that PW_t is a convolution of the Fourier transform of $h(t)$ with the Wigner distribution, i.e.,

$$PW_t(t,f) = \int H(f-\mu)W_\psi(t,\mu)d\mu. \tag{13}$$

and related to the Short-Time Fourier Transform (STFT) [8], [5]. This problem is described in Section 2.2.

Let us illustrate above definitions with an example of the test signal in the form of the sum of four Gaussian pulses shifted in time and modulated in frequency, i.e., $\psi(t) = \dfrac{1}{\sqrt{2\pi}\sigma}\sum\limits_{i=1}^{4}\mathrm{e}^{-\frac{(t-a_i)^2}{2\sigma^2}}\mathrm{e}^{j2\pi f_i t}$ with $a_1 = -2$, $a_2 = 2$, $a_3 = -2$, $a_4 = 2$, $f_1 = f_2 = 1$, $f_3 = f_4 = 4$. The Fig. 2(a) shows the WD of this signal. We observe

four auto-terms centered at points (-2, 1), (-2, 4), (2, 1) and (2, 4) and five oscillating cross-terms appearing due to the bilinear nature of the WD. Next Fig. 2(b) shows the time-domain PWD with the Hanning window (see Table 2, $\alpha = 1$) of the same signal. Notice that the cross-terms resulting from time-shifts of signal components have been completely canceloled.

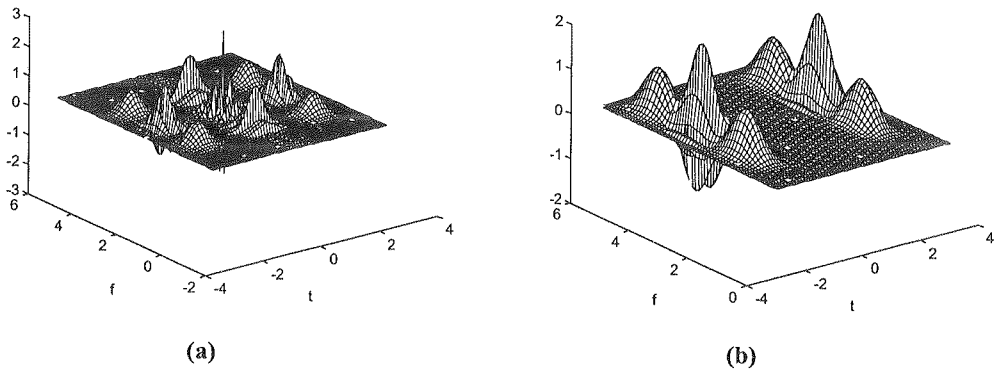

Fig. 2. Distributions of the test signal. (a) WD. (b) PW_t, Hanning time window, $\alpha = 1$

The *frequency-domain pseudo-Wigner distribution* PW_f is defined as [5]

$$PW_f(t,f) = \int G(\mu)\Gamma(f+\mu/2)\Gamma^*(f-\mu/2)e^{j2\pi\mu t}d\mu \tag{14}$$

or as a convolution of the inverse Fourier transform of G with the Wigner distribution

$$PW_f(t,f) = \int g(t-\tau)W_\psi(\tau,f)d\tau. \tag{15}$$

PW_f is also related to the so called Narrow-Band Inverse Fourier Transform (NBIFT) [5] as described in Section 2.2.

The Fig. 3 shows the frequency-domain PWD of the above mentioned test signal (the frequency Hanning window, $\alpha = 0.5$). We observe the cancellation of cross-terms resulting from frequency-shifts of signal components.

Basing on convolution relations (13) and (15), the *dual-window pseudo-Wigner distribution* PW_{tf} is defined as follows [5]

$$PW_{tf}(t,f) = \iint g(t-\tau)H(f-\mu)W_\psi(\tau,\mu)d\tau d\mu. \tag{16}$$

In literature, the distribution of the form (16) is known as the *smoothed pseudo-Wigner distribution* (SPWD) [2]. However, let us underline that the way of derivation of (16) is original and bases on the definition of PW_f which has not been defined earlier in the world scientific literature. The Table 1 shows time-frequency kernels of a few

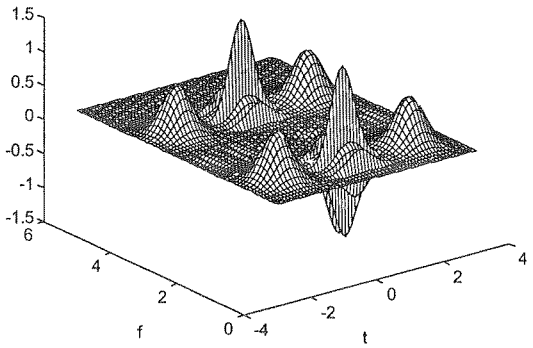

Fig. 3. PW_f of the test signal, Hanning frequency window, $\alpha = 0.5$

Table 1

Time-frequency kernels of 2-D Cohen's class

Distribution	time-frequency kernel
Wigner	$\delta(t) \otimes \delta(f)$
PW_t	$\delta(t) \otimes H(f)$
PW_f	g(t) $\otimes$ $\delta(f)$
PW_{tf}	g(t) $\otimes$ $H(f)$
spectrogram	$W_h(t,f)$
signogram	$W_G(t,f)$

distributions belonging to the 2-D Cohen's class. Next Table 2 presents commonly used window functions: time- [see (12)], frequency- [see (15)] and dual- [see (16)]. The symbol "$\otimes$" denotes the multiplication of the 1-D Dirac distribution by a 1-D function.

As an example, four chosen dual windows are presented in Figs 4 (a)-(d).

The Fig.5(a) shows the dual-window PWD of the same test signal. Applying the dual time-frequency Hanning window results in cancellation of all cross-terms. The same result has been obtained for the spectrogram (Fig. 5(b)), [10]. Generally, the difference between the spectrogram and PW_{tf} is in their time- and frequency resolution. Changing the values of parametres of a dual separable window we control simultaneously the time- and frequency resolution while in the spectrogram, the good time resolution of the window results in the bad frequency resolution and vice versa.

Table 2

Window functions used in definitions of PWDs

Window	time window $g(t)$	frequency window $H(f)$	dual window $g(t)H(f)$
Gaussian	$\exp(-\alpha t^2)$	$\exp(-\beta f^2)$	$\exp(-\alpha t^2)\exp(-\beta f^2)$
Hanning	$\Pi_{2\alpha}(t)\cos\frac{\pi t}{2\alpha}$	$\frac{4\beta}{\pi}\frac{\cos(2\pi f\beta)}{1-16\beta^2 f^2}$	$\Pi_{2\alpha}(t)\cos\frac{\pi t}{2\alpha}\cdot\frac{4\beta}{\pi}\frac{\cos(2\pi f\beta)}{1-16\beta^2 f^2}$
cosine-roll-off	$\begin{cases}\cos^2\left[\frac{\pi(t+r_1a_1)}{2a_1(1-r_1)}\right] & -a_1 \leqslant t \leqslant -r_1a_1\\ \cos^2\left[\frac{\pi(t-r_1a_1)}{2a_1(1-r_1)}\right] & r_1a_1 \leqslant t \leqslant a_1\\ 1 & \lvert t\rvert < r_1a_1\\ 0 & \lvert t\rvert > a_1\end{cases}$	$\frac{\sin(2\pi fr_2a_2)+\sin(2\pi fa_2)}{2\pi f[1-4f^2a_2^2(1-r_2^2)]}$	$g(t)H(f)$
rectangular	$\Pi_{2\alpha}(t)$	$\frac{\sin(2\pi\beta f)}{\pi f}$	$\Pi_{2\alpha}(t)\frac{\sin(2\pi\beta f)}{\pi f}$
cosinus squared	$\Pi_{2\alpha}(t)\cos^2\left(\frac{\pi t}{2\alpha}\right)$	$\frac{\sin(2\pi\beta f)}{2\pi f(1-4\beta^2f^2)}$	$\Pi_{2\alpha}(t)\cos^2\left(\frac{\pi t}{2\alpha}\right)\frac{\sin(2\pi\beta f)}{2\pi f(1-4\beta^2f^2)}$

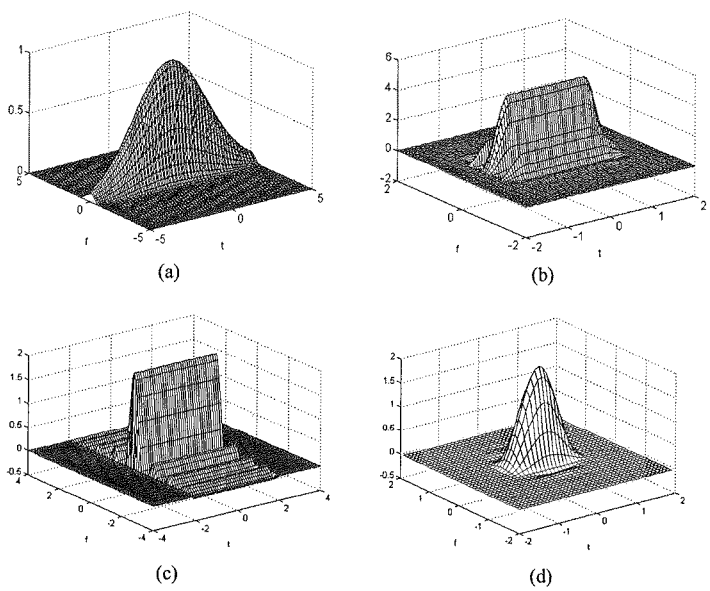

Fig. 4. Chosen dual windows. (a) Gaussian, $\alpha = 0.1$, $\beta = 5$. (b) cosine-roll-off, $a_1 = a_2 = 1$, $r_1 = r_2 = 0.6$. (c) rectangular, $\alpha = 1$, $\beta = 1$, (d) cosinus squared, $\alpha = 1$, $\beta = 2$

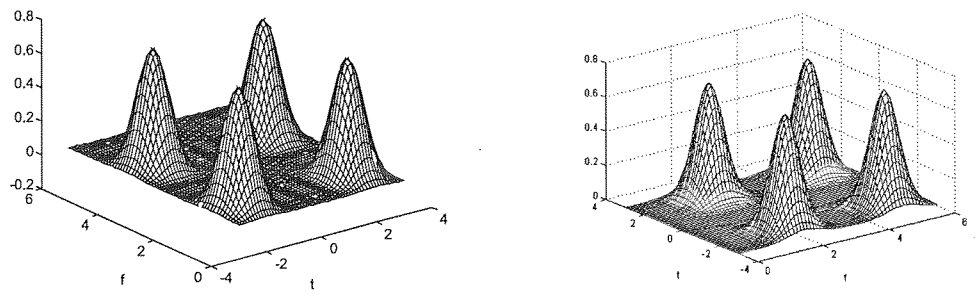

Fig. 5. The distributions of te test signal, (a) Dual-windows PWD (b) Spectrogram

2.2. RELATIONS OF PWDs WITH STFT AND NBIFT

If the window function h has a form of the product $h(\tau) = \gamma_h(\tau/2)\gamma_h^*(-\tau/2)$ where γ_h is a specific window function, the definition (12) gets the form

$$PW_t(t,f) = \int W_{\gamma_h}(0, f-\mu)W_\psi(t,\mu)\mathrm{d}\mu. \tag{17}$$

In consequence, PW_t is related to the Short-Time Fourier Transform (STFT) with the window γ_h. Here, we use the Gabor's definition of the STFT [8]. In literature, e.g., [9], an alternative definition of STFT is proposed. The relation between PW_t and STFT gets the form

$$PW_t(t,f) = \int S^{(\gamma_h)}(t, f+\mu/2)S^{*(\gamma_h)}(t, f-\mu/2)e^{j2\pi\mu t}d\mu \tag{18}$$

where $S^{(\gamma_h)}(t,f) = \int \psi(\tau)\gamma_h^*(\tau - t)e^{-j2\pi f\tau}d\tau$ [8].

Similarly, if the frequency window function $G(f)$ has a factorized form $G(f) = \gamma_G(f/2)\gamma_G^*(-f/2)$, the definition (14) can be written as

$$PW_f(t,f) = \int W_{\gamma_G}(t-\tau, 0)W_\psi(\tau, f)\mathrm{d}\tau. \tag{19}$$

If we define the so called Narrow-Band Inverse Fourier Transform (NBIFT) in the form

$$N^{(G)}(t,f) = \int G(\mu)\Gamma(f+\mu)e^{j2\pi ut}d\mu, \tag{20}$$

it is possible to derive the relation between the PW_f and NBIFT with the window γ_G as follows

$$PW_f(t,f) = \int N^{(\gamma_G)}\left(t+\frac{\tau}{2}, f\right)N^{(\gamma_G)*}\left(t-\frac{\tau}{2}, f\right)d\tau. \tag{21}$$

2.3. PSEUDO-WIGNER DISTRIBUTIONS OF TWO-DIMENSIONAL SIGNALS

The *spatial-domain* PWD is defined in the form [5]

$$PW_x(\mathbf{x},\mathbf{f}) = \iint h(\chi) r(\mathbf{x},\chi) \mathrm{e}^{-j2\pi(f_1 X_1 + f_2 \chi_2)} \mathrm{d}\chi_1 \mathrm{d}\chi_2 \quad (22)$$

where $r(\mathbf{x},\chi)$ is a 4-D signal correlation product defined as

$$r(\mathbf{x},\chi) = \psi(x_1 + \chi_1/2, x_2 + \chi_2/2)\psi^*(x_1 - \chi_1/2, x_2 - \chi_2/2). \quad (23)$$

The *frequency-domain PWD* definition [5] is

$$PW_f(\mathbf{x},\mathbf{f}) = \iint G(\mu) R(\mu,\mathbf{f}) \mathrm{e}^{j2\pi(\mu_1 x_1 + \mu_2 x_2)} \mathrm{d}\mu_1 \mathrm{d}\mu_2 \quad (24)$$

where $R(\mu,\mathbf{f})$ is the 4-D spectrum correlation product

$$R(\mu,\mathbf{f}) = \Gamma(f_1 + \mu_1/2, f_2 + \mu_2/2)\Gamma^*(f_1 - \mu_1/2, f_2 - \mu_2/2). \quad (25)$$

In analogy to the definition (16), the *dual-window PWD* is defined in the convolution form

$$PW_{fx}(x,f) = g(x) * [H(f) * W_\psi(x,f)]. \quad (26)$$

In Table 3, the spatial-frequency kernels of the 4-D Cohen's class are presented. The 4-D window functions used in definitions (22), (24) and (26) can be applied in the separable form, i.e., as products of 1-D functions from Table 2.

In Tables 3 and 4, the symbol "⊗" denotes the multiplication of the 2-D Dirac distribution by a 2-D function. To illustrate the properties of 4-D PWDs, let us take an example of a 2-D separable test signal $\psi(x_1,x_2) = \psi_1(x_1)\psi_2(x_2)$ where both ψ_1 and ψ_2

Table 3

Spatial-frequency kernels of 4-D Cohen's class

Distribution	spatial-frequency kernel
Wigner	$\delta(x_1,x_2) \otimes \delta(f_1,f_2)$
PW_x	$\delta(x_1,x_2) \otimes H(f_1,f_2)$
PW_f	$g(x_1,x_2) \otimes \delta(f_1,f_2)$
PW_{xf}	$g(x_1,x_2) \otimes H(f_1,f_2)$
spectrogram	$W_h(\mathbf{x},\mathbf{f})$
signogram	$W_G(\mathbf{x},\mathbf{f})$

and ψ_2 are sums of four Gaussian pulses shifted by 2 and -2 along the x_1-axis (resp. x_2- axis) and modulated in frequency with the factor f_{1i} (resp. f_{2i}), $i = 1,2,3,4$. The values of frequency shifts were chosen to be equal $f_{i1} = f_{i2} = 2$, $f_{i3} = f_{i4} = 5$, $i = 1,2$. This test signal is a 2-D extension of the signal used in Section 2.1. The Fig. 6 shows three cross-sections with $x_2 = 2$, $f_2 = 2$ of PW_x, PW_f and PW_{fx}. We see that the properties of all distributions are similar as for 1-D signal. In the cross-section $\mathrm{PW}_x(x_1, 2, f_1, 2)$, four auto terms are well distinguished and two pairs of bipolar oscillating cross-terms resulting from frequency modulation of signals components are still present. The cross-section $\mathrm{PW}_f(x_1, 2, f_1, 2)$ includes the cross-terms with the direction of oscillations perpendicular to the x_1-axis. The rest of cross-terms have been cancelled. The same cross-section of the dual-window PWD contains only four auto-terms.

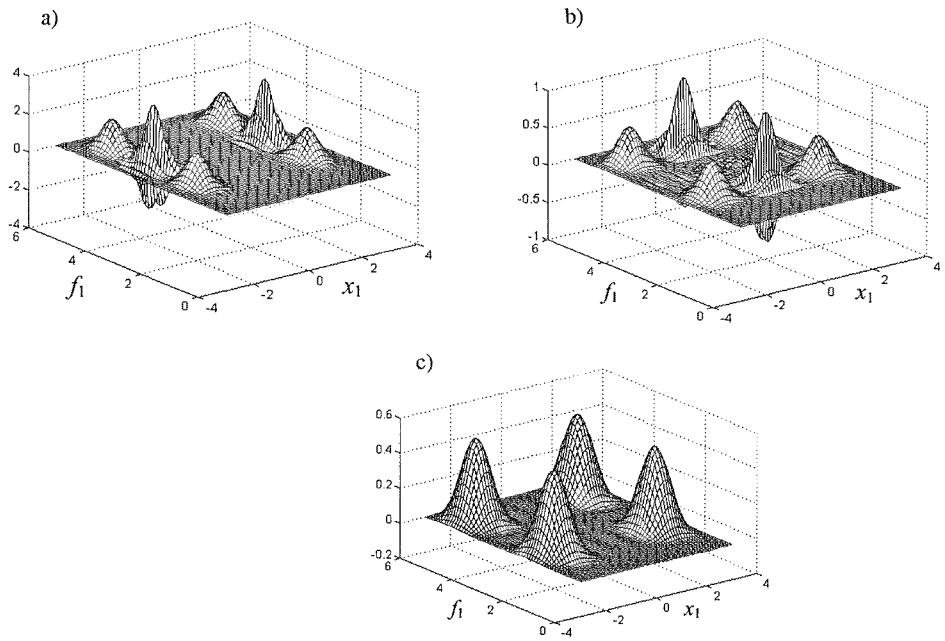

Fig. 6. Cross-sections of 4-D PWDs. (a) $\mathrm{PW}_x\ (x_1, 2, f_1, 2)$. (b) $\mathrm{PW}_f\ (x_1, 2, f_1, 2)$. (c) $\mathrm{PW}_{fx}\ (x_1, 2, f_1, 2)$

2.4. DOUBLE-DIMENSIONAL PWDs

As it was mentioned in Section 1.3, the second-order double-dimensional PWDs are defined using in (10) the window functions from Table 3 changing the variables $x_1 \to t$, $x_2 \to f$, $f_1 \to f_1$, $f_2 \to t_1$. Note that in (10), f_1 is the first-order frequency shift, while in Table 3, it represents a frequency variable. The "spatial-frequency" kernels of DDPWDs are presented in Table 4. The *second order spatial domain* DDPWD ($\mathrm{PW}_x^{(2)}$), is defined in the convolution form

Table 4

Spatial-frequency kernels of DDPWDs

Double-dimensional distributions	
Spatial-domain	$\delta(t,f) \otimes H(f_1,t_1)$
Frequency-domain	$g(t,f) \otimes \delta(f_1,t_1)$
Dual-window	$g(t,f) \otimes H(f_1,t_1)$

$$PW_x^{(2)}(t,f,f_1,t_1) = \iint H(\mu - f_1, \chi - t_1) W^{(2)}(t,f,\mu,\chi) d\mu d\chi. \tag{27}$$

The *second order frequency-domain* DDPWD ($\mathrm{PW}_f^{(2)}$) is

$$PW_f^{(2)}(t,f,f_1,t_1) = \iint g(t'-t, f'-f) W^{(2)}(t',f',f_1,t_1) dt' df' \tag{28}$$

and finally, the second order dual-window DDPWD ($\mathrm{PW}_{fx}^{(2)}$) is

$$PW_{fx}^{(2)}(t,f,f_1,t_1) = \iint \iint g(t'-t, f'-f) H(\mu - f_1, \chi - t_1) W^{(2)}(t',f',\mu,\chi) dt' df' d\mu d\chi. \tag{29}$$

We see that all DDPWDs are double or quadruple convolutions with the second-order WD.

The Fig. 7 shows the cross-sections $PW_{fx}^{(2)}(t,f,0,0)$ and $PW_f^{(2)}(t,f,0,0)$ of the test signal being a sum of two Gaussian pulses shifted in time by t_a and t_b, and modulated in frequency by f_a and f_b, i.e., $\psi(t) = e^{-a(t-t_a)^2} e^{j2\pi f_a t} + e^{-b(t-t_b)^2} e^{j2\pi f_b t}$, where $a = b = 3$, $t_a = 0.8$, $f_a = 0.8$, $t_b = 2.2$, $f_b = 2.2$. Applying the 2-D Gaussian window functions in (24) and (25) we get different results. We observe two auto-components in form of Gaussian surfaces centered at points (t_a, f_a) and (t_b, f_b) respectively and oscillating cross-terms centered at $(\frac{t_a + t_b}{2}, \frac{f_a + f_b}{2})$. The direction of oscillations is perpendicular to the line $t = f$. We observe that the slice of $\mathrm{PW}_x^{(2)}$ has a better time-frequency resolution than $\mathrm{PW}_f^{(2)}$, where all terms are distorted and only the support in the time-frequency plane remains the same.

Next Fig. 8 shows the cross-sections $\mathrm{PW}_x^{(2)}(t,f,0.5,0)$ and $\mathrm{PW}_f^{(2)}(t,f,0.5,0)$. Here, the auto- and cross-terms are well distinguished. It has been observed that when the value of μ increases considerably, the auto-terms of $\mathrm{PW}_x^{(2)}$ "draw near" each other along the line $t = f$ and for $\mu = 2.5$ almost coincide. In the case of $\mathrm{PW}_f^{(2)}$, all terms are slightly distorted. It has been noticed that for $\mu = 0.55$ [11], the cross-terms are almost totally reduced at the cost of distortions of auto-components.

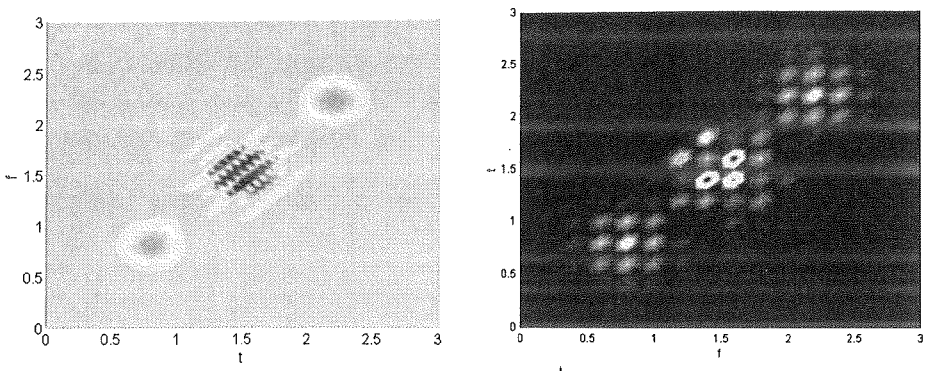

Fig. 7. Cross-sections of DDPWDs. (a) $\mathrm{PW}_x^{(2)}(t,f,0,0)$. (b) $\mathrm{PW}_f^{(2)}(t,f,0,0)$

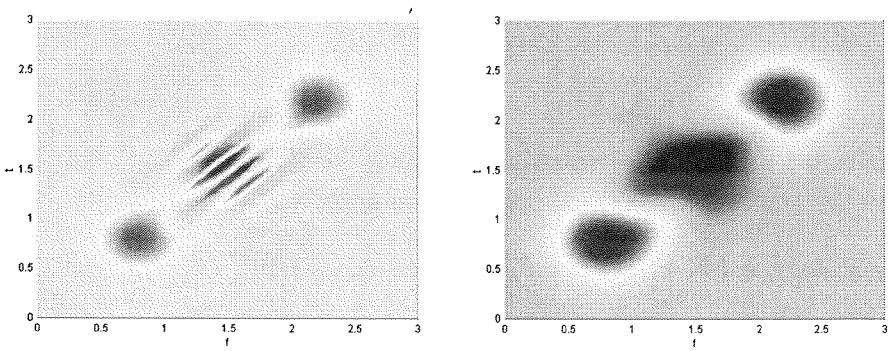

Fig. 8. Cross-sections of DDPWDs. (a) $\mathrm{PW}_x^{(2)}(t,f,0.5,0)$. (b) $\mathrm{PW}_f^{(2)}(t,f,0.5,0)$

3. SUMMARY

In this paper, the elements of the theory developed in years 2000-2005 have been presented. The basic definitions and relations have been recalled and illustrated with examples. Though the theory has been elaborated for n-D signals, we look for applications in the domain of 2-D and 3-D signals only. Most probably, the DDDs could be applied in radar signal processing. This topic has not been explored yet and actually is under consideration.

4. ACKNOWLEDGEMENTS

I would like to thank Prof. Stefan Hahn for the encouragement to prepare this paper and many helpful remarks.

5. REFERENCES

1. L. Cohen: *Time-Frequency distributions – A Review.* Proc. IEEE, 1989, vol.77, no.7, pp. 941-981.
2. P. Flandrin: *Time-frequency/time-scale analysis.* Academic Press, 1999.
3. P. M. Woodward: *Probability and Information Theory with Applications to Radar.* New York, Pergamon, 1953.
4. E. P. Wigner: *On the Quantum Correction for Thermodynamic Equilibrium.* Phys. Rev., June 1932, vol. 40, pp. 749-759.
5. K. M. Snopek: *Rozkłady klasy Cohena sygnałów wielowymiarowych i ich zastosowania (Cohen's class distributions of multidimensional signals and their applications).* PhD thesis, Warszawa 2001.
6. S. L. Hahn, K. M. Snopek: *Double-Dimensional Distributions: Another Approach to "Quartic" Distributions.* IEEE Trans. Signal Processing, vol. 50, no. 12, December 2002, pp. 2987-2997.
7. T. C. A. M. Claasen, W. F. G. Mecklenbräuker: *The Wigner Distribution – a Tool for Time-Frequency Signal Analysis, Part I – Continuous-Time Signals.* Philips J. Res., vol.35, 1980, pp. 217-250.
8. D. Gabor: *Theory of communication.* J.IEE (London), vol. 93 (III), Nov. 1946, pp.19-49.
9. L. Stanković: *A Method for Time-Frequency Analysis.* IEEE Trans. Signal Proc., vol. 42, no. 1, January 1994, pp. 225-229.
10. K. M. Snopek: *A review of the properties of the Cohen's class time-frequency distributions.* Aplikovaná Elektronika 2000, Západočeská Univerzita v Plzni, 2000, pp. 131-136.
11. K. M. Snopek: *The study of properties of double-dimensional pseudo-Wigner distributions.* XI National Symposium of Radio Science, Poznań, 7-8 April 2005, pp. 339-342.

K. M. SNOPEK

ROZKŁADY PSEUDO-WIGNERA I PODWÓJNIE WYMIAROWE ROZKŁADY PSEUDO-WIGNERA Z ROZSZERZENIEM DLA SYGNAŁÓW DWUWYMIAROWYCH

Streszczenie

Praca jest podsumowaniem teorii dwuwymiarowych i czterowymiarowych rozkładów pseudo-wignerowskich oraz podwójnie wymiarowych rozkładów pseudo-wignerowskich. Wspomniane rozkłady należą odpowiednio do klasy Cohena rozkładów wielowymiarowych i klasy Cohena rozkładów podwójnie wymiarowych. Szczegółowo opisano relacje zachodzące pomiędzy rozkładami pseudo-wignerowskimi, krótkoczasową transformatą Fouriera i wąskopasmową odwrotną transformatą Fouriera. Przedstawiono ponadto rozszerzenie teorii dla sygnałów dwuwymiarowych. Praca ilustrowana jest przykładami rozkładów pseudo-wignerowskich i podwójnie wymiarowych rozkładów pseudo-wignerowskich sygnałów testowych.

Słowa kluczowe: rozkłady czasowo-częstotliwościowe, rozkłady podwójnie wymiarowe, klasa Cohena

KWARTALNIK ELEKTRONIKI I TELEKOMUNIKACJI, 2005, 51, ZESZYT SPECJALNY, ss. 23–50

Correlations functions, power spectra and Wigner distributions of telecommunication signals

STEFAN L. HAHN

Institute of Radioelectronics,
Warsaw University of Technology
E-mail: hahn@ire.pw.edu.pl

Random M — nary baseband and the corresponding analytic modulated telecommunication signals are generated using a method described in a previous paper of the author. The paper is devoted to studies of time domain and ensemble domain correlation functions of these signals and their power spectra and Wigner time-frequency distributions. The comparison of the time domain and ensemble domain correlation functions enables the testing of the ergodic hypothesis, stationarity and so called properness of random processes representing telecommunication signals. The results depend on the applied definitions of the processes. For example, the sample functions of the baseband process may be synchroneous or asynchroneous. The carriers may have fixed or random phase. In consequence the properties of random processes representing a specific mode of transmission, *ASK*, *PSK*, *FSK* or any other depend on arbitrary assumptions. For example, the *PSK* random processes classified by some authors as improper are proper in the asynchroneous version. It was shown that calculation of the ensemble averages of the Wigner time-frequency distribution may have no sense, since the information about the modulation is lost.

Keywords: Random baseband and analytic communication signals, time domain and ensemble domain correlation functions, power spectra, Wigner time-frequency distributions.

1. MODELS OF BASEBAND TELECOMMUNICATION SIGNALS

Modern digital telecommunication uses a transmission of baseband signals using specific modulations (keying) of high frequency harmonic carriers, for example *ASK* (Amplitude Shift Keying), *PSK* (Phase Shift Keying), *FSK* (Frequency Shift Keying), *QPSK* (Quadrature Phase Shift Keying) and other. In this section we describe the properties of baseband signals. They have the form of a sequence of pulses of specific waveforms transmitted in succesive time slots of duration T, where $B = 1/T$ is called the symbol rate in bauds (frequently improperly in bits/s, since one symbol may carry

more than one bit of information). In an M-ary system the transmission alphabet consists of M different waveforms, usually the same waveforms of different weights (amplitudes). Usually $M = 2^n$. For n =1 we have a binary transmission using two symbols, for example (0, 1), for n=2 a 4-nary transmission with four symbols, for example (0,1,2,3), etc. By assuming, that the above numbers represent the amplitude of pulses, we have unipolar signals. Of course bipolar signals can be applied. However, in the case of *ASK* they should be unipolar. In this paper it is assumed that all symbols are generated with equal probabilities equal P(i) =1/M, and that symbols in successive time slots are statistically independent (no correlation). In practice, elementary pulses may have a duration greater than T yielding so called intersymbol interference.

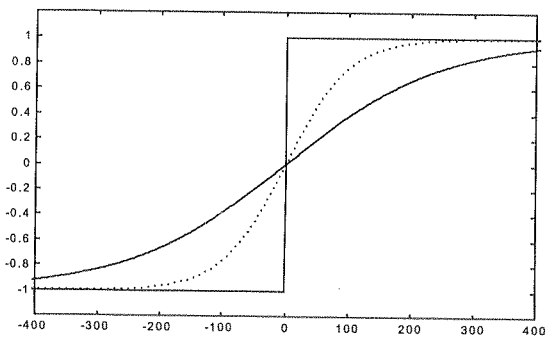

Fig. 1. The tanh(at) function with various values of a

The models of baseband signals applied in this paper use a transition between successive states modeled by the function tanh(at) [1] . The slope of the transition depends on the constant a as illustrated in Fig.1. For the large value of a we have a unit step transition with no intersymbol interference. The transmitted signal has the form of rectangular pulses of different amplitudes. Smaller values of a yield signals with intersymbol interference. The use of the tanh(at) transition has the following advantages:

1. If succesive states (symbols) are the same, the tanh(.) function saturates with no change of the saturated amplitude.
2. The waveform of the signal is defined directly in the time domain with no use of a shaping filter.

The M-ary baseband signal using the above described method is defined by the formula [1]

$$B_M(t) = \sum_{k=1}^{K} b_M(k)\{0.5 + 0.5\tanh[a(t - kT)]\} \times \{0.5 - 0.5\tanh[a(t - (k+1)T)]\} \quad (1)$$

where $b_M(k)$ are M-nary random draws with $M = 2^n$. For n =1 binary random draws, for n = 2 4-nary, e.t.c. kT is the time scale, a multiple of the elementary time slot T.

Fig. 2 shows samples of random telegraph signals generated using the Eq.(1). Remark: In C^{++} compilers $b_M(k)$ are generated using the code rand( )%M.

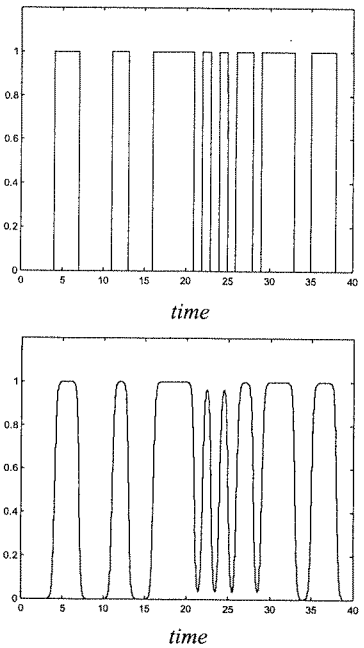

Fig. 2a. Sample function of a binary random telegraph signal. Upper: Hard keing. Lower: Soft keying

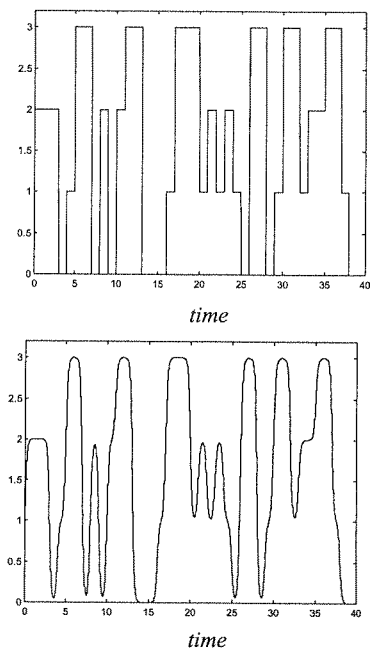

Fig. 2b. – of a 4-nary random telegraph signal. Upper: Hard keying. Lower: Soft keying

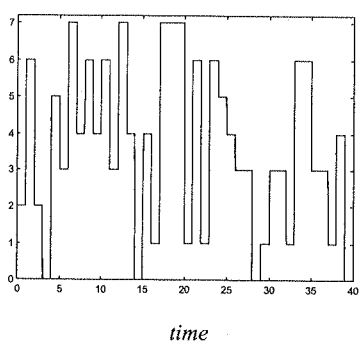

Fig. 2c. – of a 8-nary random telegraph signal

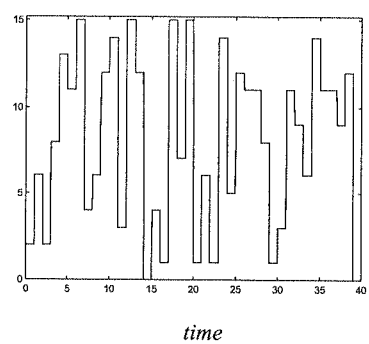

Fig. 2d. – of a 16-nary random telegraph signal

2. MODELS OF RF (modulated) TELECOMMUNICATION SIGNALS

2.1. M – NARY *ASK* (AMPLITUDE SHIFT KEYING)

A real *ASK* signal is given by the formula

$$u_{ASK}(t) = B_M(t)\cos(2\pi F_0 t + \theta) \tag{2}$$

where the instantaneous amplitude $B_M(t)$ is given by (1). If the power spectrum of $B_M(t)$ has the support limited to frequencies lower then the carrier frequency F_0, than the Hilbert transform of (2) is

$$v_{ASK}(t) = B_M(t)\sin(2\pi F_0 t + \theta) \tag{3}$$

and the analytic ASK signal due to the Bedrosian's theorem [2] has the form

$$\psi_{ASK}(t) = B_M(t)e^{f(2\pi F_0 t+\theta)} \tag{4}$$

2.2. M – NARY *PSK* (PHASE SHIFT KEYING)

2.2. M – nary *PSK* (Phase Shift Keying)

Real *PSK* signals are defined by the formula

$$u_{PSK}^{(M)}(t) = \cos(2\pi F_0 t + \theta + 2\pi B_M(t)/M) \tag{5}$$

We denote *BPSK* (Binary *PSK*) if $M = 2$, *QPSK* (Quadrature *PSK*) if $M = 4$, and in general *MPSK*. The complex form of this signal is

$$\psi_{PSK}(t) = e^{j[2\pi F_0 t+\theta+2\pi B_M(t)/M]} \tag{6}$$

and is approximately an analytic signal, if the power spectrum of ψ_{PSK} has no terms at negative frequencies [2]. The Eq.(6) defines the *QPSK* signal with a constellation $(0, \pi/2, \pi, 3\pi/4)$ (anti-clock phase rotation). Of course other constellations are possible, i.e., $(\pi/4, 3\pi/4, 5\pi/5, 7\pi/4)$.

2.3. M – NARY *FSK* (FREQUENCY SHIFT KEYING)

For hard keying let us define two modes: The instantaneous frequency of the asymetric mode is $F(t) = F_0 + B_M(t)\Delta F/(M-1)$ and of the symmetric one $F(t) = F_0 + \Delta F(2B_M(t) - M)/(2M)$. In both modes the range of frequency hopes equals ΔF with the elementary hope equal $\Delta F/(M-1)$, i.e. decreses with increasing M. In the symmetric mode, if $M = 2$, we have two states $(-\Delta F/2, \Delta F/2)$, if $M = 4$, four states $(-\Delta F/2, -\Delta F/6, \Delta F/6, \Delta F/2)$. Analogously in the asymmetric mode $(0, \Delta F)$ and $(0, \Delta F/3, 2\Delta F/3, \Delta F)$. The analytic signal for the symmetric mode is

$$\psi_{FSK}^{(M)}(t) = e^{j\{2\pi F_0 t+\Delta F(2B_M(t)-M)t/(2M)\}} \tag{7}$$

This formula is valid only for hard keying, since the instantaneous phase is given by the integtral of the instantaneous frequency. Again (7) is an analytic signal, if the power spectrum vanishes for negative frequencies. This limits the maximum value of the frequency shift. Let us mention that the correlation functions and power spectra are not the same for these modes. However, the differences are small.

3. A SHORT INTRODUCTION TO THE THEORY OF RANDOM SIGNALS

Let us recall selected notions of the theory of random signals. The name "random process" is applied to an infinite set (ensemble) of its sample functions (signals) alternatively called "realizations'. A random process is called (strictly) stationary and ergodic if its statistical properties derived from the observation of a single sample function in infinite time (in computer implementations in a long time) are the same, as derived from an infinite ensemble (in implementations a large ensemble) of its sample functions. The order of the statistics is defined by the number of fixed points of observation $(t_1, t_2, \ldots, t_n)$. A random process is called Wide Sense Stationary (*WSS*) and ergodic if the ergodic hypothesis applies for the second order statistics only, i.e., for observations in two moments t_1, t_2. Note that not all stationary processes and ergodic.

3.1. TIME DOMAIN AVERAGES

Time domain averages will be denoted by a bar over the function. For example the mean value is $u_o = \overline{u(t)}$, the correlation function $\rho(\tau) = \overline{u(t+\tau)u(t)}$ and for the zero mean signal $u_1(t) = u(t) - \overline{u(t)}$ the covariance function is $\rho_c(\tau) = \overline{u_1(t+\tau)u_1(t)}$.

3.2. ENSEMBLE AVERAGES

The capital letter E denotes the expected value of a function. The expected mean value is $u_o(t_1) = E[u(t_1)]$, the correlation function $\rho(t_1, t_2) = E[u(t_2)u(t_1)]$. For a *WSS* process u_0 is a constant independent on t_1 and the correlation function depends only on the time difference $\tau = t_2 - t_1$. A complex random process is called circularly wide sense stationary, if its correlation function is periodic w.r.t t_1. The power spectrum of a *WSS* process (Wiener-Khinschine theorem) is given by the Fourier transform

$$\rho(\tau) \overset{F}{\Leftrightarrow} G(f) = \int_{-\infty}^{\infty} \rho(\tau)\cos(2\pi f\tau)d\tau \tag{8}$$

3.3. COMPLEX ANALYTIC RANDOM PROCESSES

Let us define a complex analytic random process $\{\psi(t) = u(t) + jv(t)\}$. Each sample function of this process is an analytic function, i.e., $v(t) = H[u(t)]$, where H denotes the

Hilbert transform [3]. The terms $u(t)$ and $v(t)$ of each sample function are orthogonal, i.e.., $\overline{u(t)v(t)} = 0$. However, they are not statistically independent since the cross-correlation function $\rho_{vu}(\tau)$ equals zero only for $\tau = 0$. The complex correlation function is defined by the equation [3]

$$\rho_\psi(t_1,\tau) = E\{\psi(t_1+\tau)\psi^*(t_1)\} = \rho_{uu}(t_1,\tau) + \rho_{uv}(t_1,\tau) + j[\rho_{vu}(t_1,\tau) - \rho_{uv}(t_1,\tau)] \quad (9)$$

where $\rho_{uu}(t_1,\tau) = E\{u(t_1+\tau)u(t_1)\}, \rho_{vv}(t_1,\tau) = E\{v(t_1+\tau)v(t_1)\}$, are autocorrelation functions and $\rho_{vu}(t_1,\tau) = E\{v(t_1+\tau)u(t_1)\}, \rho_{uv}(t_1,\tau) = E\{u(t_1+\tau)v(t_1)\}$, cross-correlation functions. For a *WSS* process all are independent on t_1 , i.e., are functions of τ. In this case the power spectrum defined by this complex correlation function is one-sided. In other words the complex correlation function is an analytic function. Note that if $\{u(t)\}$ is *WSS* then $\{\psi(t)\}$ is also *WSS*. Remark: Many authors define (9) in the conjugate form $\rho_\psi(t_1,\tau) = E\{\psi(t_1)\psi^*(t_1+\tau)\}$ forgetting to mention, that this yields a power spectrum at negative frequencies.

3.4. PROPER COMPLEX RANDOM PROCESSES

A complex random process $\{\psi(t)\}$ is called proper [4] if the so called complementary correlation function vanishes, i.e.,

$$\rho_\psi(t_1,\tau) = E\{\psi(t_1+\tau)\psi(t_1\} = \rho_{uu}(t_1,\tau) - \rho_{vv}(t_1,\tau) + j[\rho_{vu}(t_1,\tau) + \rho_{uv}(t_1,\tau)] = 0 \quad (10)$$

4. CORRELATION FUNCTIONS AND POWER SPECTRA OF BASEBAND RANDOM TELEGRAPH SIGNALS

If not mentioned we present correlation functions of random telegraph signals with hard keying (unit step transitions). All functions are normalized to get $\rho(0) = 1$.

4.1. TIME DOMAIN CORRELATION FUNCTIONS

Fig. 3 presents the result of numerical calculation of the time-domain correlation functions of the random telegraph signals of Fig. 2. Theoretically, for a signal of infinite length we get a triangular function shifted vertically by the square of mean value (DC term). The mean values in Fig. 3 are not uniform due to the finite length of the signals in Fig. 2. However, the distorsions of main triangular part are negligible.

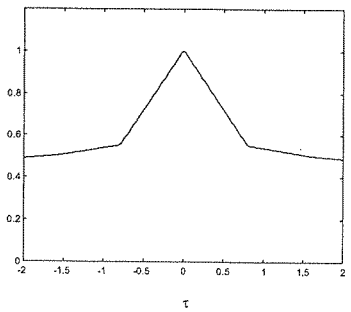

Fig. 3a. The time domain correlation function of the binary random telegraph signal of Fig. 2a.

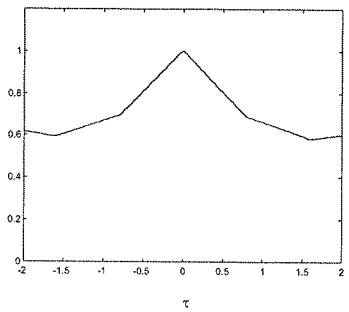

Fig. 3b. The same of the 4-nary random telegraph signal of Fig. 2b.

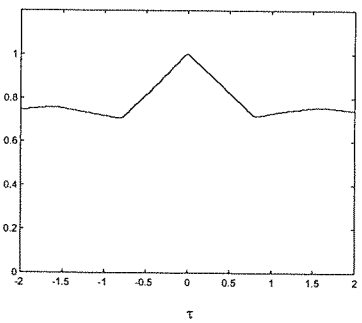

Fig. 3c. The same of the 8-nary random telegraph signal of Fig. 2c.

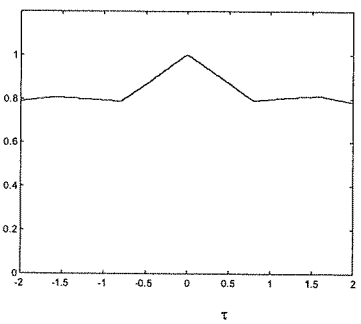

Fig. 3d. The same of the 16-nary ratelegraph signal of Fig. 2d.

4.2. ENSEMBLE CORRELATION FUNCTIONS

The sample functions of random telegraph signals do not define uniquely the corresponding random process. Let us define synchroneous SYN and asynchroneous ASYN random telegraph processes. The sample functions of the SYN process begin all at the same moments and of the ASYN at moments randomly distributed in the time slot T. The ensemble correlation functions of SYN random process are shown in Fig. 4 and of the ASYN in Fig. 5. The comparison with the time domain correlation function of Fig. 3 shows, that the ergodic hypothesis is fulfilled only for the ASYN case (triangular correlation functions) while in the SYN case we get a rectangular function. The triangular functions can be represented by the formula

$$\rho_B(\tau) = a + (1 - a)tri(\tau) \tag{11}$$

where $tri(\tau) = 1 - |\tau/T| \; for \; |\tau/T| \leq 1$; $tri(\tau) = 0$ outside this support. The value of a depends on M, as shown in Table 1.

M	2	4	8	16	32	64
a	0.5	≈ 0.64	≈ 0.71	≈ 0.715	≈ 0.725	≈ 0.75

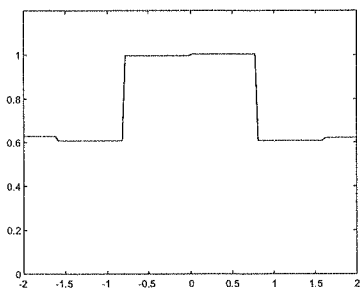

Fig. 4a. The ensemble correlation for the SYN binary process with sample functions of Fig. 2a

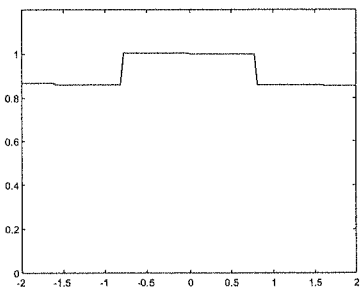

Fig. 4b. The same for the 16-nary SYN process with sample functions of Fig. 2d.

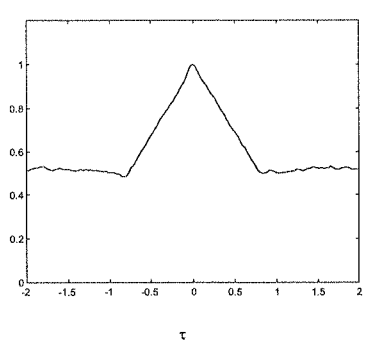

Fig. 5a. The ensemble correlation f. for the ASYN binary process with sample functions of Fig. 2a

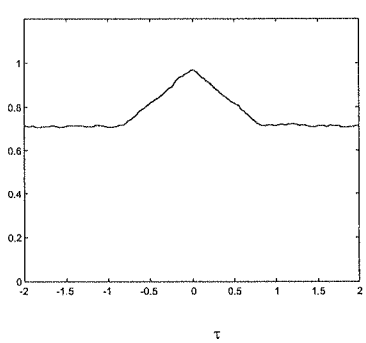

Fig. 5b. The same for the 16-nary ASYN process with sample functions of Fig. 2d.

4.3. CORRELATION FUNCTIONS BY SOFT KEYING

In principle this paper is not devoted to studying the differences between random telegraph signals with hard and soft keying. Let us present only a single example. Fig. 6 shows the time domain and ensemble correlation functions of the binary random telegraph signal of Fig. 2a (soft keying). The comparison with Figs. 5a and 5b shows that the $tri(\tau)$ function is replaced by an approximately Gaussian function. In consequence the power spectrum is also Gaussian. Notice, that $\rho(0) \approx 0.8$ since it was normalized by the crest value yielding 1 for the case of hard keying.

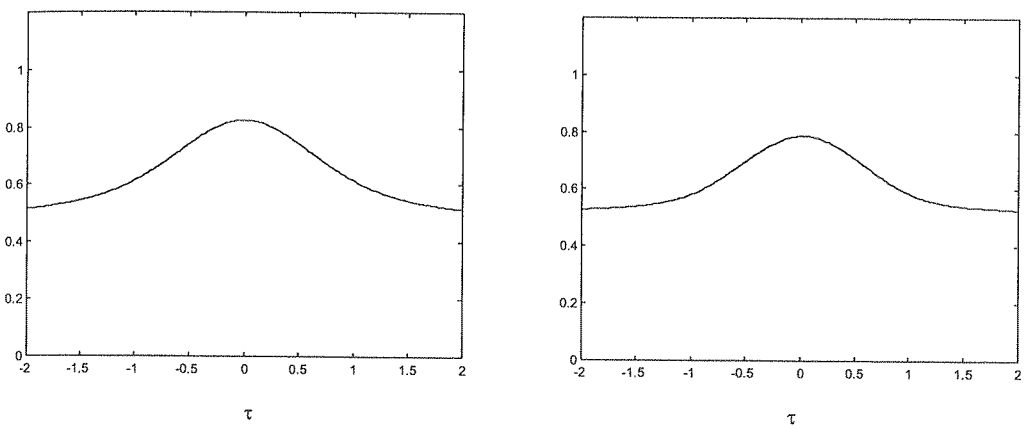

Fig. 6. Left: The time domain correlation function and right: The ensemble correlation function of the ASYN random telegraph signal of Fig. 2a., soft keying

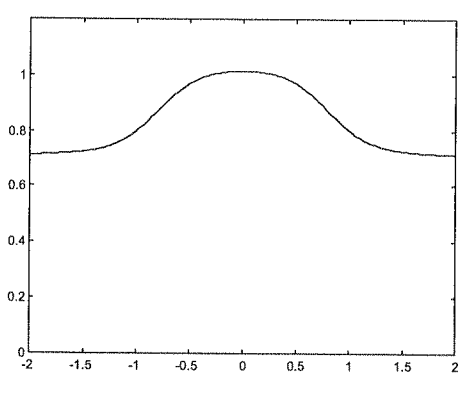

Fig. 7. The ensemble correlation function of the SYN random telegraph signal., soft keying

5. CORRELATION FUNCTION OF A HARMONIC CARRIER

As an introduction to the theory of correlations functions of modulated telecommunications signals let us present problems of calculating correlation functions of harmonic analytic carriers of the form $\psi(t) = e^{j(\Omega_0 t+\theta)}$.

5.1. TIME DOMAIN CORRELATION FUNCTION OF THE HARMONIC CARRIER

The time domain correlation function is

$$\rho(\tau) = \overline{\psi(t+\tau)\psi^*(t)} = \overline{e^{j\Omega_0(t+\tau)}e^{-j\Omega_0 t}} = e^{j\Omega_0\tau} \tag{12}$$

Let us write (12) in the form (9)

$$\rho(\tau) = \underbrace{\overline{\cos[\Omega_0(t+\tau)]\cos(\Omega_0 t)}}_{\rho_{uu}(\tau)=0.5\cos(\Omega_0\tau)} + \underbrace{\overline{\sin[\Omega_0(t+\tau)]\sin(\Omega_0 t)}}_{\rho_{vv}(\tau)=0.5\cos(\Omega_0\tau)} + j\underbrace{\overline{\sin[\Omega_0(t+\tau)]\cos(\Omega_0 t)}}_{\rho_{vu}(\tau)=0.5\sin(\Omega_0\tau)} - j\underbrace{\overline{\cos[\Omega_0(t+\tau)]\sin(\Omega_0 t)}}_{\rho_{uv}(\tau)=-0.5\sin(\Omega_0\tau)} \tag{13}$$

Elementary trigonometry shows that we get (12) and (13) since
$\overline{\cos^2(2\pi F_0 t)} = \overline{\sin^2(2\pi F_o t)} = 0.5$ and $\overline{\cos(2\pi F_0 t)\sin(2\pi F_0 t)} = 0$

5.2. ENSEMBLE CORRELATION FUNCTIONS OF THE HARMONIC CARRIER

The ensemble correlation function is defined by the formula $\rho(t_1, t_2) = E\left\{e^{j(\Omega_0 t_2+\theta)}e^{-j(\Omega_0 t_1+\theta)}\right\}$. The insertion $t_2 = t_1 + \tau$ and using trigonometric identities yields

$$\rho(t_1,\tau) = E\left\{\cos^2(\Omega_0 t_1+\theta)\right\}\cos(\Omega_0\tau) + E\left\{\sin^2(\Omega_0 t_1+\theta)\right\}\cos(\Omega_0\tau) + jE\left\{\cos^2(\Omega_0 t_1+\theta)\right\}\sin(\Omega_0\tau) - jE\left\{\sin^2(\Omega_0 t_1+\theta)\right\}\sin(\Omega_0\tau)$$

This correlation function is not uniquely defined since we should define statistical properties of the random phase θ. Let us consider two cases.
Case 1: The random variable θ or rather the random variable $\Omega_0 t_1 + \theta$ has a fixed value $\Omega_0 t_1 + \theta_0$ (its probability density has the form of a delta distribution). The derivation in Appendix1 yields

$$\rho(\tau) = \underbrace{\cos(\theta_0)\cos(\Omega_0\tau+\theta_0)}_{\rho_{uu}(\tau)} + \underbrace{\sin(\theta_0)\sin(\Omega_0\tau+\theta_0)}_{\rho_{vv}(\tau)} + j\left\{\underbrace{\cos(\theta_0)\sin(\Omega_0\tau+\theta_0)}_{\rho_{vu}(\tau)} - \underbrace{\sin(\Omega_0\tau)\cos(\Omega_0\tau+\theta_0)}_{\rho_{uv}(\tau)}\right\} \tag{14}$$

The terms ρ_{uu} and ρ_{vv} and ρ_{vu} and ρ_{uv} differ. The summation yields $\rho_{uu}+\rho_{vv} = \cos(\Omega_0\tau)$ and $\rho_{vu} - \rho_{uv} = \sin(\Omega_0\tau)$. Therefore, again $\rho(\tau) = e^{j\Omega_0\tau}$ is independent on t_1 . The process is stationary and ergodic. However, $\rho_{uu} - \rho_{vv} \neq 0$ and $\rho_{vu} + \rho_{uv} \neq 0$ and the complementary correlation function do not vanish. The process is improper.

Fig. 8 shows the changes of the terms ρ_{uu} and ρ_{vv} with θ_0. There was an excellent agreement between the pictures calculated using (14) and calculated numerically directly from the definition of the corresponding correlation functions.

Case 2. The phase is uniformely distributed in the interval 0 to 2π. We have $E\{\cos^2(\Omega_0 t_1 + \theta)\} = E\{\sin^2(\Omega_0 t_1 + \theta)\} = 0.5$ and the ensemble and time domain correlation function are the same. The process is stationary, ergodic and proper.

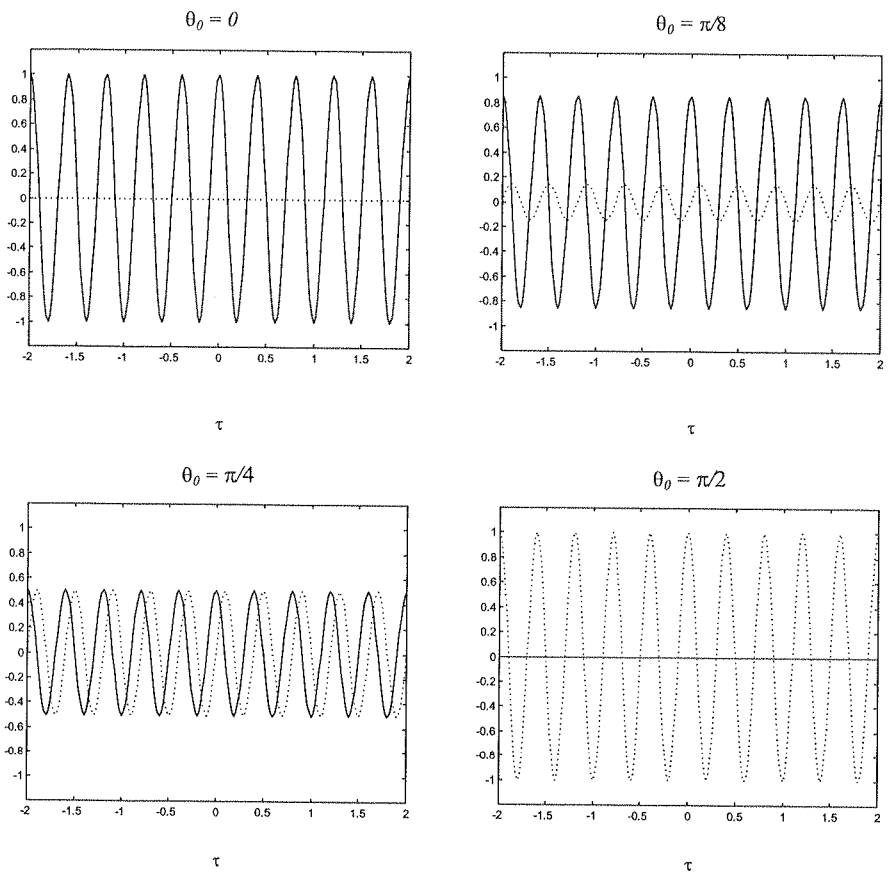

Fig. 8. The auto-terms of ensemble correlation functions for a harmonic carrier with a fixex values of the phase $\theta_0 = 0$, $\pi/8$, $\pi/4$ and $\pi/2$. Slolid line ρ_{uu}, dotted line ρ_{vv}

Note, as will be shown in next sections, that the properties of processes representing modulated signals depend on the definition of the random phase of the carrier. In consequence any statement about the properness is meaningless if the carrier phase is undefined.

6. CORRELATION FUNCTIONS OF MODULATED TELECOMMUNICATION SIGNALS

The considerations of Section IV and V shows that the ensemble correlation functions of modulated telecommunication signal are different depending on:

1. The sample functions of modulating signals are synchroneous [SYN] or asynchroneous [ASYN].
2. The sample functions of the carrier have a deterministic [DET] or random [RAN] phase.

In consequence we have four options denoted [SYN-DET], [ASYN-DET], [SYN-RAN], [ASYN-RAN]. Only the last option satisfies both the ergodic hypothesis and properness. This statement will be illustrated with examples.

6.1. CORRELATION FUNCTION OF *ASK* SIGNALS

Fig. 9 shows the real and imaginary parts of the time domain correlation function of binary *ASK*. The real part is a cosine and imaginary part a sine function with the envelope given by the correlation function of the base-band random telegraph signal displayed in Fig.3a. Let us denote the baseband correlation function of Fig. 3a by $\rho_B(\tau)$. Then the the time domain correlation function of Fig. 9 is given by the formula

$$\rho_t(\tau) = \rho_B(\tau)\, e^{j\Omega_0\tau} = [a + (1-a)\, tri(\tau)]\, e^{j2\pi F_0\tau} \tag{15}$$

(see Eq.(11)). The corresponding ensemble correlation function, case [ASYN-RAN], displayed in Fig. 10 is exaxctly the same. The ergodic hypothesis is fulfilled and the so defined *ASK* random process is proper. However, in the case [SYN-RAN] shown in Fig.11, the rectangular envelope of $\rho_B(\tau)$ corresponds to Fig. 4.

The power spectrum of the [ASYN-RAN] *ASK* process is using (8)

$$G_{ASK}(f) = a\delta(f - F_0) + (1-a)\, T \left[\frac{\sin[\pi(f - F_0)\, T]}{\pi(f - F_0)\, T}\right]^2 \tag{16}$$

The first term of (16) represents the carrier term of the spectrum and the second term the spectrum of the $tri(\tau)$ term. The ratio of the sidebands to carrier power is equal (1-a)/a. In the case [SYN-RAN] shown in Fig.11, the rectangular envelope of $\rho_B(\tau)$ corresponds to Fig. 4 and the ergodic hypothesis is not fulfilled.

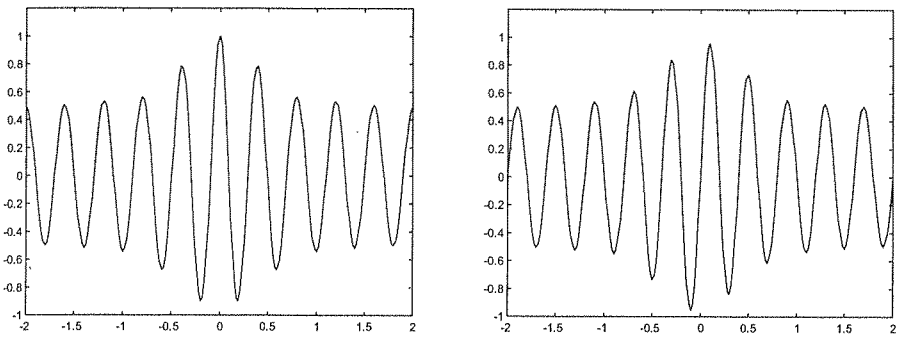

Fig. 9. Binary ASK. Terms of the complex time domain correlation function. Left the real part $\rho_{re}(\tau) = \rho_{uu} + \rho_{vv}$, right the imaginary part $\rho_{im}(\tau) = \rho_{vu} - \rho_{uv}$

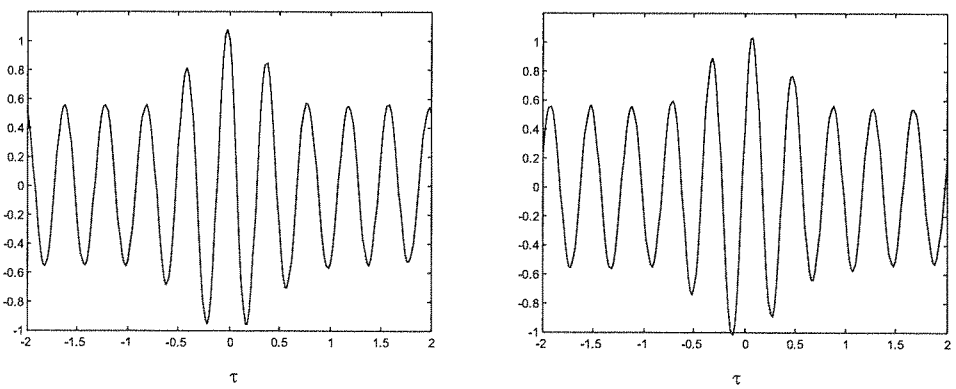

Fig. 10. Binary ASK. Terms of the complex ensemble domain corelation function. Case ASYN-RAN Left the real part $\rho_{re}(\tau) = \rho_{uu} + \rho_{vv}$, right the imaginary part $\rho_{im}(\tau) = \rho_{vu} - \rho_{uv}$

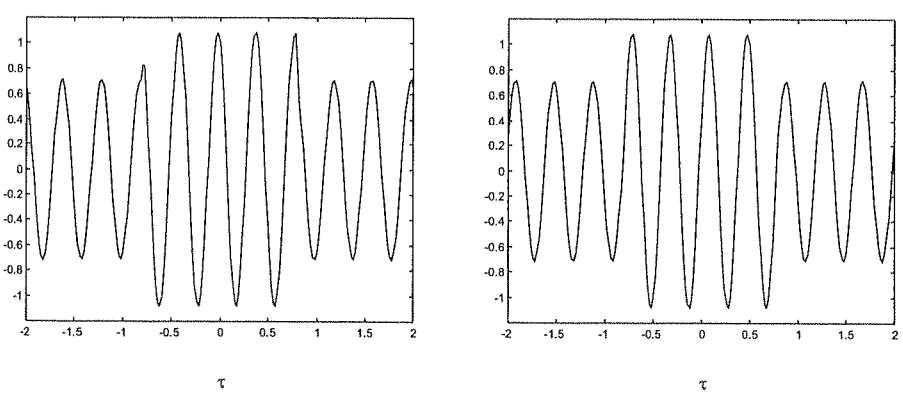

Fig. 11. Binary ASK. Terms of the complex domain correlation function. Case SYN-RAN Left the real part $\rho_{re}(\tau) = \rho_{uu} + \rho_{vv}$, right the imaginary part $\rho_{im}(\tau) = \rho_{vu} - \rho_{uv}$

6.2. CORRELATION FUNCTIONS OF *BPSK* SIGNALS

6.2.1. Case ASYN-RAN

The binary *BPSK* signal is defined by (6) and the real and imaginary parts of its time domain correlation function are presented in Fig. 12. The corresponding parts of the ensemble correlation function, case ASYN-RAN shown in Fig. 13 are the same as in Fig. 12. Therefore, the ergodic hypothesis is fulfilled. As well, the *BPSK*, case ASYN-RAN is proper. A good model of this complex quasi-analytic correlation function has the form (dotted lines in Fig. 12)

$$\rho_t(\tau) = \rho_E(\tau) = e^{-0.68\tau^2} e^{j\Omega_0 \tau} \tag{17}$$

i.e., a harmonic function with a Gaussian envelope. The ensemble normalized correlation functions of *BPSK* and *QPSK* and *MPSK* are the same, as illustrated by comparison of Figs. 13, 14 and 15. In consequence the power spectra are also the same and Gaussian since the Fourier transform of a Gaussian correlation function is Gaussian and given by the formula

$$G(f) = \sqrt{\frac{\pi}{\alpha}} e^{-\frac{\pi^2 (f-F_0)^2}{\alpha}} \tag{18}$$

where $\alpha = 0.68$

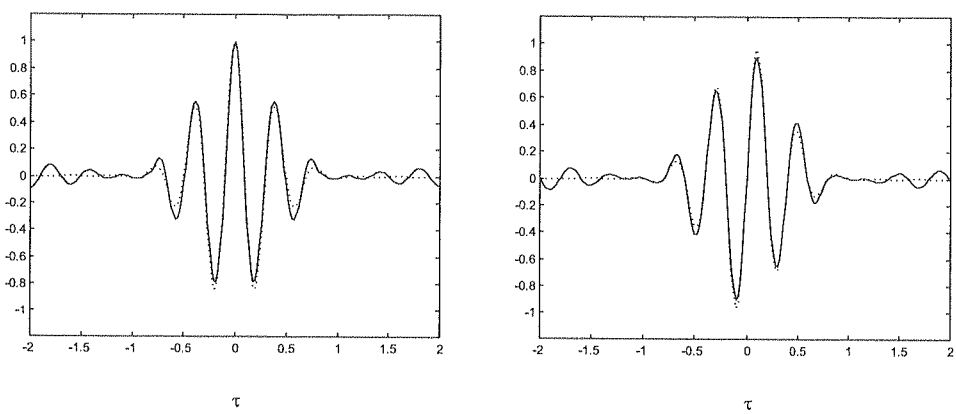

Fig. 12. Time domain correlation functions of *BPSK* signals. $\rho_{uu}(\tau) = \rho_{vv}(\tau)$ (dotted line), right: $\rho_{vu}(\tau) = -\rho_{uv}(\tau)$ (dotted line)

These figures show that the *BPSK* random process, case ASYN-RAN, is stationary, ergodic and proper. This contradicts the statements in [5], [6] and [7] that *BPSK* signals are improper. The authors of the above papers have not defined the various cases including the case ASYN-RAN

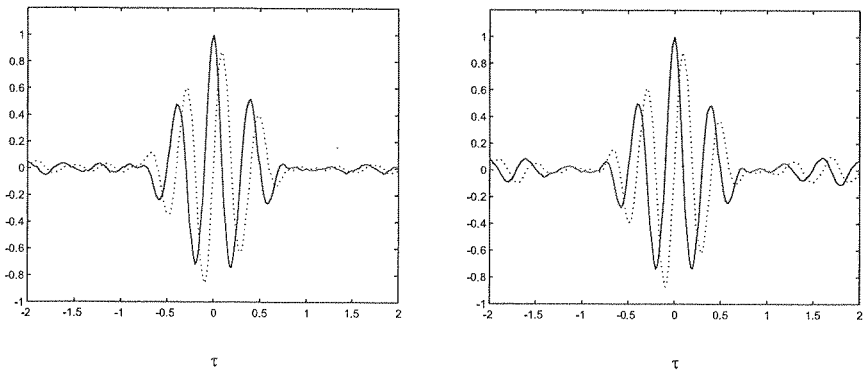

Fig. 13. Ensemble correlation functions of *BPSK* signal, case ASYN- RAN, calculated for two time moments $t_1 = 4$ and $t_1 = 32$. The functions $\rho_{uu}(\tau) = \rho_{vv}(\tau)$ are the same (ρ_{uu} — solid line) and the functions $\rho_{vu}(\tau) = -\rho_{uv}(\tau)$ are of opposite signs (ρ_{vu} — dotted line)

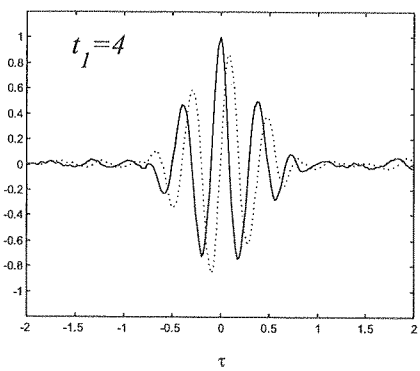

Fig. 14. Ensemble correlation function of *QPSK*. Solid line $\rho_{uu} + \rho_{vv}$, dotted line $\rho_{vu} - \rho_{uv}$

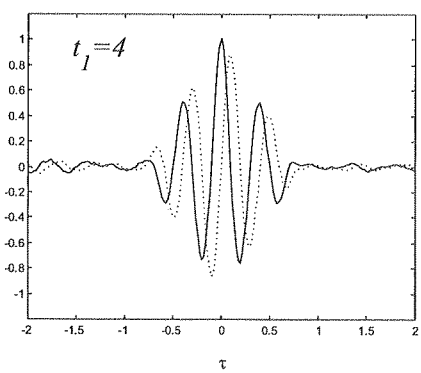

Fig. 15. Ensemble correlation function of *16PSK*. Solid line $\rho_{uu} + \rho_{vv}$, dotted line $\rho_{vu} - \rho_{uv}$

6.2.2. Case ASYN-DET

The correlations functions of *BPSK* signals with asynchroneous keying and a deterministic phase of the carrier are shown in Fig. 16. They have the form given by (17) with the carrier term given by (14). Compare Fig. (8) and Fig. 16 for the phase $\theta_0 = \pi/4$.

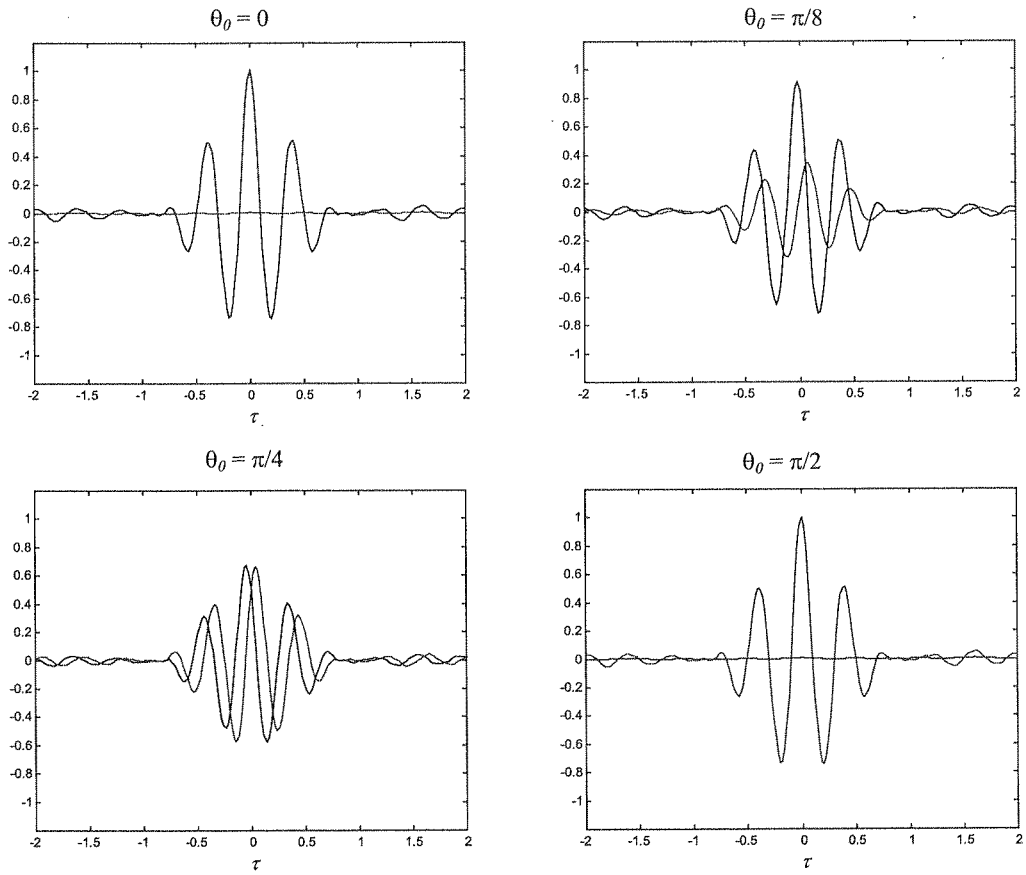

Fig. 16. Auto-terms of the ensemble correlation function of *BPSK*, case ASYN-DET, for selected values of the fixed phase of the carrier $\theta_0 = 0$, $\pi/8$, $\pi/4$ and $\pi/2$. Solid lines ρ_{uu}, dotted lines ρ_{vv}. The addition $\rho_{uu} + \rho_{vv}$ yields for any θ_0 the functions of Fig. 16a or 16d. The pictures are the same for any value of t_1

6.3. CORRELATION FUNCTIONS OF *FSK* SIGNALS

The time domain correlation function is displayed in Fig. 17. The ensemble correlation function, case ASYN-RAN, displayed in Fig.18 is periodic, i.e., $\rho_E(t_1, \tau) = \rho_E(t_1 + kT_p, \tau)$, where k= 0, 1, 2 ...., and T_p is a period. Therefore, the ASYN-RAN *FSK* process is cyclostationary [7]. Of course the ergodic hypothesis is not fulfilled. The same statement applies for *MFSK*. However, the analysis of the power spectra defined by 2-D Fourier transforms of the cyclostationary correlation function is out of the scope of this paper. Fig. 17 yields the evidence, that for the *FSK* process the conditions of properness are still fulfilled.

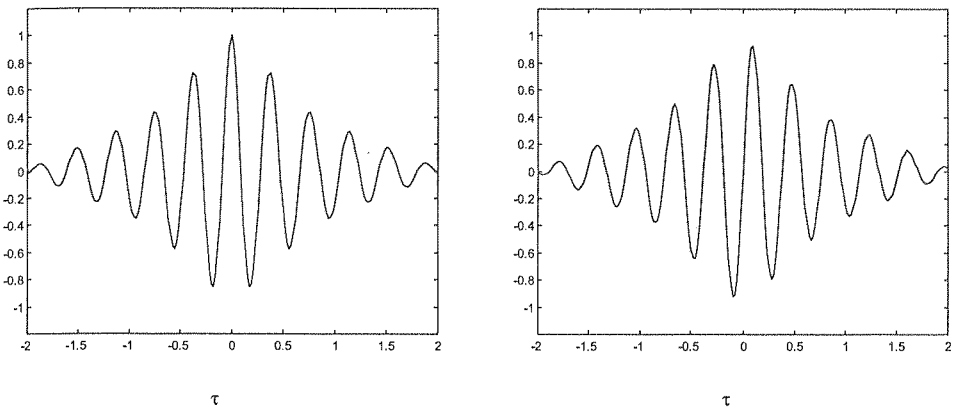

Fig. 17. Time domain correlation functions of the *FSK* signal. Left the auto-correlation functions $\rho_{uu}(\tau) = \rho_{vv}(\tau)$, and right the cross-correlation functions $\rho_{vu}(\tau) = -\rho_{uv}(\tau)$

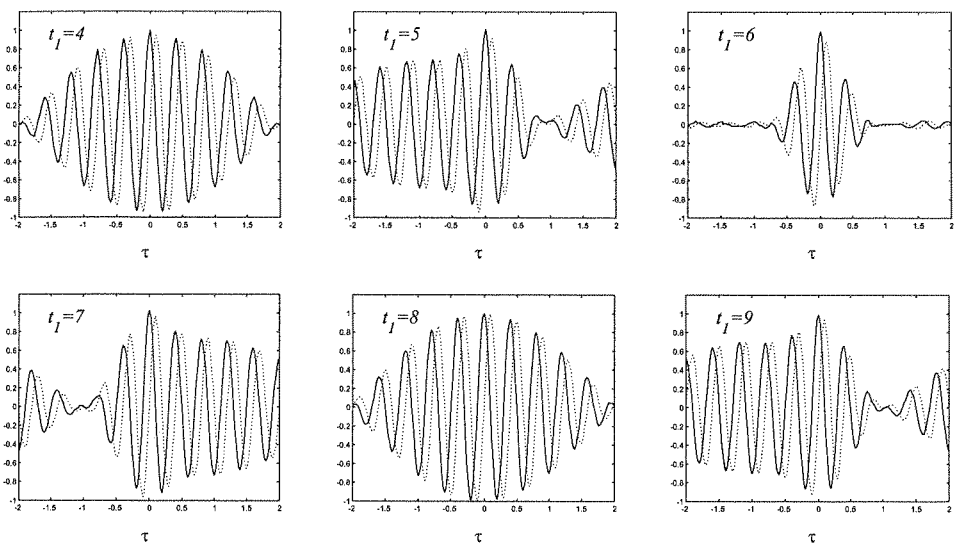

Fig. 18. A galery of ensemble correlation functions of *FSK* random process at successive time moments t_1 illustrate the cyclostationary property. The solid lines diplay the autocorrelations functions and dotted lines- the cross- correlations functions. The property that $\rho_{uu}(\tau) = \rho(\tau)$ and $\rho_{vu}(\tau) = -\rho_{uv}(\tau)$ is still valid

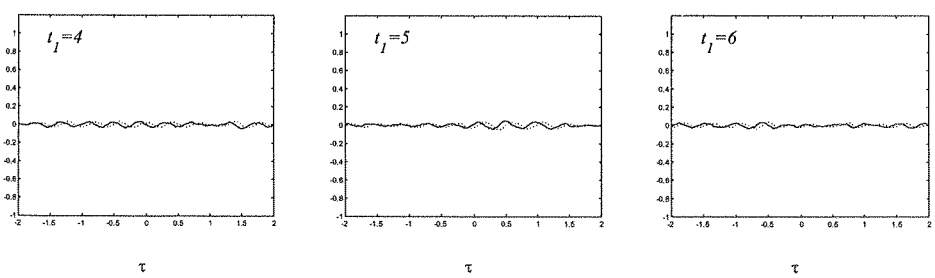

Fig. 19. Solid lines- the difference $(\rho_{uv} - \rho_{vv})/2$, Dotted lines- the sum $(\rho_{vu} + \rho_{uv})/2$

All the above correlation functions are calculated for symmetric keying. For asymmetric keying the envelopes are the same. However, the zero crossings are nonuniform yielding a "chirp" like behaviour. We do not present pictures of this effect.

7. WIGNER DISTRIBUTIONS OF RANDOM TELECOMMUNICATION SIGNALS.

7.1. RECALL OF THE BASIC PROPERTIES OF *WD*'S OF ANALYTIC SIGNALS

The time-frequency distribution called Wigner distribution [8] of a complex signal $\psi(t) = u(t) + jv(t)$ is defined by the Fourier transform w.r.t the time shift variable τ of the correlation product

$$r_\psi(t,\tau) = \psi(t+0.5\tau)\,\psi^*(t-0.5\tau) \tag{19}$$

$$W_\psi(t,f) = \int r_\psi(t,\tau)\, e^{-j2\pi f\tau} d\tau \tag{20}$$

The *WD* of any complex signal is a real function and of analytic signals is a one-sided function of frequency in the half-plane $f > 0$. The WD of the conjugate analytic signal $W_{\psi^*}(t,f) = W_\psi(t,-f)$ is a one-sided function in the half-plane $f < 0$ and is a mirror image of $W_\psi(t,f)$ w.r.t. the axis $t = 0$. Since the real part of the analytic signal is $u(t) = 0.5[\psi(t) + \psi^*(t)]$ and analogously $v(t) = 0.5j[\psi^*(t) - \psi(t)]$, the *WD's* of the real functions $u(t)$ and $v(t)$ are

$$W_u(t,f) = \int u(t+\tau/2)\,u(t-\tau/2)\cos(2\pi f\tau)\,d\tau = \frac{1}{4}W_\psi(t,f) + \frac{1}{4}W_{\psi^*}(t,f) + \frac{1}{2}W_{cross}(t,f)$$

$$W_v(t,f) = \int v(t+\tau/2)\,v(t-\tau/2)\cos(2\pi f\tau)\,d\tau = \frac{1}{4}W_\psi(t,f) + \frac{1}{4}W_{\psi^*}(t,f) - \frac{1}{2}W_{cross}(t,f)$$

and differ by the sign of the cross term. The subtruction yields the following form

$$W_\psi^{cross}(t,f) = 2\,[W_u(t,f) - W_v(t,f)] \tag{21}$$

The WD is a bilinear operation and (21) represents cross-terms due to the interaction of W_ψ with W_ψ^*, i.e., between terms in the half-planes $f > 0$ and $f < 0$ Analogously to the definition of the complementary correlation function given by the Eq.(10) , let

us define the complementary correlation product $r_{\psi}^{comp}(t,\tau) = \psi(t+0.5)\psi(t-0.5\tau)$ and define the complementary WD

$$W_{\psi}^{comp}(t,f) = \int r_{\psi}^{comp}(t,\tau)\, e^{-j2\pi f\tau} d\tau \tag{22}$$

This is a complex function. However, it can be shown that $W_{\psi}^{cross}(t,f)=2\,\mathrm{Re}\left\{W_{\psi}^{comp}(t,f)\right\}$ Consider the following marginal of the WD

$$E_{\psi} = \iint W_{\psi}(t,f)\, dtdf = \int |\psi(t)|^2\, dt \tag{23}$$

which equals the energy of the analytic signal. For many random signals the WD has the form of a bipolar random field. Let us call the integral

$$E_{\psi}^{+} = \iint \frac{1}{2}\left\{W_{\psi}(t,f) + \left|W_{\psi}(t,f)\right|\right\} dtdf \tag{24}$$

the positive energy and the integral

$$E_{\psi}^{-} = \iint \frac{1}{2}\left\{W_{\psi}(t,f) - \left|W_{\psi}(t,f)\right|\right\} dtdf \tag{25}$$

the negative energy of the random field. Evidently (23) is satisfied only if $E_{\psi}^{+} > E_{\psi}^{-}$. Let us mention that the energy of the $W_{\psi}^{cross}(t,f)$ equals zero, since

$$E_{\psi}^{cross} = \iint W_{\psi}^{cross}(t,f)\, dtdf = 0 \tag{26}$$

7.2. TIME AVERAGE OF THE WIGNER DISTRIBUTION

The time average of the WD of an analytic signal is defined by the integral [3]

$$\overline{W(t,f)} = \lim_{T\to\infty}\left\{\frac{1}{2T}\int_{-T}^{T}\left[\psi(t+\tau/2)\,\psi^{*}(t-\tau/2)\, e^{-j2\pi f\tau} d\tau\right] dt\right\} \tag{27}$$

Let us change the order of integration

$$\overline{W(t,f)} = \int_{-\infty}^{\infty}\left\{\lim_{T\to\infty}\int_{-T}^{T}\psi(t+\tau/2)\,\psi^{*}(t-\tau/2)\, dt\right\} e^{-j2\pi f\tau} d\tau \tag{28}$$

The limit in paranthesis yields the complex analytic autocorrelation function. Therefore, we get

$$\overline{W(t,f)} = 2\int_{-\infty}^{\infty}\left[\rho_{uu}(\tau) + j\rho_{vu}(\tau)\right] e^{-j2\pi f\tau} d\tau = 2\left[1+\mathrm{sgn}(f)\right] G(f) \tag{29}$$

This is the Fourier transform of the analytic correlation function equal to the one sided power spectrum (Wiener- Khinschine theorem).

7.3. ENSEMBLE AVERAGE OF THE WIGNER DISTRIBUTION

Consider a complex analytic random process $\{\psi(t)\}$ with sample functions $\psi_1(t)$, $\psi_2(t)$, ... Let us denote the Wigner distribution of each sample function by W_i and define the ensemble average

$$E\left\{W_\psi(t,f)\right\} = \left[\lim_{N\to\infty}\sum_{i=1}^{N} W_i(t,f)\right]/N \tag{30}$$

Of course in computer simulations the value of N is finite and should be sufficiently large. The ensemble average differs much from the WD of a single sample function. Let us define the normalized energy difference

$$\varepsilon = \frac{E_\psi^+ - E_{\psi^-}}{E_\psi^+ + E_\psi^-} \tag{31}$$

For the WD of a single sample function $\varepsilon << 1$ and rises asymptotically to 1 for large N. Therefore, in the limit $N \to \infty$ $E\{W_\psi\}$ defines a positive valued distribution.

7.4. WIGNER DISTRIBUTION OF THE HARMONIC CARRIER

The Wigner distribution of the harmonic carrier $\psi(t) = e^{j(2\pi f_0 t+\theta)}$ is $W(t,f) = \delta(f - f_0) \otimes 1_t$, where $1_t = 1$ for all t and is represented by a delta ridge displayed in Fig. 19, left. However, in computer simulations we deal with carriers of finite length and the delta ridge collapses to a triangular ridge of Fig.19, right..

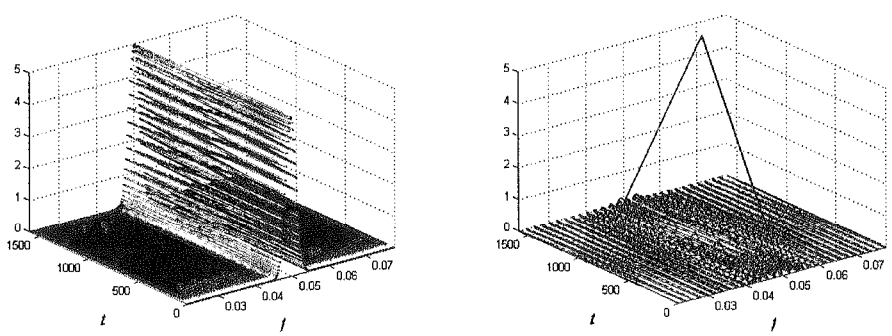

Fig. 19a. Left: The computer simulation of $W(t,f) = \delta(f - f_0) \otimes 1_t$. Right: The same for a carrier of finite lenght

7.5. WIGNER DISTRIBUTION OF BINARY *ASK*

Fig. 20 shows the WD of a single sample function of the *ASK* signal, case ASYN-RAN and Fig. 21 the corresponding ensemble average for 150 samples. We

observe the cancellation of the side-bands of the amplitude modulation. The cross WD of a single sample function is shown in Fig. 22 and the corresponding ensemble average in Fig. 23. It represents the triangle version of the the cross terms of a real harmonic carrier $u(t) = \cos(2\pi f_0 t)$, $W^{cross}(t,f) = 2\delta(f)\cos(4\pi f_0 t)$. Again, the side-bands are cancelled.

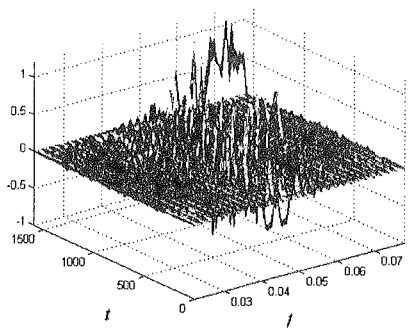

Fig. 20. The WD of a single sample of ASK

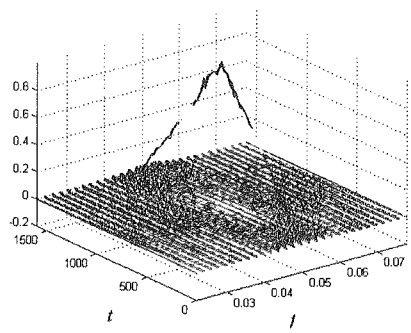

Fig. 21. The ensemble average of 150 $WD's$ of ASK signals

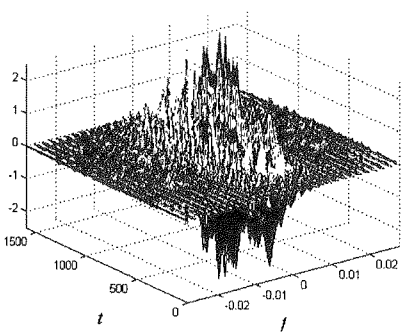

Fig. 22. The W_{ψ}^{cross} of a single sample of ASK

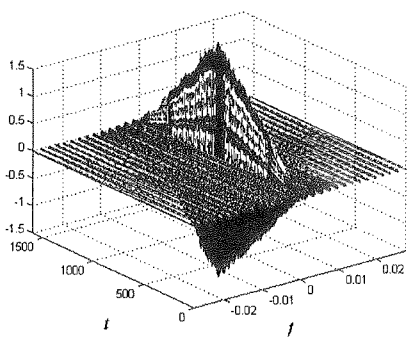

Fig. 23. The ensemble average of 150 samples of $W_{\psi^{cross}}$ of ASK

7.6. WIGNER DISTRIBUTION OF *BPSK*

The WD of a single sample of a random $BPSK$ signal is displayed in Fig. 24 and has the form of a bipolar random field. Its ensemble average for 50 sample functions is shown in Fig. 25 and exactly as in the case of ASK is a triangular delta ridge of a WD of the carrier signal. We obseve again, that in the ensemble average any information

about the side-bands of the *BPSK* signal is lost. The same statement applies to the cross WD's shown in Figs. 26 and 27.

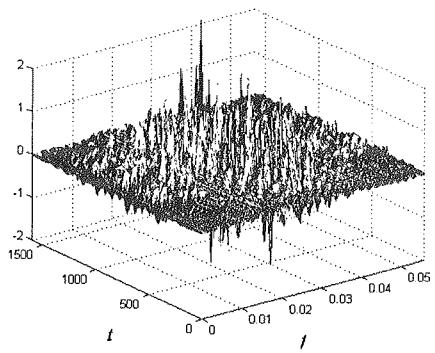

Fig. 24. The *WD* of a single sample of *BPSK*

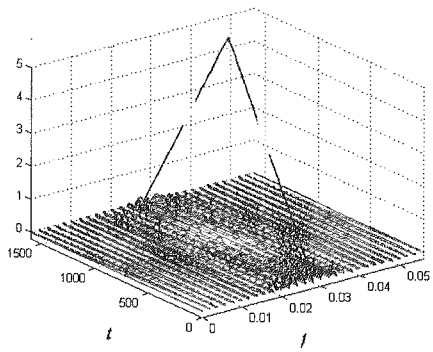

Fig. 25. The ensemble average of 50 samples of *WD's* of *BPSK* signals

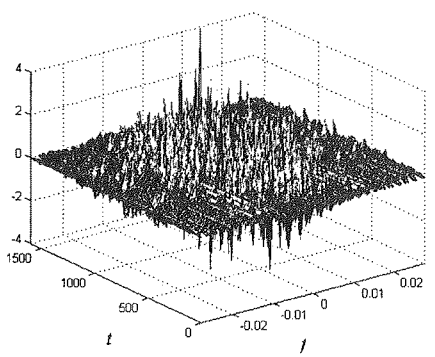

Fig. 26. W_{ψ}^{cross} of a single sample of *BPSK*

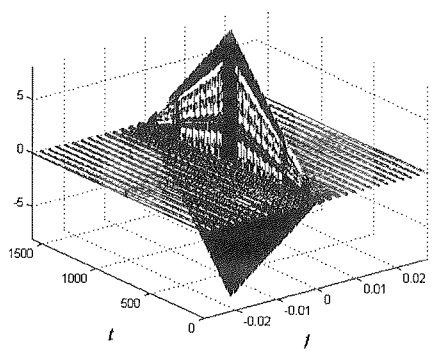

Fig. 27. The ensemble average of 50 samples of the W_{ψ}^{cross} of *BPSK*

7.7. WIGNER DISTRIBUTION OF BINARY *FSK*

Fig. 28 shows the Wigner distribution of a single sample function of *FSK* . The corresponding ensemble average for 50 samples is shown in Fig. 29. It differs from the analogous distributions of the *ASK* (Fig. 21) and *BPSK* (Fig. 25) having not the form of the delta ridge of the *WD* of the carrier. The corresponding cross *WD* for a single sample is shown in Fig. 30 and the ensemble average for 150 samples are displayed in Fig. 31.

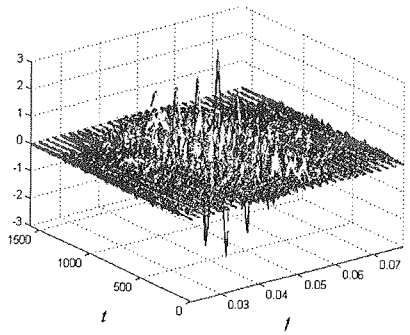

Fig. 28. The WD of a single sample of a FSK signal

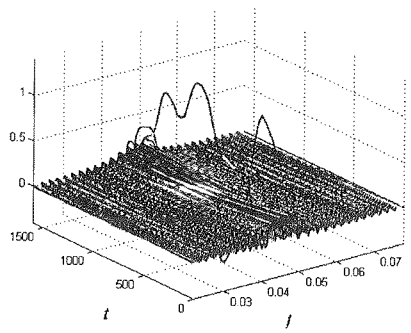

Fig. 29. The ensemble average for 50 samples of the $WD's$ of FSK

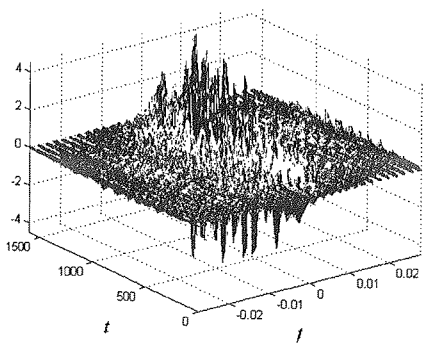

Fig. 30. The W_{ψ}^{cross} of a single sample of a FSK

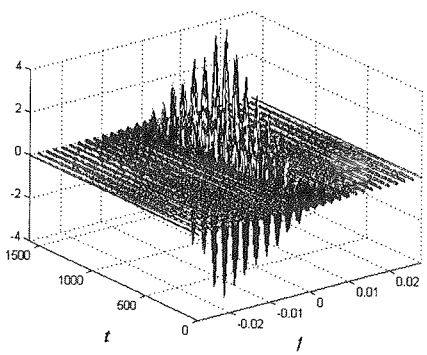

Fig. 31. The ensemble average for 50 samples of the W_{ψ}^{cross} of FSK signals

7.8. WIGNER DISTRIBUTION OF 4FSK

The $WD's$ of $4FSK$ displayed in Figs. 32 and 33 are similar as the corresponding $WD's$ of binary FSK (Figs. 28 and 29). However, to get good resolution a larger number of samples is needed.

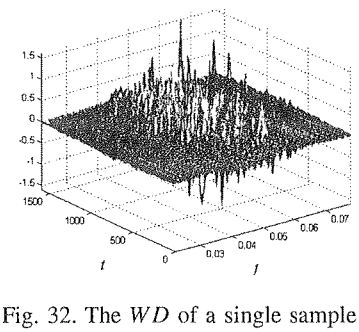

Fig. 32. The WD of a single sample of a $4FSK$ signal

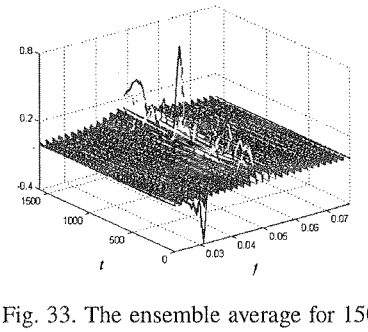

Fig. 33. The ensemble average for 150 samples of the WD of $4FSK$ signals

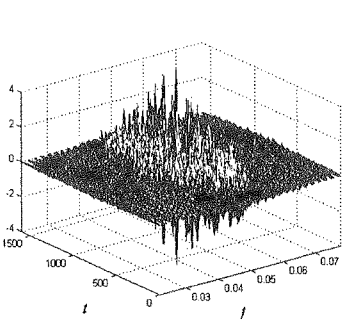

Fig. 34. The W_{ψ}^{cross} of a single sample of a $4FSK$ signal

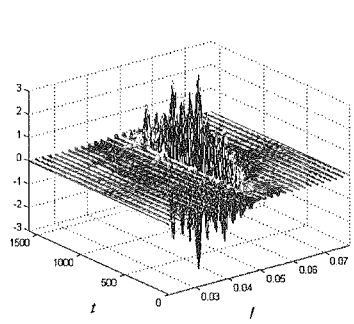

Fig. 35. The ensemble average for 150 samples of the W_{ψ}^{cross} of $4FSK$ signals

8. CONCLUSIONS

The models of telecommunications signals used in this paper to study the corresponding correlation functions, power spectra and Wigner distributions are efficiently implemented using the transition between states described by the tanh() function. Binary and M — nary baseband random telegraph signals are generated using a single formula (1). A single parameter controls the slope of the transition enabling realizations of unit step transitions or soft transitions.

It was shown that the notions of random processes representing baseband signals and modulated signals are not unique. Especially the set of the sample functions of a baseband random process can be synchroneous or asynchroneous Actually the author has no knowledge, whether this fact has been described in any source. As well, the sample functions of the harmonic carrier can be defined to have a fixed phase (probability density given by a delta distribution) or a random phase uniformely distributed in the intarval $0 - 2\pi$. Most examples of correlation functions, power spectra and Wigner distributions presented in this paper apply asynchronrous baseband signals and random phase of the carrier. With these assumptions it was shown:

1. The *ASK* and *BPSK* processes are ergodic, stationary and proper. Let us mention that other authors classify *BPSK* processes as improper [5], [6] and [7]. It seems that they overlooked to define, whether the sample functions are synchroneous or asynchroneous.
2. The *FSK* signal, binary or M-nary are cyclostationary and proper.
3. Two processes may have equal real and imaginary parts of the complex correlation function (9), i.e., equal shapes of $\mathrm{Re} = \rho_{uu}(\tau + \rho_{vv}(\tau)$ and $\mathrm{Im} = \rho(\tau) - \rho_{uv}(\tau)$ with different shapes of $\rho_{uu}(\tau), \rho_{vv}(\tau), \rho_{vu}(\tau)$ and $\rho_{uv}(\tau)$. However, for the cmplementary correlation function the terms $\mathrm{Re}^{compl} = \rho_{uu}(\tau) - \rho_{vv}(\tau)$ and $\mathrm{Im}^{compl} = \rho_{vu}(\tau) + \rho_{uv}(\tau)$ are equal zero only, if $\rho_{uu}(\tau) = \rho_{vv}(\tau)$ and $\rho_{vu}(\tau) = -\rho_{uv}(\tau)$. Therefore, two processes with equal correlation functions and equal power spectra may differ as regards properness. A good example is the process with sample functions of a harmonic carrier and the corresponding process of *BPSK*.
4. Thw usefulness of calculation of the ensemble averages of Wigner distributions of ASK and PSK signals is questionable since the information about the sidebands is lost. Of course, consequently there is no sense to calculate the complementary Wigner distributions [5].

Not all aspects of the problems presented in this paper are sufficiently described. Further research is needed for better descriptions.

9. REFERENCES

1. S. L. Hahn: *Applications of the Hyperbolic Tangens Function in Signal Processing, Proceedings*, XI National Symposium of Radio Science, URSI 2005, Poznań, pp. 329-333.
2. E. Bedrosian: *A Product Theorem for Hilbert Transforms*, Proc.IEEE (Lett.), vol. 51, No. 5, May 1963, pp. 868-869.
3. S. L. Hahn: *Hilbert Transforms in Signal Processing*, Artech House, Boston-London, 1996.
4. F. D. Neeser, J. L. Massey: *Proper Complex Random Processes with Applications to Information Theory*, IEEE Trans.on Information Theory, vol. 39, No. 4, July 1993, pp. 1293-1302.
5. P. J. Schreier, L. L. Scharf: *Stochastic Time-Frequency Analysis Using the Analytic Signal: Why the Complementary Distribution Matters.*, IEEE Trans.on Signal Processing, vol. 51. No. 12., December 2003, pp. 3071-3079.
6. P.J. Schreier, L. L. Scharf: *Second-Order Analysis of Improper Complex Random Vectors and Processes*, IEEE Trans.on Signal Processing, vol. 51. No. 3., March 2003, pp. 714-725
7. A. Napolitano, C. M. Spooner: *Cyclic Spectral Analysis of Continous-Phase Modulated Signals*, IEEE Trans.on Signal Processing, vol.49. No. 3., January 2001, pp. 30-44.
8. E. P. Wigner: *On the Quantum Correction for Thermodynamic Equilibrium*, Phys. Rev. Vol. 40, 1932, pp. 749-759.

10. APPENDIX 1

The correlation function of the random process $\{e^{j(\Omega_0 t=\theta)}\}$ is defined by the formula

$$\rho(t_1, t_2) = E\left\{e^{j\{\Omega_0 t_2+\theta\}} e^{-j(\Omega_0 t_1+\theta)}\right\} \tag{A1}$$

The insertion $t_2 = t_1 + \tau$ and the application of trigonometric identities yiels

$$\begin{aligned}\rho(t_1,\tau) = {} & E\left\{\cos^2(\Omega_0 t_1 + \theta)\right\}\cos(\Omega_0\tau) + E\left\{\sin^2(\Omega_0 t_1)\right\}\cos(\Omega_0\tau) \\ & + jE\left\{\cos^2(\Omega_0 t_1 + \theta)\right\}\sin(\Omega_0\tau) + jE\left\{\sin^2(\Omega_0 t_1)\right\}\sin(\Omega_0\tau)\end{aligned} \tag{A2}$$

Consider a random variable $\theta_t = \Omega_0 t_1 + \theta$ with a probability density function

$$p(\theta_t) = \delta(\theta_t - \theta_0) \tag{A3}$$

Let us derive the expected value of the random variable

$$Y = \cos^2(\theta_t) \tag{A4}$$

The characteristic function of the random variable Y is

$$C_Y(\omega) = \int_{-\infty}^{\infty} e^{-j\omega Y} p(\theta_t)\, d\theta_t = \int_{-\infty}^{\infty} e^{-j\omega\cos^2(\theta_t)}\delta(\theta_t - \theta_0)\, d\theta_t = e^{-j\omega\cos^2(\theta_0)} \tag{A5}$$

The probability density function of the random variable Y is given by the inverse Fourier transform of $C_Y(\omega)$, i.e.,

$$p_Y(Y) = \frac{1}{2\pi}\int_{-\infty}^{\infty} e^{-j\omega\cos^2(\theta_0)} e^{j\omega Y} d\omega = \delta\left[Y - \cos^2(\theta_0)\right] \tag{A6}$$

Therefore,

$$E\{Y\} = \int_{-\infty}^{\infty} Y\delta\left[Y - \cos^2(\theta_0)\right] dY = \cos^2(\theta_0) \tag{A7}$$

Notice, that the this expected value do not depend on t_1. Analogously we can derive

$$E\left\{\sin^2(\theta_t)\right\} = \sin^2(\theta_0) \tag{A8}$$

and

$$E\{\sin(\Omega_0 t + \theta_0)\cos(\Omega_0 t + \theta_0)\} = \sin(\theta_0)\cos(\theta_0) \tag{A9}$$

The insertion of (A7) and (A8) in (A2) yields the correlation function (14).

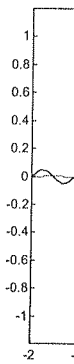

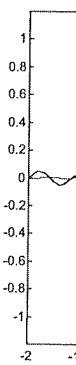

Fig. 3
BPSK, c
Solid li

Opi
losowych

11. APPENDIX 2

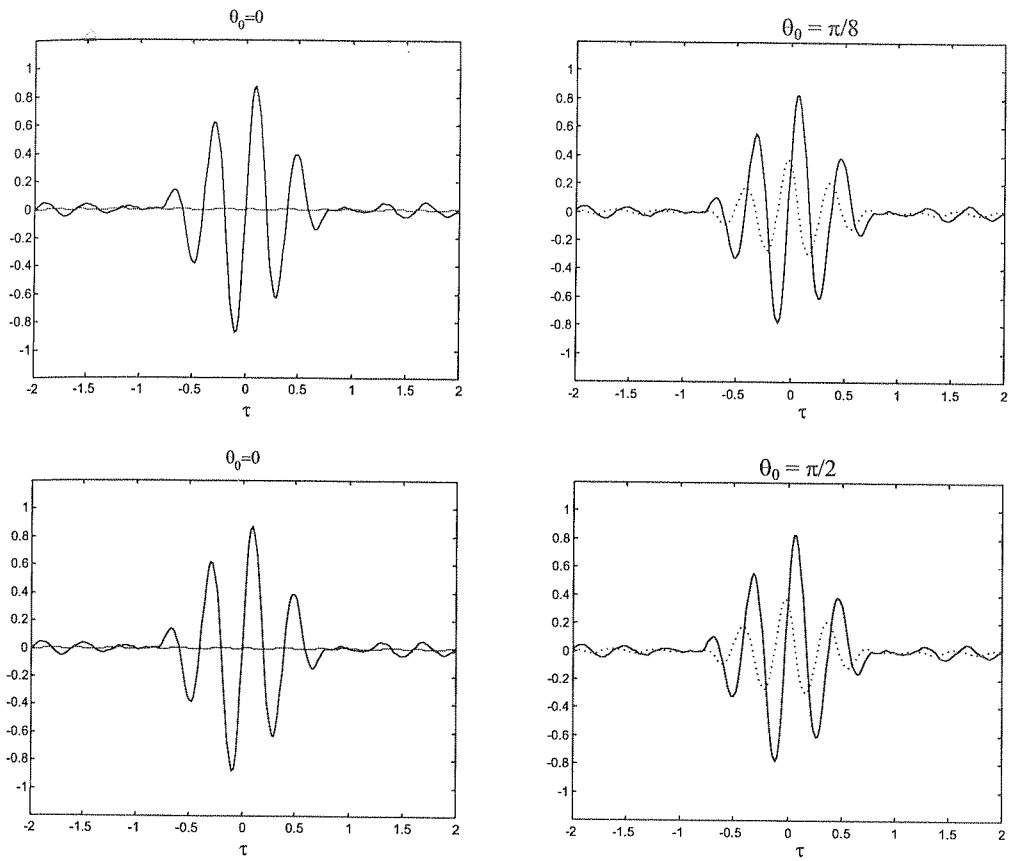

Fig. 36. The second part of Fig. 16 presents the cross terms of the ensemble correlation function of *BPSK*, case ASYN-DET, for selected values of the fixed phase of the carrier $\theta_0 = 0$, $\pi/8$, $\pi/4$ and $\pi/2$. Solid lines ρ_{vu}, dotted lines ρ_{uv}. The subtraction ρ_{vu}, - ρ_{uv} yields for any θ_0 the function sin $(\Omega_0\tau)$. The pictures are the same for any values of t_1

S. L. HAHN

FUNKCJE KORELACJI, WIDMA MOCY I ROZKŁADY WIGNERA SYGNAŁÓW TELEKOMUNIKACYJNYCH

Streszczenie

Opisano właściwości funkcji korelacji, widm gęstości mocy i rozkładów Wignera czas-częstotliwość losowych sygnałów telekomunikacyjnych. Sygnały zarówno w paśmie podstawowym jak i modulowane

(kluczowane) generowano za pomocą metody opisanej w innej pracy autora. Porównanie funkcji korelacji obliczanych w dziedzinie czasu i po zbiorze realizacji pozwala ocenić hipotezę ergodyczną, stacjonarność i tak zwaną „właściwość" (properness) procesów losowych reprezentujących sygnały telekomunikacyjne. Wyniki oceny zależą od definicji danego procesu. W szczególności realizacje procesów w paśmie podstawowym mogą być synchroniczne lub asynchroniczne. Fale nośne mogą mieć fazę deterministyczną lub losową. Dlatego właściwości procesów losowych reprezentujących określony rodzaj transmisji, na przykład *ASK*, *BPSK*, *FSK* lub inne uzależnione są od arbitralnych założeń. Na przykład proces losowy *BPSK* sklasyfikowany przez niektórych autorów jako niewłaściwy okazuje się być właściwym w wersji asynchronicznej. W pracy pokazano, że obliczanie wartości oczekiwanej rozkładów Wignera może dla sygnałów telekomunikacyjnych nie mieć sensu, gdyż informacja o wstęgach bocznych modulacji może być zatarta.

Słowa kluczowe: losowe sygnały komunikacyjne (w paśmie podstawowym, analityczne), funkcje korelacyjne w dziedzinie czasu i po zbiorze realizacji widma mocy, rozkłady czasowo-częstotliwościowe Wignera

KWARTALNIK ELEKTRONIKI I TELEKOMUNIKACJI, 2005, 51, ZESZYT SPECJALNY, ss. 51–65

Linear prediction of the rayleigh fading channel

ARKADIUSZ TROJANOWSKI, JACEK WOJCIECHOWSKI

Institute of Radioelectronics,
ul. Nowowiejska 15/19
00-665 Warsaw, Poland
email: A.Trojanowski@ire.pw.edu.pl, J.Wojciechowski@ire.pw.edu.pl

This paper investigates the use of the linear MMSE prediction methods for the prognosis of non-stationary non-selective Rayleigh fading signals. It is shown that a properly chosen and configured prediction algorithm offers much better knowledge of the radio channel then the raw channel state estimate. The paper explores necessary conditions for successful prognosis and reveals methods for improving prediction effectiveness. Presented simulations show that the linear prediction is potentially a highly efficient tool for the narrowband signalling over the Rayleigh fading channel.

Keywords: Rayleigh channel, adaptive transmissions, linear prediction.

1. INTRODUCTION

One of the challenges in digital mobile communication systems is a destructive nature of the fading radio channels [1, 2]. Multipath signal propagation produces the power fading phenomena and mobile station motion inflicts Doppler's frequency shift. Significant power fluctuations of the received signal — both constructive peaks and destructive deep fades (Fig. 1), when a mobile station moves across the area, causes that even with a constant noise power the Signal to Noise Ratio (SNR) varies with time and the Bit Error Rate (BER) may intermittently increase. Therefore, wireless systems designers for robust transmissions are forced to make their systems adaptive to the channel conditions using various methods, e.g. adaptive channel coding, adaptive power control, adaptive modulation etc. ([21, 14, 15]).

However, for the practical implementation of the adaptive techniques, the Channel State Information (CSI) should be available at the transmitter. Obtaining exact CSI is practically non-feasible. Estimation errors, processing and retransmission delays and other factors cause that CSI is always outdated, distorted, and often improper. Consequently, adaptation is ineffective.

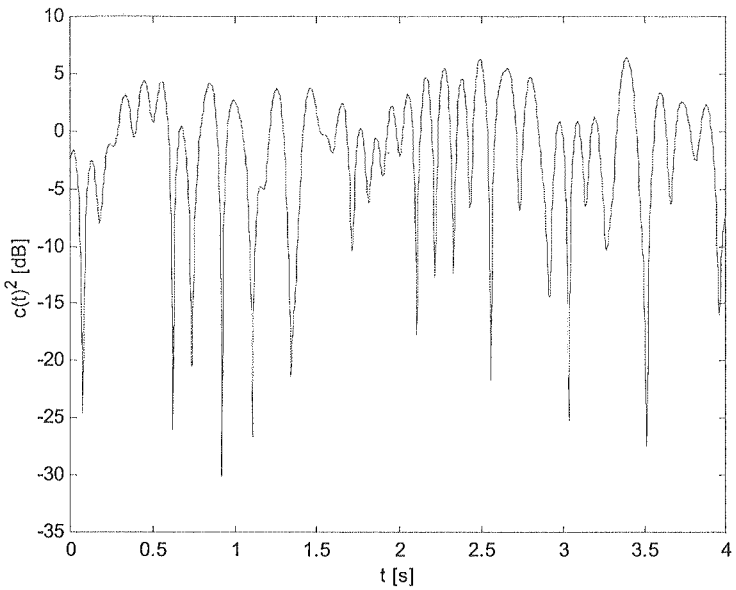

Fig. 1. Power fading in the Rayleigh channel

This paper explores ways to improve CSI quality and adaptation efficacy by reducing the effect of calculations and retransmission delays. A technique that is under consideration is the linear Minimum Mean Square Error (MMSE) predictor. Linear MMSE prediction is a classical method ([2,3,4]) widely applied to telecommunication systems, for example in speech compression, echo cancellation etc., to estimate future samples of time-series using second-order statistics. Due to significant correlations between successive samples of the fading signal, it can be also utilized in reduction of the CSI estimation errors ([6, 8, 13]). In the literature also other methods for prediction of the fading channel have been discussed. In [7], spectrum estimation, MUSIC and the minimum norm algorithms, have been applied to estimate the parameters of incident waves. In [9], an ESPRIT-type algorithm is introduced to estimate the dominant incident sinusoids in the composite channel signal. In [10], a nonlinear predictor using multivariate adaptive regression splines is proposed. Low computation-, low memory-cost polynomial approximation for short range prediction is presented in [11].

However, as it is basing on our research shown in Section 2, the linear MMSE method provides long term prediction with a strong precision [16, 17] and various algorithms allowing for the exchange of estimation accuracy for estimation time were suggested ([18]). Predicted CSI is significantly closer to the real values then the outdated CSI in wide range of channel conditions including fading signal non-stationarity. Section 3 shows, that linear prediction applied to simplified adaptive transmission systems ([19, 20]) greatly improves adaptation efficiency. In a BPSK system with the power adaptation prediction reduced BER and enhanced power control. Sample MQAM transmission system with CSI prognosis as a adaptation criteria gains successful ad-

aptation of the constellation dimension, which is not effective with outdated channel samples.

2. LINEAR MINIMUM MEAN SQUARE PREDICTION OF THE RAYLEIGH FADING

Let us consider a flat (frequency non-selective) Rayleigh fading radio channel without the line of sight, where all delayed components of the received wave arrive within a small fraction of the symbol duration. For simplification we assume at the beginning, that the channel is stationary.

Due to mobile station motion, the nth scatterer undergoes the Doppler frequency shift given by

$$f_n = f_c \frac{v}{c} \cos\theta_n = f_M \cos\theta_n, \tag{1}$$

where f_c is the carrier frequency, v is the speed of mobile station, c is the speed of light, θ_n is the incident wave angle with respect to the direction of the motion of the mobile station, and f_M denotes the maximum Doppler frequency shift. Signal at the output of the flat fading channel is given by [2]

$$y(t) = c(t)x(t) + n(t), \tag{2}$$

where $x(t)$ is the complex envelope of the transmitted signal, $n(t)$ is the white additive Gaussian noise and $c(t)$ is the flat fading signal expressed as

$$c(t) = \sum_{n=1}^{\infty} \gamma_n e^{j(2\pi f_n + \phi_n)} = \gamma(t) e^{j\phi(t)}, \tag{3}$$

where γ_n is the amplitude of the nth scatterer, f_n is the Doppler frequency shift (1), and ϕ_n is the phase.

It is known ([1]) that (3) can be modeled as a zero mean complex-valued Gaussian random process with the autocorrelation function

$$R_c(\tau) = J_0(2\pi f_M \tau), \tag{4}$$

where $J_0(.)$ is the zero-order Bessel function of the first kind (Fig. 2). The envelope $\gamma(t)$ is a Rayleigh-distributed random process and $\phi(t)$ is uniformly distributed over the interval $(-\pi, \pi)$.

Let us consider a discrete-time realization of the signal (2) at the output of matched filter and sampler

$$y_n = c_n x_n + w_n, \tag{5}$$

where x_n is transmitted symbol, w_n sampled realization of the white Gaussian noise, and c_n is the flat fading signal sampled at the symbol rate. Due to significant correlations

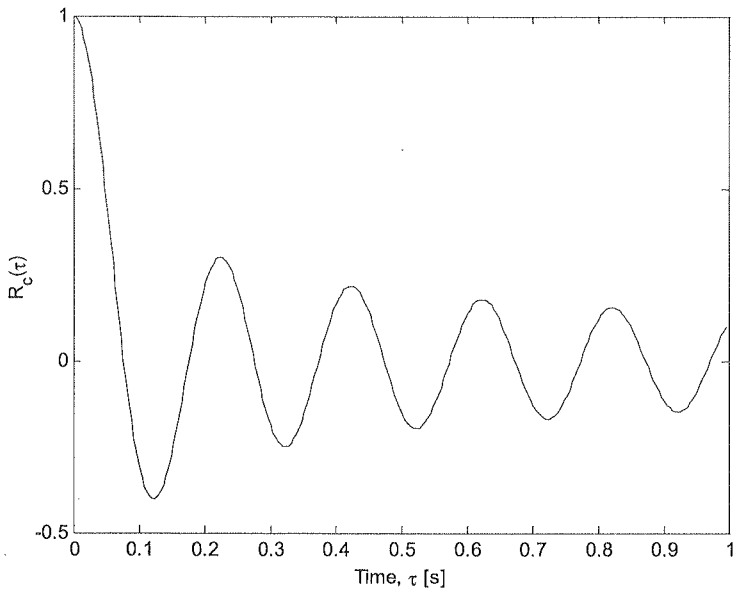

Fig. 2. Autocorrelarion of the fading signal in the flat Rayleigh channel

between successive samples of the fading signal (4), channel state in every sample can be, with a certain error

$$e_n = c_n - \hat{c}_n, \tag{6}$$

estimated as a combination of the previous samples. Note, that for the random second--order Gaussian process, like the flat Rayleigh fading, the linear model is optimal ([3]). Therefore, we express the next fading signal sample as a linear combination of the previous samples

$$\hat{c}_n = \sum_{p=1}^{P} a_p c_{n-p}. \tag{7}$$

Although autocorrelation function of c_n is time unlimited, the size of the linear model is limited to an arbitrary integer P. The optimal vector of coefficients $\mathbf{a}^T = [a_1, ..., a_P]$ is determined by minimization of the mean square error ([4, 5])

$$Q_P^e = \mathrm{E}\left[\left(c_n - \sum_{p=1}^{P} a_p c_{n-p}\right)^2\right] \tag{8}$$

and can be calculated from the equation

$$\mathbf{Ra} = \mathbf{r}, \tag{9}$$

where $\mathbf{r}$ is the $p \times 1$ autocorrelation vector $r_m = \mathrm{E}[c_n c_{n-m}^*]$, and $\mathbf{R}$ is the $p \times p$ autocorrelation matrix $R_{kl} = \mathrm{E}\left[c_{n-k} c_{n-l}^*\right]$ of the fading signal $\{c_n\}$. Note that $\mathbf{R}$ is the

Teoplitz matrix ([4]) and a fast Levinson-Durbin algorithm can replace matrix inversion to solve (9).

Increase of the model size P reduces the prediction error, which approaches zero as $P \to \infty$. However, in the considered case it becomes significantly small if the degree of the linear model is related to the relatively small number of the signal spectrum poles, for example not larger than 20 in urban area [2]. More important is influence of the noise signal power σ_w^2. The expression of the total prediction error is given by the formula

$$Q_P^e = 1 + \sigma_w^2 - \mathbf{a}^{\mathrm{T}}\mathbf{r}, \tag{10}$$

which draws the limits for prediction effectiveness ([13]).

2.1. MMSE PREDICTION OF STATIONARY RAYLEIGH FADING CHANNEL

Linear model size and noise power are very important system parameters affecting prediction errors. Equally important is a ratio of sampling frequency to the maximum Doppler frequency, defined as

$$\rho = f_s/f_M. \tag{11}$$

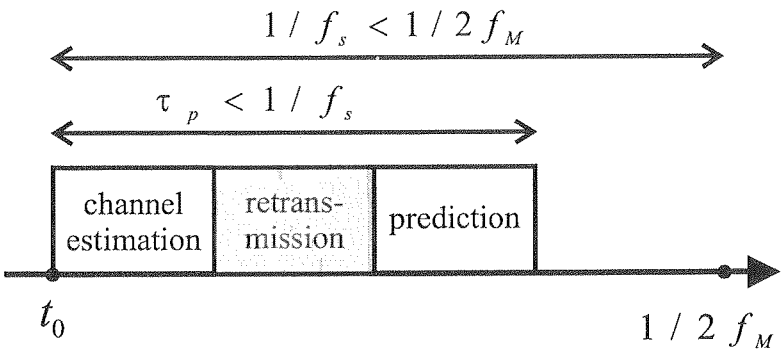

Fig. 3. Time limitations for the prognosis rate

Larger f_s (ρ) offers more accurate prediction [17] (Fig. 4), but it makes shorter prediction range. Contrary, small f_s, if it only is at least equal to the Nyquist rate, $f_s > 2f_M$ ($\rho > 2$), provides long range prediction at the much slower rate. However, time span τ_p (Fig. 3) is limited by the Doppler shift, thus maximum prediction range will depend on the maximal mobile station velocity. In Figure 4 theoretical curve of MMSE vs. linear model size P is shown for SNR=30 dB and different values of ρ. Prediction error Q_P^e with $P \to \infty$ and $\rho \to \infty$ reaches minimal asymptotic value limited by the power of the noise signal σ_w^2.

Practical implementation of the prediction algorithm reveals two problems. Firstly, samples of the fading signal $\{c_n\}$ have to be estimated. Estimation proceeds at the

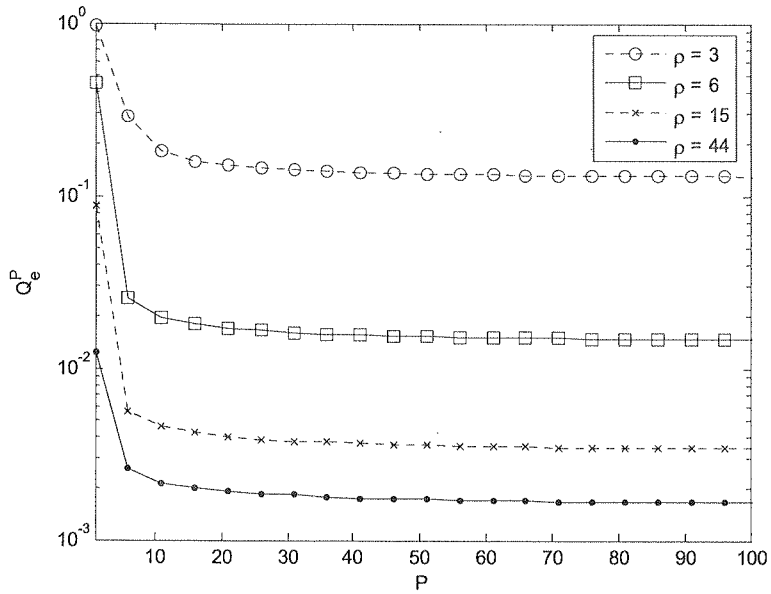

Fig. 4. Theoretical evaluation of the Q_P^e for SNR=30 dB

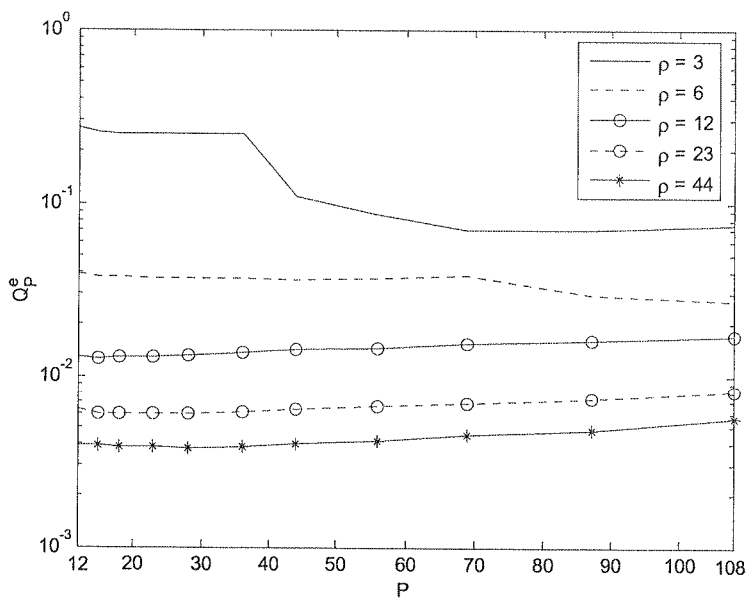

Fig. 5. Simulated Q_P^e vs. P and, ρ for SNR=30 dB

frame rate, as well sampling rate is equal to the frame rate and constant. Therefore, ρ varies with mobile station acceleration or decelerations and theoretical value of Q_P^e changes. Moreover, $2f_M$ can outgrow f_s. Hence, the most safe is prognosis with the frame rate close to $1/\tau_p$. It is also important to keep τ_p small. Assuming constant channel estimation and retransmission times (as required for minimal realization of the adaptation loop), the remaining time spent on solving equation (9) has to be kept possibly short.

Secondly, the autocorrelation function of the fading signal is unknown, varies with time, and has to be estimated. We assume quasi-stationary character of the channel during the observation time (next subsection shows when such an assumption is justified), but autocorrelation function still has to be estimated for every frame. Following, prediction coefficients have to be recalculated.

Due to numerical complexity of the prediction algorithms [18], it is necessary to balance prediction accuracy and execution time. For that reason an appropriate prediction method and linear model degree P should be chosen.

Levinson-Durbin algorithm with biased autocorrelation function estimation [16, 17] has been pointed out as the best combining prediction accuracy with numerical complexity [18]. Simulations for stationary fading channel (Fig. 5), showed that the optimal linear model size does not exceed 40.

2.2. MMSE PREDICTION OF NON-STATIONARY RAYLEIGH FADING CHANNEL

The most important challenge in prediction of real fading signals is their non-stationarity. The value of f_M changes according to the mobile station acceleration or deceleration. It forces that autocorrelation function and linear model coefficients have to be recalculated in every prediction step. Additionally, system developer has to decide either to use more complex algorithms for non-stationary signals or to assume a quasi-stationary character of the channel during the observation.

The quasi-stationary assumption was chosen due to limited time slot for prediction. To check the influence of the non-stationary channel on the prediction gain, three non-stationary channel profiles were defined and examined ([18]): pedestrian ($\bar{\rho} \approx 50$), downtown ($\bar{\rho} \approx 8$) and highway ($\bar{\rho} \approx 3$) (Fig. 6-8).

In each of them $f_M(t)$ oscillates harmonically with certain amplitude Δf_M and period T_{osc} around a specific $E[f_M]$. This simulates the worst transmission conditions, i.e. periodic acceleration and deceleration of the mobile station.

As mentioned, the Levinson-Durbin algorithm utilizing the biased estimator of the autocorrelation function was used in our research. Therefore, aside from the linear model degree P, there is a second parameter for this method, N – the number of the fading signal samples used for estimation of the autocorrelation function. It is known [5] that the number of samples should be at least equal to 50 and also larger then $4P$. Otherwise estimation errors will be significant (Fig. 5, N=108), and Q_P^e will increase regardless of the higher computational cost.

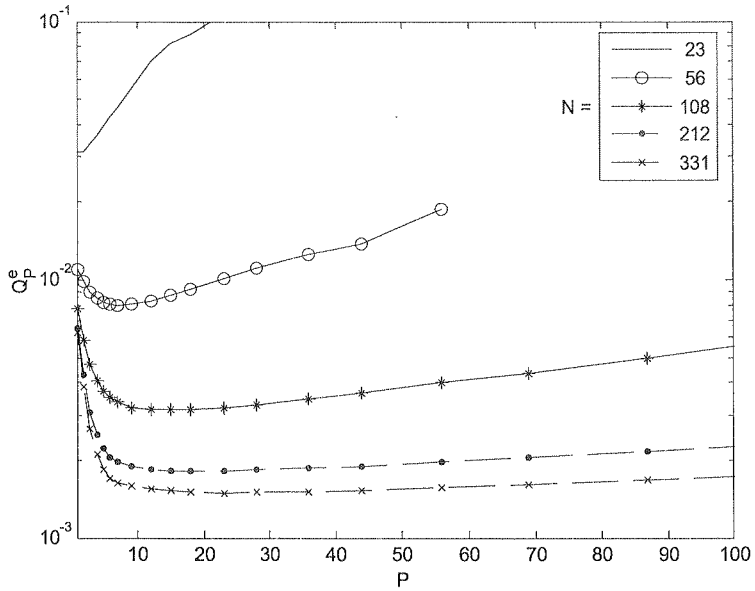

Fig. 6. MMSE as a function of the linear model degree P and the number of samples N (pedestrian profile)

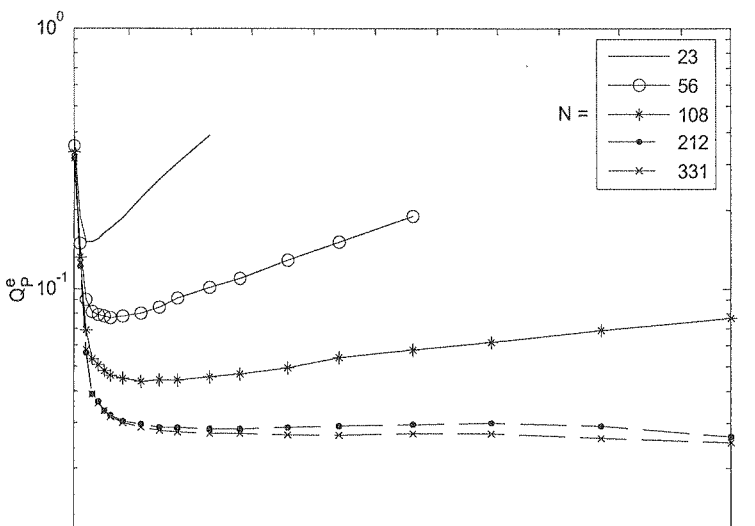

Fig. 7. MMSE as a function of the linear model degree P and the number of samples N (downtown profile)

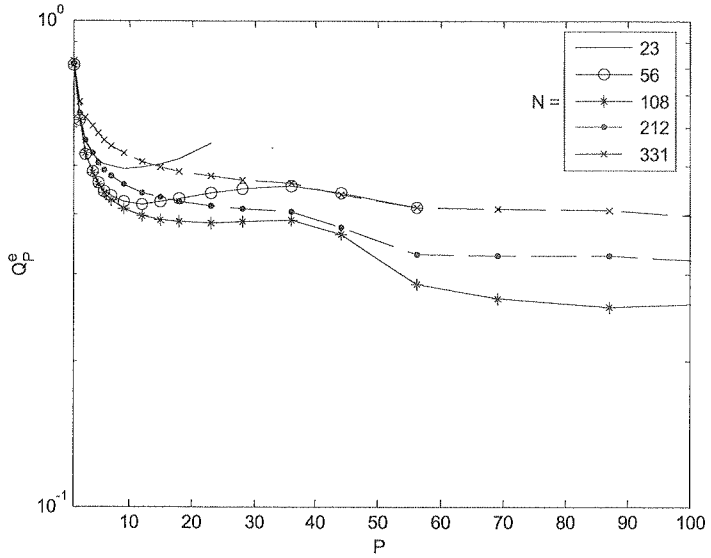

Fig. 8. MMSE as a function of the linear model degree P and the number of samples N (highway profile)

As seen from Fig. 6 increasing P results in decreasing MMSE only to the some minimal value. Above this optimal P, larger model size causes larger prediction errors and computational load. Due to bias of the autocorrelation function estimation [18] more channel is non-stationary, the more decreases optimal value P (Fig. 6-9).

Increasing the value of N, with constant P has its own limits regarding signal non-stationarity. For the downtown profile (Fig. 7) considerable increase of N from 212 to 331, products negligible, in comparison to Fig. 6, MMSE decrease. For highway profile (Fig. 8) effects of the non-stationary character of the fading signal are noticeable, and quasi-stationary assumption limits can be determined: larger number of samples results in the MMSE growth. However, in spite of non-stationarity, if reasonable model parameters are utilized, prognosis gained from the prediction is usually much more accurate then from the outdated CSI ([18]).

Estimation of the autocorrelation function and solving (9) can be avoided by using different prediction algorithms ([18]). There are two groups under consideration: adaptive filters and lattice predictors. First provides very low computational load - for example LMS numerical complexity is $O(P)$. But decrease of prognosis accuracy (Fig. 9) and filter stability problems are observed. Second group opens a way to improve knowledge of CSI, but in exchange for high complexity of prediction filter. The most important, adaptive algorithms, lattice filters and the Levinson-Durbin algorithm complement each other and enable system developers to exchange prediction accuracy for power of the signal processors.

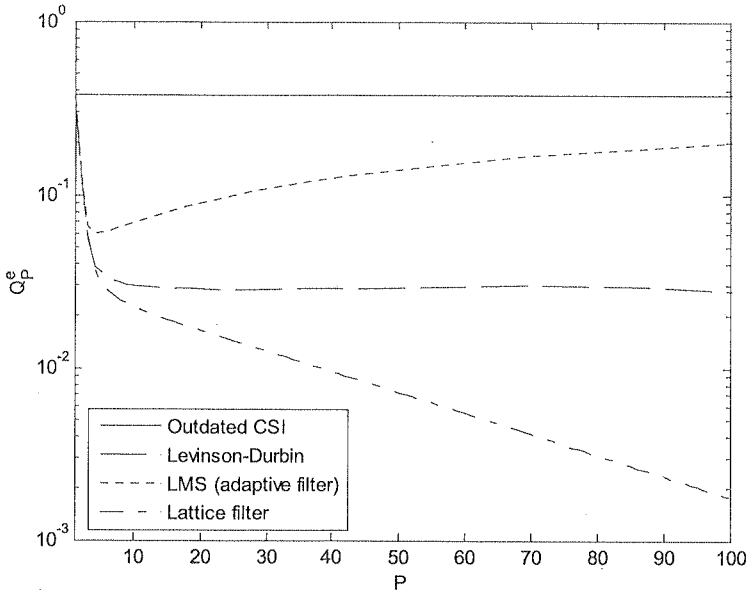

Fig. 9. Comparison of prediction algorithms (Q_P^e vs. P for downtown profile and SNR = 10 dB)

3. ADAPTIVE TRANSMISSIONS WITH FADING PREDICTION

In this section we verify by computer simulations the thesis that prediction of the fading signal in the flat Rayleigh channel improves effectiveness of adaptive transmissions systems by giving better knowledge of the CSI. In [14] prediction is utilized in adaptive OFDM system. Our attention is limited to single carrier narrowband transmissions: BPSK with power adaptation ([19, 6]) and QAM with the adaptation of constellation size ([21, 6]).

For BPSK system two transmission scenarios were defined. First, Channel Power Inversion (CPI), where transmitted signal power is an inversion of the predicted power gain of the channel. Theoretically, assuming ideally $\hat{c}_n = c_n$ and prediction with the symbol rate, this adaptation should eliminate influence of the fading. Both received signal power and BER should be the same for adaptive transmission and transmission in the AWGN channel.

But, in practical implementation adaptation proceeds at the frame rate and also prediction errors appear. Therefore, CPI performance is inferior to that of AWGN. Moreover it is infeasible to build a transmitter that can meet requirements of such transmission (maximum output power, which theoretically can reach infinity, and dynamics). Furthermore, the most critical prediction errors occur for deep power fades. Therefore, it is rational to break transmission when a deep fade is expected.

The second investigated transmission method is the Truncated Channel Inversion (TCI). In this scheme subsequent frame is not transmitted, if predicted channel gain

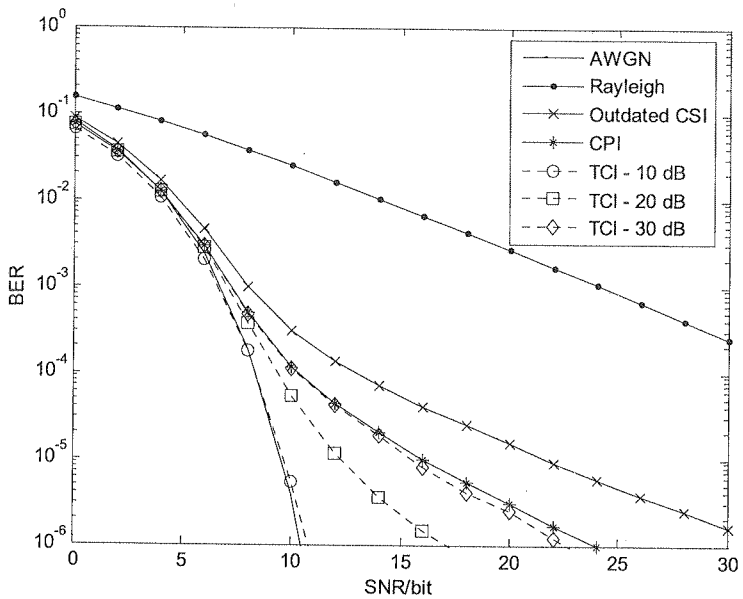

Fig. 10. BER in BPSK transmission over AWGN and Rayleigh channels vs. SNR/bit (pedestrian profile)

is smaller than some cutoff threshold. With the cutoff threshold rising BER decreases but, due to transmission breaks decrease of the bandwidth efficiency also occurs.

Adaptive transmission in the Rayleigh channel, even if based on the outdated CSI, results in lower BER. When the adaptation is based on the prognosis, due to the lower MMSE (Fig. 9), transmission suffer fewer errors. For the CPI systems (Fig. 10) the prediction gain, defined as a difference between BER in adaptive transmissions based on the outdated and predicted CSI, reaches even 5 dB.

For TCI systems, where prediction gain increases with the cutoff threshold rise, adaptive transmission reaches BER comparable to transmission in the AWGN channel. Decrease of the bandwidth efficiency (due to transmission breaks) to 0.9 bit/symbol is negligible.

Due to MMSE increase (Fig. 6-8), adaptation becomes less successive with fading signal non-stationarity increase (Fig. 11). However, compared to the adaptation based on the outdated CSI, where small BER gain can be explained by significant received power increase, our prediction is more effective.

It reduces BER by 8 dB compared to outdated CSI and by 10 dB compared to AWGN system without adaptation. Note that TCI transmission for SNR/bit below 2 dB suffers fewer errors than AWGN transmission. It is due to the use of CSI predictor as a power prognosis. Such a channel power predictor is biased [13] and its prognosis to pessimistic.

We also examined two adaptive MQAM systems. Both adaptations aimed in keeping error rate lower than some assumed BER_{max}. Constellation size and bandwidth efficien-

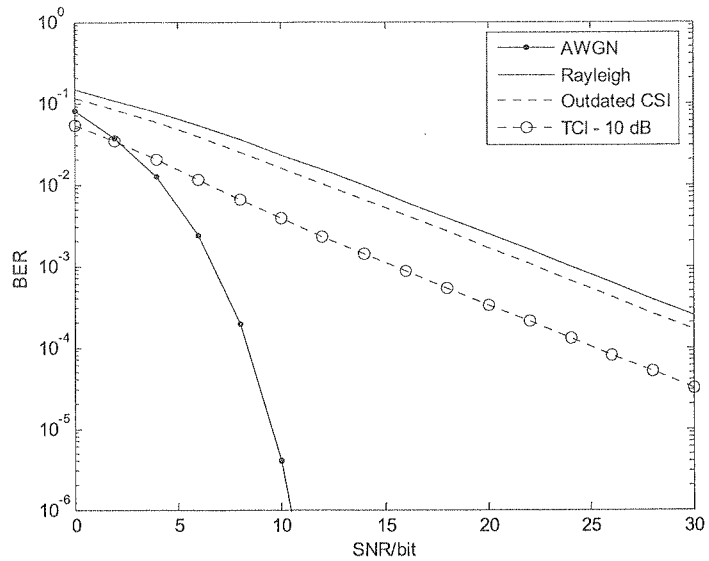

Fig. 11. BER in BPSK transmission over AWGN and Rayleigh channels vs. SNR/bit (highway profile)

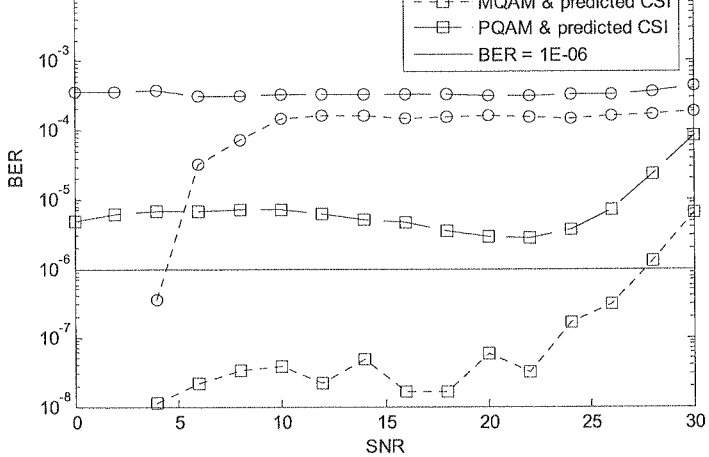

Fig. 12. BER in MQAM transmission over AWGN and Rayleigh channels vs. SNR/bit ($BER_{max} = 1e-06$, pedestrian profile)

cy were varying [20]. First, marked in Fig. 12 as a MQAM, adapted only constellation dimension. Second, marked as PQAM, adapted both constellation size and transmitted signal power according to the scheme described in [21]. Since adaptation basing on the outdated CSI does not work properly and BER exceeds assumed BER_{max}, in both cases prediction gain was noticeable. Only with prognosis as the adaptation criteria MQAM systems worked correctly.

4. CONCLUSIONS

In this paper the prediction of stationary and non-stationary fading Rayleigh channels with respect to adaptive transmissions were examined. In Section 2, basing on statistical characterization of the fading signal, linear predictors was selected and physical limitations for prognosis were described. We conjectured, that prediction accuracy is bounded by the power of noise in the channel, linear model size, prediction range, and by the algorithm limitations. Conditions for a proper selection of the sampling rate were formulated. Subsequently, influence of the fading non-stationarity was examined and limits of practical implementation revealed. However, also advantages of the predicted CSI over the outdated were exposed. It was concluded, that the number of various prediction algorithms make systems development more flexible. In Section 3 sample adaptive transmissions systems were simulated. Presented results demonstrated, that the utilization of CSI prognosis as a adaptation criterion can offer considerable improvement of the transmission conditions. Assuming, basing on our research it was shown, that a properly chosen and configured linear prediction algorithm provides channel information significantly closer to the real values then the outdated CSI. Also ways to practical implement of the long-range prediction were drawn. Let us notice, that investigated transmissions conditions do not limit conclusions. Real carrier, sampling and maximum Doppler frequencies and other physical parameters like moving speed, accelerations etc. are less important than resulting ρ and its variability, linear model size P or σ_w^2. Although narrowband signaling era fades slowly, we still find prediction of the fading signal as a highly potential tool, for example for link adaptation in OFDM systems ([14]), where separate carriers comply with the non-selectivity condition.

5. REFERENCES

1. W. C. Jakes: *Microwave Mobile Communications*. Wiley Interscience, 1974.
2. J. G. Proakis: *Digital Communications*. McGraw-Hill, 1995.
3. J. Zarzycki: *Orthogonal Digital Filtering of Stochastic Signals*. WNT (in Polish), Warsaw 1998.
4. S. V. Vaseghi: *Advanced Signal Processing and Digital Noise Reduction*. Wiley & Teubner, 1996.
5. G. E. P. Box, G. M. Jenkins: *Time Series Analysis: Forecasting and Control*. Second Edition, San Francisco, Holden-Day Press, 1976.

6. A. Duel-Hallen, S. Hu, H. Hallen: *Long-Range Prediction of Fading Signals.* IEEE Signal Processing Magazine, May 2004, vol. 17, no. 3, pp. 62-75.
7. R. Vaughan, P. Teal, R. Raich: *Short-Term Mobile Channel Prediction Using Discrete Scatterer Propagation Model and Subspace Signal Processing Algorithms.* Proc. IEEE International Vehicular Technology Conference, Sep. 2000, pp. 751-758.
8. T. Eyceoz, A. Duel-Hallen, H. Hallen: *Deterministic Channel Modeling and Long Range Prediction of Fast Fading Mobile Radio Channels.* IEEE Communications Letters, Sep. 1998, vol. 2, pp. 254-256.
9. J. Andersen, J. Jensen, S. Jensen, F. Frederiksen: *Prediction of Future Fading Based on Past Measurements.* Proc. IEEE International Vehicular Technology Conference, Sep. 1999, pp. 15- 55.
10. T. Ekman, G. Kubin: *Nonlinear Prediction of Mobile Radio Channels: Measurements and MARS Model Designs.* in Proc. IEEE International Conference on Acoustics, Speech, and Signal Processing, May 1999, vol. 5, pp. 2667-2670.
11. Z. Shen, J. G. Andrews, B. L. Evans: *Short Range Wireless Channel Prediction Using Local Information.* Proc. IEEE Asilomar Conf. on Signals, Systems, and Computers. Pacific Grove, CA USA, Nov. 2003, vol. 1, pp. 1147-1151.
12. P.D. Teal, R.A. Kennedy: *Bounds on Extrapolation of Field Knowledge for Long-Range Prediction of Mobile Signals.* IEEE Transactions on Wireless Communications. March 2004, Vol. 3, no. 2, pp. 672- 676.
13. T. Ekman: *Prediction of Mobile Radio Channels.* PhD dissertation, 2002, Uppsala University.
14. Tung-Sheng Yang: *Performance Analysis of Adaptive Transmission Aided by Long-Range Channel Prediction for Realistic Single- and Multi-Carrier Mobile Radio Channels.* PhD dissertation, 2004, North Carolina State University, Raleigh.
15. D. Mihai Ionescu, Adrian Boariu: *Predictive Closed-Loop Power Control for Frequency-Division Duplex Wireless Systems.* IEEE Comm. Lett. June 2001, vol. 5, no. 6, pp. 248-250.
16. A. Trojanowski: *Digital Trasmission in Rayleigh Fading Channel Using Long-Range Prediction.* Ms.C. thesis (in Polish), Warsaw Unieversity of Technology, Warsaw, 2002.
17. A. Trojanowski, J. Wojciechowski: *Prediction of the Fading in the Rayleigh Radio Channel Using Linear Prediction Methods.* Proc. KKRRiT 2003 (in Polish), Wrocław (Poland), June 2003, pp. 267-270.
18. A. Trojanowski, J. Wojciechowski: *Linear Prediction of the Fading Channel – Comparision of the Algorithms.* Proc. KKRRiT 2004 (in Polish), Warsaw (Poland), June 2004, pp. 88-91.
19. A. Trojanowski, J. Wojciechowski: *Adaptive BPSK Transmission in the Rayleigh Channel With the Linear Minimum Mean Square Error Power Fading Prediction.* Proc. 6th NATO RCMCIS 2004, Zegrze (Poland), September 2004, pp. 330-338.
20. A. Trojanowski, J. Wojciechowski: *Adaptive Digital Transmissions in the Rayleigh Channel with Power Fading Prediction as a Adaptation Cirteria.* Submitted and accepted to the KKRRiT 2005, Kraków (Poland), September 2005.
21. A. J. Goldsmith, S. G. Chua: *Variable-Rate Variable-Power MQAM for Fading Channels.* IEEE Trans. Commun., Oct. 1997, vol. 45, pp.1218-1230.

A. TROJANOWSKI, J. WOJCIECHOWSKI

PROGNOZA LINIOWA KANAŁU RADIOWEGO Z ZANIKIEM RAYLEIGHA

Streszczenie

Jednym z podstawowych problemów, z jakimi spotykają się projektanci cyfrowych systemów radiokomunikacji ruchomej lądowej, jest destruktywny wpływ wielodrożnej propagacji fal radiowych na odbierany sygnał niosący informację. Szybkie i znaczące zmiany odbieranej mocy wymagają, aby parametry stosowanych zabezpieczeń, moc nadawanego sygnału, siła kodowania kanałowego itd., podlegały ciągłej adaptacji do panujących warunków. W tym celu niezbędne jest posiadanie informacji o aktualnym stanie kanału (CSI). Informacja estymowana w odbiorniku, jest opóźniona o czasy obliczeń oraz transmisji zwrotnej, więc przedawniona, a zastosowane zabezpieczenia często nieskuteczne, bo nieadekwatne do warunków w kanale.

W artykule, jako rozwiązanie problemu przedawnienia CSI proponujemy wykorzystać średniokwadratową prognozę liniową do estymacji przyszłych wartości sygnału zaników na podstawie zebranej w odbiorniku najnowszej historii kanału (Punkt 2). Pokazujemy, że w zastosowaniu do nieselektywnego zaniku o rozkładzie Rayleigha daje ona dokładniejszą od przedawnionego CSI wiedzę o kanale radiowym zarówno dla kanałów stacjonarnych (Punkt 2.1), jak i niestacjonarnych (Punkt 2.2). Jednocześnie wskazujemy użyteczne algorytmy prognozy, ich ograniczenia oraz metody konfiguracji w celu uzyskania najlepszej dokładności predykcji pogodzonej z krótkim czasem obliczeń.

W Punkcie 3 przedstawiamy wyniki symulacji komputerowych, które prezentują, w jakim stopniu lepsza wiedza o kanale radiowym, uzyskana dzięki zastosowaniu predykcji, poprawia wydajność adaptacyjnych systemów transmisji. Symulacje numeryczne dwóch systemów: BPSK z adaptacją mocy oraz MQAM z adaptacją wielkości konstelacji, pozwalają przekonać się, że zastosowanie prognozy zmniejsza bitową stopę błędów transmisji, poprawia kontrolę mocy, ogólnie pozwalając lepiej wypełniać kryteria adaptacji.

Słowa kluczowe: kanał Rayleigha, transmisja adaptacyjna, prognoza liniowa

des
ape
alg
use
the
red
sub

Key

Now
reduce a
function
aperture
e.g. at va
aperture
frequenc
shape. T
conducti
layers or

Seve
tennas. T
the first
field-effe

KWARTALNIK ELEKTRONIKI I TELEKOMUNIKACJI, 2005, 51, ZESZYT SPECJALNY, ss. 67–83

An Impedance Model of a Reconfigurable Antena

YEVHEN YASHCHYSHYN

Warsaw University of Technology, Institute of Radioelectronics,
ul. Nowowiejska 15/19, 00-665 Warsaw,
Poland, Phone (48 22) 6607833
email: e.jaszczyszyn@ire.pw.edu.pl

The general model of the reconfigurable aperture in the impedance approximation is described in this paper. The integral equation for the magnetic currents being excited on a aperture with the variable surface impedance is formulated. A highly effective numerical algorithm is used to obtain the solution of the integral equation. The Genetic Algorithm is used in the optimization of the desired radiation pattern. The optimizer tries to determine the configuration of a conductive pattern on a semiconductor substrate to obtain the desired radiation pattern. Theoretical results are compared with measurement for cases of the substituted microstrip structure and show a very good agreement.

Keywords: Reconfigurable antenna, surface impedance.

1. INTRODUCTION

Nowadays, radioelectronic systems employ multiple antenna systems. In order to reduce and improve performance characteristics it is desirable to combine multiple functions into a single antenna system. To satisfy multi-mission functionalities, a single aperture requires an antenna array that can be quickly reconfigured to operate efficiently, e.g. at various application frequencies [1] - [3]. The main purpose of a reconfigurable aperture is to reduce the complexity of an antenna system operating on a desired frequency band, with the control over antenna gain and beam pointing direction or shape. The reconfigurability can be achieved by dynamically forming arbitrarily shaped conductive surfaces (patterns) by the use of space-charge injection in semiconductor layers or by other means [4].

Several approaches have been proposed for implementing the reconfigurable antennas. The reconfigurable aperture structures can be divided into two main groups: the first one, which uses fixed separated switches (e.g. based on the PIN diode, the field-effect transistor — FET, microelectromechanical system — MEMS) placed on

the aperture and, the second one, which uses temporarily created switches, e.g. on a semiconductor substrate or waveguide. An example of the first group is a reconfigurable aperture concept derived from fragmented aperture design where the configuration of the fragmented aperture may be switched by the user to obtain different functionalities [5], [6]. These reconfigurable apertures are derived from the new class of antenna, which consists of a matrix of conducting patches with switches between some or all of the patches. These reconfigurable apertures can change functionality by opening or closing different connections between these patches. An example of the second group are the plasma regions with fairly high electrical conductivity, which are temporarily created on a silicon substrate [7] – [9]. These regions define the antenna structure, and they can be changed to create different antennas. The key element of the antenna, which has been presented, e.g. in [9], is a semiconductor chip that contains a set of individually controlled PIN structures. Electromagnetic waves propagate through the chip, which also serves as a planar dielectric waveguide. The PIN structures locally affect the wave propagation velocity and the antenna can form a beam in practically any direction within a wide steering angle (like a leaky-wave antenna).

The leaky-wave antennas are well known due to their pencil beam radiation patterns, frequency [10] and electrical [11] beam scanning and beam steering using photo-induced plasma [12].

The basic physical phenomenon of directional radiation of a leaky wave travelling along a periodically loaded infinite waveguide [13] – [15], along nonuniform aperiodic arrays of finite extent [16] or along microstrip line with the first higher order mode [11], [17] is under active study. So it is appropriate to consider more general design situations in which not only a waveguide is loaded with nonuniform aperiodic finite arrays, but also when the waveguide is limited. Taking into consideration the finite dimensions of an antenna aperture is very important, because the influence of the surface wave diffraction at the edges of substrate can be significant. An exact solution for plane-wave scattering by a wedge with two uniform impedance faces is presented in [18].

The aim of the present work is to propose an effective impedance model for the analysis of a planar reconfigurable aperture of finite extent. It is assumed that the reconfigurable antenna is excited by e.g. the lowest surface wave mode E of the semiconductor substrate. The radiation characteristics of the reconfigurable array are treated as a result of surface wave diffraction by a finite number of inhomogeneities (temporarily created) and by edges of substrate with whole mutual relations. The analysis is based on the use of the impedance boundary condition. Therefore, the integral equation for the electric and magnetic currents being excited on an aperture with the variable surface impedance has been formulated. The variable surface impedance means that surface impedance of the aperture can be varied arbitrarily by changing the conductivity of semiconductor substrate. There are different mechanisms of the conductivity change (see, e.g. [7], [19]-[20]).

The highly effective numerical algorithm has been used for the solution of the integral equation. The Genetic Algorithm has been used in the optimization of the desired radiation pattern. The optimizer tries to determine the configuration of a conductive pattern on a semiconductor substrate to obtain the desired radiation pattern.

2. MODEL OF A RECONFIGURABLE APERTURE

The analysis of the antenna array can carried out by the use of the solution of the external boundary problem of electrodynamics where the quantity of the boundary subareas is equal to the number of array radiators. Such boundary problem can be solved by different methods. The boundary problems for the second order differential equations can be reduced to the integral equations. In electrodynamics the integral equations can be obtained from the boundary conditions either by using the Lorentz lemma or the equivalence theorem.

The proposed model of a reconfigurable aperture makes use of the impedance boundary conditions. The change of a precise boundary condition on the dielectric and conductor surface into impedance boundary conditions allows to simplify the solution of the problem substantially. A semiconductor planar waveguide with high conductivity areas ([7] – [9]) may be considered as the simplest impedance structure. We assume high- purity silicon as the semiconductor material. At mm-wave frequencies silicon behaves as a lossy medium whose conductivity changes almost proportionally to the plasma density [7]. So we can consider two main states of the silicon: as a dielectric area (without plasma) and as a high conductivity area (with plasma).

Fig. 1 shows the process of transforming a real reconfigurable structure to a surface with a variable surface impedance. It is assumed that the reconfigurable antenna is planar and thin.

The width of the structure is bigger than its thickness, $w >> h$. In that case constant-amplitude and constant-phase field distribution along the high conductivity areas (in x-direction) is considered. The radiation pattern can be derived from its two-dimensional model with no field variations along the "x"-axis. The finite width of the substrate in this direction (perpendicular to the direction of the surface wave propagation) can be taken into account by means of an effective dielectric constant as has been previously noted in [13].

The distances between high conductivity areas in the semiconductor waveguide as well as their widths can be varied. Distances d_i and widths b_i are equal to any multiple of the minimum spacing between the individual PIN's

$$\Delta = L/N; \; d_i = q_i \cdot \Delta, \; b_i = p_i \cdot \Delta; \tag{1}$$

where L is the aperture length; N is the maximum number of temporary created individual PIN structures in the semiconductor waveguide. The values of q and p will be considered later.

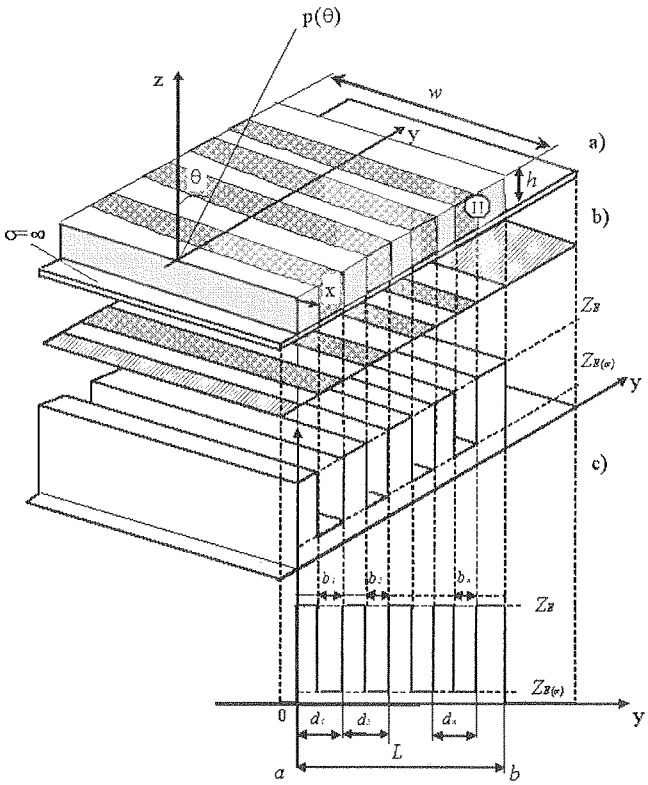

Fig. 1. The process of transformation of real structure to surface with a variable surface impedance

By turning on the PIN structures selectively it is possible to obtain the desired conductive pattern. Thus, the main beam direction can be electronically switched among several directions at a fixed frequency.

The semiconductor waveguide, which usually works on the lowest mode E can be represented by the normalized (to the free-space intrinsic impedance Z_0) surface impedance Z_E^n. From the condition that the propagation constant of a surface wave χ_s, normalized to k_0 (the free-space wavenumber), is known, this impedance value can be obtained from:

$$Z_E^n = i\sqrt{\chi_s^2 - 1}, \tag{2}$$

where χ_s is the solution of dispersive equation and in the case of the lowest mode it can be found from the characteristic equation:

$$\begin{aligned}&\sqrt{\chi^2 - \varepsilon_2}\cdot\sinh(2\pi h\sqrt{\chi^2 - \varepsilon_2}) + \\ &+\varepsilon_2\cdot\sqrt{\chi^2 - 1}\cdot\cosh(2\pi h\sqrt{\chi^2 - \varepsilon_2})\,|_{\chi=\chi_s} = 0\end{aligned} \tag{3}$$

where h is the thickness of a semiconductor layer normalized to the wavelength λ; ε_2 is the relative substrate permittivity of the semiconductor without plasma normalized to the permittivity of free space ε_0. In the case of accounting the losses, the value of ε_2 is complex.

A conductor can replace the high conductivity areas, the impedance of which can be represented as follows:

$$Z_{E(\sigma)} = \sqrt{\frac{\omega \cdot \mu_{a2}}{\sigma}} \cdot \frac{1+i}{\sqrt{2}}, \tag{4}$$

where ω is the angular frequency; σ is the conductivity; $\mu_{a2} = \mu_0$ in the case of non-magnetic material.

Therefore, along the "y" — axis the surface impedance varies in a discrete manner at the locations of conductor discontinuities.

Consider the integral equation for currents being excited on the plane with the variable surface impedance. A harmonic time-dependence $\exp(i\omega t)$ is assumed and suppressed. Taking the effect of the edges into account, we present the impedance structure as a wide strip parallel to "x"- axis. On the assumption that the impedance is homogeneous in the "x" direction and arbitrarily variable in the "y" direction, the electric waves (E_Z, E_Y, H_X) being considered within the impedance strip should satisfy the boundary condition:

$$Z_E(y)_{|z=0} = \frac{E_Y}{H_X} = \frac{J_X^M(y)}{J_Y^E(y)}, \tag{5}$$

where $\bar{J}^M(y) = \left[\bar{n}\bar{E}\right]$ is the surface magnetic current; $\bar{J}^E(y) = \left[\bar{H}\bar{n}\right]$ is the surface electric current [21].

In the further part of the surface plane where $Z_E(y) = 0$, which corresponds to the perfectly conducting ($\sigma = \infty$), the boundary condition should be carried out:

$$E_\gamma = 0. \tag{6}$$

The field over the plane $z = 0$ can be described by the electric and the magnetic vector potentials, which can be expressed in integral form by:

$$\begin{cases} \mathbf{A}^{\mathbf{E}}(y,z) = \int\limits_{S'} \mathbf{j}^{\mathbf{E}}(y',z') \cdot G^{\mathbf{E}}(y,y';z,z')\,ds'; \\ \mathbf{A}^{\mathbf{M}}(y,z) = \int\limits_{S'} \mathbf{j}^{\mathbf{M}}(y',z') \cdot G^{\mathbf{M}}(y,y';z,z')\,ds'; \end{cases} \tag{7}$$

where S' is the cross section of the current density volume V' at $x = const$; $G^{E/M}$ is the Green's function, which is described later. The primed coordinate (y', z') specifies the location of the current density (sources) within the volume V', while the unprimed coordinate (y, z) is the position of the observer.

The volume densities of the electric and magnetic currents in (7) consist of the source currents in volume V' and currents, which are induced on the impedance strip and perfect conductivity screen:

$$\mathbf{j}^{\mathrm{M/E}}(y',z') = \mathbf{j}^{\mathrm{M/E}source}(y',z') + \mathbf{j}^{\mathrm{M/E}induced}(y',z') \tag{8}$$

The induced currents are surface currents:

$$\mathbf{j}^{\mathrm{M/E}source}(y',z') = \mathbf{J}^{\mathrm{M/E}induced}(y') \cdot \delta(z'-0) \tag{9}$$

where $\delta(z'-0)$ is a Dirac's delta.

The induced electric currents exist on both the impedance strip and the perfect conductivity screen. However, the induced magnetic currents exist only on the impedance strip, where surface impedance is not equal to zero. The field generated by currents in the exterior upper region ($z \geq 0$) can be written follows:

$$\begin{cases} \mathbf{E} = \dfrac{1}{i\omega\varepsilon_{a0}}\left(k^2\mathbf{A}^{\mathrm{E}} + grad \cdot div\mathbf{A}^{\mathrm{E}}\right) - rot\mathbf{A}^{\mathrm{M}}; \\ \mathbf{H} = \dfrac{1}{i\omega\mu_{a0}}\left(k^2\mathbf{A}^{\mathrm{M}} + grad \cdot div\mathbf{A}^{\mathrm{M}}\right) + rot\mathbf{A}^{\mathrm{E}} \end{cases} \tag{10}$$

where

$$\begin{cases} \mathbf{A}^{\mathrm{E}} = \displaystyle\int_V \mathbf{j}^{\mathrm{E}source} \cdot G_1^{\mathrm{E}} dv + \int_S \mathbf{J}^{\mathrm{E}} \cdot G_2^{\mathrm{E}} ds; \\ \mathbf{A}^{\mathrm{M}} = \displaystyle\int_V \mathbf{j}^{\mathrm{M}source} \cdot G_1^{\mathrm{M}} dv + \int_S \mathbf{J}^{\mathrm{M}} \cdot G_2^{\mathrm{M}} ds; \end{cases} \tag{11}$$

ε_{a0}, μ_{a0} is the absolute free space permittivity and permeability respectively.

The Green's function $G_{1/2}^{\mathrm{E/M}}$ has to satisfy a two-dimensional wave equation, radiation condition and boundary condition on a screen. These functions are based on the sum (for $\mathbf{E}$) and the difference (for $\mathbf{M}$) of 2-D Green's function in free space. Thus, the function $G_2^{\mathrm{E}}(z=0) = 0$. The rest can be presented as follows:

$$G_1^{\mathrm{M}} = -\frac{i}{2}H_0^{(2)}\left(k\sqrt{(y-y')^2 + (z-z')^2}\right), \tag{12}$$

$$G_2^{\mathrm{M}} = -\frac{i}{2}H_0^{(2)}\left(k\left|y-y'\right|\right), \tag{13}$$

$$G_1^{\mathrm{E}} = G_1^{\mathrm{M}}, \tag{14}$$

where $H_0^{(2)}(kr)$ is the Hankel function of the second kind of order zero.

Next, magnetic field H_x generated by the currents (8) in the exterior upper region can be defined as:

$$H_x = \frac{k^2}{i\omega\mu_{a0}}\left(\int_{V'} j_x^{\mathrm{M}source} G_1^{\mathrm{M}} dv' + \int_{S'} J_x^{\mathrm{M}} G_2^{\mathrm{M}} ds'\right) + \\ + \frac{\partial}{\partial y}\left(\int_{V'} j_z^{\mathrm{E}source} G_1^{\mathrm{E}} dv'\right) - \frac{\partial}{\partial z}\left(\int_{V'} j_Y^{\mathrm{E}source} G_1^{\mathrm{E}} dv'\right) \tag{15}$$

Using the relations (5) and (15), in case we can write the integral equation for unknown surface magnetic currents in the following way

$$J_X^M(y) + \\ + \frac{kZ_E(y)}{2 \cdot Z_0} \int_a^b J_X^M(y') \cdot H_0^{(2)}(k\,|y - y'|) dy' = U^{source}(y). \tag{16}$$

In the case of the surface wave excitation with amplitude U_0 the function $U^{source}(y)$ can be determined from the following expression

$$U^{source}(y) = -\frac{kZ_E(y)}{2 \cdot Z_0} \cdot U_0 e^{-i\chi_{sy}}. \tag{17}$$

If the structure is excited only by a line magnetic current (it is equivalent to the slot-line in a screen) then the function $U^{source}(y)$ can be given by:

$$U^{source}(y) = -\frac{kZ_E(y)}{2 \cdot Z_0} \int_S j_x^{\mathrm{M}.source}(y', z') \cdot \\ \cdot H_0^{(2)}(k\sqrt{(y - y')^2 + z'^2}) ds' \tag{18}$$

If magnetic current is presented as follows: $j_x^{\mathrm{M}source}(y', z') = I_x^{\mathrm{M}source} \cdot \delta(y' - y_0) \cdot \delta(z' - z_0)$, then the function $U^{source}(y)$ can be written as:

$$U^{source}(y) = -\frac{kZ_E(y) I_X^{\mathrm{M}source}}{2 \cdot Z_0} \cdot \\ \cdot H_0^{(2)}(k\sqrt{(y - y_0)^2 + z_0^2}). \tag{19}$$

where $I_X^{\mathrm{M}source}$ is the amplitude of the current; y_0, z_0 are coordinates of the line magnetic current.

The function $U^{source}(y)$ can be easily determined by known distribution of the source currents.

The integral equation (16) is the Fredholm integral equation of a second kind with a difference kernel. The solution of it can be found by using difference methods [22]. The simplest method assumes that integral of the unknown current and kernel from a to b can be replaced by the sum of the integrals over small intervals, where unknown current distribution is assumed to have small changes. The amplitude of these currents in the centre of the intervals is elevated from the integrals over small intervals. As a result we obtain a set of the linear algebraic equations of the order N in unknowns

$$J_X^{\mathbf{M}}(y_m)+ \\ + \sum_{n=1}^{N} \frac{kZ_E(y_n)J_X^{\mathbf{M}}(y_n)}{2 \cdot Z_0} \int_{y_n-\frac{\Delta y_n}{2}}^{y_n+\frac{\Delta y_n}{2}} H_0^{(2)}(k\,|y_m - y'|)dy' = \\ = U^{source}(y_m). \quad m = 1, 2, ..., N \tag{20}$$

In the matrix form the expression (20) can be represented as:

$$(\|E\| + \|Y\| \cdot \|Z\|) \cdot \|I\| = \|U\| \tag{21}$$

where $\|Y\|$ -is the difference kernel (Teplitz matrix) of the integral equation; $\|Z\|$ - is the diagonal matrix which includes the surface impedance variation along the "y" - axis; $\|E\|$ - is the diagonal unit matrix; $\|I\|$ - is the matrix of the unknown amplitude of the surface currents, being defined during the solution process; $\|U\|$ - is the matrix which denotes the function $U^{source}(y_m)$.

By applying the method of the conjugate gradient with the fast Fourier technique to (21) (see, e.g. [23]) it is possible to obtain an effective numerical algorithm. With this combination, the computational time required to solve large aperture is much less than the time required by the ordinary conjugate gradient method and the method of moments. Furthermore, because the spatial convolution is replaced with simple multiplications in the spectral domain, some of the computational difficulties presented in the ordinary methods do not exist here. Since the method is iterative, it is possible to determine the accuracy of the solution.

The E-plane radiation pattern can be obtained from the integral representation of the total scattered field outside the reconfigurable structure using the asymptotic steepest descent method. Writing the radial component of the Poynting vector in the far-zone region of the array, we obtain the following angular function describing the relative power radiation pattern

$$|F_r(\theta)|^2 = \frac{|F(\theta)|^2}{|F(\theta)|^2_{\max}} = \frac{\left|\sum_{n=0}^{N} J_X^{\mathbf{M}} \cdot e^{ik\Delta \cdot n \cdot \sin\theta}\right|^2}{\left|\sum_{n=0}^{N} J_X^{\mathbf{M}} \cdot e^{ik\Delta \cdot n \cdot \sin\theta}\right|^2_{\max}} \tag{22}$$

where θ is the angle of the direction of radiation with respect to the "oz"-axis. The relative radiated power is calculated by integrating the (22) over the angle θ (in the case of two-dimensional model of the array)

$$P_{rad} = \int_{-\pi/2}^{\pi/2} |F_r(\theta)|^2 \, d\theta \tag{23}$$

3. ANALYSIS OF A RECONFIGURABLE APERTURE

The proposed model was first applied to the analysis of reconfigurable antennas formed by identical high conductivity areas of width $b_i = b$ separated by equal distances $d_i = d$ (as in case of a typical leaky-wave periodical array), which can be obtained from the expression

$$d = \frac{1}{\beta_s - \sin(\theta_0)} \tag{24}$$

where $\beta_s = real(\chi_s)$ is the phase constant; $\chi_s = \beta_s - i \cdot \alpha_s$ is the propagation constant of the surface wave; θ_0 is the desired direction of radiation. The width b has been chosen equal to $d/3$.

Since the reconfigurable structure under test is discrete, the distance d and width b is not continuous

$$q = round(d/\Delta), \tag{25a}$$

$$p = round(b/\Delta) \tag{25b}$$

where q and p is the number of minimum spacing between the individual PIN's Δ which can be inserted in the distance d and width b, respectively; function "*round*" denotes rounding to the nearest integer value.

Due to the discontinuities, the "discrete direction" of radiation can differ from the desired one.

Fig. 2 shows a plot of the main beam direction θ_0 as function of the discrete distance q given by (24) and (25a) for various values thickness of the h. It is found that the main beam direction can be controlled over a wide range but only in a discrete direction.

The parameters of the reconfigurable antenna are chosen as follows: $\varepsilon_2 = 11.8 - i \cdot 0.00163$ (for silicon without plasma), $f = 33.5GHz$, $N = 128, L/\lambda = 10$, $\Delta = L/N = 0.078\lambda$.

As it can be seen in Fig. 2 the maximum difference between neighbouring discrete radiation angle value can be as high as 40° (for $h = 0.65mm$). This difference will decrease if the maximum number N of individual PIN structures increases. For example, if N equals 256, then the maximum difference will equal 25°.

In Fig. 3, an example of normalized computed (solid line) and desired (dotted line) E-plane radiation patterns, is shown. Desired radiation pattern has been calculated on

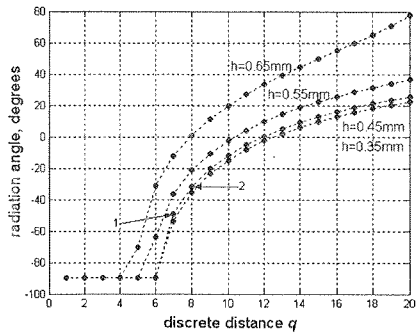

Fig. 2. Radiation angle as a function of the discrete distance q for various thickness h

the assumption that the magnitude current distribution on a continuous structure is uniform. Desired direction of radiation is 40° (for the case when $h = 0.45mm$ and $N = 128$).

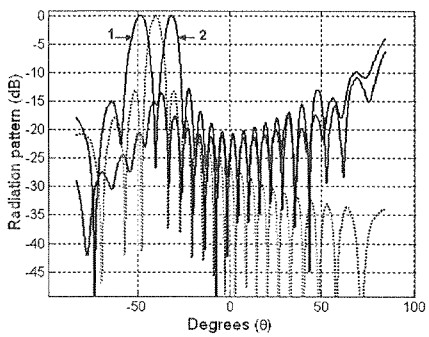

Fig. 3. The computed (solid lines) and desired (dotted line) E-plane radiation patterns

However, the nearest to the desired radiation patterns (the calculated radiation patterns of the discrete reconfigurable antenna) have the maximum direction of radiation equal to 47° (line 1) and equal to 32° (line 2) respectively. This is due to the discrete distance q, as it has been mentioned earlier. It is also seen that the side lobes level (SLL) of the calculated pattern is much higher than SLL of the desired one. The reason for this is the relatively small structure. The structure is only about 10λ. So the radiation field is under the influence of the surface wave diffraction on the substrate edge, because significant part of the surface wave power runs in to a substrate edge.

Fig. 4 shows the computed current distribution for the radiation pattern, which is shown in Fig. 3 (line 1). The current distribution for radiation pattern which is shown with line 2 in Fig. 3 is similar to the first one and thus is not shown here.

Referring to Fig. 4, it can be seen that the induced magnetic currents exists only on the impedance strip, where surface impedance is not equal to zero. For the first radiation pattern (line 1, Fig. 3) the discrete distance q equals 7 ($d_i = d = 7 \cdot \Delta$) and the discrete width p equals 4 ($b_i = b = 4 \cdot \Delta$). For the second one q equals 8 and p equals 4 respectively.

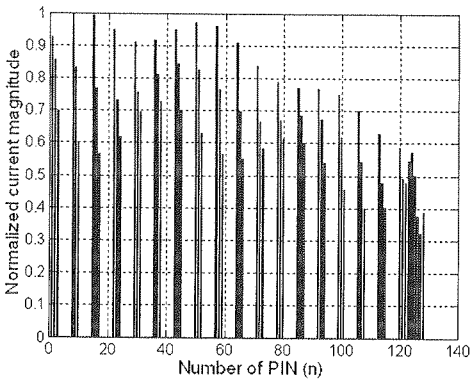

Fig. 4. The normalized distribution of magnetic currents along the variable surface impedance

4. OPTIMIZATION OF THE CONDUCTIVE PATTERN OF A RECONFIGURABLE APERTURE

To create the desired radiation pattern or the nearest to it, it is necessary to have a specific type of amplitude-phase field distribution along the radiating structure. It can be obtained by choosing both the optimum width b_i (or p_i) of the discontinuities and the distance d_i (or q_i) between them.

For the purpose of practical implementation it was assumed that the turned on controlled individual PIN is presented as "1" and turned off — as "0". From Fig. 5 we can see that such representation gives a binary resolution, which equals q. Here, q bits are used for discrete width (p_i) control in each segment. The number of segments NP is determined as $NP = round\,(L/d)$. This number will undergo changes since the distance d depends on the desired direction of radiation. For example: $NP = 17$ for $\theta_0 = -40$, and $NP = 11$ for $\theta_0 = 0$.

The binary code, which represents the minimum and maximum width is "000...00" and "111...11" respectively. It means that in the first case the width equals 0 and in the second case it equals $d = q \cdot \Delta$.

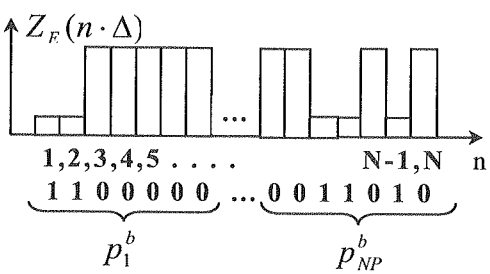

Fig. 5. Forming of binary chromosome represents reconfiurable structure setting (conductive pattern)

The genetic algorithm [24] determines the optimal configuration of reconfigurable conductive pattern for a particular goal.

Each binary string representing the width p_i^b is concatenated together to form a single string — binary chromosomes.

In the first step, the genetic algorithm processes a random population of binary chromosomes. In the first approach to adaptation, each chromosome represents reconfigurable structure settings. These chromosomes are then assigned cost function value. Then in the iterative manner new populations are created by application of selection, crossover and mutation operations giving gradual improvement of cost function value that is maximised.

The cost function Q has been used in the form:

$$Q = \frac{1}{\max \|f(\theta) - F_r(\theta)\|^2} + D(\theta_0) \tag{26}$$

where $f(\theta)$ is the desired radiation pattern; $F_r(\theta)$ — is the calculated radiation pattern; $D(\theta_0)$ — is the directivity in the desired direction of maximum radiation θ_0. Directivity is determined as follows

$$D(\theta_0) = \frac{2\left|F_r(\theta_0)\right|^2}{P_{rad}} \tag{27}$$

The progress of reproduction and survival selection continues until a satisfying result is obtained or preset maximum number of iteration is reached.

Fig. 6 shows the normalized E-plane radiation patterns before and after optimization to the desired direction of radiation, which equals −40°. This result shows that

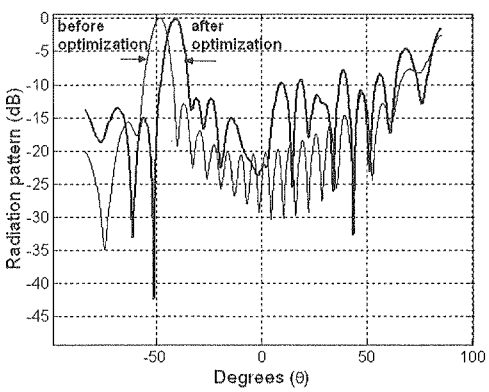

Fig. 6. Normalized radiation pattern before and after optimisation to the desired direction of radiation $\theta_0 = -40$

for such a small PIN number N (in our case $N = 128$) the radiation pattern can be optimized to desired direction but in the meantime, the side lobe level increases. The PIN structure (binary chromosomes) generating optimized radiation pattern (it is shown in Fig.6) is shown at Table 1.

To validate the impedance model, a test was performed on the substituted microstrip structure. The frequency of operation (33.5 GHz), the number N (128) and the

Table 1

The PIN structure generates optimized radiation pattern shown in Fig. 6.

p_1^b	p_2^b	p_3^b	p_4^b	p_5^b	p_6^b
0011100	0110111	0001110	0011111	1001010	1000111
p_7^b	p_8^b	p_9^b	p_{10}^b	p_{11}^b	p_{12}^b
1001111	1100111	1100001	1110101	1101001	1101010
p_{13}^b	p_{14}^b	p_{15}^b	p_{16}^b	p_{17}^b	p_{18}^b
1110010	1011010	1111000	1111010	1110100	000000000

dimension structure (10λ) were the same as in the semiconductor case. The dielectric substrate was 2-mm-thick Teflon. The radiation aperture was formed from a printed circuit board 90×30 mm in size, with the strips etched from the copper cladding on one side of the board.

The strip configuration (Fig. 7) was obtained after optimization of the radiation pattern to desired direction of radiation. In this case the direction was equal to $\theta_0 = -20$.

Fig. 7. The strip configuration of substituted microstrip structure

Fig. 8 shows the normalized calculated (before and after optimization) and measurement radiation pattern. It can be seen that simulated and measured patterns are nearly the same.

Same difference between them can be caused by the finite size of the conductive screen on which the impedance structure is placed, whereas in the theoretical model this surface is infinite in size.

The microstrip structure (binary chromosomes) generating optimized radiation pattern (it is shown in Fig. 8) is shown at Table 2.

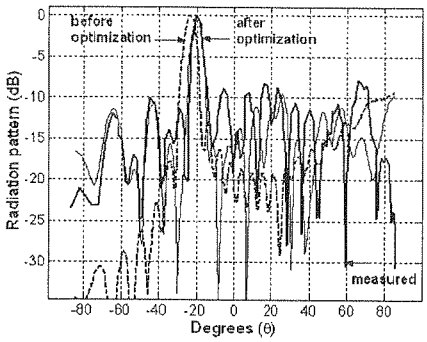

Fig. 8. Normalized radiation pattern before and after optimization to the desired direction of radiation $\theta_0 = -20$ (calculed and measured)

Table 2

The binary chromosomes of the substituted microstrip structure generates optimized radiation pattern shown in Fig. 8.

p_1^b	p_2^b	p_3^b	p_4^b	p_5^b	p_6^b
00100101	10010111	00010111	10010111	01100101	10100001
p_7^b	p_8^b	p_9^b	p_{10}^b	p_{11}^b	p_{12}^b
01100011	01100001	10100001	11011000	01110010	11010000
p_{13}^b	p_{14}^b	p_{15}^b	p_{16}^b	p_{17}^b	p_{18}^b
01101101	10101000	00101011	00000000	—	—

5. CONCLUSION

This paper discusses an effective approximate approach, based on impedance boundary condition, to the analysis and design of the reconfigurable aperture. The integral equation for the magnetic currents being excited on an aperture with the variable surface impedance is formulated. The variable surface impedance means that surface impedance of an aperture can be varied arbitrarily by changing the conductivity of a semiconductor substrate. The Genetic Algorithm is used in the optimization of the configuration of a conductive pattern on a semiconductor substrate to obtain the desired radiation pattern. Theoretical results are compared with measurement for cases of the substituted microstrip structure and show a very good agreement.

It should also be noted that the proposed impedance model can be applied to the analysis and design of a broad class of microwave and mm-wave flat structure which can be presented in impedance approximation including structures with MEMS.

6. REFERENCES

1. J. C. Veihl, R. E. Hodges, D. McGrath, C. Monzon: *Reconfigurable Aperture Decade Bandwidth Array*. IEEE AP Symp. Salt Lake City, 2000, pp. 314-317.
2. J. H. Schaffner, D. F. Sievenpiper, R. Y. Loo: *A Wideband Beam Switching Antenna Using RF MEMS Switches*. IEEE AP Symp., Salt Lake City, 2000, pp. 658-661.
3. J. H. Schaffner, R. Y. Loo, D. F. Sievenpiper, F. A. Dolezal, G. L. Tangonan, J. S. Colburn, J. J. Lynch: *Reconfigurable Aperture Antenna Using RF MEMS Switches for Multi-Octave Tunability and Beam Steering*. IEEE AP Symp., Salt Lake City, 2000, pp. 321-324.
4. M. El. Sherbiny, A. E. Fathy, A. Rosen, G. Ayers, S. M. Perlow: *Holografic Antenna Concept, Analysis, and Parameters*. IEEE Trans. Antennas Propagat., vol. AP-52, pp. 830-839, March 2004.
5. J. C. Maloney, M. P. Kesler, L. M. Lust, L. N. Pringle, T. L. Fountain, P. H. Harms: *Switched Fragmented Aperture Antennas*. IEEE AP Symp., Salt Lake City, 2000, pp. 310-313.
6. L. N. Pringle, P. H. Harms, S. P. Blalock, G. N. Kiesel, E. J. Kuster, P. G. Friederich, R. J. Prado, J. M. Morris, G. S. Smith: *A Reconfigurable Aperture Antenna Based on Switched Links Between Electrically Small Metallic Patches*. IEEE Trans. Antennas Propagat., vol. AP-52, pp.143-1445, June 2004.
7. M. Matsumoto, M. Tsutsumi, N. Kumagai: *Radiation of Millimeter waves form a Leaky Dielectric Waveguide with a Light-Induced Grating Layer*. IEEE Trans. Microwave Theory Tech., vol. MTT-35, pp. 1033-1042, Nov. 1987.
8. A. Fathy, A. Rosen, F. McGinty, G. Taylor, S. Perlow, M. ElSherbiny: *Silicon Based Reconfigurable Antennas*. IEEE AP Symp., Salt Lake City, 2000, pp. 325- 313.
9. V. A. Manasson, I. Sadovnik, M. Aretskin, A. Brailovsky, P. Grabiec, D. Eliyahu, M. Felman, V. Khodos, V. Litvinov, J. Marczewski, R. Mino: *Electronically Controlled Beam-Steering Antenna*. The 27th Annual Antenna Application Symposium, Monticello, Illinis, 2003, pp.355- 359.
10. T. Itoh: *Application of gratings in a dielectric waveguide for leaky-wave antennas and band-reject filters*. IEEE Trans. Microwave Theory Tech., vol. MTT-25, pp. 1134-1138, Dec. 1977.
11. Y. Yashchyshyn, J. Modelski: *Rigorous Analysis and Investigations of the Scan Antennas on a Ferroelectric Substrate*. IEEE Trans. Microwave Theory Tech, vol. MTT-53, pp. 427-438, Feb. 2005.
12. V. A. Manasson, L. S. Sadovnik, V. A. Yepishin, D. Marker: *An Optically Controlled MMW Beam-Steering Antenna Based on a Novel Architecture*. IEEE Trans. Microwave Theory Tech., vol. MTT-45, pp. 1497-1500, Aug. 1997.
13. R. Mitra, R. Kastner: *A spectral domain approach for computing the radiation characteristics of a leaky-wave antenna for milimeter waves*. IEEE Trans. Antennas Propagat., vol. AP-29, pp.652-654, July 1981.
14. Y.-D. Lin, T. Itoh: *Frequency-scanning using the crosstieoverlay slow-wave structures as transmission lines*. IEEE Trans. Antennas Propaga., vol. AP-39, pp.377-380, Mar. 1991.
15. M. Gugliemi, G. Boccalone: *A novel theory for dielectric-inset waveguide leaky-wave antennas*. IEEE Trans. Antennas Propagat., vol. AP-39, pp.497-504, Apr. 1991.
16. V. I. Kalinichev: *Analysis of Planar Slot Arrays Using Magnetic Currents and Magnetomotive Force*. IEEE Trans. Antennas Propagat., vol. AP-43, no. 2, pp. 1434 -1445, Febr. 1995.
17. W. Menzel: *A new Traveling-Wave Antenna in Microstrip*. Electronics and Communication, Band 33, Heft 4, pp. 137-140, Apr. 1979.
18. G. D. Maliuzhinets: *Excitation, reflection and emission of surface waves from a wedge with given face impedances*. Sov. Phys. Dokl., vol. 3, pp. 752-755, 1958.

19. V. F. Fusko, Q. Chen: *Direct-signal modulation using a silicon microstrip patch antenna.* IEEE Trans. Antennas Propagat., vol. AP-47, pp.1025-1028, June 1999.
20. G. C. Taylor, A. Rosen, A. E. Fathy, P. K. Swain, S. M. Perlow: *Surface PIN device.* U.S. Patent US 6617670 B2, Sep. 9, 2003
21. G. T. Markov, A. F. Chaplin: *Electromagnetic waves exitation. Energia*, 1967 (in Russian).
22. A. F. Verlan, V. S. Sizikov: *Integral equation. Methods, algorithms and program.* Kyjiv, Naukova dumka, 1986 (in Russian)
23. T. K. Sarkar, E. Arvas, S. M. Rao: *Application of FFT and the Conjugate Gradient Method for the Solution of Electromagnetic Radiation from Electrically Large and Small Conducting Bodies.* IEEE Trans. Antennas Propagat., vol. AP-34, pp.635-640, May 1986.
24. D. E. Goldberg: *Genetic Algorithm in Search, Optimization, and Machine Learning.* Addison-Wesley Publishing Company, Inc., 1989.

E. JASZCZYSZYN

MODEL IMPEDANCYJNY ANTENY Z REKONFIGUROWANĄ APERTURĄ

Streszczenie

Anteny o rekonfigurowanej aperturze mogą być wykorzystane przez różne systemy radiowe w różnych momentach czsowych. Wspólne wykorzystanie jednej rekonfigurowanej apertury przez różne systemy radiowe umożliwia "zmniejszenie" sumarycznej apertury fizycznej zespołu anten, z którego każda antena miałaby być wykorzystywana przez poszczególny system. Wydaje się, że jest to jedyny skuteczny sposób na "miniaturyzację" anten, której w porównaniu z osiągnięciami w mikroelektronice jeszcze nie udało się osiągnąć. Apertury takie pozwalają także osiągnąć dodatkowe możliwości w procesie adaptacji.

Do opracowania apertur rekonfigurowanych elektronicznie, proponuje się wykorzystanie nowoczesnych osiągnięć technologii elektronowej. Generalnie anteny o rekonfigurowanej elektrycznie aperturze można podzielić na dwie grupy. Do pierwszej grupy należą anteny wykorzystujące poszczególne przełączniki, wykonane m.in. na diodach PIN, tranzystorach oraz systemach MEMS. Do drugiej grupy można zaliczyć struktury wykorzystujące czasowo tworzone obszary przewodzące na powierzchni np. półprzewodnika.

Przykładem struktur pierwszej grupy jest apertura fragmentowana, której konfiguracja może być przełączana do uzyskania różnych możliwości funkcjonalnych. Struktura bazuje na matrycy przewodzących łatek wraz z przełącznikami pomiędzy nimi. Taka apertura jest rekonfigurowana przy pomocy włączania/wyłączania elementów łączących poszczególne łatki.

Przykładem anten drugiej grupy są struktury, które mogą dynamicznie zmieniać przewodność niektórych części apertury przy pomocy, m.in. aktywacji określonych obszarów półprzewodnika. Podstawowym elementem takiej anteny jest struktura półprzewodnikowa zawierająca dużą liczbę diod PIN, które są sterowane niezależnie. Fala elektromagnetyczna rozchodząca się wzdłuż struktury półprzewodnikowej (wykonanej w postaci falowodu dielektrycznego) rozprasza się na włączonych diodach PIN, co powoduje promieniowanie i z kolei kształtowanie charakterystyki kierunkowej, podobnie jak w przypadku anteny z falą wyciekającą.

W niniejszej pracy główną uwagę skupiono na opracowaniu metodyki analizy oraz syntezy apertury rekonfigurowanej, która "generowałaby" pożądany kształt charakterystyki kierunkowej. W tym celu został opracowany model impedancyjny, który w większości przypadków pozwala transformować rzeczywistą strukturę promieniującą w powierzchnię ze zmienną impedancją poprzez zamianę rygorystycznych warunków brzegowych na powierzchni na warunki impedancyjne. Takie podejście znacznie upraszcza

zagadnienie elektrodynamiczne. Zapisane równanie całkowe względem nieznanych rozkładów prądów powierzchniowych na powierzchni zmiennej impedancji można rozwiązać, stosując np. metodę gradientów sprzężonych z wykorzystaniem szybkiej transformaty Fouriera. Charakterystyczną osobliwością takiego algorytmu numerycznego jest fakt, że skuteczność jego rośnie wraz ze wzrostem wymiaru struktury promieniującej.

Synteza apertury rekonfigurowanej polega na poszukiwaniu optymalnego rozkładu obszarów przewodzących (tworzonych przestrzennymi dodami PIN), który odpowiadałby pożądanej charakterystyce kierunkowej. Synteza taka odbywa się na drodze optymalizacji numerycznej przy wykorzystaniu algorytmu genetycznego.

Weryfikacja zaproponowanego modelu impedancyjnego została przeprowadzona przy pomocy zastępczego modelu paskowego. Porównanie teoretycznych oraz eksperymentalnych wyników wykazało bardzo dobrą zgodność.

Zaproponowany model impedancyjny do analizy i syntezy anten z rekonfigurowaną aperturą może być stosowany do projektowania rozmaitych struktur, które można zastąpić strukturą impendancyjną, włącznie z systemami MEMS.

Słowa kluczowe: apertura rekonfigurowana, impendancja powierzchniowa

a n
wit
are
lon
con
Thi
-35
and
des
usi

Key

Curr
the dema
the reaso
The micr
are essen
ding radi
warfare [

The
MOSFET
sites. Bro

KWARTALNIK ELEKTRONIKI I TELEKOMUNIKACJI, 2005, 51, ZESZYT SPECJALNY, ss. 85–104

The electro-thermal modeling of high power microwave FET and its applications

WOJCIECH WOJTASIAK

Institute of Radioelectronics,
Warsaw University of Technology
E-mail: wwojtas@ire.pw.edu.pl
ul. Nowowiejska 15/19 00-665 Warsaw, Poland

A complete electro-thermal model (*E-T*) for a high power microwave FET based on a nonlinear channel current equation and small signal extraction methodology combined with a solution of 3D thermal problem for an arbitrary pulsed thermal excitation in the area of transistor is presented. The temperature dependencies of the *E-T* model describing long-term as well as short-term thermal effects have been derived from solution of heat conducting equation (*HCE*) using *3D-FDTD* thermal method and experimental results. This model is used to predict the performance of a high power amplifier (*HPA*) over a -35°C to +60°C temperature range in a wide frequency band for different operating class and modes (cw, pulsed and keyed bias). The *E-T* model was experimentally verified for designing *L*, *S* and *C*-band high power amplifiers with an output power level up to 200W using *LDMOSFET's* and *MESFET's*.

Keywords: Electro-thermal FET model, 3D-FDTD thermal method, high power FET, LDMOS-FET, MESFET

1. INTRODUCTION

Currently, due to the development of wireless personal communication market, the demand for high-power solid-state transmitters is on the rise. This demand is also the reason for the fast development of high power microwave transistors technology. The microwave solid-state amplifiers, first of all with *LDMOSFETs* and *MESFETs*, are essential devices in a broad spectrum of microwave systems applications including radiommunications, satellite communications and radiolocation with electronic warfare [1].

The *Laterally Diffused Metal Oxide Semiconductor Field Effect Transistors* (*LDMOSFET*) were originally designed for use in *GSM* and *PCS* base station cellular sites. Broad deployment of wireless communications has created a demand for cost

effective — using silicon technology, linear, high-gain and high-power RF transistors for base station transmitters. Such requirements are fulfilled by the *LDMOS* technology.

The high power *MEtal Semiconductor Field Effect Transistors* (*MESFET*) are currently the most common devices used to design the microwave transmitters' amplifiers for military and professional applications above L-band. For example, new generations of 200÷300W high power GaAs *MESFETs* have been developed for *W-CDMA* and *WLL* (*Wireless Local Loop*) base stations [2]. The military area of *MESFETs* applications includes amplifiers designing for *T/R* modules of *Active Phased Array Radar* (*APAR*) [3]. The main disadvantage of high power *MESFETs* is the very high cost.

The typical military and some commercial applications of *HPA* (*High Power Amplifier*) require keeping performances over a wide temperature range. The required ambient temperature often ranges from -55°C up to 125°C. In addition, the *HPA's* especially operating in systems with subtle modulations such as *QAM* or chirp should be characterized by very low transmittance distortions. It is claimed that the transmittance distortions of even linear *HPAs* are caused by changes of temperature inside an active area of transistor [4]. This temperature changes result from a dissipated power in the transistor.

Various approaches to microwave *FETs* temperature-dependent modeling have been proposed [5], [6], [7]. The very popular nonlinear *MOSFET* model in time domain is implemented in Spice simulator [8]. The common feature of these approaches is the self-heating modeling by drain current changes versus temperature in the steady-state analysis. To calculate the temperature inside an active area of FET, on the base the electro-thermal analogy [9], a simple low-pass thermal circuit is used. These models were usually verified for small power *FETs* and cw excitation or over a limited temperature range. The comparison of these models has been reported [10].

The electro-thermal (*E-T*) model of a high power *FETs*, which incorporates electrical and temperature dependencies of the elements of an equivalent circuit, is needed to predict the amplifier temperature behavior during design. It allows us to optimize the amplifier structure with respect to chosen parameters (output power level, gain, nonlinear distortions, spectral requirements, transmittance stability during RF pulse, etc.). This approach reduces the time and costs of design.

The proposed model concept, in thermal part, is based on the solution of *HCE* equation by means of the *3D-FDTD* (*3-Dimensional Finite Difference method in Time Domain*) thermal method [11]. The thermal problem is solved in a thermal structure consisting of three regions: chip, flange and radiator, with a thermal excitation within the thin semiconductor layer — in the channel of the transistor. The thermal excitation is represented by dissipated power P_{DIS}, in the form of heat, in the transistor. Obviously the dissipated power is determined by DC-bias and AC excitation conditions and expresses as:

$$P_{DIS} = P_{DC} - P_{OUT} + P_{IN} \tag{1}$$

As a result of thermal part, we obtain a transient temperature distribution in an active area of the transistor. The transient temperature of the *FET* channel is substituted into the electrical part of the *E-T* model. Generally, the electrical model is extracted by matching DC-characteristics and small signal parameters without pulsed measurements. It can be emphasized that proposed *E-T* model allows simulating the parameters of *HPAs* with *LDMOSFETs* and *MESFETs*. The concept of the electro-thermal (*E-T*) model of microwave power *FETs* is illustrated in Fig. 1.

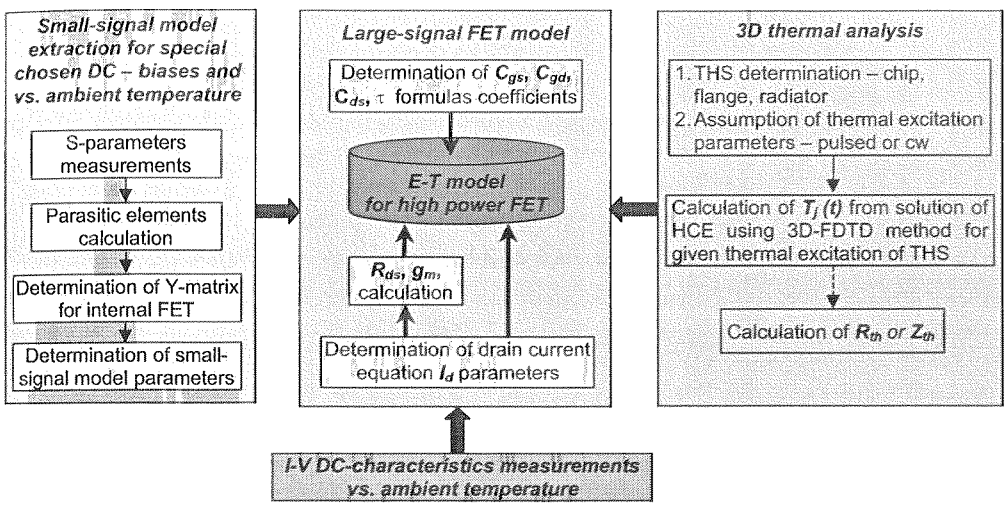

Fig. 1. The concept of the $E-T$ FET model

2. TRANSISTOR MODELING

2.1. TRANSIENT TEMPERATURE DISTRIBUTION

The transient temperature distribution $T = T(x, y, z, t)$ in an active are of *FET* is calculated from the solution of the *HCE* equation for the *Transistor Heat Structure (THS)* as shown in Fig. 2.

In the case of isotropic, linear and homogeneous mediums and on the assumption that the material parameters are constant, the *HCE* can be depicted as:

$$\nabla^2 T(x, y, z, t) + \frac{1}{\lambda_i} g(x, y, z, t) = \frac{1}{\alpha_i} \cdot \frac{\partial T(x, y, z, t)}{\partial t} \tag{2}$$

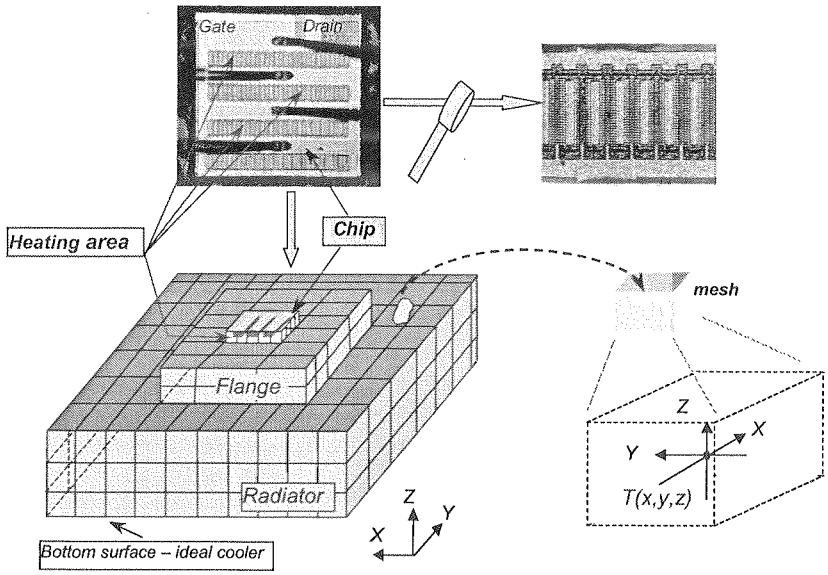

Fig. 2. The view of the typical *FET* chip and *Transistor Heat Structure (THS)*

where: $T = T(x, y, z, t)$ — the transient temperature distribution
$g(x, y, z, t)$ — the thermal power density emitted (dissipated) in a volume V
α_i — thermal diffusion
λ_i — thermal conductivity
for i — area of THS : chip (c), flange (f) and radiator (r).

The analytical solution of the HCE (2) is practically impossible for the microwave high power FET structure. A numerical method is the only sensible way to solve this problem. Due to the easiness of application, the explicit $3D$-$FDTD$ thermal method was chosen. The $FDTD$ method based on the substitution of derivatives in HCE (2) for finite differences is easy to use in a numerical implementation [12]. It leads to discretization of the THS in space and time (Fig.2). The explicit $FDTD$ method consists in the solution of HCE in a node for a next time step based on the current temperature distribution.

The HCE have been solved under the following assumptions:

- the THS includes three mediums: chip (semiconductor), metal flange and radiator
- the mediums (chip, flange, radiator) of the THS are linear, homogeneous and isotropic
- the material parameters α_i, λ_i of the THS do not depend on temperature, and are constant depending on a doped level of semiconductor in chip
- the initial temperature of the THS is:

$$T(y, x, z, t = 0) = T_o \tag{3}$$

- the temperature on the bottom of an equivalent radiator is:

$$T(y, x, z = 0, t) = T_o \tag{4}$$

- the thermal excitation (heat source) is located in the channel of FET within a thin chip layer, which is geometrically determined by the metallization of gate, drain and source
- the thermal excitation is represented by thermal power density $g(x, y, z, t)$ given as:

$$g(x, y, z, t) = \frac{P_{DIS}(t)}{V} \tag{5}$$

where: P_{DIS} — dissipated power (1) in transistor
V — volume of heating area (channel of FET)

- the heating is evenly distributed in volume V — the thermal power density $g(x, y, z, t)$ does not depend on the co-ordinates
- the top and side surfaces of the radiator, flange and chip (Fig. 2) are isolated — the lack of a heat exchange with the environment
- the heat flux and temperature on the boundaries of the mediums in z- direction (chip-flange, flange-radiator) are continuous

The temperature in a given node of *THS* can be calculated either from energy conservation law or direct substituting the finite differences into *HCE*. As an example, two situations of nodes located inside chip are considered below:

- internal node of the *THS* with heating source, as illustrated in Fig. 3,

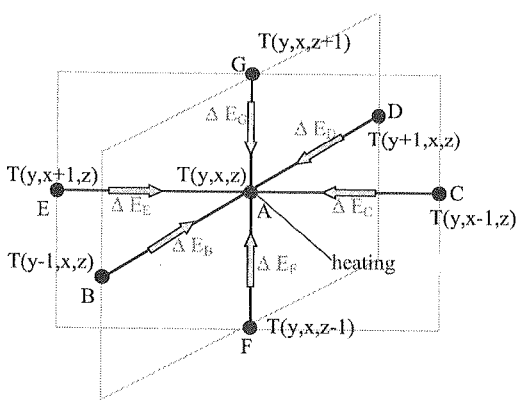

Fig. 3. The internal node of *THS* with heating source

The temperature T_A at the internal heating node A for next time step $p+1$ is calculated from the following equation:

$$T_A^{p+1} = \alpha_c \cdot \Delta t \cdot \left[\frac{T_B^p + T_D^p}{\Delta y^2} + \frac{T_C^p + T_E^p}{\Delta x^2} + \frac{T_F^p + T_G^p}{\Delta z^2} \right] + T_A^p \cdot \left[1 - 2\alpha_c \cdot \Delta t \cdot \left(\frac{1}{\Delta y^2} + \frac{1}{\Delta x^2} + \frac{1}{\Delta z^2} \right) \right] + \\ + \frac{P_{DIS} \cdot \Delta t}{N \cdot \Delta x^2 \cdot \Delta y^2 \cdot \Delta z^2 \cdot \left(\frac{\lambda_c}{\alpha_c} \right)} \tag{6}$$

where: N — a number of heating nodes

T_{nb}^p — the temperature in neighbouring nodes (nb) at p time moment

• internal node of the THS without heating source

The temperature T_A at the internal node A is calculated from the following equation:

$$T_A^{p+1} = \alpha_c \cdot \Delta t \cdot \left[\frac{T_B^p + T_D^p}{\Delta y^2} + \frac{T_C^p + T_E^p}{\Delta x^2} + \frac{T_F^p + T_G^p}{\Delta z^2} \right] + T_A^p \cdot \left[1 - 2\alpha_c \cdot \Delta t \cdot \left(\frac{1}{\Delta y^2} + \frac{1}{\Delta x^2} + \frac{1}{\Delta z^2} \right) \right] \tag{7}$$

The explicit FDTD method [12] is limited by a stability condition (8) which tides time step Δt and grid dimension Δy, Δx, Δz:

$$1 - 2\alpha_c \cdot \Delta t \cdot \left(\frac{1}{\Delta y^2} + \frac{1}{\Delta x^2} + \frac{1}{\Delta z^2} \right) > 0 \tag{8}$$

As an example, the transient temperature distribution in the THS of the Si-LDMOSFET (PTF10119 made by Ericsson) excited by heat power unit step of P_{DIS} = 6W is presented in Fig. 4. The temperature characteristics were simulated by means of the own software [13]. The description of THS for PTF10119 transistor includes Tab. 1.

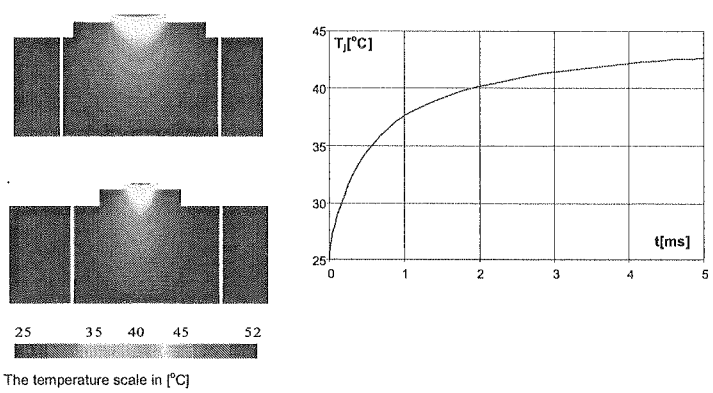

Fig. 4. The temperature distribution in the THS of LDMOSFET (PTF10119), seen in XZ, YZ cross-sections at the time moment: *1.2ms* and the channel temperature $T_j(t)$. The excitation: the heat power unit step of P_{DIS} =6W

Table 1

The parameters of the *THS* for PTF10119 LDMOSFET (Fig. 2)

	dimensions [*mm*]			thermal parameters	
	x	y	z^*	$\alpha_i[m^2/s]$	$\lambda_i[W/mK]$
chip (silicon)	0.65	0.8	0.12	0.9e-4	150
flange (copper)	6	15	2	1.02e-4	350
radiator (copper)	30	30	4.5	0.88e-4	300

– thickness of chip, flange and radiator

2.2. MODELING OF HIGH POWER FET

The equivalent circuit of the proposed *E-T* model of a microwave high *FET* is shown in Fig. 5.

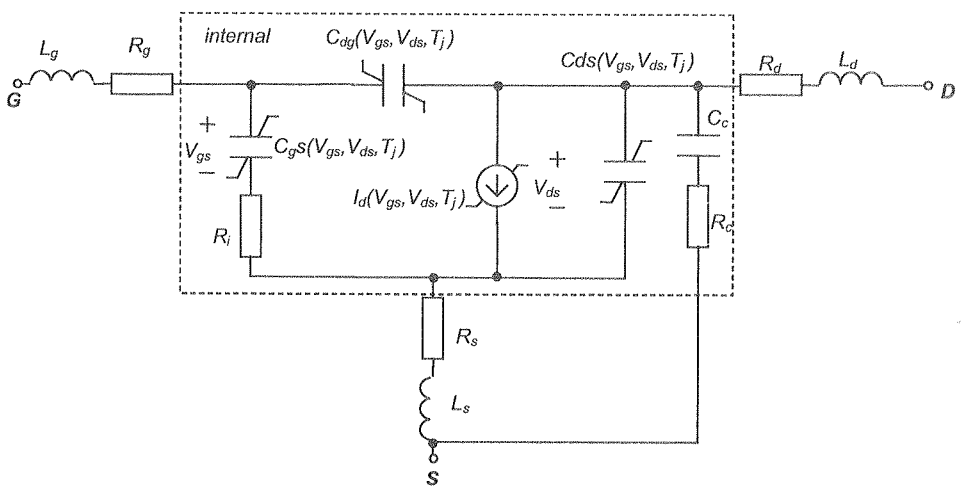

Fig. 5. The *E-T* model of a high power *FET*

The developed $E-T$ model of FET was implemented in Agilent's Tech. simulator *Advanced Design System* (ADS) using *Symbolic Defined Device* (SDD) [14] as shown in Fig. 6. The *SDD* technique proposed by Agilent Tech. allow users to add their own custom nonlinear models such as nonlinear resistor, diode, nonlinear amplifier, mixer, voltage-controlled oscillator (VCO) etc. in their design project. The *SDD* is represented on the circuit schematic as an *n*-port device, with up to 10 ports. The equations that specify the voltage and current of a port are defined as functions of other voltages

and currents. A well-defined n port is described by n equations, called *constitutive relationships* that relate the n port currents and the n port voltages. For linear devices, the constitutive relationships are often specified in the frequency domain (for example, as admittances), but since the *SDD* is used to model nonlinear devices, its constitutive relationships are specified in the time domain.

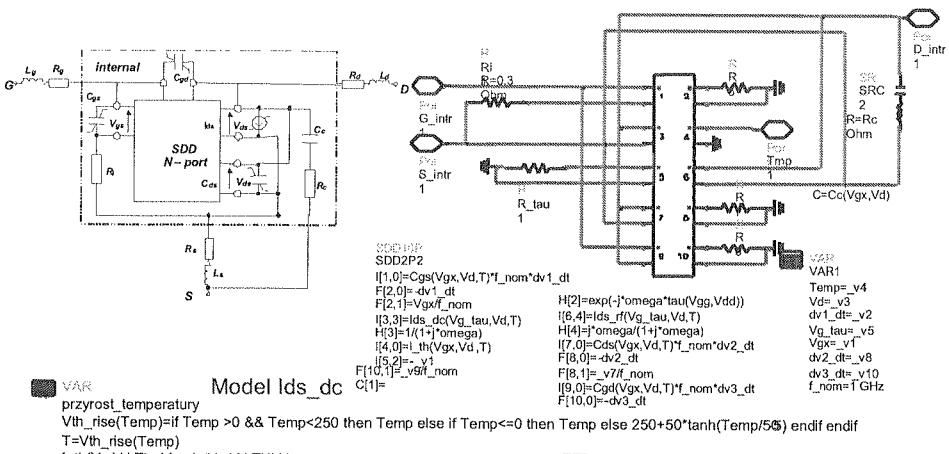

Fig. 6. The *E-T* FET model as the symbolic defined device *SDD* — the idea and a sample of ADS — notation

The constitutive relationships may be specified in either *explicit or implicit* representations. With the explicit representation, the current at k port is specified as a function of port voltages only, and the implicit representation uses an implicit relationship between any of the port currents and any of the port voltages. The explicit representation is a voltage-controlled representation and can implement only voltage-controlled expressions. Explicit equations use a standard nodal analysis based on Kirchoff's current law. Due to the complexity of *E-T* model, the explicit as well as the implicit representation of *SDD* have been used.

After a survey of the literature and analysis of the accuracy of many formulas, the nonlinear drain current I_d equation proposed by Yang [5] was chosen and implemented in *ADS* — simulator. The Yang's equation was specially derived for the modeling of a drain current source of Si-LDMOSFET. We modified and generalized this equation for

describing of a drain current of GaAs MESFET. This modification improves the fitting I-V characteristics for a small value of $|V_{gs}|$. The complete nonlinear drain current I_d equation used in *E-T* model is expressed as follows:

$$I_d = \beta(T, f_S) \cdot \left[V_{gm} + \ln\left(e^{V_{gm}} + e^{-V_{gm}}\right)\right] \cdot \tanh\left[\frac{\alpha(t) \cdot V_{ds}}{VST \cdot \ln\left(e^{\frac{V_{gm}}{VST}} + 1\right)}\right] \cdot [1 + \lambda(T) \cdot V_{ds}] \quad (9)$$

with:

$$V_{gm} = A \cdot \left(1 - \frac{1}{V_{gm1}^{VGMEXP}}\right) - C \quad (10)$$

$$V_{gm1} = 10^{-6} + 0.5 \cdot \left\{\tanh\left[10^6 \cdot \left(1 + V_{gs} - V_T\right)\right] + 1\right\} \cdot \left|1 + V_{gs} - V_T\right| \quad (11)$$

$$V_T(T_j) = V_{TOO} + V_{TOT} \cdot (T_j - T_o) + \gamma \cdot V_{ds} \qquad \beta(T_j, f_s) = d \cdot f_S \cdot \beta_0 + \beta_T \cdot (T_j - T_o) \quad (12)$$

$$\alpha(T_j) = \alpha_0 + \alpha_T \cdot (T_j - T_o) \qquad \lambda(T_j) = \lambda_0 + \lambda_T \cdot (T_j - T_o) \quad (13)$$

where: $\beta_o[1/\Omega]$, $\beta_T[1/(\Omega°C)]$, α_o, α_T, d, $\lambda_o[1/V]$, $\lambda_T[1/(V°C)]$, $VST[V]$, $VGMEXP$, A, C, $V_{TOO}[V]$, $V_{TOT}[V/C°]$, $R_C[\Omega]$, $C_C[F]$ are the parameters to be determined during the extraction process from DC-characteristics.

The f_S is the switching parameter for the low frequency dispersion correction [15]. The temperature dependencies modeling nonlinear elements of the equivalent circuit of *E-T* model were obtained from I-V characteristics and S-parameters measured for different ambient temperatures at the proper chosen operating points. The formulas describing the capacitances C_{gs}, C_{dg}, $C_{ds.}$, and time delay τ were only extracted from small-signal measurements for a few bias points and temperatures, and expressed as follows:

$$C_{ds} = [a_0 + a_1 \cdot tanh(a_2 \cdot V_{gs} + a_3 \cdot V_{ds.} + a_4) \cdot tanh(a_5 + a_6 \cdot V_{ds.}) \cdot tanh(a_7 \cdot V_{gs})] \cdot (1 + a_8 \cdot T_j) \quad (14)$$

$$C_{gd} = \left\{b_0 + b_1 \cdot [1 + tanh(b_2 \cdot V_{gs} + b_3)] \cdot ln\left(1 + exp\left[\frac{b_4 \cdot V_{ds} - b_5}{b_6}\right]\right)\right\} \cdot (1 + b_7 \cdot T_j) \quad (15)$$

$$C_{gs} = \{c_0 + c_1 \cdot tanh(c_2 \cdot V_{gs} + c_3) + c_4 \cdot tanh(c_5 + c_6 \cdot V_{ds}) + tanh(c_7 \cdot V_{ds} + c_8 \cdot V_{gs} + c_9) \cdot tanh(c_{10} \cdot V_{ds.} + c_{11} \cdot V_{gs} + c_{12})\} \cdot (1 + c_{13} \cdot T_j) \quad (16)$$

$$\tau = (d_0 \cdot log(1 + exp(d_3 \cdot V_{gs} + d_4 \cdot V_{ds})) \cdot log(d_1 \cdot V_{ds} + d_2)) \quad (17)$$

where:
a_i, b_i, c_i, d_i are the parameters to be determined during the extraction process.
The transconductance g_m and conductance g_{ds} are obtained from the differentiating drain current I_d (9), as follows:

$$g_m(V_{gs}, V_{ds}, T_j) = \frac{\partial I_d(V_{gs}, V_{ds}, T_j)}{\partial V_{gs}} \tag{18}$$

$$g_{ds}(V_{gs}, V_{ds}, T_j) = \frac{\partial I_d(V_{gs}, V_{ds}, T_j)}{\partial V_{ds}} \tag{19}$$

The other linear elements of the model, such as R_g, R_d, R_s, L_g, L_d, L_s are determined from *cold-FET* measurements [15], [16].
The electrical part of *E-T* model includes 57 parameters to describe the behavior of microwave power FET. This fact leads to the complex extraction procedure. However, the other advanced FET models need more and more parameters. For example, the Berkley's BSIM1-3 model requires more than 90 parameters [17]. The simplified FET models implemented in popular simulators characterize good accuracy only in the normal operating range of the transistor. The proposed *E-T* model also achieves an excellent agreement with experiments in the saturated, threshold and subthreshold regions.
In practice, the parameters of the *E-T* model are calculated by means of scaling and matching procedures using [S]-matrixes in conditions: $V_{gs} < U_p$, $V_{gs} = U_p$ and $V_{gs} > U_p$ for a few V_{ds} (for 6÷7 voltages) and for at least two different temperatures. Based on the experience, the determination of the *E-T* model parameters is relatively easy to perform.

3. MODEL VERIFICATION

3.1. TRANSISTORS FOR *E-T* MODEL VERIFICATION

The proposed model of high power *FET* was experimentally verified. For this purpose, the S-band *LDMOS* transistor *PTF*10119 made by *ERICSSON* of output power P_{out} = 12W and 4W *GaAs MESFET FLM5359-4F (FUJITSU)* for C-band were chosen. Both transistors include internally pre-matching sections for 2.1÷2.17GHz and 5.3÷5.9GHz frequency band, respectively. The RF specifications of chosen transistors are given in Tab. 2.

Additionally, the performances of *E-T* modeling of very high power FETs (200W LDMOS and 80W push-pull GaAs MESFET) are presented.

Table 2

RF specification of *PTF10119* and *FLM5359-4F* for $T_a = 25°C$

Parameter	Output power	Gain	Operating class	R_{th}
PTF10119	12W	12dB	$AB - U_{DS} = 28V I_{DQ} = 160mA$	3.2°C/W
FLM5359-4F	4W	10.5dB	$A - U_{DS} = 10V I_D = 1.1A$	5°C/W

3.2. *E-T LDMOSFET* MODEL VERIFICATION

The *E-T* model of the *PTF10119* transistor was implemented in *ADS* simulator in the form of the *SDD* block as shown in Fig. 6. The parameters of drain current source equation (8) for this transistor were calculated and given in Tab. 3.

Table 3

Drain current equation parameters of *PTF10119 E-T* model

parameter	**value**
$\beta_o[1/\Omega]$	1.720
$\varphi_o[1/V]$	1.31
$\kappa_o[1/V]$	0.00008
β_T	-0.0025
φ_T	0.004
κ_T	0
$V_{TO}[V]$	3.51
V_{TOT}	-0.002
$\gamma[1/V]$	-0.001
$A[V]$	7.03
$C[V]$	2.531
$VST[1/V]$	1.731
$VGMEXP$	0.45
$R_{th}[°C/W]$	3.2

Table 4

Parameters of nonlinear elements formulas of *E-T* model of PTF10119

parameter C_{gs}	value	parameter C_{dg}	value	parameter C_{ds}	value	parameter τ	value
c0	22.54	b0	0.713	a0	41.63	d0	2.31
c1	-12.98	b1	1.12E+4	a1	31.57	d1	2.01
c2	-4.71	b2	0.331	a2	-2.731	d2	0.163
c3	21.85	b3	-6.895	a3	1.368	d3	6.5E+2
c4	-2.851	b4	9.609	a4	15.61	d4	2.3
c5	1.785	b5	68.61	a5	-12.61		
c6	-7.41	b6	24.39	a6	-0.179		
c7	0.217	b7	-3.6E-3	a7	-3.718		
c8	7.1E-5			a8	-2.84E-3		
c9	5.4E-2						
c10	-2E-2						
c11	0.603						
c12	-7.5E-2						
c13	-5.032E-3						

The coefficients of functions describing the nonlinear elements (9), (14)÷(19) of the PTF10119 *E-T* equivalent circuit are included in Tab. 4.

The measured and simulated I-V characteristics and S-parameters of PTF10119 transistor are compared in Fig. 7.

To verify *E-T* model of *LDMOSFET*, the *W-CDMA* band amplifier operating in AB-class with the *PTF10119* transistor was designed for the maximum output power level of P_{out} = 12W. The layout of the amplifier and its power characteristics $P_{out} = f(P_{in})$ are shown in Fig. 8.

To emphasize short-term thermal effects, the *HPA* were measured for pulsed mode. The phase transmittance changes during RF-pulse $\Delta arg(S_{21})$ are a good marker for the estimation of the channel transient temperature [4]. This measurement was performed in homodyne test fixture, as shown in Fig. 9 [18].

The comparison of simulated and measured $\Delta arg(S_{21})$ during RF pulse for high output power level of P_{out} = 12W is presented in Fig. 10c. The test conditions are

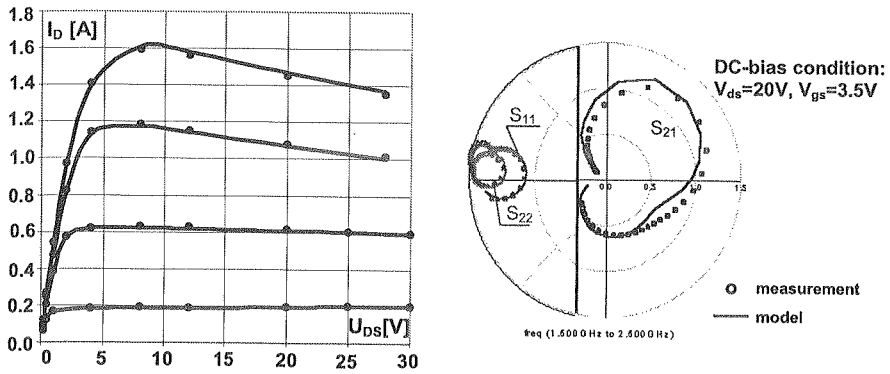

Fig. 7. Measured and modeled DC-characteristics and S-parameters of *PTF10119*

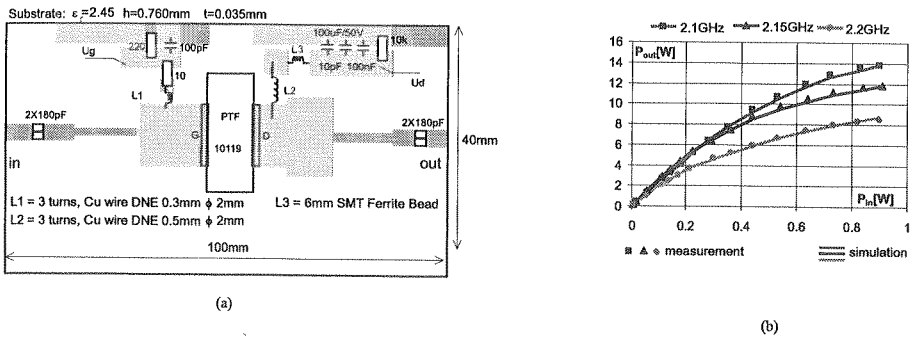

(a) (b)

Fig. 8. The $P_{out} = f(P_{in})$ characteristic (b) of the AB-class *HPA* with PTF10119 (a)

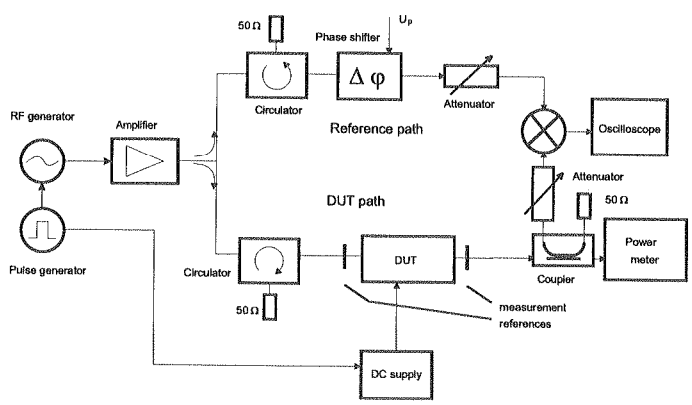

Fig. 9. The test fixture for $\Delta arg(S_{21})$ measurements during RF pulse

shown in Fig. 10a. The simulations of temperature changes in the active area of the transistor by means of *3D-FDTD* thermal method are illustrated in Fig. 10b.

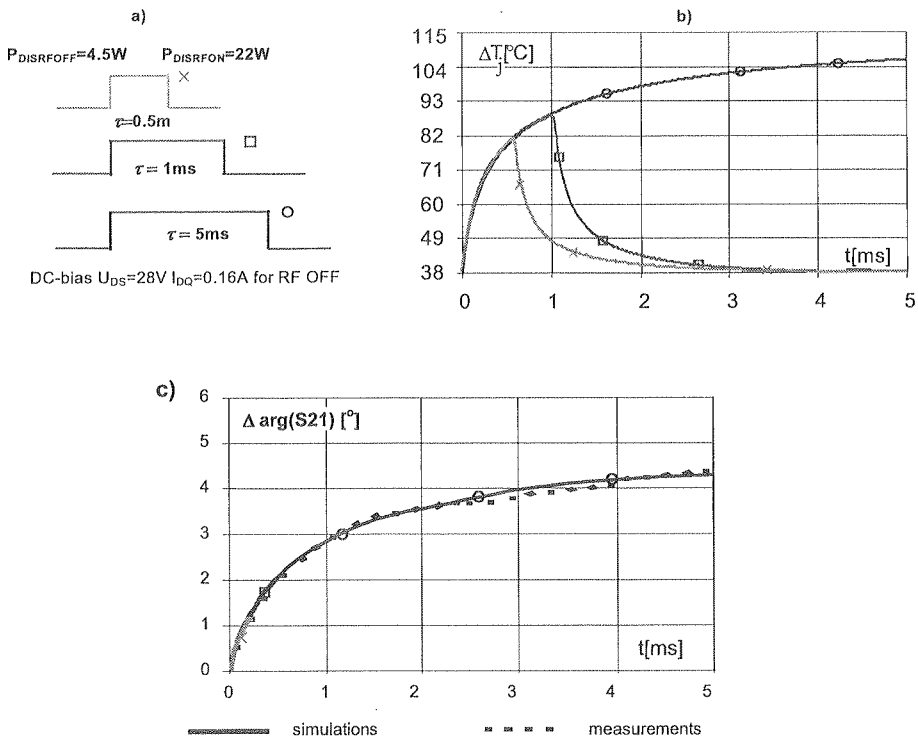

Fig. 10. The simulations and measurements $\Delta arg(S_{21})$ during RF pulse of *HPA* with *PTF10119* for P_{out} = 12W (c), the test conditions (a), the simulated temperature changes in transistor channel (b)

The simulated and measured characteristics of $\Delta arg(S_{21})$ during RF pulse for different output power level of P_{out} = 12W, 6W and 3W are presented in Fig. 11c. The test conditions and the temperature distribution are shown in Fig. 11a and Fig. 11b, respectively.

The *E-T* model was also used to design a very high pulsed power amplifier for IFF (*Identity Friend or Foe*) system [20]. The photography of the *HPA* with avionic LDMOSFET BLA1011-200 (PHILIPS) and its power characteristics are shown in Fig. 12.

The matching sections of the *HPA* were optimized for minimum $\Delta arg(S_{21})$ during RF pulse using *E-T* model. The phase transmittance deviation during avionic radar long pulse (*Duration* – τ = 50μs, $t_r = t_f$ = 50ns, *Duty cycle* δ = 1%) for different operating class of *BLA1011-200* transistor in *HPA* homodyne test fixture (Fig. 9), are included in Tab. 5.

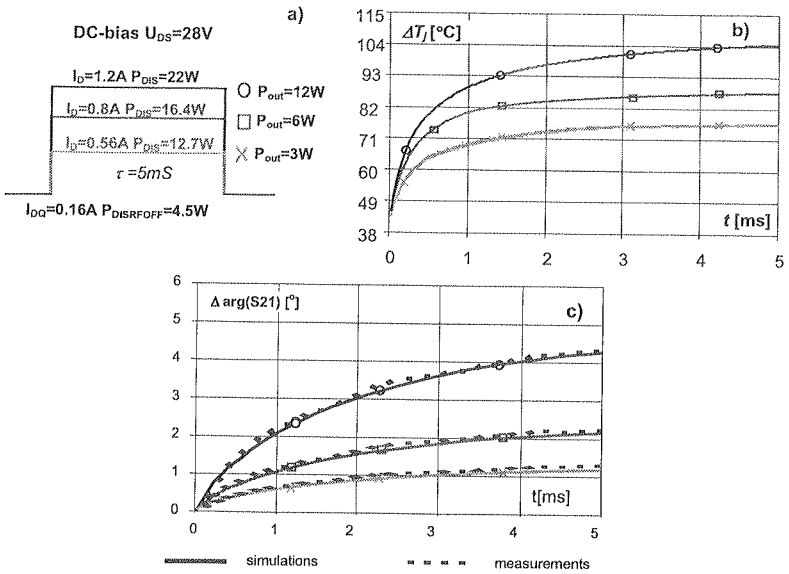

Fig. 11. The measurements and calculations of $\Delta arg(S_{21})$ of *HPA* with PTF10119 for output power levels — P_{out} = 12W, P_{out} = 6W, P_{out} = 3W (c), the test conditions (a), the simulated temperature changes (b)

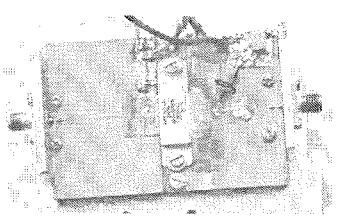

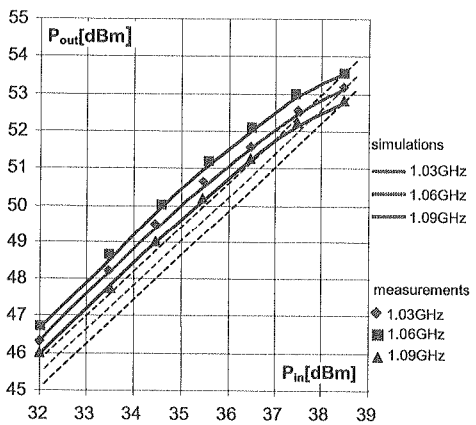

Fig. 12. The view of the 200W *HPA* with avionic *LDMOSFET BLA1011-200* and its $P_{out} = f(P_{in})$ characteristics for $I_{DQ} = 150mA$, $V_{DS} = 36V$ (RF OFF)

The results from Tab. 5 confirm capabilities of the proposed *E-T* model for the designing of the pulsed *HPAs* working with phase modulations.

Table 5

The $\Delta arg(S_{21})$ of *HPA* with BLA1011-200 for different operating class

$f[GHZ]$	1.03	1.06	1.09	Class
$\Delta arg(S_{21})[^o]$	0.18	0.14	0.16	A (keyed)
$\Delta arg(S_{21})[^o]$	0.48	0.47	0.48	AB
$\Delta arg(S_{21})[^o]$	0.61	0.82	0.72	B

3.3. *GaAS MESFET* MODEL VERIFICATION

To verify the *E-T* model of *GaAs MESFET*, the *HPA* with *FLM5359-4F* for C-band T/R module for *APAR* was worked out. Due to linearity, the *E-T* model was simplified, because the transistor works in keyed A-class. It is biased only during the RF-pulses. However, it is clear that the bias duration of the transistors is a little longer than RF-pulse width. The small-signal *E-T* model of *FLM5359-4F* transistor for room temperature is shown in Fig. 13.

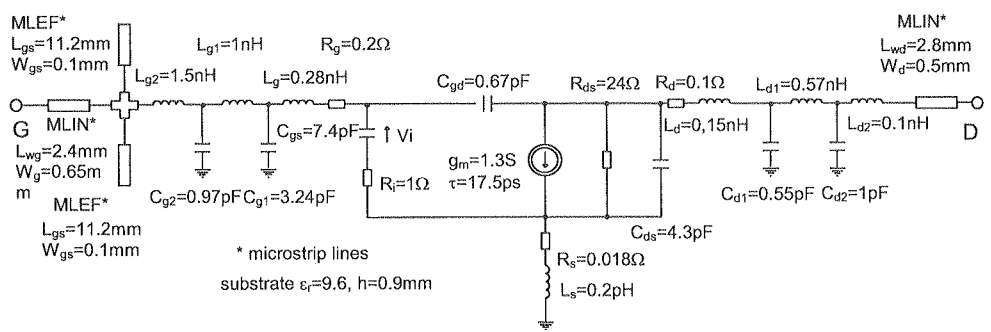

Fig. 13. The small-signal *E-T* model of *FLM5359-4F MESFET*

The external matching sections of the amplifier were optimized for minimum phase transmittance changes during the radar pulse. The view of the amplifier and its power characteristics are shown in Fig. 14.

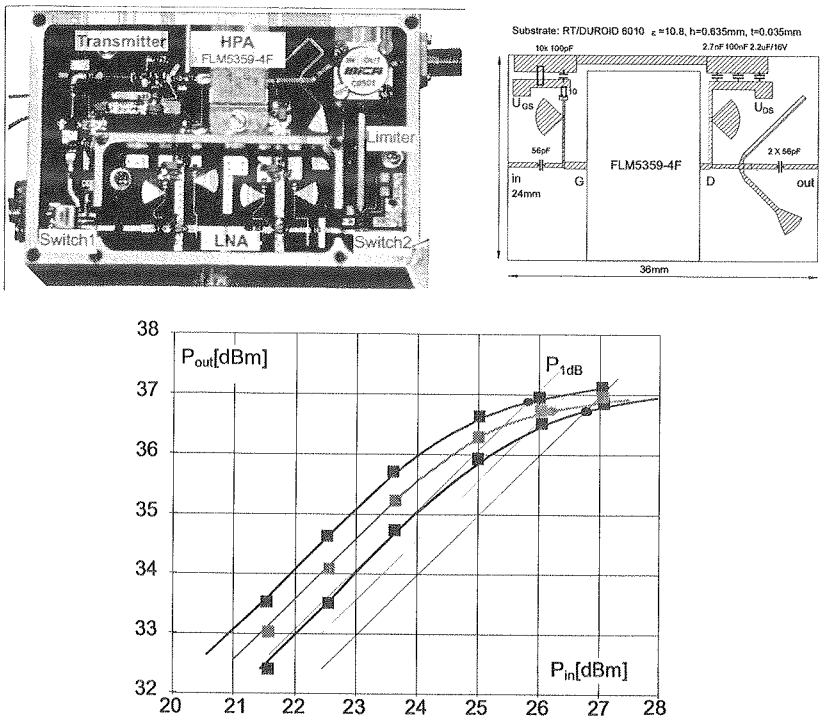

Fig. 14. The view of *T/R* module for APAR, the *HPA* topology, and its measured and simulated $P_{out} = f(P_{in})$ characteristics

The $\Delta arg(S_{21})$ of *HPA* with *FLM5359-4F* were measured by means of the test system shown in Fig. 9. The results of the measurements and simulations of the amplifier are compared in Fig. 15. The description of *THS* for $FLM5359-4F$ MESFET includes Tab. 6.

Table 6

The parameters of the *THS* for *FLM5359-4F* MESFET (Fig. 2)

	dimensions [mm]			thermal parameters	
	x	y	z	$\alpha_i[m^2/s]$	$\lambda_i[W/mK]$
chip (GaAs)	0.4	2.5	0.07	0.44e-4	40
flange (copper)	13	21	1.5	1.02e-4	350
radiator (copper)	30	30	4.5	0.88e-4	300

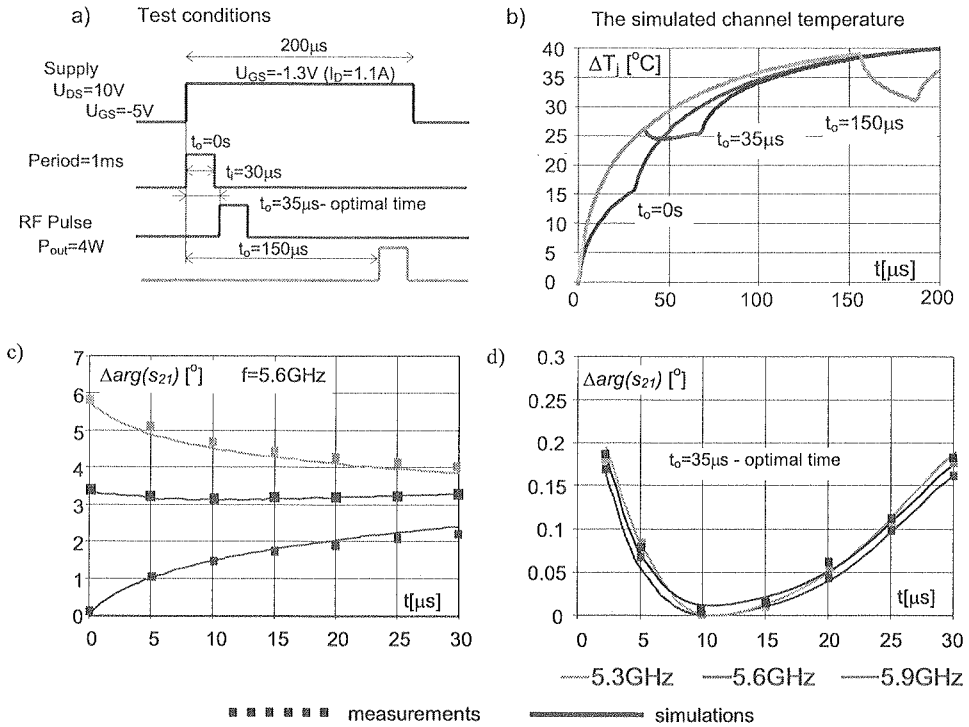

Fig. 15. The phase transmittance changes (c) and (d) during RF pulse (a), and the simulated channel temperature (b)

For a time delay $t_o = 30\mu s$, the minimum phase deviation during RF-pulse has been achieved. This fact confirms the influence of channel temperature changes on transmittance stability.

Due to a very long thermal time constant, the phase transmittance changes during RF pulse conditions are neglected for *Si-LDMOSFETs* (τ_{th} ~ msec) compared to *GaAs MESFETs*. It follows from the better thermal conductivity for Si than *GaAs* for the similar chip thickness. This feature is particularly demanded for *APAR* applications.

To verify the drain current equation, the IV-characteristics of the push-pull high power *GaAs FET-E* (*Enhancement mode*) made by FUJITSU (FLL810IQ-3C) has been modeled. The comparison of the measured and simulated IV-characteristics is shown in Fig. 16.

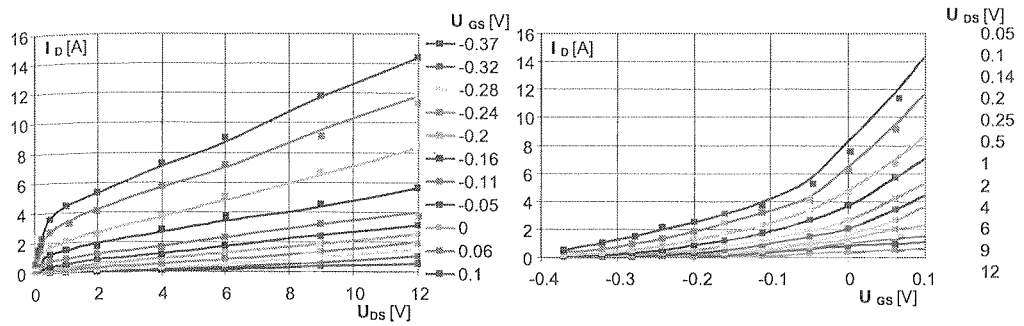

Fig. 16. The measured and simulated IV-characteristics of FLL810IQ-3C FET

4. CONCLUSION

The temperature-dependent model for a high power *FET* has been proposed. This electrical part of *E-T* model is based on the nonlinear drain current equation and small-signal approach for the determination of *C-V* characteristics vs. DC-bias and temperature. The novelty of the electrical part of the *E-T* model is the modification of the current equation in order to better fit I-V characteristics in a small V_{gs} range. In addition, the Yang's equation was generalised for describing the drain current source of the GaAs MESFET *E-T* model. The self-heating effect for *FETs* is modeled using the solution of *HCE* by means of explicit *3D-FDTD* thermal method. The thermal problem is solved in three areas: chip, flange and radiator, for an arbitrary pulsed thermal excitation. It has been demonstrated that the use of the thermal analysis cooperatives with an electrical model formulas implemented in Agilent's program (*ADS*) can be a very useful, efficient and simple solution in way to design high power amplifiers. The *E-T FET* model was successfully verified and used to design the high power amplifier with LDMOSFETs and *MESFETs*.

5. REFERENCES

1. J. L. B. Walker: *High Power GaAs FET Amplifiers*. Artech House, Inc. 1993.
2. K. Inoue, K. Ebhara, H. Haematsu, T. Igarashi, H. Takahashi, J. Fukaya: *A 240W Push-Pull GaAs Power FET for W-CDMA Base Station*. IEEE MTT-S Digest, pp. 1719-1722, 2000.
3. W. Wojtasiak, D. Gryglewski, T. Morawski, E. Sędek: *Designing T/R module for active phased array radar*. XIV International Conference on Microwaves Radar and Wireless Communications, MIKON'2002, Gdańsk, maj 20-22 2002, pp. 631-634, vol. 2.
4. W. Wojtasiak, D. Gryglewski: *Temperature- dependent modeling of high power MESFET using thermal FDTD method*. IEEE MTT-S Digest, International Microwave Symposium Digest, Phoenix, Arizona, May 20-25, 2001, vol. 1 pp. 411-414.
5. Y. Yang, J. Yi, B. Kim: *Accurate RF large- signal model of LDMOSFET's including self-heating effect*, IEEE Trans. MTT, vol. 49, pp. 387-390, Feb. 2001.

6. Ce-Jun Wei, Y. Tkachenko, D. Bartle: *An Accurate Large-Signal Model of GaAs MESFET Which Accounts for Charge Conservation, Dispersion, and Self-Heating.* IEEE Trans. MTT, vol. 46, pp. 1638-1644, Nov. 1998.
7. W. R. Curtis, J. A Pla, D. Bridges, T. Liang, E. E Shumate: *A new dynamic electro-thermal nonlinear model for silicon RF LDMOS FETs*, IEEE MTT-S Digest 1995.
8. P. Antognetti, G. Massobrio: *Semiconductor device modeling with SPICE, Mc GrawHill.*
9. W. Janke: *Zjawiska termiczne w elementach i układach półprzewodnikowych.* WNT 1992.
10. S. M. Lardizabal, A. S. Fernandez, P. Dunleavy: *Temperature-Dependent Modeling of Gallium Arsenide MESFET's*, IEEE Trans. on MTT vol. 44, no. 3, pp. 357-363, March 1996.
11. R. W. Lewis, F. Morgan, B. A. Schrefler: *Numerical Methods in Heat Transfer.* John Wiley & Sons, New York 1998.
12. R. Domański, M. Jaworski, M. Rebow: *Thermodynamics, Heat-Flow.* LUXUS Warsaw 1995.
13. R. Michnowski, W. Wojtasiak: *The Electro-Thermal Model of High Power LDMOS Transistor.* 11th GaAs Symposium EUMC, Munich 2003, pp. 243-246.
14. Agilent Tech.: Advanced Design System Manual 2004.
15. J. M. Golio: *Microwave MESFETs and HEMTs.* Artech House 1991.
16. D. Lovelace, J. Costa, N. Camilleri: *Extracting Small- Signal Model Parameters of Silicon MOSFET Transistors.* IEEE MTT-S Digest 1994, pp. 865-868.
17. Department of Electrical Engineering and Computer Science, BSIMV3 Manual, University of California, Berkley, 1995.
18. D. Gryglewski: *PhD Thesis, Minimization transmittance changes of A-class microwave pulsed power amplifier.* Warsaw University of Technology 2001.

W. WOJTASIAK

ELEKTRYCZNO-TERMICZNE MODELOWANIE MIKROFALOWYCH TRANZYSTORÓW POLOWYCH DUŻEJ MOCY I JEGO ZASTOSOWANIA

Streszczenie

W artykule przedstawiono elektryczno-termiczny (E-T) model mikrofalowych tranzystorów polowych dużej mocy, który bazuje na nieliniowym równaniu prądu drenu w połączeniu z małosygnałowym procesem ekstrakcji. Temperaturowe zależności parametrów E-T modelu opisujące zarówno długo- jak i krótkoterminowe efekty termiczne wyprowadzono na podstawie rozwiązania równania przewodnictwa ciepła w obszarze chipu i podstawki tranzystora oraz radiatora za pomocą 3-wymiarowej metody różnic skończonych FDTD dla zagadnień termicznych wspartej danymi eksperymentalnymi. Zaproponowany model pozwala na projektowanie mikrofalowych wzmacniaczy dużej mocy z tranzystorami polowymi w rożnych klasach i rodzajach pracy, w przedziale temperatur od -35°C do +60°C i w szerokim zakresie częstotliwości. W celu weryfikacji E-T modelu zaprezentowano wyniki badań praktycznie zrealizowanych wzmacniaczy z wykorzystaniem tranzystorów typu LDMOSFET i MESFET na pasma L, S i C o mocy wyjściowej sięgającej 200W

Słowa kluczowe: elektryczno-termiczny model tranzystora FET, metoda różnic skończonych FDTD, LDMOSFET, MESFET, równanie przewodnictwa ciepła

KWARTALNIK ELEKTRONIKI I TELEKOMUNIKACJI, 2005, 51, ZESZYT SPECJALNY, ss. 105--113

Microwave 5-bit phase shifter

DANIEL GRYGLEWSKI[1], TADEUSZ MORAWSKI[1], EDWARD SĘDEK[2], JOLANTA ZBOROWSKA[2]

[1]*Warsaw University of Technology*
Institute of Radioelectronics,
ul. Nowowiejska 15/19, 00-665 Warsaw, Poland
[2]*Telecomunications Research Institute,*
ul. Poligonowa 30, 04-051 Warsaw, Poland

Paper presents description of a method for designing multistate phase shifters comprising varactor diodes and quadrature couplers. It has been shown that it is possible to construct 32-state phase shifter with the 360° range of phase change (11.25° multiplied by 32) in a frequency band 15% wide as a series combination of two couplers connected with varactor diodes. Appropriate digital steering system is also presented, as well as results of measurements of the shifter.

Keywords: microwave, microwave devices, multistate phase shifters

1. INTRODUCTION

Multistate phase shifters and modulators are often applied in radio-communication, radiolocation and measuring systems as well as in phased arrays. Sweeping of the microwave signals phase is obtained either by means of heterodyne actions — by up-converting signal from operating bandwidth at MHz to operating bandwidth at GHz [1], or directly — by switching semiconducting elements or changing the parameters of the media (usually ferrite) in witch microwave signal propagates [2].

Switched phase shifters operating on a base of switching the number of diodes are typically transmission (comprising Shiffman phase shifters [3]) or reflecting (comprising directional couplers 3dB/90°) circuits comprising PIN diodes. Phase shifters with PIN diodes can be fed with signals carrying significant power. Modulator providing 2^N states of phase consist of the cascade of N binary units [4] switched in various combinations. Each of aforementioned units causes phase errors and losses which are then cumulating.

In some applications, for instance steering a receiving antenna or an antenna with T/R modules, low signals modulators or measuring systems, where power carried by

signal is not at high level (approximately up to level of 10mW), phase shifter may be simplified by introducing a number of varactor diodes instead of greater number of PIN diodes. This paper proves that combination of two units, each comprising coupler and two diodes, is sufficient for obtaining phase shifter providing 32 states (in classical solution with PIN diodes five such units would be required). However reduction of the number of semiconductor elements may be obtained at expense of more complex bias circuit, since PIN diodes operates only with two bias voltage values ("on" and "off") and for varactor diodes each state corresponds with different value of bias voltage.

2. THE DESIGN OF 5-BIT PHASE SHIFTER WITH VARACTOR DIODES

A diagram of considered phase shifter is shown in fig. 1.

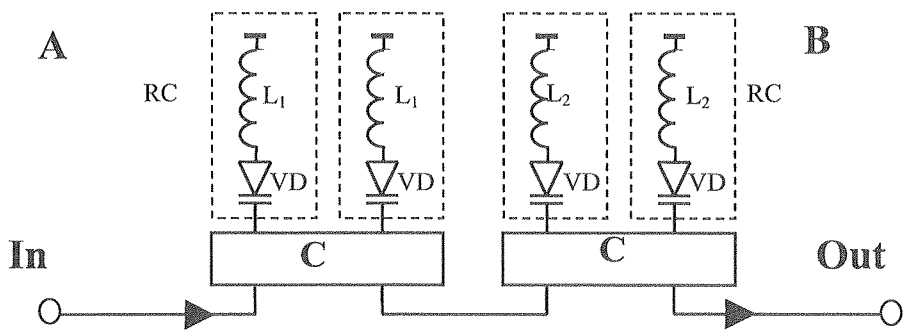

Fig. 1. 32-state phase shifter comprising varactor diodes VD, 3dB/90° couplers C, series inductances L_1, L_2 which in combination with the diodes form reflecting circuits RC. A, B — switched units

Cascade connection of switched units A and B (each of them may be considered as a single phase shifter) provides phase changes up to 360 degrees. Directional couplers are initially assumed to be ideal ones. In such case there is no reflection from input port and changes of S_{11} of reflecting circuits causes same changes of the transmittance S_{21} of whole phase shifter. Analysis of phase shifter may be then reduced to the analysis of the reflecting circuits. The most widespread type is simple circuits shown in fig. 2. Process of designing broadband analog phase shifters according to diagrams shown in fig. 1 and fig. 2 is described in detail in [5]. Results and equation presented there are applicable in analysis of multistate phase shifters and for that reason are further quoted. If, during the switching, capacitance of varactor diode varies between maximal value C_1 and minimal value C_2, then it can be characterized by capacitance change coefficient:

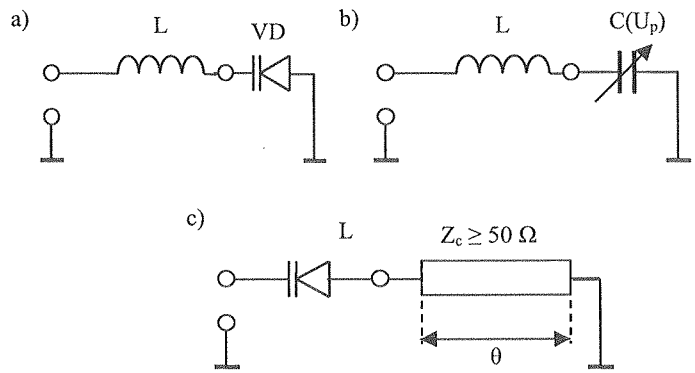

Fig. 2. Reflecting circuits a) schematic diagram b) equivalent circuit comprising lumped inductance L c) equivalent circuit comprising high impedance line segment, described by characteristic impedance Z_c and electrical length θ

$$k = \sqrt{\frac{C_1}{C_2}} \tag{1}$$

Introduction of two additional dimensionless parameters:

— normalized average circuit impedance:

$$z = \frac{1}{Z_c}\sqrt{\frac{C_1}{C_2}} \tag{2}$$

— reduced varactor diode susceptance:

$$b = \omega\sqrt{C_1 C_2}\cdot Z_c \tag{3}$$

where Z_c is reference impedance

allows to write formula, defining the range of phase change:

$$\Delta\varphi = 2arctg\left(\frac{k - \frac{1}{k}}{b^3\cdot z^4 + b\cdot\left[1 - z^2\cdot\left(k + \frac{1}{k}\right)\right] + \frac{1}{b}}\right) \tag{4}$$

It is possible to show that the maximum of the characteristic $\Delta\varphi(b)$ appears for value:

$$b_0 = \sqrt{\frac{2}{1 - z^2\left(k + \frac{1}{k}\right) + \sqrt{12z^4 + \left[z^2\left(k + \frac{1}{k}\right) - 1\right]^2}}} \tag{5}$$

Formulas (4) and (5) are very contributory to the designing process, since they provide criteria for choosing proper varactor diode by determining values C_1, C_2 such that maximum of phase characteristic $\Delta\varphi(f)$ was located at the center of required frequency band. When capacitance change coefficient is relatively high (k>3), the range of phase change close to 180 degrees is obtainable even for very small values of inductance L. It appears that, at relatively low microwave frequencies, close to zero inductance in one unit and small lumped inductances connected in series with varactor diodes in the second are sufficient. In such case $\Delta\varphi_A = 180°$ and $\Delta\varphi_B > 180°$ and consequently whole range of phase change is obtained.

3. AN EXAMPLE OF DESIGN FOR L FREQUENCY BAND

A 32-state phase shifter for L band (1.2 — 1.6 GHz) has been designed by means of methods presented above. Formulas (1 — 5) led to chose of MA4H202-1088 (MACOM) diodes, characterized by: $C_1(U_p$=-1V) = 8.2pF, $C_2(U_p$=-20V) = 0.8pF, what gives capacitance change coefficient k = 3.2.
Directional coupler has been realized as a segment of concentric coupled line BJCB1 produced by SAGE LABORATORIES [7]. Analysis shows that for small series inductance (it was taken L_1=0.5nH – inductance of diodes mounted in series) $\Delta\varphi_A = 160°$. In order to achieve greater value of $\Delta\varphi_B$ enabling sweeping 360° range, greater series inductance L_2 = 4nH was chosen. Resulting maximal phase change of second unit was $\Delta\varphi_B = 210°$. In this circumstances the problem to be solved is how to control cumulative phase change $\Delta\varphi = \Delta\varphi_A + \Delta\varphi_B$ of whole phase shifter, in whole range (0 — 360°) in quite broad frequency band.
In some application, for instance electronically steered antennas or multistate phase modulators of radio link transmitter signal, small level of phase errors is required. In order to achieve that, appropriate system of digital steering has been designed and constructed and sets of values of varactor diodes bias voltages have been selected. Different sets of voltage values are applied in frequency sub- bandwidth 1.2–1.4GHz and sub-bandwidth 1.4–1.6GHz

4. PHASE SHIFTER STEERING AND OBTAINED RESULTS

Criteria of selection of sets of bias voltages for both phase shifter sections and both sub-bandwidths was to obtain maximally flat phase characteristics for every phase state $\Delta\varphi_i$. Phase characteristics for each sub-bandwidth were being observed separately. Measurements have been made by means of vector analyzer ZVRE made by RHODE SHWARTZ. Device of concern is shown in fig. 3.
After preliminary measurements and simulations it became apparent that matching requirements is impossible if diodes in both sections (A and B) are polarized by equal voltages. Further experiments showed that an advantageous reference bias voltage

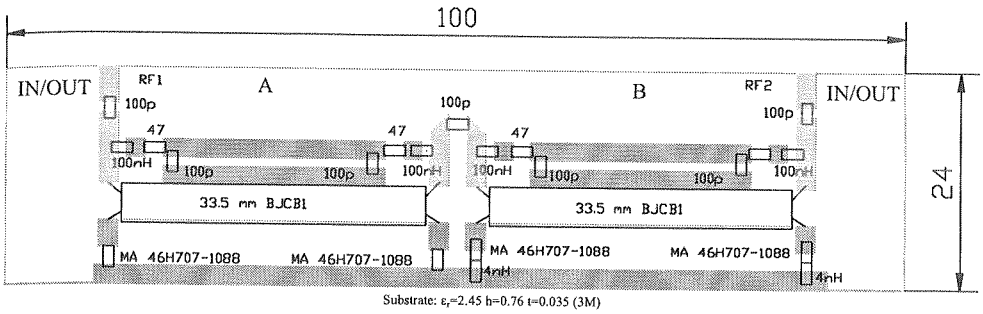

Fig. 3. Mounting schematics of microwave part of phase shifter

value for section A is – 1V and for section B higher value ie. – 3.5V and – 5V for sub-bandwidths 1.2 – 1.4 GHz and 1.4 – 1.6GHz, respectively.

Fig. 4 shows block diagram of digital steering system for phase shifter. Values of bias voltages sections of the phase shifter were digitalized and are stored in memory consisting of three FLASH-EPROM's 28C64 (read access time equal to 150ns) made by ATMEL. There were also used three digital-to-analog converters TVL 5619 (made by TEXAS INSTRUMENTS, with setting time equal to $1\mu s$ and output devices AD797 (ANALOG DEV.) working as buffers/amplifiers. Such set of components enables obtaining the time of switching less than $2\mu s$. Static tests were the first to be performed

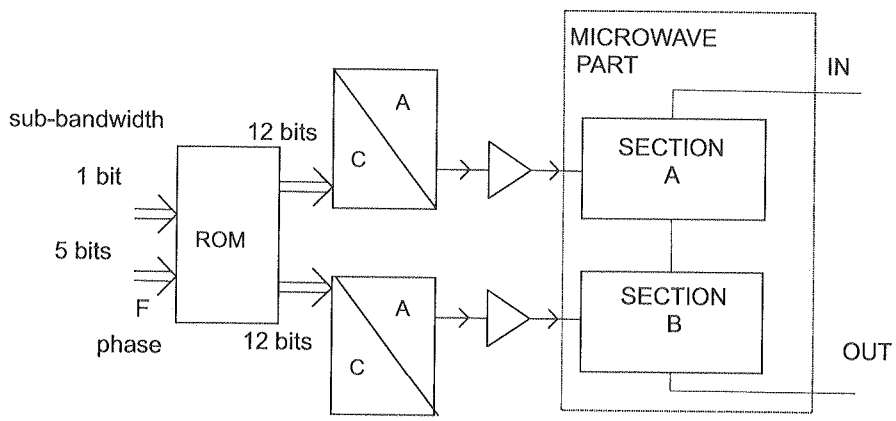

Fig. 4. Block diagram of the phase shifter steering system

during the examination of the device. Results are presented in fig Fig.5-8. These tests showed that for both sub-bands $|S_{11}| < -10$dB, which means that standing wave ratio is less than 1.9.

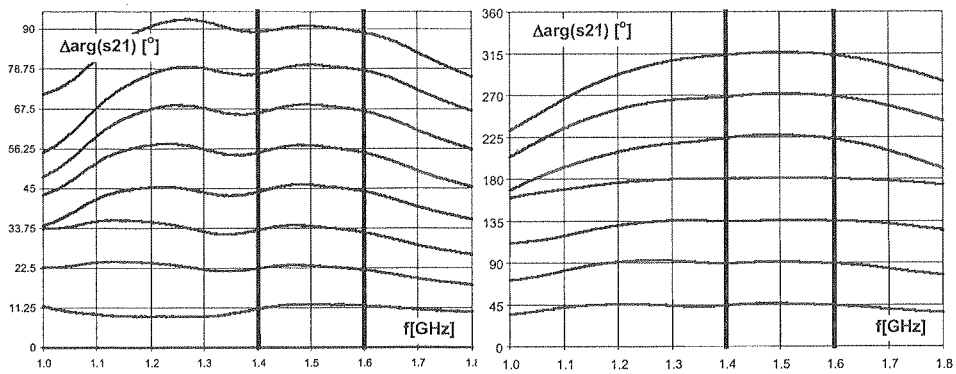

Fig. 5. Phase characteristics for selected states of constructed device, in sub-bandwidth 1.4–1.6 GHz

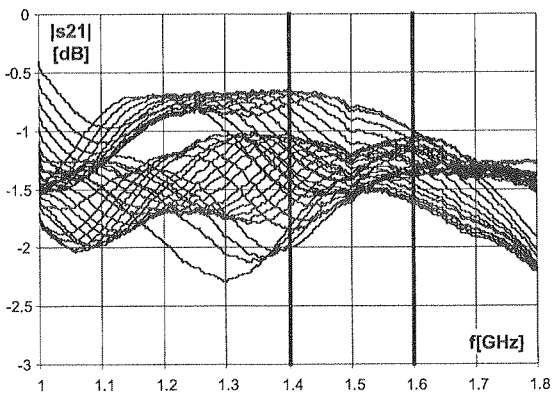

Fig. 6. Amplitude characteristics of transmittance of constructed device, for all phase states, in sub-bandwidth 1.4–1.6 GHz;

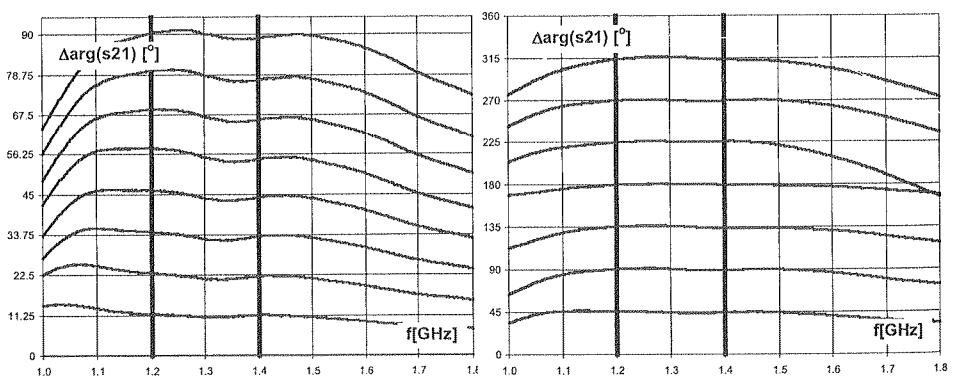

Fig. 7. Phase in sub-bandwidth 1.2–1.4 GHz characteristics for selected states of of constructed device,

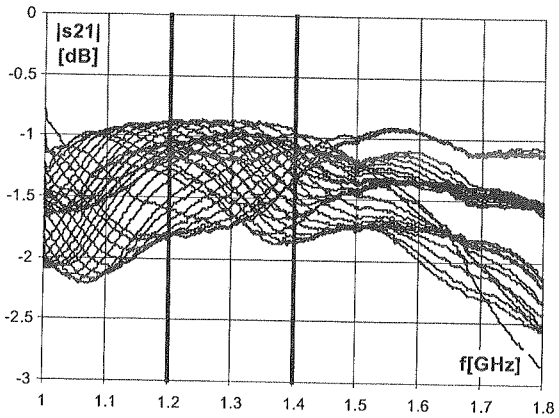

Fig. 8. Amplitude characteristics of transmittance of constructed device, for all phase states, in sub-bandwidth 1.2–1.4 GHz;

Static tests were followed by measurements of the switching times and the lengths of transient periods. For this task a homodyne system was set up. It comprises a mixer, which under certain conditions may be considered as phase detector [4].

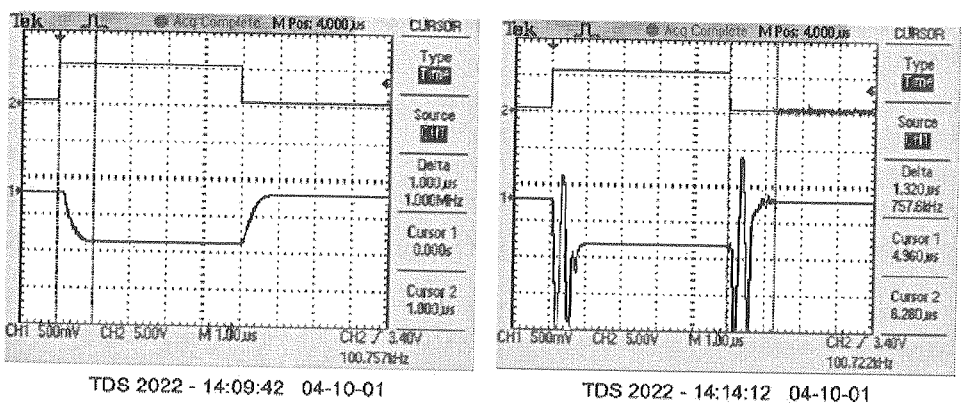

Fig. 9. Dynamic characteristics of the phase shifter during the changes of states fazy przesuwnika przy zamianach stanów 0-11.25° (the two differing most)

Fig. 9 and fig. 10 show exemplary oscillograms of the mixer output voltage showing the dynamical change of phase shifter state. In all following drawings upper oscillogram lower oscillogram represent respectively driving voltage and output signal of a mixer, which is proportional to the phase change.

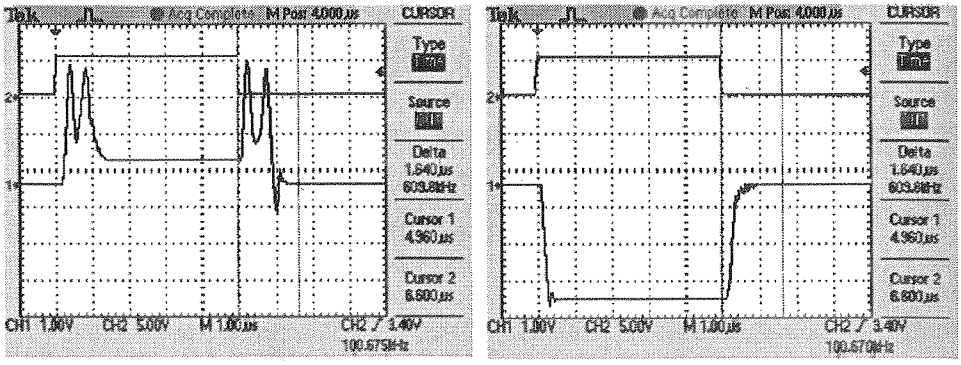

Fig. 10. Dynamic characteristics of the phase shifter during the changes of states (a) 202.5° i 213.75°, (b) 0° i 78.75°

5. CONCLUSIONS

A method for designing varactor diode phase shifter has been presented. An example of 32-state phase shifter proves that it is possible to replace five binary PIN diode units with two units comprising varactor diodes steered by additional bias digital system.

Device which has been designed and constructed has satisfactory static parameters: — phase error in 15% frequency band does not exceed 2°, total loss is less than 2dB, input reflectance is less than 0.3. Possible applications of that phase shifter are limited, however, by the level of signal power. Nevertheless, examination proved that it works properly with signal levels up to 50mW.

Measurements of the dynamic characteristic of the shifter showed that switching time is not grater than than $2\mu s$. Moreover, it can be further minimized by application of faster components.

There were also performed preliminary temperature tests of the device. Results showed that phase deviation in temperature ranging from -30 to 50 Celsius degrees is less than one degree.

Parameters of the device which were listed above are good enough as for application in phased arrays or automatic measurement systems.

6. REFERENCES

1. Back to Basics Seminar, p.4, Source Basics – Hewlett Packard, 1998.
2. S. K. Koul, B. Bhat: *Microwave and milimeter wave phase shifters*, ArtechHouse, Boston-London 1991.
3. T. Morawski, J. Zborowska, C. Mroczkowski, J. Skupiński: *Wielostanowe mikrofalowe modula-tory fazy*. Przegląd Telekomunikacyjny, nr 6, 1983, ss. 193-196.

4. W. Wojtasiak (kier.): Grant KBN, *Minimalizacja wpływu temperatury na parametry użytkowe mikrofalowych wzmacniaczy tranzystorowych dużych mocy*, 2000-2001, nr 8 T11B 055 16.
5. T. Morawski, J. Zborowska: *Szerokopasmowe mikrofalowe przesuwników fazy z diodami waraktorowymi*, Krajowa Konf. Elektroniki, Kolobrzeg 2002, tom 1, ss. 337-342.
6. T. Morawski, J. Zborowska: *Broad-Band Microwave Phase Shifters and Their Applications*, Intern. Conference MIOP 87, Wiesbaden 1987, vol. 1, pp. 4B-4.

D. GRYGLEWSKI, T. MORAWSKI, E. SĘDEK, J. ZBOROWSKA

MIKROFALOWY 5-BITOWY PRZESUWNIK FAZY

Streszczenie

W artykule przedstawiono metodę projektowania wielostanowych przesuwników fazy z diodami waraktorowymi. Przedstawiono uniwersalne wzory analityczne pomocne przy doborze typu diody waraktorowej do wymaganych parametrów elektrycznych (pasmo pracy, przesunięcie fazy) oraz przy wstępnym projektowaniu układów odbijających, zawierających waraktory i dołączone do nich indukcyjności skupione lub w postaci krótkich odcinków linii wysokoomowej zawartej na końcu. Zaprojektowano i przeprowadzono komputerową analizę przesuwnika o zakresie zmian fazy 360° na pasmo L (1.2 – 1.6 GHz). Pokazano, że przy odpowiednim doborze napięć polaryzujących diody można osiągnąć 32 stany pracy przesuwnika. Dla uzyskania małych błędów fazy całe pasmo podzielono na dwa podpasma: 1.2 – 1.4 GHz i 1.4 – 1.6 GHz. W obu podpasmach działa ten sam układ mikrofalowy przesuwnika fazy, ale zestawy napięć sterujących są dobrane oddzielnie. Uzyskano bardzo prosty i tani układ przesuwnika fazy — składa się on z dwóch łańcuchowo połączonych stopni. Każdy z tych stopni zawiera jeden sprzęgacz 3dB/90° i diw diody waraktorowe.

Skonstruowano układy cyfrowego sterowania przesuwnika. Cały układ przetestowano, uzyskując bardzo dobre wyniki badań statycznych (błąd fazy 2° dla każdego stanu przy mocach nie przekraczających 50 mW, straty całego przesuwnika nie przekraczające 2dB) i dynamicznych czas przełączania poniżej 2 μs) w akresie temperatur od -30° do 50°C.

Opisany układ przesuwnika jest znacznie tańszy od klasycznych rozwiązań z diodami PIN (cztery waraktory zamiast dziesięciu diod PIN) i może znaleźć zastosowanie w antenach sterowanych elektronicznie — nadawczych (z zastrzeżeniem małego poziomu mocy) lub odbiorczych.

Słowa kluczowe: mikrofale, urządzenia mikrofalowe, wielostanowe przesuwniki fazy

A f

GRZE

Th
or
ana
cor
me
esp

Key

Opti
especiall
with bio
physiolog
these wa
haemoglo
The
more pre
posed inv
the most
Two
of light i
asuremen

KWARTALNIK ELEKTRONIKI I TELEKOMUNIKACJI, 2005, 51, ZESZYT SPECJALNY, ss. 115–125

A fast nodal method for simulation of light propagation in turbid media

GRZEGORZ DOMAŃSKI, BOGUMIŁ KONARZEWSKI, ZDZISŁAW PAWŁOWSKI, KRZYSZTOF ZAREMBA, JANUSZ MARZEC, ROBERT KURJATA, ARTUR TRYBUŁA

Institute of Radioelectronics,
Warsaw University of Technology
ul. Nowowiejska 15/19
00-665 Warsaw, Poland

A fast nodal method for simulation of light propagation in turbid media was proposed. The method enables simulations of light propagation in heterogeneous media with internal or external light reflections. The comparison of simulation results of the nodal method and analytical formulas for uniform cube was made. A fixed geometry optical tomograph was constructed. Series of measurements of the cylindrical phantoms were made. The nodal method enables fast reconstruction of optical parameter distribution in examined objects, especially for non-linear method of reconstruction.

Keywords: optical tomography, light propagation, nodal method

1. INTRODUCTION

Optical tomography is a promising method for medical and biological imaging, especially for functional imaging [1]. Visible light and near-infrared (NIR) light interact with biological tissue predominantly by absorption and scattering. There are many physiologically interesting molecules, which have characteristic absorption spectra at these wavelengths. In particular, the spectra of oxy-haemoglobin (HbO) and deoxy-haemoglobin (HHb) differ significantly.

The main stream of progress in optical tomography field has focused on developing more precise and efficient models of light transport in tissue, and on solving the ill-posed inverse problem. The using of prior morphological (anatomical) information is the most promising improvement in the reconstruction techniques.

Two processes are required to reconstruct an optical image. First, the transport of light in tissue must be modelled. This stage, the *forward problem*, allows the measurements to be simulated from the model, and generates (explicitly or implicitly) a

sensitivity matrix, which relates the measurements to the internal optical properties. Second, the image is reconstructed by inverting the Jacobian and solving the *inverse problem*. In conventional x-ray CT, scatter of the x-rays is marginal, so the forward problem reduces to a series of integrals along straight lines (a Radon transform). The inverse problem is linear and well posed. In optical imaging, however, scattering is the main process, so that the forward problem becomes a series of integrals over the entire volume. Each measurement depends on the whole volume, so that the inverse problem is ill-posed and under determined.

A full description of steady light propagation in tissue is defined by the radiative transport equation (RTE, equation (1)). This is a conservation equation which states that the radiance (the number of photons per unit volume), $L(\vec{r},\vec{\Omega})$ for photons travelling from point $\vec{r}$ in direction $\vec{\Omega}$ is equal to the sum of all the mechanisms which increase L minus those effects which reduce it.

$$\vec{\Omega}\cdot\nabla L(\vec{r},\vec{\Omega})+(\mu_a(\vec{r})+\mu_s(\vec{r}))\,L(\vec{r},\vec{\Omega})=S(\vec{r},\vec{\Omega})+\mu_s(\vec{r})\cdot\int_{4\pi}L(\vec{r},\vec{\Omega}')p(\vec{\Omega}\cdot\vec{\Omega}')d\vec{\Omega}' \quad (1)$$

The equation above includes the source term S and phase distribution of the scattering $p(\vec{\Omega}\cdot\vec{\Omega}')$. The optical properties of medium are described by:

- absorption coefficient $\mu_a[mm^{-1}]$,
- scattering coefficient $\mu_s[mm^{-1}]$,
- scattering anisotropy coefficient g, (the mean cosine of the scattering angle).

Unfortunately, the solving of RTE for all points in a large 3D volume, as is required in optical tomography, is computationally expensive and simpler models are required. The most important and widely used simpler model of light propagation is a diffusion equation

$$-\nabla\cdot(D(\vec{r})\cdot\nabla\Phi(\vec{r}))+\mu_a(\vec{r})\Phi(\vec{r})=S(\vec{r}) \quad (2)$$

where:
$\Phi[\mathrm{Wm}^{-2}]$ is the photon fluence rate defined by

$$\Phi(\vec{r})=\int_{4\pi}L(\vec{r},\vec{\Omega})d\vec{\Omega}, \quad (3)$$

D is the diffusion constant defined as

$$D=\frac{1}{3\,(\mu_a+\mu_s(1-g))}. \quad (4)$$

The diffusion equation is valid in the case of bulk tissue; but it is not true near the source, near the surface, near internal boundaries, in anisotropic tissues, and in regions of either high absorption or low scatter.

The reconstruction procedure in optical tomography requires fast and reliable simulation methods of light propagation in turbid media. There are three main methods of solution of light transport equation:

- Monte Carlo method — it gives the most precise results, especially in problems with sources of big anisotropy, at media borders, for non-uniform media and media with complex geometry [2].
- Discrete ordinate method — the light flux is determined only at nodes of numerical grid and for finite set of angles [3]. The nodal method is a special version of this method.
- diffusion approximation method — the light transport equation is approximated by diffusive equation and this equation is solved by analytical or numerical methods, for example: finite differences or finite element method [4].

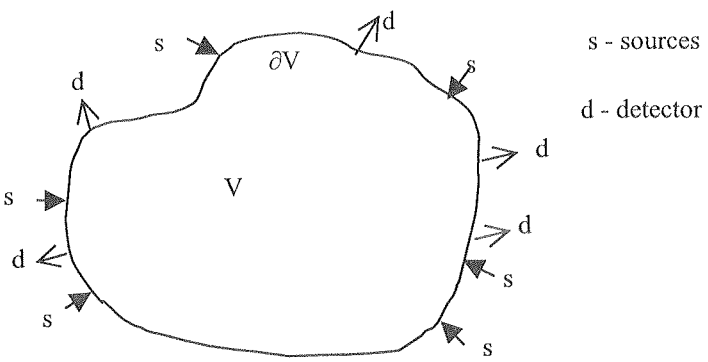

Fig. 1. The geometry of the forward problem in optical tomography

The forward problem (Fig. 1) involves calculating simulated data, given a forward operator F and knowledge of the sources q and distribution of optical properties x (absorption and scattering coefficient). The forward problem may therefore be formulated as

$$y = F(x, q) \tag{5}$$

To reconstruct an image, it is necessary to solve the inverse problem, which is to calculate the internal optical properties x, given data y and sources q:

$$x = F^{-1}(y, q). \tag{6}$$

The fast, flexible nodal method was proposed, which may be used for solving transport equation and diffusion equation.

2. NODAL METHOD FOR SOLVING TRANSPORT EQUATION

At first the nodal method for solving two-dimensional problems will be presented. The considered two-dimensional object is decomposed into set of elements, each with

dimensions Δx [mm] Δy [mm]. The nodal method assumes that light is transmitted only in the selected directions, usually these directions are axes X, Y, Z of cartesian system (Fig. 2). The light flux going along axis OX, which enters element at lower x coordinates is designated as I^{in}_{x-}, the light flux, which enters at higher x coordinates is designated as I^{in}_{x+}. The light flux going along OX axis, which exits element is designated as I^{out}_{x-} i I^{out}_{x+}. The similar rules are valid for other axes. The two-dimensional element with dimensions Δx , Δy and light fluxes which enter this element (in) and exit this element (out) are presented in Fig. 2. Within each element optical parameters μ_a, μ_s, g are constant.

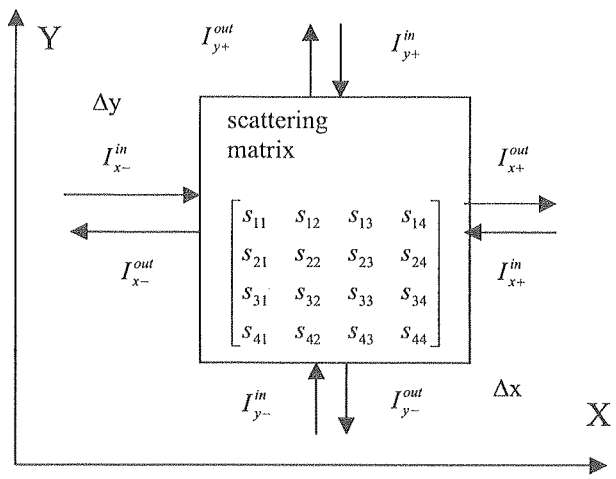

Fig. 2. Two-dimensional nodal method schematics — coordinates and angles discretisation

The light fluxes, which quit nodal element (output fluxes), are described by set of linear equations:

$$\begin{bmatrix} I^{out}_{x-} \\ I^{out}_{x+} \\ I^{out}_{y-} \\ I^{out}_{y+} \end{bmatrix} = \begin{bmatrix} s_{11} & s_{12} & s_{13} & s_{14} \\ s_{21} & s_{22} & s_{23} & s_{24} \\ s_{31} & s_{32} & s_{33} & s_{34} \\ s_{41} & s_{42} & s_{43} & s_{44} \end{bmatrix} \cdot \begin{bmatrix} I^{in}_{x-} \\ I^{in}_{x+} \\ I^{in}_{y-} \\ I^{in}_{y+} \end{bmatrix} \tag{1}$$

in short:

$$\vec{I}_{out} = \mathbf{S} \cdot \vec{I}_{in}, \tag{2}$$

where S — scattering matrix.

Provided that nodal element is small as compared with a photon free path (reciprocal of linear attenuation coefficient) and that scattering is isotropic (g = 0) or diffusive approximation is valid, the elements of matrix S may be determined by linear approximation of absorption and scattering. This procedure allows the forward light transmission with efficiency $1-(\mu_a+\mu_s)h$, where — h thickness of element along considered direction and

isotropic scattering into four directions. Finally, for linear approximation, the elements of matrix S for two-dimensional geometry are described by equations:

$$s_{12} = s_{21} = 1 - (\mu_a + \mu_s) \cdot \Delta x + \frac{1}{4}\mu_s \cdot \Delta x, \tag{3}$$

$$s_{34} = s_{43} = 1 - (\mu_a + \mu_s) \cdot \Delta y + \frac{1}{4}\mu_s \cdot \Delta y, \tag{4}$$

$$s_{11} = s_{22} = s_{31} = s_{32} = s_{41} = s_{42} = \frac{1}{4}\mu_s \cdot \Delta x, \tag{5}$$

$$s_{33} = s_{44} = s_{13} = s_{14} = s_{23} = s_{24} = \frac{1}{4}\mu_s \cdot \Delta y. \tag{6}$$

The equations (3)-(6) for elements of matrix S are valid only if dimension h of element is small comparing to reciprocal of light attenuation coefficient:

$$(\mu_a + \mu_s) \cdot h << 1. \tag{7}$$

For three-dimensional geometry the equation (1) has a form:

$$\begin{bmatrix} I^{out}_{x-} \\ I^{out}_{x+} \\ I^{out}_{y-} \\ I^{out}_{y+} \\ I^{out}_{z-} \\ I^{out}_{z+} \end{bmatrix} = \begin{bmatrix} s_{11} & s_{12} & s_{13} & s_{14} & s_{15} & s_{16} \\ s_{21} & s_{22} & s_{23} & s_{24} & s_{25} & s_{26} \\ s_{31} & s_{32} & s_{33} & s_{34} & s_{35} & s_{36} \\ s_{41} & s_{42} & s_{43} & s_{44} & s_{45} & s_{46} \\ s_{51} & s_{52} & s_{53} & s_{54} & s_{55} & s_{56} \\ s_{61} & s_{62} & s_{63} & s_{64} & s_{65} & s_{66} \end{bmatrix} \cdot \begin{bmatrix} I^{in}_{x-} \\ I^{in}_{x+} \\ I^{in}_{y-} \\ I^{in}_{y+} \\ I^{in}_{z-} \\ I^{in}_{z+} \end{bmatrix}. \tag{8}$$

The elements of matrix S are described by equations:

$$s_{12} = s_{21} = 1 - (\mu_a + \mu_s) \cdot \Delta x + \frac{1}{6}\mu_s \cdot \Delta x, \tag{9}$$

$$s_{34} = s_{43} = 1 - (\mu_a + \mu_s) \cdot \Delta y + \frac{1}{6}\mu_s \cdot \Delta y, \tag{10}$$

$$s_{56} = s_{65} = 1 - (\mu_a + \mu_s) \cdot \Delta z + \frac{1}{6}\mu_s \cdot \Delta z, \tag{11}$$

$$s_{11} = s_{22} = s_{31} = s_{32} = s_{41} = s_{42} = s_{51} = s_{52} = s_{61} = s_{62} = \frac{1}{6}\mu_s \cdot \Delta x, \tag{12}$$

$$s_{33} = s_{44} = s_{13} = s_{14} = s_{23} = s_{24} = s_{53} = s_{54} = s_{63} = s_{64} = \frac{1}{6}\mu_s \cdot \Delta y, \tag{13}$$

$$s_{15} = s_{16} = s_{25} = s_{26} = s_{35} = s_{36} = s_{45} = s_{46} = s_{55} = s_{66} = \frac{1}{6}\mu_s \cdot \Delta z. \qquad (14)$$

The simulation procedure at zero iteration step determines the stimulation for each element (for border elements — external stimulations and for elements within two-dimensional or three-dimensional region — internal sources) and next at each iteration step the output fluxes from given nodes are attributed to in-fluxes for adjacent elements. For example, two-dimensional simulation algorithm may be presented in the pseudo-code:

for k = 1 to number of iterations

for (i, j)∈ considered region

{

$I_{x-}^{in(k+1)}(i,j) = I_{x+}^{out(k)}(i-1,j)$

$I_{x+}^{in(k+1)}(i,j) = I_{x-}^{out(k)}(i+1,j)$

$I_{y-}^{in(k+1)}(i,j) = I_{y+}^{out(k)}(i,j-1)$

$I_{y+}^{in(k+1)}(i,j) = I_{y-}^{out(k)}(i,j+1)$

calculate out vector for element (i, j) according equation (1)

}

The boundary conditions in nodal method are defined by attributing right values to in-fluxes for boundary elements. For non-reflecting free surface, boundary condition is defined that all in-fluxes equal zero. For reflecting surface (i. e. surface with internal light refection) in-fluxes are determined as out-fluxes multiplied by reflection coefficient.

When elements of a region may not be considered small (equation (7) not valid), the scattering matrix may be determined by another method, for example, by Monte Carlo method or by diffusive approximation but without use of equations (3)-(6) or (9)-(14). Also the fast nodal method may be used but with dividing big nodal element into number of smaller elements — for these elements the condition (7) should be valid.

3. SIMULATION RESULTS

The specialized software in Pascal language (Borland Delphi environment) was developed, the NODDEL program solves transport equation by nodal method. The program enables simulation of light propagation in such geometrical shapes as cube, sphere and cylinders.

The number of simulations were carried out for cubic object with dimensions 50 mm × 50 mm × 50 mm. This object was decomposed into nodal elements (voxels) with dimensions 1 mm × 1 mm × 1 mm. Isotropic light source was placed in the centre of this cube. The simulation results were compared to analytical solution of diffusive

equation – the photon fluence rate $\Phi[\mathrm{W/m^2}]$ for infinitive medium, determined by equation (15), was the output parameter [5]:

$$\Phi(\vec{r},\vec{r}_0) = \frac{1}{4\pi D} \cdot \frac{\exp\left(-\mu_{eff}\left|\vec{r}-\vec{r}_0\right|\right)}{\left|\vec{r}-\vec{r}_0\right|}, \tag{15}$$

where:

$\vec{r}_0$ — source position, $\vec{r}$ — detector position.

Parameter μ_{eff} is the effective attenuation coefficient, given by [5]

$$\mu_{eff} = \sqrt{\frac{\mu_a}{D}}. \tag{16}$$

The photon fluence rate calculated by equation (15) and that simulated by nodal method at distance $r[mm]$ from source, for optical parameters: $\mu_a = 0,04[mm^{-1}]$, $\mu_s = 3,0[mm^{-1}]$, $g = 0$, are presented in Fig. 3.

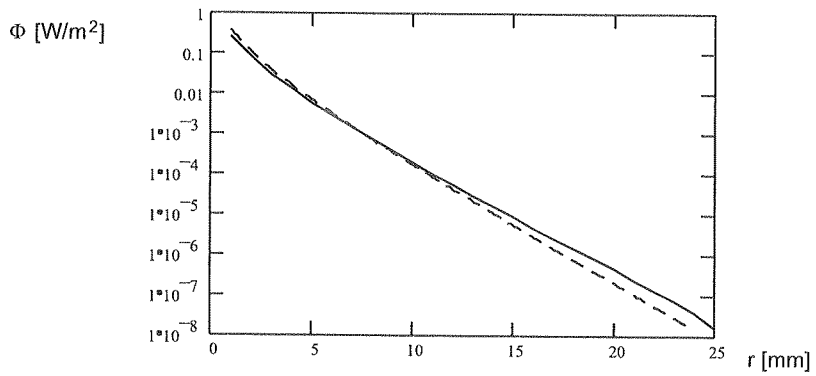

Fig. 3. Comparison of nodal method simulation results (solid line) and analytical solution of diffusive equation (dashed line) for infinitive medium with optical parameters $\mu_a = 0,04[mm^{-1}]$, $\mu_s = 3,0[mm^{-1}]$

The photon fluence rate calculated by equation (15) and simulated by nodal method at distance $r[mm]$ from source, for optical parameters: $\mu_a = 0,01[mm^{-1}]$, $\mu_s = 3,0[mm^{-1}]$, $g = 0$ is presented in Fig. 4.

For both examples the simulation results are in good agreement with analytical calculations. The test of iterative algorithm convergence was also carried out – the most critical conditions (nodal element far from source) were analyzed. The cubic object had dimensions 40 mm × 40 mm × 40 mm with nodal elements (voxels) 1 mm × 1 mm × 1 mm and optical parameters $\mu_a = 0,01[mm^{-1}]$, $\mu_s = 3,0[mm^{-1}]$, $g = 0$. Light source was placed in the centre of this cube and analyzed voxel was at the border, 20 mm from source.

The relative error of solution for border voxel as a function of iteration number was presented in Fig. 5. For about first 150 iterations the relative error is equal 1 (any

light form source has not reached yet this voxel). During the next iterations the solution got the correct value and the error decreased exponentially.

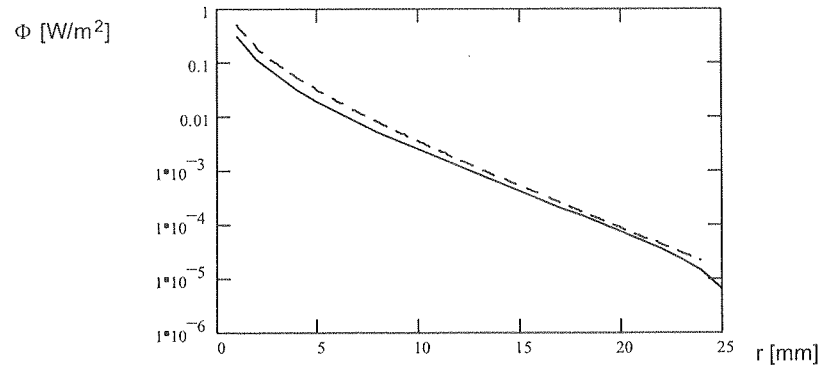

Fig. 4. Comparison of nodal method simulation results (solid line) and analytical solution of diffusive equation (dashed line) for infinitive medium with optical parameters : $mu_a = 0,01[mm^{-1}]$, $\mu_s = 3,0[mm^{-1}]$

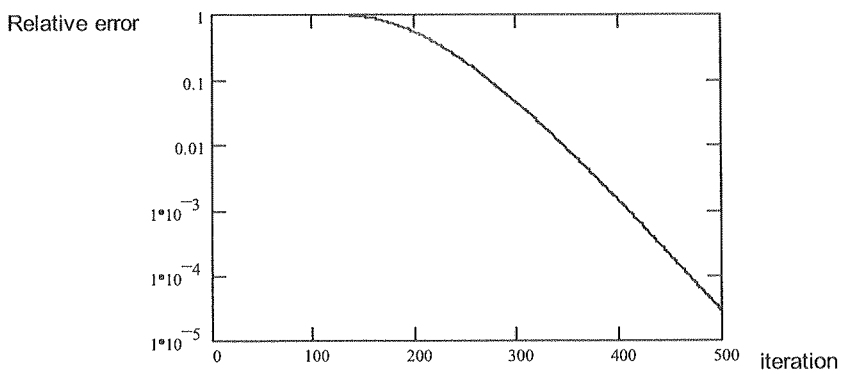

Fig. 5. Relative error of the solution for boundary voxel as a function of iteration number

4. RESULTS OF MEASUREMENT ON CYLINDRICAL PHANTOMS

A fixed geometry optical tomograph was designed and built. There is a detector wchich moves around rotating object. Block scheme is shown in Fig. 6. source the laser module LM12-650 was used (650 nm wavelength and 3 mW output power) as the light. The detector consists of silicon pin photodiode BPW34 (sensitivity spectrum 400 nm — 1100 nm, peak at 700 nm). The photocurrent is integrated by switched integrator and converted by 10-bit ADC built in Atmel's ATMEGA8535 microcontroller. This microcontroller is also a driver for both stepper motors. The whole system

communicates with PC computer, which controls acquisition process by RS232 serial link.

Such a system can be used only for small samples (a few centimeters diameter), but it gives a possibility to make more measurements with simple hardware.

The optical tomograph was used for measurements of cylindrical phantoms. The phantoms were made of white paraffin wax. One phantom was homogenous, others were inhomogenous - with internal regions of increased absorption (blue paraffin wax).

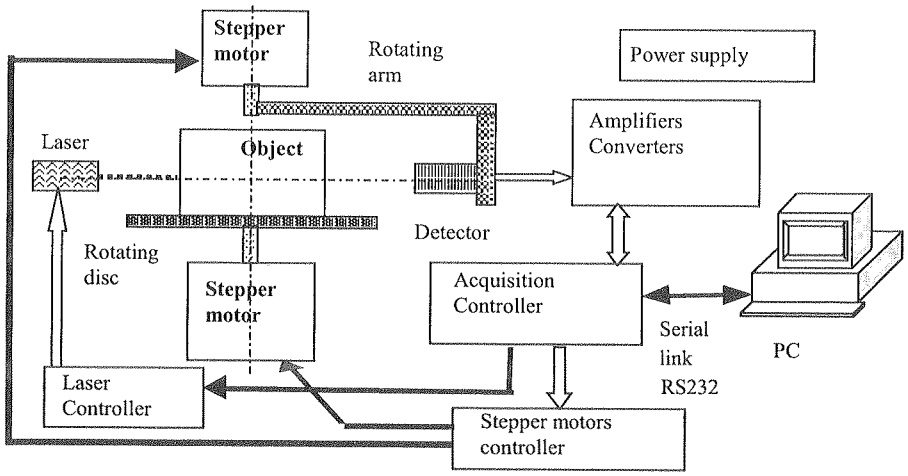

Fig. 6. Block scheme of fixed geometry optical tomograph

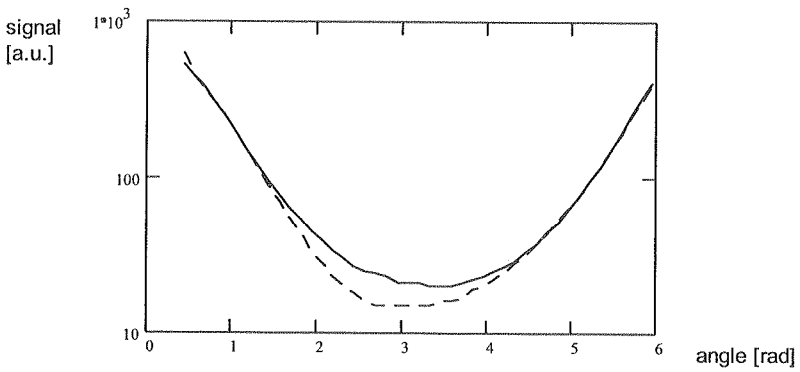

Fig. 7. Measured signal for homogenous phantom (solid line) and inhomogenous phantom (dashed line) as a function of projection angle

The results of exemplary measurement were shown in Fig. 7. There are differences in measured signal (in arbitraly units) between homogenous phantom (solid line) and

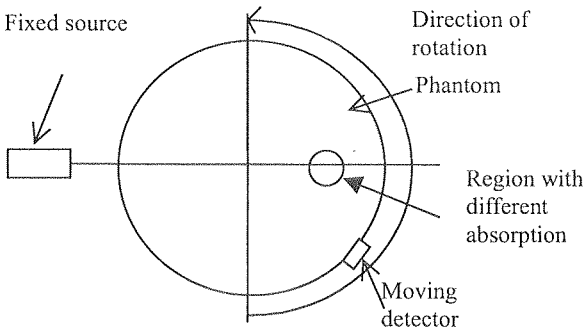

Fig. 8. The measurement geometry for the inhomogenous phantom (top view)

inhomogenous phantom with region of increased absorption (dashed line). The region of big absorption was placed in opposite of the source (i.e. for angle equals π in radians). The geometry of the inhomogenous phantom measurement was shown in Fig. 8.

5. CONCLUSIONS

The proposed nodal method is computationally efficient and has a simple algorithm. It may be used with different types of border conditions. The analyzed medium may have very sophisticated distribution of optical parameters with internal light reflections. Nodal element dimension may be bigger than photon mean free path, provided that scattering matrix was determined by another method with sufficient precision. A discretisation of angles is the main disadvantage of nodal method — it leads to substantial errors for medium with anisotropic scattering. But in medical applications of optical tomography the analyzed media are highly scattering and diffusive approximation may be used with light propagation only in selected directions.

The developed system of the fixed geometry optical tomograph was used as a flexible tool for evaluation of different reconstruction algorithms. A cylindrical coordinates system used here enables performing of full measurements with a single pair of the source and detector.

The nodal method enables fast reconstruction of optical parameter distribution in examined objects, especially for non-linear method of reconstruction.

6. REFERENCES

1. A. B. Milstein, S. Oh, J. S. Reynolds, K. J. Webb, C. A. Bouman, R. P. Millane: *Three-dimensional optical diffusion tomography with experimental data*, Optics Letters, vol. 27, no. 2, 2002, 95-97.
2. L. Wang: „*Hybrid model of Monte Carlo simulation and diffusion theory for light reflectance by turbid media*", J. Opt. Soc. Am. A, vol. 10, (1993), pp. 1746- 1752.
3. A. H. Hielscher, R. E. Alcouffe, R. L. Barbour:„*Comparison of finite-difference transport and diffusion calculations for photon migration in homogenous and heterogenous tissues*", Physics in Medicine and Biology, vol. 43 (1998), pp. 1285-1302.
4. B. W. Pogue, S. Geimer, T. O. McBride: „*Three- dimensional simulation of near-infrared diffusion in tissue: boundary condition and geometry analysis for finite-element image reconstruction*", Applied Optics, vol. 40 (2001) pp. 588- 600.
5. L. Wang: „*Rapid modeling of diffuse reflectance of light in turbid slabs*", J. Opt. Soc. Am. A, vol. 15, (1998), pp. 936-944.

G. DOMAŃSKI, B. KONARZEWSKI, Z. PAWŁOWSKI, K. ZAREMBA, J. MARZEC, R. KURJATA, A. TRYBUŁA

SZYBKA METODA NODALNA SYMULACJI PROPAGACJI ŚWIATŁAW OŚRODKACH MĘTNYCH

Streszczenie

Zaproponowano szybką metodę nodalną symulacji propagacji światła w ośrodkach mętnych. Metoda ta umożliwia symulację rozchodzenia się światła w ośrodkach niejednorodnych z odbiciami wewnętrznymi i zewnętrznymi. Przedstawiono porównanie wyników symulacji metodą nodalną z wynikami obliczeń analitycznych dla jednorodnego sześcianu. Skonstruowano tomograf optyczny o stałej geometrii pomiaru. Przeprowadzono szereg pomiarów fantomów cylindrycznych. Metoda nodalna umożliwia szybką rekonstrukcję rozkładu parametrów optycznych w badanych obiektach, szczególnie w nieliniowych metodach rekonstrukcji.

Słowa kluczowe: tomografia optyczna, propagacja światła, metoda nodalna

Me

V

f
o
a
n
f
I
s
T
a

K

Ele
ssibility
of imag
permitti
betwee
are perf
measure
In a cha
The cha
grated c
reaching

KWARTALNIK ELEKTRONIKI I TELEKOMUNIKACJI, 2005, 51, ZESZYT SPECJALNY, ss. 127--137

Measurement circuit based on programmable integrators and amplifiers for electrical capacitance tomography

W. SMOLIK, J. MIRKOWSKI, T. OLSZEWSKI, D. RADOMSKI, P. BRZESKI, R. SZABATIN

Institute of Radioelectronics,
Warsaw University of Technology,
ul. Nowowiejska 15/19, 00-665 Warsaw, Poland,
wsmolik@ire.pw.edu.pl

The paper presents novel design of charge-discharge capacitance measurement circuit for electrical tomograph. In electrical capacitance tomography, a sensor consists of a set of electrodes surrounding an object. The sensing electronics measures the capacitances for all possible independent electrode combinations. The main measurement problem is high measurement range. For typical sensor, the range of capacitance value for electrode pair is from a few picofarads for adjacent electrodes to a few femtofarads for opposite electrodes. In this paper the application of programmable integrators and amplifiers is presented as solution of this problem. The electrical signal courses and tomographic images are shown. The results show influence of charge-discharge circuit modifications on signal to noise ratio and image quality.

Keywords: electrical capacitance tomography, charge-discharge capacitance measurement method, programmable integrator

1. INTRODUCTION

Electrical capacitance tomography (ECT) measurement technique gives the possibility of imaging electrical permittivity distribution inside an object. The process of image creation requires sequential measurements of charge and reconstruction of permittivity distribution from these data. First, the sequential measurements of charge between transmitting and receiving electrodes placed peripherally around the object are performed. Next, the permittivity distribution is reconstructed from the set of these measurements (projections).

In a charge-discharge circuit the charge flow through sensor electrodes is measured. The charging pulses are integrated on one integrator and discharging pulses are integrated on the second integrator. The signals from both integrators are summed after reaching steady state determined by the integrators time constant. The signal amplitude

is proportional to the measured capacitance of electrode pair. For a typical sensor, the range of capacitance value for electrode pair is from a few picofarads for adjacent electrodes to a few femtofarads for opposite electrodes.
For charge-discharge measurement method the relative measurement error is large for small capacitances. One solution of this problem is to change the amplification (by changing resistance in integrator feedback loop) for small and large capacitance. The other solution is to replace the integrators by charge amplifiers. In such a circuit the voltage signal increases linearly at each charge pulse. In this mode it is possible to charge amplifier to the same voltage for small and large measured capacitance by using different number of charging impulses. It decreases measurement error for small capacitances.
In our tomograph the programmable electronic devices allow switching of integrator feedback loop elements in order to switch amplification and time constant. The circuit can be also switched to work using charge amplifiers. Here only the solution with switched amplification is presented.

2. PROGRAMMABLE CHARGE-DISCHARGE CAPACITANCE MEASUREMENT CIRCUIT

The basic electrical circuit for the capacitance sensor based on charge detector is described in (Pląskowski, 1995) and in (Huang, 1998). The next, differential version of sensor electronics – the charge-discharge measuring circuit is described in (Yang, 1996). Although the description given by the authors includes even the operational calculus, some aspects of this circuits' operation are omitted. Below the operation of charge-discharge circuit is shortly described and shape of voltage signal at output of charge detector is discussed.
The schematic diagram of charge detector is shown in figure 1. The measurement consists in switching of constant voltage $V_{in} = const$ on unknown capacitance C_x and measuring charging current using operational amplifier. The switches A, B, C and D are operated at frequencies of about several MHz, allowing for the cyclic charging and discharging of the measured capacitance. During the charge phase, switches A and B are closed and switches C and D are open. During the discharge phase, switches C and D are closed and switches A and B are open. The charge transferred by capacitance C_x at one impulse is $Q = V_{in}C_x$. If the charging impulse frequency is f, the mean value of charging current is $I_{mean} = fV_{in}C_x$. If C_f is not present, the ideal operational amplifier is working as current-voltage converter. The mean voltage at the output is

$$V_{mean} = -fV_{in}R_fC_x \tag{1}$$

and is proportional to the unknown capacitance C_x. To measure the mean value of voltage the integration is necessary. The time constant of integrator $\tau = R_fC_f$ must be chosen to achieve constant output voltage in a relatively short time.

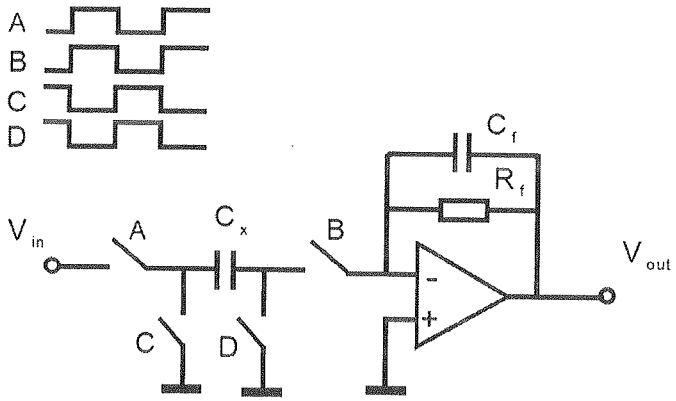

Fig. 1. The charge detector circuit and switching control signals

The shape of voltage signal at output of charge detector is determined by voltage steps from charging impulses and voltage falling as a result of $R_f C_f$ circuit discharging. The transmittance of charge detector from figure 1 when switches A, B are closed and C, D are open is

$$\frac{\tilde{V}_{out}(s)}{\tilde{V}_{in}(s)} = -\frac{sR_f C_x}{sR_f C_f + 1} \tag{2}$$

where $\tilde{V}_{in}$, $\tilde{V}_{out}$ are Laplace transfoms of $V_{in}(t)$, $V_{out}(t)$ respectively. For small time e.g. $|sR_f C_f| >> 1$

$$V_{out}(0) = -\frac{C_x}{C_f} V_{in}(0) \tag{3}$$

The voltage change due to discharging by $R_f C_f$ circuit is given by formula

$$V_{out}(t) = V_{out}(0) e^{\frac{t}{R_f C_f}} \tag{4}$$

The output voltage in function of charging impulse number may be written down using sequence of equations

$$V_{out}(1) = -\frac{C_x}{C_f} V_{in}$$

$$V_{out}(2) = V_{out}(1) e^{-\frac{1}{fR_f C_f}} - \frac{C_x}{C_f} V_{in}$$

$$V_{out}(n) = -\frac{C_x}{C_f} V_{in} \left[1 + e^{-\frac{1}{fR_f C_f}} + e^{-\frac{2}{fR_f C_f}} + \ldots + e^{-\frac{n}{fR_f C_f}} \right]$$

The expression in square brackets is geometric series and if fR_fC_f is very large value, the output voltage after n charging impulses could be expressed by

$$V_{out}(n) \cong -fV_{in}R_fC_x\left(1 - e^{-\frac{n}{fR_fC_f}}\right) \tag{5}$$

where $t = \frac{n}{f}$ is a time. After certain number of pulses the steady state is achieved — the charging current equals discharging current. The relative pulsation amplitude at integrator output after reaching steady state depends on integrator time constant and pulses frequency and is equal

$$\frac{\Delta V_{out}}{V_{out}} = \frac{1}{fR_fC_f} \tag{6}$$

Figure 2 shows the voltage setting at integrator output. The values of capacitance formed by electrode pairs in one of our tomographic sensor with 12 electrodes are given in table 1. Figure 2 presents the situation for extreme values of measured capacitances — the largest capacitance for neighboring electrode pairs and the smallest capacitance for opposite electrode pairs — and different values of R_f and C_f. The input constant voltage of 12 V is switched with the frequency of 1.5 MHz.

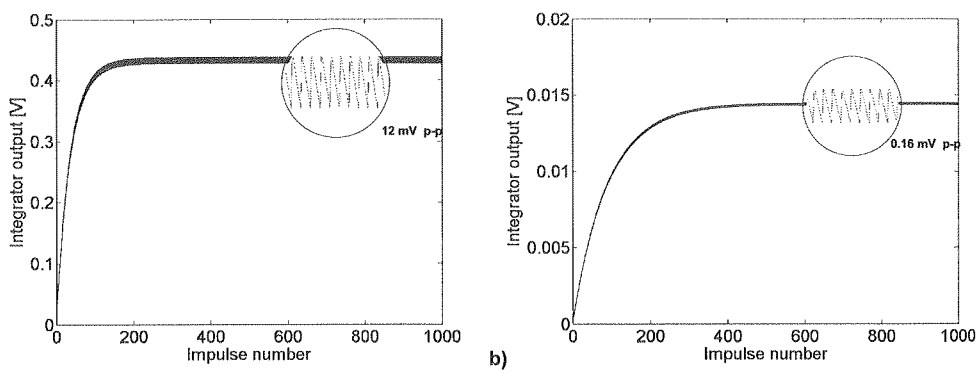

Fig. 2. The output voltage at integrator. Absolute value. Measurement of capacitance values for typical tomographic sensor. V_{in} = 12 V, f = 1.5 MHz. (a) Neighboring electrodes — large capacitance value — C_x = 1.5 pF, R_f = 16 kΩ, C_f = 1.5 pF. (b) Opposite electrodes — small capacitance value — C_x = 0.02 pF, R_f = 40 kΩ, C_f = 1.5 pF

For the measurement of capacitances formed by electrode pairs of tomographic sensor the switching of feedback elements of the operational amplifier is essential. The time constant R_fC_f must be large to obtain small voltage pulsation. The increase of R_f has to compensate for the decrease of C_x. The voltage setting time changes adequately to the increase of R_f so the number of charging pulses also has to be changed. From equation 1 and 6 it can be seen that increasing frequency of charging pulses has fundamental influence on measurement quality.

Table 1

The values of capacitances for 12 electrode tomographic sensor

Electrode pair	Capacitance [pF]
1-2	1,530
1-3	0,130
1-4	0,053
1-5	0,033
1-6	0,025
1-7	0,023

The charge-discharge circuit with programmable feedback loop and programmable amplifiers elaborated by us is presented below (figure 3). The differential version of sensor electronics consists of two integrators for measuring charging and discharging current. This increases signal twice. The switches TK1, TK2, RK1 and RK2 (ADG442) are operated at frequency 1.5 MHz, allowing for the cyclic charging and discharging of the capacitance of electrodes. The charging pulses are integrated by one operational amplifier AD8620. The discharging pulses are integrated by the other AD8620 amplifier. The two signals of the same value but different sign from integrators are summed by instrumental programmable amplifier PGA206. The second PGA206 instrumental amplifier together with the first one allows to obtain signal amplification from 1 to 64.

The presented charge-discharge circuit was used for the construction of electrical capacitance tomograph prototype ET1 and ET2 (Olszewski, 2002). The ET3 (figure 4) prototype is designed for sixteen-electrode sensor, however it can work in an eight, twelve, sixteen, thirty two or two times eight, or two times twelve electrodes setup. The tomograph has a modular structure. It consists of 16 analog amplifier boards, a motherboard and a control board with an analog to digital converter. The analog amplifier board works as a transmitter and receiver. The motherboard consists of a signal bus, sixteen slots for amplifier boards and one slot for the ADC board and the control logic designed by using programmable logic devices. The control board consists of a 16-channel multiplexer, a 16-bit analog to digital converter, a control logic and a RS-232 interface. The control logic on this board is designed by using programmable logic devices (Altera). The control board sequentially switches the amplifier boards. At a given moment one board generates the signal on the application electrode. The voltage signals on the remaining electrodes are amplified by the analog boards and sequentially sampled by the ADC. The control board transmits the measured data to a computer using a RS-232 serial port.

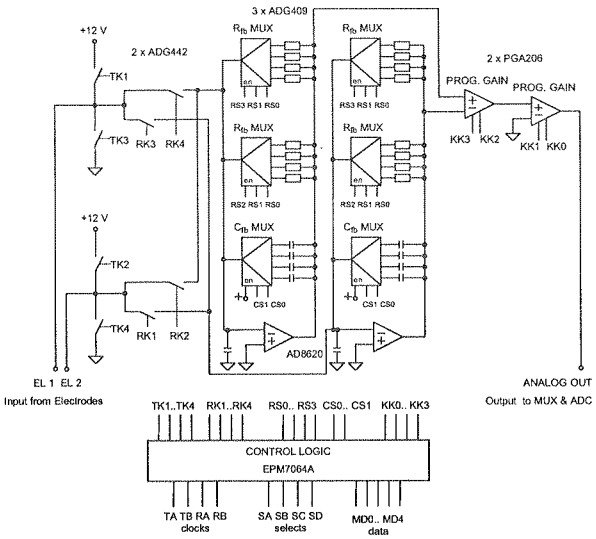

Fig. 3. The charge-discharge circuit with programmable integrators and amplifiers

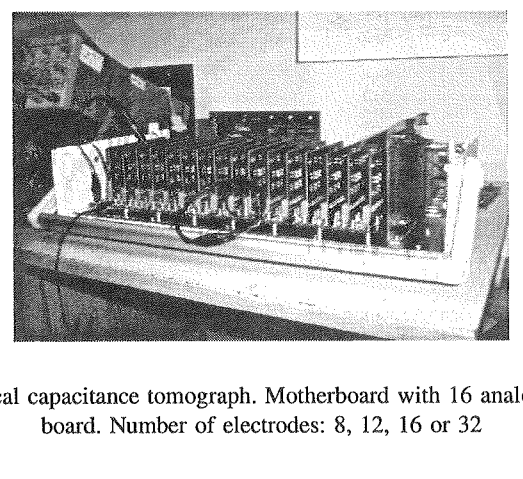

Fig. 4. The ET3 electrical capacitance tomograph. Motherboard with 16 analogue boards and control board. Number of electrodes: 8, 12, 16 or 32

3. RESULTS OF MEASUREMENT

The measurements were performed using ET3 electrical capacitance tomograph. The tomographic sensor with 12 electrodes was used. The empty sensor and sensor with objects are used. The signals from analog board (charge-discharge circuit) were captured by an oscilloscope.

Figure 5 presents voltage signal at the output of 12-th electrode when the sensor was empty. The 12- th electrode is receiver when other transmitting electrodes are switched in turn. This results in 11 voltage levels for electrode pairs: 1-2, 1-3, 1-4, 1-5, 1-6, 1-7, 1-8, 1-9, 1-10, 1-11, 1-12. The example values of capacitance for electrode pairs

are grouped in table 2 according to their values. The values of feedback element R_f, C_f and total amplification A on instrumental amplifiers are given.

Table 2

The electrode capacitance, elements of integrators and amplification

Electrode pair	C_x [pF]	R_f [kΩ]	C_f [pF]	A
1-2 (1-12)	1,530	16	1.5	4
1-3 (1-11)	0,130	25	1.5	32
1-4 (1-10)	0,053	25	1.5	32
1-5 (1- 9)	0,033	40	1.5	64
1-6 (1- 8)	0,025	40	1.5	64
1-7	0,023	40	1.5	64

The voltage signal course is captured when the analog circuit is working without switching integrator and amplifiers and when the switching is on. In the first case, the signals from pairs of opposite electrodes are very small in comparison with signals from neighboring electrodes. The differences between the signals from opposite electrodes are not distinguishable because they are less than voltage pulsation. In the second case, the signals from opposite electrodes are comparable to the signals from neighboring electrodes and are distinguishable.

The level of voltage pulsation seen on the picture is higher than in the simulation (figure 2) because of the charge injection effect. The charge is injected and pulled out to and from the integrator by analogue switches. The charge injection increases amplitude of voltage pulsation but it does not change the mean value of voltage at the integrator output because the switch is opened and closed at one cycle. The relative amplitude of voltage pulsation for differential version of measurement circuit can be expressed by

$$\frac{\Delta V_{out}}{V_{out}} = \frac{1}{2fR_fC_f} + \frac{Q_{infect}}{V_{inf}R_fC_fC_x} \tag{7}$$

where Q_{infect} is charge injected by the switch. The second element plays big role even if the charge injection of the analogue switch is relatively small. The used analogue switches ADG442 used here have a very low charge injection and are specially powered by low voltage (+/– 5 V) for further reduction of a charge injection effect. To minimize charge injection effect the high amplification (using R_f) and lowpass filtering is used.

The measurements using the sensor filled with the test object were performed. The electrical tomograph was working with and without switching amplifiers. 66 measurement data are obtained for 12 electrodes sensor. The images of tomographic

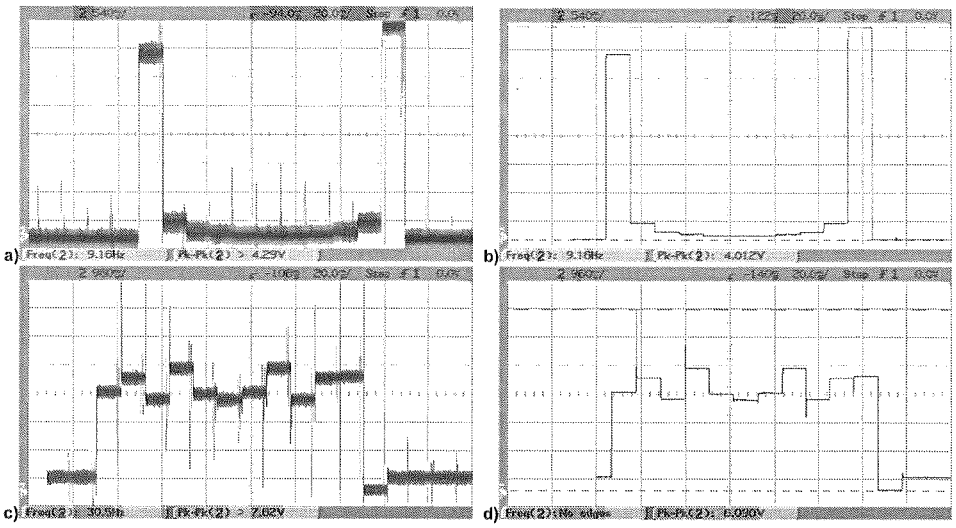

Fig. 5. The voltage at output of 12-th electrode. V_{in} = 12 V, f = 1.5 MHz. (a) (b) Not switched elements R_f = 16 kΩ, C_f = 1.5 pF. Constant amplification A=4 for all electrodes combinations; (c) (d) Switched elements of integrator and amplification of instrumental amplifiers. Electrode pairs 1-2, 1-12: R_f = 16 kΩ, C_f = 1.5 pF, A=4; electrode pairs 1-3, 1-11: R_f = 25 kΩ, C_f = 1.5 pF, A=16; electrode pairs: 1-4, 1-5, 1-9, 1-10: R_f = 25 kΩ, C_f = 1.5 pF , A=32; electrode pairs: R_f = 40 kΩ, C_f = 1.5, 1-6, 1-7, 1-8, A=64; (a) (c) Signals without filtering, (b) (d) Signals after 1024 points averaging

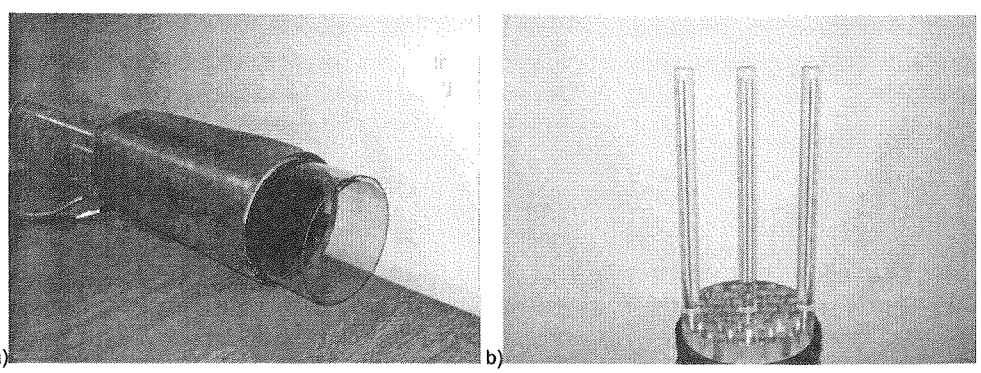

Fig. 6. (a) The tomographic capacitance sensor. (b) The test object — three rods made of Plexiglas

slices were reconstructed from these data using the model based iterative algorithm (Mirkowski, 2004). The model based algorithm modifies the measurement model — so called sensitivity matrix – in successive steps. The first stage of one step is calculation of a sensitivity matrix for a given permittivity distribution. The sensitivity matrix is determined by mathematical modeling of electrical field for the current estimate of permittivity distribution. The second stage is inverse problem solving by SIRT (Herman, 1980). The sensor and the test object – three rods made of Plexiglas – are shown in figure 6. The images of reconstructed permittivity distribution obtained for two work modes of tomograph are shown in figure 7.

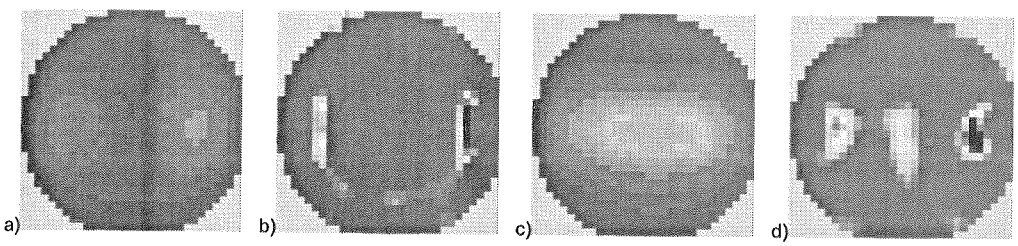

Fig. 7. The reconstructed images of electrical permittivity. 32×32 pixel matrix. Two algorithms of image reconstruction: the LBP and the iterative model based algorithm (400 iterations, sensitivity matrix modification after each 100 iterations). The capacitance values are measured in two modes: without and with switched amplification. (a) Measurement w/o switched amplification, LBP; (b) Measurement w/o switched amplification, iterative algorithm; (c) Measurement with switched amplification, LBP; (d) Measurement with switched amplification, iterative algorithm

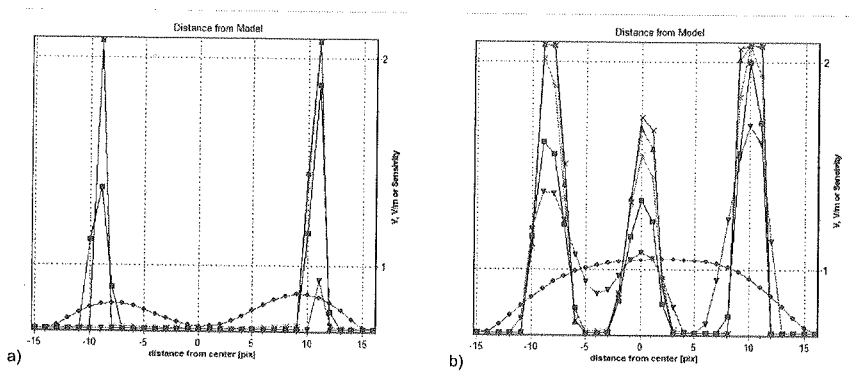

Fig. 8. The profiles of electrical permittivity image (central horizontal cut line). The profile after LBP reconstruction (circles) and successive steps of model based iterative reconstruction (after four modifications of sensitivity matrix). The capacitance values are measured in two modes: without and with switched amplification. (a) Measurement w/o switched amplification, (b) Measurement with switched amplification

4. CONCLUSIONS

The novel design of charge-discharge capacitance measurement circuit for electrical tomograph was elaborated. The application of programmable integrators and amplifiers allows measurement of capacitance of electrode pairs in high range from a few picofarads to a few femtofarads. The modifications of charge-discharge circuit increases signal to noise ratio. The influence on image quality is essential. The performed experiments show that proper distribution of permittivity can not be reconstructed from the data obtained without amplification switching. In such case the sensitivity in the center of image is very poor. For the presented object — three Plexiglas rods — the central rod is not visible on the reconstructed image. The image quality is not improved even with iterative reconstruction. The amplification switching makes possible the measurement of objects in the central part of images. In case of these data the iterative reconstruction improves quality of image. The quantitative evaluation of influence of charge-discharge circuit modification on tomographic image quality will be the subject of our future work.

5. REFERENCES

1. A. Plaskowski, M. S. Beck, R. Thorn, T. Dyakowski: *Imaging industrial flows. Applications of electrical process tomography*. IOP Publishing Ltd, 1995.
2. S. M. Huang, R. G. Green, A. Plaskowski, M. S. Beck: *A high frequency stray-immune capacitance transducer based on the charge transfer principle*, IEEE Trans. Instrum. Meas. 37, 1998, pp. 368-373.
3. W. Q. Yang: *Hardware design of electrical capacitance tomography systems*, Meas. Sci. Technol., 7, pp. 225-232, 1996.
4. T. Olszewski, P. Brzeski, J. Mirkowski, A. Pląskowski, W. Smolik, R. Szabatin: *Capacitance Tomograph — Design and Preliminary Results*, Proc. of 2nd International Symposium on Process Tomography in Poland, Wroclaw, Poland, 2002, pp. 159-168.
5. P. Brzeski, J. Mirkowski, T. Olszewski, A. Pląskowski, W. Smolik, R. Szabatin: *Multichannel capacitance tomograph for dynamic process imaging*, Opto-Electronics Review, 11(3), pp. 175-180, 2003.
6. J. Mirkowski, W. Smolik, P. Brzeski, T. Olszewski, D. Radomski, R. Szabatin: *Software For Sensor Modeling In Electrical Capacitance Tomography*. Proceedings of 3rd International Symposium on Process Tomography in Poland, Łódź, 2004, pp. 106-110.
7. G. Herman: "Image Reconstruction From Projections", Accademic Press Inc., 1980.

W. SMOLIK, J. MIRKOWSKI, T. OLSZEWSKI, D. RADOMSKI, P. BRZESKI, R. SZABATIN

UKŁAD POMIAROWY NA BAZIE PROGRAMOWALNYCH INTEGRAFÓW I WZMACNIACZY DO ELEKTRYCZNEJ TOMOGRAFII POJEMNOŚCIOWEJ

Streszczenie

Artykuł przedstawia układ do pomiaru pojemności w tomografie elektrycznym. W metodzie tej czujnik składa się z zestawu elektrod otaczających mierzony obiekt. Układ elektroniczny związany z czujnikiem mierzy pojemność we wszystkich możliwych kombinacjach elektrod. Głównym problemem pomiarowym w tomografii pojemnościowej jest zakres wielkości mierzonej. Wartości pojemności dla par elektrod zmieniają się od kilku pikofaradów dla przyległych elektrod do kilku femtofaradów dla przeciwległych elektrod. W artykule przedstawiono rozwiązanie tego problemu poprzez zastosowanie programowalnych integratorów i wzmacniaczy. Przedstawiono również przebiegi elektryczne wybranych sygnałów oraz tomograficzne przykładowych obiektów.

Słowa kluczowe: elektryczna tomografia pojemnościowa, integrator programowalny

KWARTALNIK ELEKTRONIKI I TELEKOMUNIKACJI, 2005, 51, ZESZYT SPECJALNY, ss. 139–158

Petri nets in measuring systems

ROBERT ŁUKASZEWSKI[1)], WIESŁAW WINIECKI[2)]

[1)] *Warsaw University of Technology, Institute of Radioelectronics, Nowowiejska 15/19, 00-665 Warsaw, r.lukaszewski@ire.pw.edu/pl, www.ire.pw.edu.pl*
[2)] *Warsaw University of Technology, Institute of Radioelektronics, ul. Nowowiejska 15/19, 00-665 Warsaw, w.winiecki@ire.pw.edu.pl, www.ire.pw.edu.pl*

The paper presents research on a methodology of design Measuring Systems (MS) with time limitated data flow. A new method of describing MS model based on Petri Nets is proposed. Examples of MS modelling with ExSpecT and CPN/Tools are included. The paper provides an overall description of informal and formal methods, which can be used while designing systems.

Keywords: measuring systems, formal methods

1. INTRODUCTION

It is hard to speak of well-organized Measuring Systems (MS) design rules. Nowadays there exists a poorly integrated set of directions. There is thus a need to formalize the methods of designing MS.

Software plays an important role in MS. The quality of a system depends on the software to a larger and larger extent. It is not usually possible to carry out comprehensive testing of complex MS software and researches do not go further than just to examine the most important test cases. Such an approach is not satisfactory because in case of some systems (e.g. "safety-critical" and "mission- critical" systems) simplifying the approach to correctness is unacceptable.

In software engineering several software lifecycle models are proposed [12]. However in a general interpretation of waterfall model other models can be seen as variations or enhancements of this model. These models introduce certain phases of software lifetime, determine actions taken in particular phases and set the order of their realisation.

Considering the subject of this paper a model based on **formal transformations** is particularly interesting. Formal system creation is an approach, which has a lot to

do with watefall model. However the creation process is based here on mathematical transformations of system specification into an executable program. In the transformation process formal mathematical representation is methodically transformed into more detailed but still mathematically correct system representation. Defining the project process [20] does not give directions how particular stages should be carried out. It only describes a framework in which detailed methods are employed defining a way of work in one or more stages. Most of practically employed methods are based on more or less formal model. Most often used models are: control flow model, data flow model, subject related object model, abstract data types model and entered and extracted data structure model.

It is necessary to elaborate a methodology of effective employment of Formal Methods (FM) to analyse, specify and support designing MS software (also Distributed MS — DMS) with time requirements. To create such a methodology one needs to elaborate methods of forming a model describing various aspects of information flow within a process and between the processes inside MS and suggest formalized methods of describing such a model. Furthermore verification of created model is necessary.

2. INFORMAL METHODS OF PRODUCING SOFTWARE

Informal, industrial approach to the problems of software producing usually boils down to using certain heuristic patterns of systematic analysis, specification and designing.

The basic tools to design the software are diagrams. A set of diagrams can be treated as a language to describe a model of a system. Methodologies of designing are usually certain algorithms of employment of systems' description languages used to make a design. For instance on the basis of structural diagrams, such as: Data Flow Diagram (DFD), Entity-Relationship Diagrams (ERD) structural methodologies of analysing and designing real-time systems have been elaborated, among others Ward-Mellor methodology (Real-Time Structured Analysis — RTSA) [20, 21, 22] and MASCOT methodology (Modular Approach to Software Construction Operation and Test) [21, 22]. Using UML — an object-oriented design language [1, 16] — several object-oriented methodologies of real time systems modelling were introduced including COMET (Concurrent Object Modelling and architectural design mEThod with UML) [9] and ROPES (Rapid Object-oriented Process for Embedded Systems) [6]. Some of the system description languages were defined together with the development of design methodologies and for the sake of depicting features of a given methodology. HOODTM/HRT-HOODTM methodology [11, 21, 22] and LACATRE language and methodology [21, 22] can serve as an example. Object-oriented design methods proposed for languages with object-oriented features such as SaMI methodology [21, 22] are also to be noted.

3. FORMAL METHODS

The possibility to formally prove the correctness of a software project in a formal way is expected for a growing number of information systems including time-critical and safety-critical systems. Formal methods are mathematically based techniques for the specification, analysis, development and verification of software and hardware systems. A formal approach to the initial specification, analysis and designing is based on creating a model of the constructed system with the application of the language of Mathematics and transforming the created description in a systematic way using strictly defined transformations. The initial specification expressed in a formal language (FL) is to be further defined through successive mathematically described transformations until the model of the system is ready for implementation. The elaboration of fully formal methodology of software designing has so far been an open scientific problem. Another way to apply FL is to combine them with engineering methodologies. The basic limitations are: lack of effective mathematical specification languages, difficulty of strict definition of specification fully reflecting actual requirements, lack of developed methods of transforming subsequent system versions and small effectiveness or inability to generate output code [21]. Regardless of the above limitations modern formal languages of system description are more and more widely used in solving a large number of software manufacturing problems. The specification expressed by means of the mathematical language of description can be formally analysed in order to evaluate the properties of the system being defined. FL enable the scientist to prove the correctness of the description of systems (verification) [7], and to prove the existence of key properties such as absence of deadlocks or overflows [13]. FL also enables one to prove the compliance with time limitations in the systems [2, 25].

Formal methods of software design usually include definition of system models and demonstration of their properties using a given description language [2]. Another way of formal language employment is their association with engineering methods. A system description defined with an engineering method is transformed to mathematical language according to defined rules. An ability of formal analysis of a system originally developed using informal methodology is thus reached [7, 23, 24].

In general formal methods can be divided into finished state automata, temporary logic, process algebras and Petri Nets.

There are over 90 different FM [26]. Individual notations characterize the methods. Application of the methods is mostly dependent on the adequate program tools. Particular methods were created and have been developed by different academic research centers, corporate research centers and commercial software companies. Particular interest in formal methods can be seen in following fields: business process modelling, real time systems specification and analysis, software engineering of systems or critical elements, industrial automation system modelling, and embedded systems analysis. Formal methods are employed also in biology, chemistry and medicine. Most of FL enabling the definition of time properties of systems constitute an extension

of mathematical forms of describing classical systems (without time requirements) e.g. **Timed Process Algebras, Time/Timed Petri Nets** [2, 4, 10, 13, 14, 19], time extensions Temporal Logics [5, 15]. A broader review of FL describing time systems as well as the methodologies formed on the basis of the given languages can be found in: [3, 5].

4. PETRI NETS

Petri nets are regarded as a formalism particularly suited for asynchronous and parallel system specification and analysis. The net's basic feature is the capability of simultaneous presentation of control flow and data flow in concurrent systems. Formally Petri net [20] is a four $C = (P, T, I, O)$ where $P = \{p_1, p_2, ..., p_n\}$ is a finite set of **places**, $T = \{t_1, t_2, ..., t_m\}$ is a finite set of **transitions**, $I : T \rightarrow P^*$ is an input function, and $O : P \rightarrow T^*$ is an output function. Graphic representation is a graph consisting of two types of input nodes called *places* and *transitions* respectively. Places (circles or ellipses) represent conditions and transitions (rectangles) represent events. Places of the net may contain tokens marked as dots. Token placement sets marking of net and travelling tokens mark system dynamics.

The ability to create a system model as an executable graph builds a link between an engineering, practical system description method in the form of a diagram and a theoretical approach, which describes the system model in the form of a set of strict mathematical dependencies, which can be formally analysed. The classic form of Petri nets has been successfully to model and analyse different types of systems including production processes, communication protocols, calculation processes and multiprocessor systems [21, 22].

From a MS design methodology definition point of view net's basic behavioural features are of high importance: reachability, boundedness and liveness [21, 22]. The analysis of net's boundedness enables identification of overflows (e.g. buffers, registers) in the system. The net's liveness in regards to software guarantees the absence of dead code in any state of program execution (no deadlocks). Deadlock means the inability to run any transition, which means the suspension of all processes of the program. Showing these features for net described system is possible through the analysis of limited net based on its reachability tree [21, 22].

From the point of view of the subject of this paper two areas are of particular interest. Studies of Petri Nets enhancements with broadened expressiveness and the research of net definition enhancements to enable the projection of features of systems with time rigours (e.g. real-time systems). High-Level Petri Nets are a result of these works. Among them Environment Relationship Nets [5] and Coloured Petri Nets — **CPN** [13, 21, 22] can be distinguished. High-Level Petri Nets in comparison with classic nets (places and transition nets) offer a more consistent way of system description and simplify the modelling and analysis of complex systems. In CPN every token (**colour**) has an associated value (e.g. integer, record). To model complex systems

effectively, CPN permit dividing fragments of net into subnets and thus enabling the creation of complex hierarchical CPN. **Time** enhancements of Petri Nets were proposed for places and transitions nets [2, 4, 10, 14] as well as for High-Level Petri Nets [13, 19]. Timed CPN (**TCPN**) use the idea of a global clock. Tokens can transport a time value (time stamp), which denotes the earliest value of model time where the token can be used. Time stamps are modified by expressions linked to output transition arcs or transitions. TCPN modelling and analysis can be aided by software tools (e.g. CPN Tools) which usually enable automatic generation of timed reachability tree and analysis of that tree according to set values.

5. METHODOLOGY OF DESIGN MEASURING SYSTEMS

5.1. CURRENT METHODOLOGIES OF DESIGN MEASURING SYSTEMS

Methodology of designing MS [20] is used to describe a process, which begins with specifying the need to create a new system, and ends in releasing a product of appropriate quality. The scientists' interests are thus focused on not only preparing diagrams of devices and programming but also on analysing the field of application, specifying the user's needs and testing the components of systems as well as recording the course of a project and describing the structure of the equipment, the software and its usage.

General methodologies of designing MS have been elaborated on the basis of a direct systematic approach to measurements [18]. MS design rules are currently poorly integrated and are based mainly on the knowledge and experience of the designers.

MS software engineering is based on the extensions of classical (engineering) methodologies of developing information systems [27]. Most of currently applied methodologies of designing MS software can be described as informal structural methods. There are attempts to create MS models. These models mostly show the physical structure of MS or describe the metrological properties of MS. The common fault of the MS software design methods being applied at the moment is neglecting time dependence in the process of designing MS. Nor do the methods provide mechanisms of verifying the correctness and quality of the created MS.

5.2. MS MANUFACTURING METHODOLOGY BASED ON FORMAL METHODS

To include a FL effectively in the methodology of creating MS software (also DMS) with time limitations the following two operations can be done:

1. Choosing the right perspective for the description of a system according to an engineering method and establishing rules of transforming the perspective into a specified FL. The language is used in some of the stages of manufacturing pro-

cess e.g. timed process algebras temporary logic and time automata are mainly employed in formulating system descriptions in early stages of manufacturing.

2. Indicating a FL, which allows elaborating an autonomous design methodology.

Formal approach to specification, analysis and designing is based on **formulating a model** of the constructed system with the use of the language of Mathematics and transforming the created description systematically using strictly defined transformations. To make up a model of the processes occurring in system the following needs to be done:

- defining the necessary external objects, processes, streams and sets;
- deciding what sort of relations there should be between those elements;
- creating a diagram showing the elements and relations between them.

A good model should present project problems as accurately as possible. It should strictly emulate the operations within the designed system. It should be characterized by clarity and accessibility to the tools. It should also be standardized.

5.2.1. FORMAL METHOD CHOICE CRITERIA

Formulating formal methods choice criteria, which can be used to define MS creation methodology, are a result of years long thorough analysis of these systems' properties. Criteria listed below are based on thorough experience in different measuring systems design.

In general it can be said that those methods, which enable the support of at least several stages of MS manufacturing can be helpful. **The ability of system analysis, formal specification and verification** is necessary. Those methods must permit the creation of a relevant and accurate model of as broad as possible range of measuring systems. The model should reflect the character and features of processes occurring during normal system operation. It should also enable simulation of exceptions (breakdowns, out-of-range parameters). Considered methods must assure the **ability of simulation and analysis of time phenomenons** occurring in MS processes. Because of the fact that in a lot of cases these phenomenons cannot be strictly defined must permit time **stochastic process modelling**. Complex character of a large number of MS generally leads to the creation of a very complicated model of such a system. It is thus necessary to decompose those kinds of systems into functional blocks or logical processes. The proposed method should in this case take in to consideration **model's hierarchical character and/or object-oriented character** of model components. In a lot of cases process occurring in MS are executed parallelly in time, which determines the necessity of both **sequential and parallel** simulation. A very important element of proposed MS manufacturing methodology is the possibility of its employment by engineers, who design such systems. Choosing the right formal method must be thus limited to those among them, which are implemented as **software tools**. Those tools must, in an **intuitive** way through a **graphic user interface**, allow the creation of MS model its verification, simulation and visualisation.

Using formulated criteria Petri Nets were chosen to create MS models. To project time requirements of measuring systems usage of Petri Nets **time enhancements** will be useful. Time events occurring in DMS often have non- eterministic character, for example in systems using global computer networks or cellular networks. **Stochastic** Petri Nets can be used to describe these phenomenons. Because of a possibility of MS decomposition as well as particular of their blocks Petri Nets **hierarchical or object-oriented enhancements** are very useful. **Coloured** Petri Nets facilitate modelling of different kinds of signals or messages sent during MS work.

5.2.2. SOFTWARE TOOLS CHOICE CRITERIA

Formulating criteria of choice of appropriate software tools, which could be useful in the process of designed measuring system model analysis, specification and verification is determined by an earlier choice of formal method. Searched tool should use Petri Nets in the above design phases. It should particularly include appropriate enhancements of these nets (time, stochastic, colour, hierarchical/object-oriented). Additional choice criteria of appropriate software tool are availability of an intuitive graphic user interface, broad model verification module, thorough documentation or built-in help and software stability. Among over 50 [17] different software tools using PN to create MS manufacturing methodologies using FM the usage of following tools can be considered: ExSpecT, Mathlab — PN Toolbox, Artifex, CPN-AMI for Linux, GreatSPN, PEP, TimeNET, CPN/Tools. Examples of MS creation in ExSpecT and CPN/Tools environments are explained below.

5.2.3. MODELLING MEASURING SYSTEMS USING PETRI NETS AND EXSPECT TOOL

ExSpecT [14] is a Microsoft Windows based environment that enables discreet processmodelling. ExSpecT enables the usage of High-Level Petri Nets: stochastic, co-

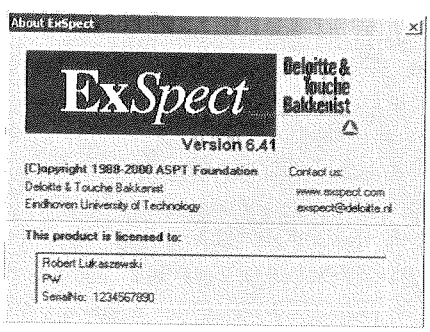

loured and hierarchic. ExSpecT has a very intuitive graphic user interface. It provides simulation with animated graphics as well as maximum performance mode simulation without the animation. ExSpecT uses a functional native language of transition (here

called processor) specification. Model created with ExSpecT describes system's behaviour as a set of hierarchically defined processes and subprocesses which communicate with each other through messages. Model of this kind can be analysed in regard to structural correctness and behavioural features. The analysis can be done step by step, continuously or using breakpoints. Because of the above reasons ExSpecT was chosen for further research on creating a simple MS model and its analysis. The modelled measuring system consists of IEC 625 controller and three devices connected to it (Fig. 1).

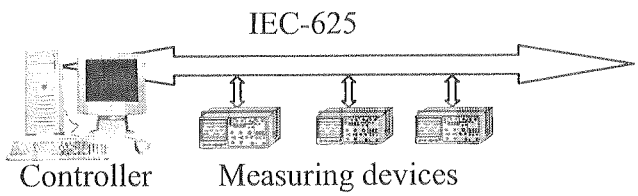

Fig. 1. Block diagram of the system

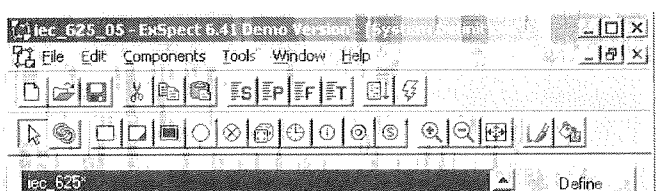

Fig. 2. System definition

A model of the system has been built in ExSpecT environment. The Model is hierarchical. Defining of the modelled measuring system relied on creation of a set of subnets communicating with each other. The set consists of 7 nets of different levels (Fig. 2). It should be noticed that most of them is used to describe more than one system block, process or event. For example an "instrument" — a net defining measuring device (Fig. 4) is used three times to describe three measuring devices. Of course subnets of lower levels than *instrument* subnet such as *read_proc* (Fig. 5) are also automatically used multiple times making the project object-oriented.

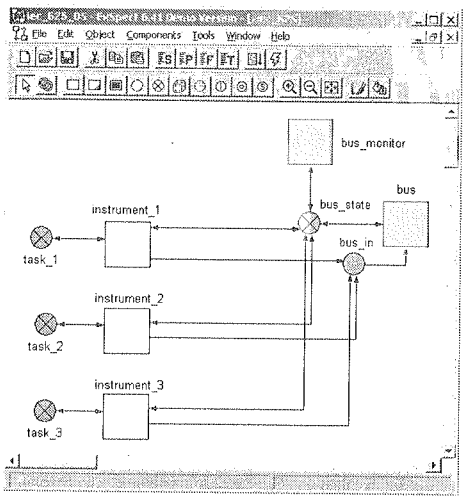

Fig. 3. System model

To be precise a block view of system leads to a high level model. In this view blocks representing measuring devices, communication interface and IEC-625 interface synchronization lines logical state monitor are the elements of system model (Fig. 3). System functional block definitions were formulated with lower level nets in a nested way. For example a subnet *instrument_1* is a definition of device 1 and consists of two lower level nets definitions and two processors (Fig. 4). Lower level net represent write (*write_proc*) (Fig. 5) and read (*read_proc*) procedures of IEC-625.1 interface. Those net consist only of processors and places. Processor definition (counterparts of transitions in places and transition net) relies on defining subnets' connections with other level nets and defining, in a special native language, the processor's reaction to an incoming token of a particular colour. According to a given definition *bus_delay_proc* processor (Fig. 6) increases or decreases *number_of_L* variable counter in relation to the value of a token transmitted from a higher level net. It also defines token transition time (*delay* directive) after which the token is transmitted to a place *bus_state_temp* (Fig. 7) without the change of its value. Token value represents the logical state of IEC-625 interface line defined by higher level net. IEC-625 interface synchronisation bus model is defined by *bus* subnet (Fig. 8) and time parameters are determined by *bus_delay* process (Fig. 7), in particular the already mentioned *bus_delay_proc* processor (Fig. 6). All blocks of the modelled system were defined in a similar way.

System model allows a simulation, which permits token animation monitoring and graphically shows the state of interface synchronization lines (Fig. 9). The simulation allows defining system features in normal working conditions as well as critical conditions such as device failure or interface synchronisation bus failure (e.g. line disconnection). The system model permits change of time parameters of particular system elements and as a consequence a change of message transmission times in the system.

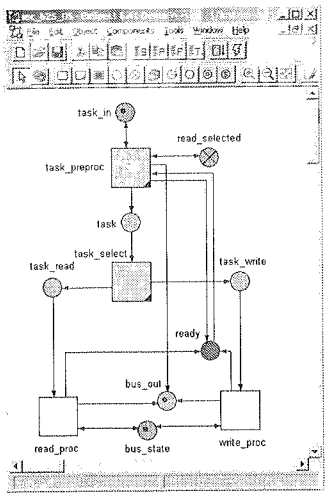

Fig. 4. *Instrument* subnet

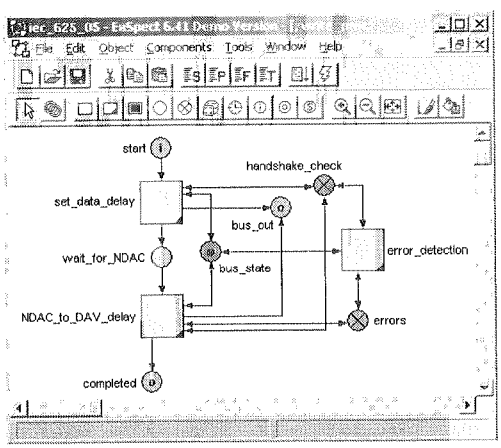

Fig. 5. *write_proc* process

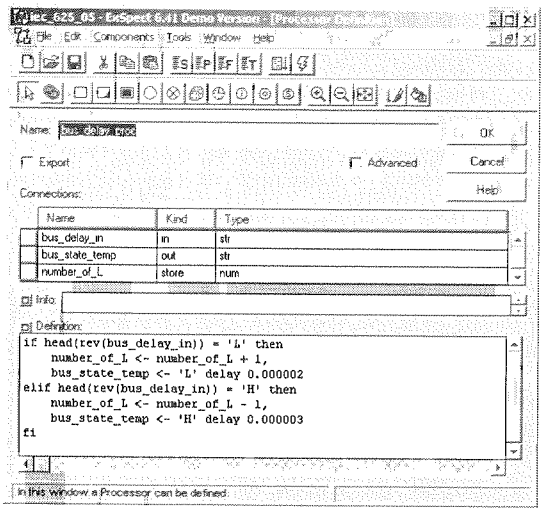

Fig. 6. *bus_delay_proc* processor definition

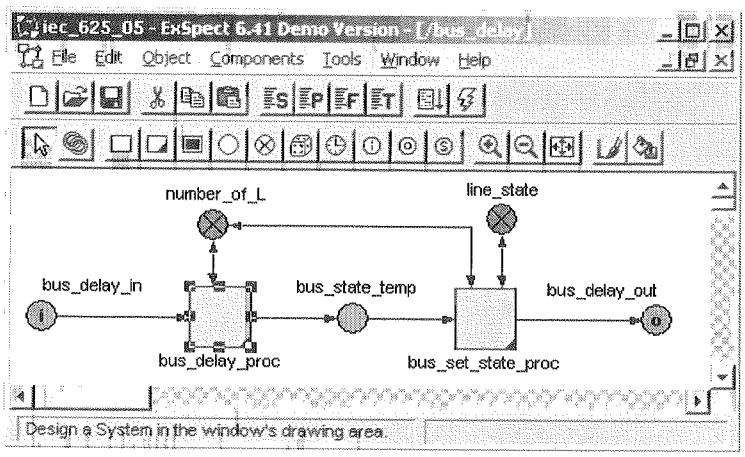

Fig. 7. *bus_dealy* process

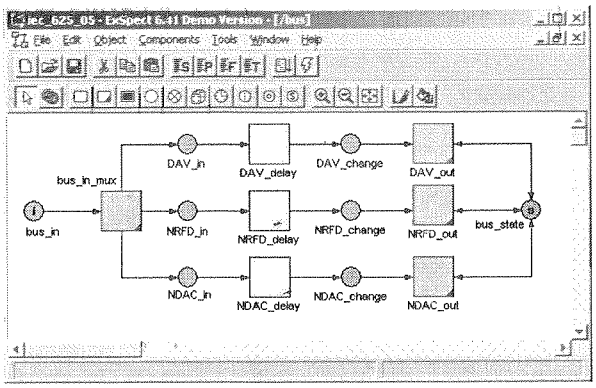

Fig. 8. *bus* subnet

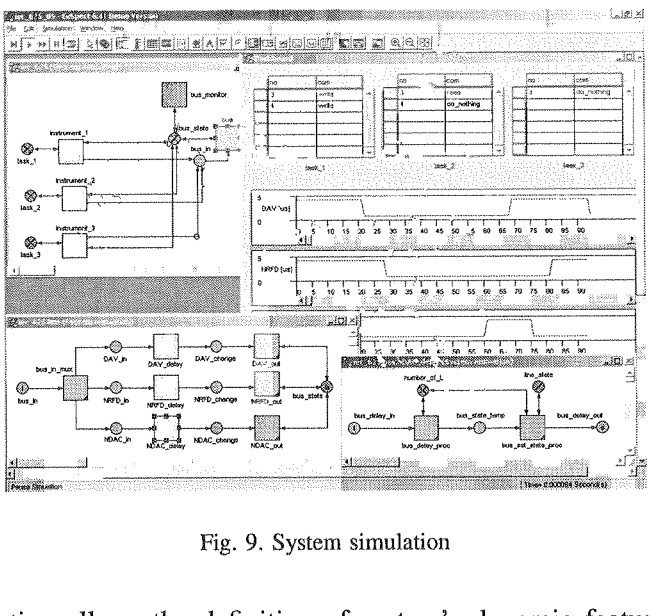

Fig. 9. System simulation

Thus the simulation allows the definition of system's dynamic features according to different time parameters of particular elements.

Unfortunately the authors do not have access to a full version of ExSpecT environment and a limited demo version does not permit to model more complicated systems nor the modelling of systems with a higher level of complexity. Because of the above limitations further research of more complex system modelling will be done using CPN/Tools environment.

5.2.4. MS CREATION METHOD USING PERTI NETS AND CPN/TOOLS TOOL

CPN Tools [28] is a tool for editing, simulating and analysing Coloured Petri Nets. The GUI is based on advanced interaction techniques, such as toolglasses, marking me-

nus, and bi-manual interaction. Feedback facilities provide contextual error messages and indicate dependency relationships between net elements. The tool features incremental syntax checking and code generation, which take place while a net, is being constructed. A fast simulator efficiently handles both untimed and timed nets. Full and partial state spaces can be generated and analysed, and a standard state space report contains information such as boundedness properties and liveness properties.

CPN Tools uses the CPN ML [29] language for declarations and net inscriptions. This language is an extension of a well-known functional programming language, Standard ML (SML), developed at Edinburgh University.

CPN Tools use CPN ML, which is obtained by extending Standard ML in three different ways. The first two extensions make the language easier to use. The third extension is made to be able to define the scope of reference variables. The first extension adds syntactic sugar for colour set declarations. This makes it very easy to declare the most common kinds of colour sets. It also means that the user can include a number of predefined functions, just by mentioning their name in a colour set declaration. The second extension of SML allows the user to introduce typed variables, as a part of the declarations. Instead a value may be bound to a name, and this determines the current type of the name. Later the name may get a new value, and then it gets a new type. It would be possible to use the same strategy for CP-nets. However, we have found it more fruitful to demand that the user explicitly declares the type of each variable. This makes it possible to perform an exhaustive type checking. The third extension allows the user to declare reference variables.

A model of a client-server architecture distributed system model (Fig. 10) was created in CPN/Tools environment. Server part of the modelled system consists of a PC, further called measuring server, with IEC-625 interface card and DAQ data acquisition card installed. HP33120A generator was connected to the IEC-625 interface. A signal from the generator is provided to the input of object under test Q. Signal is measured on the output of the object under test by DAQ acquisition card.

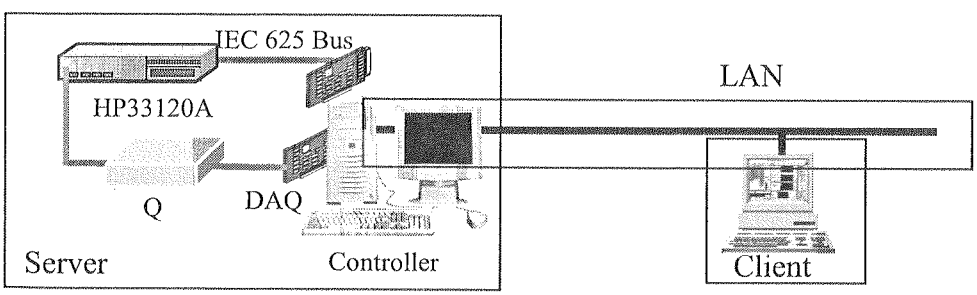

Fig. 10. Diagram of modelled distributed measuring system

The measuring algorithm is based on frequency characteristic Uout = F(f) identification of object under test. Input of the tested object is stimulated with a signal from the generator. Measurement is done by DAQ data acquisition card. Equipment's work

parameters are set by the measuring system's server software. A measuring service, which remotely starts the measuring procedure and provides the client with results, is shared by the server via a computer network. Moreover, the server allows the remote client to change parameters before the proper measuring procedure is started. Client provides the user with the possibility to change the parameters and sends them to the server. Client collects results from the server as they are ready, displays them on user's panel and saves them in the database. Modelled system uses a computer network to transmit data. The exchange of data and messages is assured by DataSocket protocol.

Creating a system model in CPN/Tools environment is based on defining a hierarchical Petri Net describing dynamic properties of system elements. The model uses global timer, timed colours and timed variables. A block view of system description leads to defining a high level model as a supernet *Top* (Fig. 11). The model consists of three high level elements defining client, server and communication medium. The net contains four places defining measuring system server and client network interfaces. System elements in a CPN/Tools model are defined as three substitution transitions associated with the subnets: Client, Network and Server (Fig. 11).

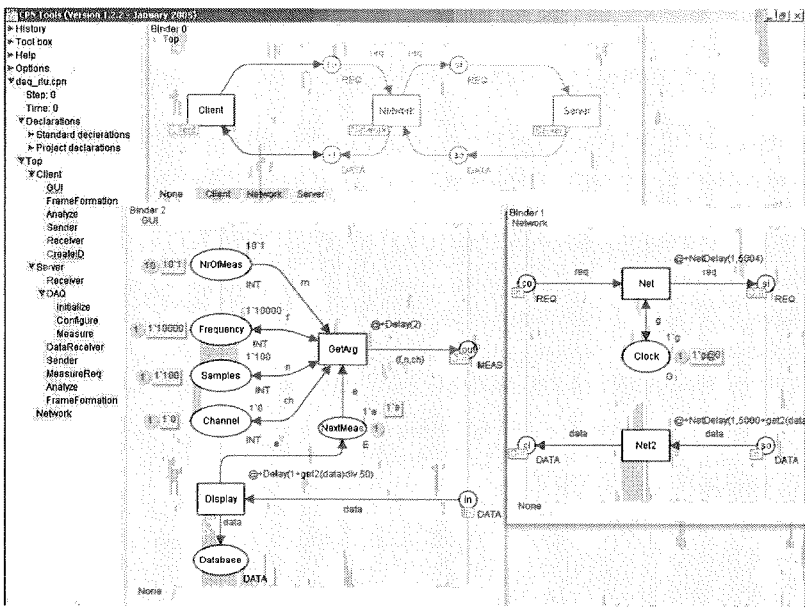

Fig. 11. DMS model in CPN/Tools (supernet *Top*, subnets: *GUI, Network*)

In the described example a very simplified network example is used (*Network* subnet). Message transmission time is defined by probability distribution. The distribution is defined by *NetDelay* function (1). A detailed DataSocket protocol model is a subject of current works.

$$\text{funNetDelay(cl, length)} = 20 + \text{round(erlang(cl} + 1, 1000.0/\text{Real.fromInt(length)))}; \quad (1)$$

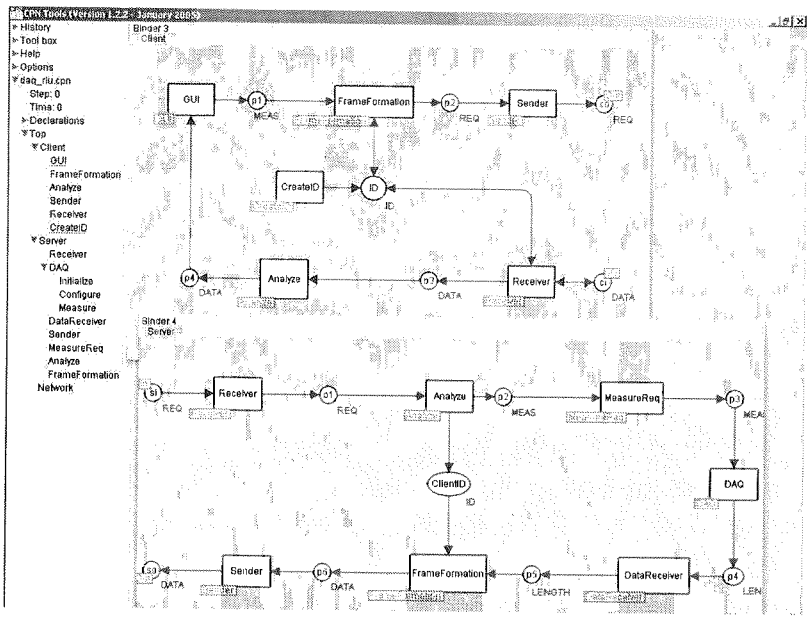

Fig. 12. DMS model in CPN/Tools (subnets: *Server* and *Client*)

where *erlang* is a function for generating values from n-Erlang distributions.
Modelled system's server and client parts are defined by Client and Server subnets (Fig. 12)

Client model (*Client* subnet) contains substitution transitions associated with the following subnets: GUI, *FrameFormation, Analyze, Sender, Receiver* and *CreateID* (Fig. 12). For example graphic user interface model is defined by *GUI* subnet (Fig. 11). The model consists of places related to graphic controls of client's interface. The places in their initial states are stimulated by tokens containing values associated with client's GUI control values. *GetArg* transition sets argument acquisition time from graphical elements using a previously defined Delay function (2).

$$\text{funDelay(i)} = \text{binomial(2*i, 0.5)} \tag{2}$$

where *binomial* is a function for generating values from binomial distributions.

Values of acquired parameters (actual measuring parameters) are transmitted by *out* port to *P1* socket of *Clients* submodel. After the measurement, the measured value is submitted to port *in* by defined variable *data* of a defined colour *DATA*. A diagram on a graphic user interface panel is modelled by *display* place. Measurement result display time is defined as: Delay(1+get2(data)div50). *Database* place symbolises saving data to an external database. A detailed database model will be a subject of further work. The model is limited by the scope of research described in this paper.

Other client measuring system logic blocks were modelled analogously.

System's server part model contains several subnets defining particular elements of this part of the system. For Example *DAQ* subnet (Fig. 13) modelling data acquisition in the system consists of three substitution transitions associated with the subnets: Initialize, Configure, Measure. Another example is *Measure* subnet. It consists of two *ports* assigned to sockets — input and output nodes of the substitution transition in a superpage *DAQ*. Transition modelling measurement time is the third element of *Measure* subnet. The time is defined by *MeasDelay* function (3).

$$\text{MeasDelay}(f, n) = n^*1000 \quad \text{div } f + \text{binomial}(5, 0.5) \tag{3}$$

Remaining measuring system server's logic blocks were modelled similarly. The created system model enables the analysis of the system's dynamic properties with different time parameters of elements of the system. System elements' breakdown simulation and the analysis of system reaction are possible. The model allows defining border parameters of information flow. The simulation enables defining border data acquisition time values with set time parameters of particular system elements. However detailed research requires a more accurate definition of models of some of the system blocks.

It should be stated that the created models being described do not copy the real system elements' parameters. Examples were created to present measuring system elements' modelling methods. Precise parameters, however, can be employed within such models. Time parameters of elements of the model can be taken from catalogue data or elementary events' times evaluated experimentally, such as data acquisition time. Moreover it is possible to develop the presented models by further specifying the model's elements. The specification is possible in the process of sequential decompositions. The creation of a library of such models in particular environments shall be one of the final stages of the research.

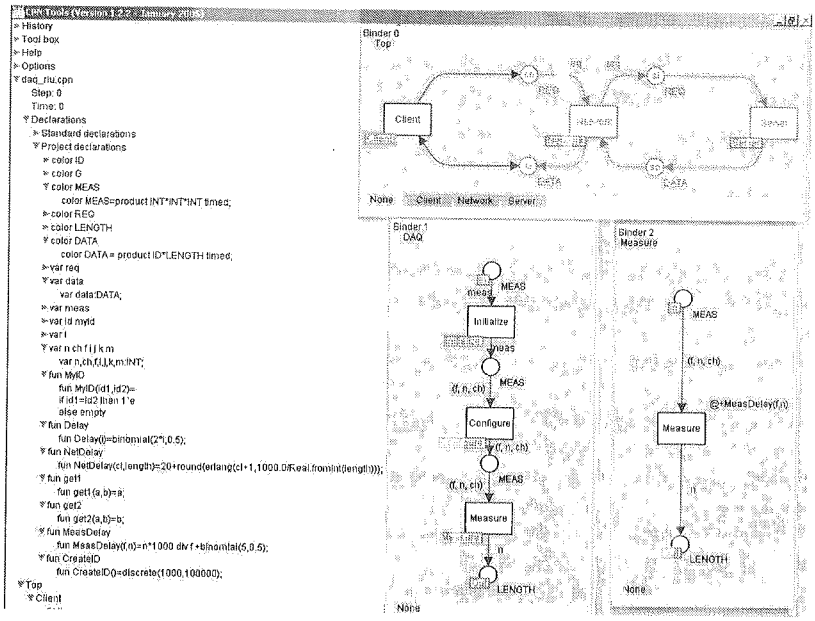

Fig. 13. DMS model in CPN/Tools (subnets: *DAQ* and *Measure*)

6. SUMMARY

Modern formal languages offer the ability of exact demonstration of given properties of systems described by them. In times of high faultlessness of microprocessor equipment and the tendencies to move more and more system components to software the ability to formally assess the correctness of designed system software is gaining more importance. Furthermore a measuring systems design methodology with relation to time dependencies does not yet exist.

Petri Nets enhancements allow modelling of complex systems with time requirements in a consistent way without loosing the details of description. Works and research presented up to date show Perti Nets useful in MS modelling.

Works and research presented so far show Petri Nets useful in MS modelling. The modelling can be employed to predict the necessity of preventing possible breakdowns, which might occur within the system. The thesis on the possibility of simulating the influence of time parameter changes of particular processes or system elements on the functioning of the system as a whole was verified positively. In particular the possibility of defining criteria of MS time limitations based on the model was confirmed.

At the same time the research show that TCPN employment allows the creation of MS with time requirements systematic design methodology. Including TCPN in DMS design can be combined with the use of existing software tools such as ExSpecT or CPN/Tools. However there exists a need to create a library of typical MS models in these environments.

Creation of an as general as possible model of typical distributed measuring systems blocks will be one of the main elements of the research. Eventually a distributed measuring systems design methodology will be formulated. This methodology would use TCPN and an existing software environment together with formulated general DMS element models. Effects of this research will be the subject of future publications.
In the current state of research it can be said that formulating wholly autonomic DMS creation methodology requires the creation of new software tools enabling effective DMS modelling based on TCPN. This kind of tool can be developed until a measuring system specific CASE tool is created

7. REFERENCES

1. G. Booch, J. Rumbaugh, I. Jacobson: *UML przewodnik użytkownika*, WNT, Warszawa, 2001.
2. G. Bucci, E. Vicario: *Compositional Validation of Time-Critical Systems Using Communicating Time Petri Nets*, IEEE Transactions on Software Engineering, Vol. 21, No. 12, December 1995, 969-992.
3. J. Carlson: *Languages and Methods for Specifying Real- Time Systems*, MRTC (Malardalen Real-Time Research Center), Technical Report, August 2002.
4. A. Cerone, A. Maggiolo-Shettini: *Time-Based Expressivity of Time Petri Nets for System Specification*, Theoretical Computer Science, Vol. 216, 1999, pp. 1-53.
5. A. M. K. Cheng: *Real-Time Systems, Scheduling, Analysis, and Verification*, John Wiley & Sons 2002.
6. B. P. Douglass: *Doing Hard Time, Developing Real- Time Systems with UML, Objects, Frameworks, and Patterns*, Addison-Wesley, 1999.
7. M. Felder, D. Mandrioli, A. Morzenti: *Proving Properties of Real-Time Systems Through Logical Specifications and Petri Net Models*, IEEE Transactions on Software Engineering, Vol. 20 No. 2, February 1994, 127-141.
8. M. Felder, M. Pezze: *A Formal Design Notation For Real-Time Systems*, ACM Transactions on Software Engineering and Methodology, Vol. 11, No. 2, April 2002, 149-190.
9. H. Gomaa: *Designing Concurrent, Distributed, and RT Applications with UML*, Addison-Wesley 2000.
10. H. M. Hanisch: *Analysis of Place/Transition Nets with Timed Arcs and its Application to Batch process Control*, LNCS Vol. 691, Springer- Verlag, 1993, 282-299.
11. HOOD Technical Group: *HOOD Reference Manual, Release 4.0*, June 1995.
12. A. Jaszkiewicz: *Inżynieria oprogramowania*. HELION, Gliwice, 1997.
13. K. Jensen: *Coloured Petri Nets, Basic Concepts, Analysis Methods and Practical Use*, Vol. 1-3, Springer, 1996.
14. E. Y. T. Juan, J. J. P. Tsai, T. Murata, Y. Zhou: *Reduction Methods for Real-Time Systems Using Delay Time Petri Nets*, IEEE Transactions on Software Engineering, Vol. 27, No. 5, May 2001, 422-448.
15. R. Klimek: *Zastosowanie logiki temporalnej w specyfikacji i weryfikacji oprogramowania — w stronę czasu rzeczywistego*, VII Konferencja Systemy Czasu Rzeczywistego, Kraków, 25-28 września 2000, Wykłady Zaproszone, Kraków, 2001, 63-115.
16. Object Management Group: *OMG UML Specification, Version 1.5*, March 2003, http://www.omg.org.
17. http://www.daimi.au.dk/PetriNets, *Petri Nets World Web Pages*, January 2005.

18. A. Platonov, W. Winiecki: *Statistical synthesis and optimal decomposition in intelligent monitoring systems design*, Computer Standards & Interfaces 24, 2002, 101-110.
19. K. Sacha: *Projektowanie oprogramowania systemów wbudowanych*, Politechnika Warszawska, Prace Naukowe Elektronika z. 115, Oficyna Wydawnicza Politechniki Warszawskiej, Warszawa, 1996.
20. K. Sacha: *Projektowanie oprogramowania systemów sterujących*, Oficyna Wydawnicza Politechniki Warszawskiej, Warszawa, 1996.
21. T. Szmuc: *Modele i metody inżynierii oprogramowania systemów czasu rzeczywistego*, Uczelniane Wydawnictwa Naukowo Dydaktyczne AGH, Kraków, 2001.
22. T. Szmuc: *Zaawansowane metody tworzenia oprogramowania systemów czasu rzeczywistego*, Krakowskie Centrum Informatyki Stosowanej, Kraków, 1998.
23. T. Szmuc, S. Oskwarek: *Projektowanie poprawnego oprogramowania czasu rzeczywistego wspomagane formalizmem algebry procesów*, VII Konferencja Systemy Czasu Rzeczywistego, Kraków, 25-28 września 2000, 109-124.
24. B. Trybus: *Zagadnienia czasowe w modelowaniu strukturalnym i ich konwersja do czasowych sieci Petriego*, VIII Konferencja Systemy Czasu Rzeczywistego, Krynica, 24-27 września 2001, 93-103.
25. E. Vicario: *Static Analysis and Dynamic Steering of Time- Dependent Systems*, IEEE Transactions on Software Engineering, Vol. 27, No. 8, August 2001, 728-748.
26. http://vl.fmnet.info/, *Virtual Library formal methods pages*, November 2004.
27. W. Winiecki, J. Nowak, S. Stanik: *Graficzne Zintegrowane Środowiska Pomiarowe*, MIKOM, Warszawa, październik 2001.
28. http://www.daimi.au.dk/CPNTools/, *CPN Tools home page*, May 2005.
29. http://www.standardml.org/, *The web page for the Standard ML SourceForge project*, May 2005.

R. ŁUKASZEWSKI, W. WINIECKI

WYKORZYSTANIE SIECI PETRIEGO W PROJEKTOWANIU SYSTEMÓW POMIAROWYCH

Streszczenie

Zasady projektowania systemów pomiarowo-kontrolnych (SPK) w chwili obecnej mają charakter heurystyczny. Wzrost złożoności oprogramowania SPK sprawia, że zwykle nie jest możliwe przeprowadzenie wyczerpującego testowania a poprzestaje się na sprawdzeniu najważniejszych przypadków testowych. Istnieje, zatem potrzeba przeprowadzenia badań zmierzających do opracowania metodyki efektywnego zastosowania metod formalnych do analizy, specyfikacji i wspomagania projektowania oprogramowania SPK (w tym rozproszonych — RSPK) z wymaganiami czasowymi.

Współczesne języki formalne (JF) opisu systemów znajdują coraz szersze zastosowanie w rozwiązywaniu wielu zagadnień związanych z wytwarzaniem oprogramowania, umożliwiają wykazanie zgodności opisu systemów [7], udowodnienie kluczowych właściwości systemu [13], pozwalają na wykazanie spełnialności ograniczeń czsowych w systemach [2, 25]. Na uwagę zasługują: czsowe algebry, rozszerzenia logik temporalnych [5, 15] oraz czsowe sieci Petriego (TPN) [2, 3, 4, 10, 13, 14, 19], w tym sieci wysokiego poziomu [5] oraz kolorowane sieci Petriego [13, 21, 22].

Efektywne włączenie JF do metodyki wytwarzania oprogramowania SPK (w tym RSPK) z ograniczeniami czasowymi może się odbyć poprzez wybranie JF i jego zastosowanie w niektórych etapach procesu wytwarzania w metodzie inżynierskiej. Możliwe jest również sformułowanie autonomicznej metodyki projektowania wykorzystującej wybrany JF.

W artykule przedstawiono przykład wykorzystania środowiska ExSpecT do stworzenia prostego modelu SPK i jego analizy. Modelowany SPK składa się z kontrolera IEC-625 oraz dołączonych do

niego trzech urządzeń (rys. 1). Model systemu umożliwia symulację, która pozwala obserwować animację znaczników oraz w sposób graficzny pokazuje stan linii synchronizacji interfejsu (rys. 9). Symulacja poxwala na określenie właściwości systemu wwarunkach pracy normalnej, jak też w warunkach krytycznych (awaria urządzeń lub szyny synchronizacji interfejsu). Model umożliwia zmiany parametrów czsowych poszczególnych elementów systemu a w konsekwencji zmiany czasów transmisji komunikatów w systemie. Symulacja pozwala, więc na określenie właściwości dynamicznych systemu przy różnych parametrach czasowych poszczególnych elementów.

W artykule opisano również stworzony model RSPK (rys. 10) o architekturze klient-serwer w środowisku CPN/Tools. Serwer pomiarowy modelowanego systemu składa się z komputera PC z kartą interfejsu IEC-625, kartą akwizycji danych DAQ oraz dołączonego generatora HP33120A. Sugnał z generatora odawany jest na wejście badanego obiektu Q. Pomiary sygnału na wyjściu badanego obiektu dokonywany jest za pomocą karty akwizycji. System wykorzystuje sieć komputerową oraz protokół DataSocket do transmisji danych i komunikatów. Zbudowany model systemu pozwala na analizę właściwości dynamicznych systemu przy różnych wartościach parametrów czsowych elementów systemu. Możliwa jest symulacja i analiza awarii elementów systemu. Model pozwala określić graniczne parametry czsowe przepływu informacji oraz wyznaczenie granicznych wartości szybkości akwizycji danych pry zadanych ustalonych parametrach czasowych elementów systemu.

Przeprowadzone symulacje wykazały celowość modelowania SPK z wykorzystaniem TPN i istniejących narzędzi programowych. W szczególności potwierdzono możliwość określenia krytycznych ograniczeń czasowych SPK na podstawie modelu. Włączenie TPN do projektowania RSPK może odbywać się z wykorzystaniem istniejących narzędziprogramowych, takich jak ExSpecT lub CPN/Tools.

Słowa kluczowe: systemy pomiarowe, metody formalne

KWARTALNIK ELEKTRONIKI I TELEKOMUNIKACJI, 2005, 51, ZESZYT SPECJALNY, ss. 159–171

Bitratecontrol algorithm for video coding with regions of interest

ADAM PIETROWCEW, ANDRZEJ BUCHOWICZ, WŁADYSŁAW SKARBEK

Institute of Radioelectronics,
ul. Nowowiejska 15/19, 00-665 Warsaw
{A.Pietrowcew, A.Buchowicz, W.Skarbek}@ire.pw.edu.pl

The bit-rate control algorithm for video sequence encoding with Region Of Interest (ROI) is presented in this paper. The algorithm distributes available bit budget among image layers taking into consideration both the distance from ROI and the local complexity. It improves the image quality in ROI by lowering the image quality outside ROI with the preservation of the global constraint of the encoded stream bit-rate. The algorithm also ensures the gradual image quality degradation outside ROI.

Keywords: video coding, vate control, H.264/AVC

1. INTRODUCTION

The trade-off between compression ratio and the quality of the reconstructed signal is the main issue in a video coding. It is obvious that better quality can be achieved with smaller compression ratio and higher encoded stream bit-rate. The optimal coder control, that is the selection of appropriate set of coding parameters, that will guarantee the demanded bit-rate with minimal lost in fidelity of the reconstructed video sequence requires the knowledge of the rate-distortion (R-D) model for the particular coding scheme. The R-D model is usually build in such a way that the quality of the whole frames in a video sequence is taken into account. However in many applications, e.g. video monitoring and surveillance, telemedicine, videophone and video conferencing some areas in the consecutive frames of the video sequence are more important than others. It is desirable to encode those areas, called region of interest (ROI) with smaller distortion than the rest of the sequence (background).

Such feature is available in a natural way in object-based video coding algorithms introduced by the MPEG-4 standard [1, 2], since all objects, including those belonging to the ROI, are encoded independently from the others. It can also be realized by bit-plane shifting in frame-based algorithms with bit-plane coding e.g., in MPEG-4

FGS [1]. The modified rate-control algorithm is required for the traditional frame-based video coding techniques in order to ensure ROI encoding. Several solutions to this problem have been presented in the literature. The dynamic sub-window skipping method for multipoint video conferencing has been proposed in [3]. ROI enabled MC-DCT algorithm based on standard MPEG-1 encoder has been described in [4]. Bit allocation strategies allowing bit budget transfer from background to foreground to be used with H.261 encoder have been presented in [5]. Another approach with two separate DCT-based encoders for robust wireless video transmissions have been discussed in [6]. A fuzzy logic control algorithm for quantization parameter adjustment on the macroblock basis has been presented in [7]. The ROI functionality has also been proposed [8] for the emerging Scalable Video Coding standard [9].

The algorithm presented in this paper is based on the linear rate-distortion(R-D) model in ρ-domain [10]. It distributes the available bit budget among level sets in the encoded frame taking into consideration both their distance from ROI and local image complexity. ROI is encoded with higher bit-rate ensuring better image quality and the image quality gradually decreases outside ROI. The algorithm has been integrated and tested with the H.264/MPEG-4AVC [11] reference software [12].

1.1. INEAR R-D MODEL IN THE ρ- DOMAIN

The video coding process can be divided into following steps (Fig. 1):

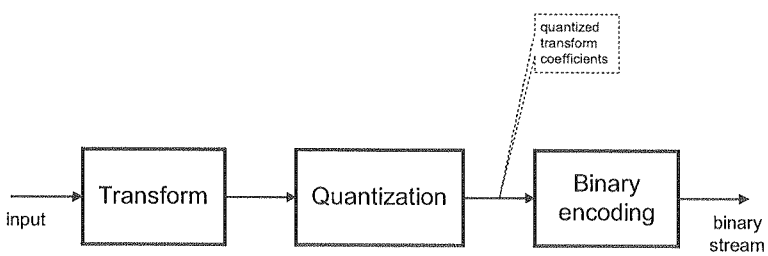

Fig. 1. General transform coding system

— **Transform coding:** input signal samples are transformed into a transform coefficients. This step decorrelates the input samples and concentrate the signal energy in a small number of transform coefficients. The Discrete Cosine Transform (DCT) or Discrete Wavelet Transform (DWT) are usually used.
— **Quantization:** transform coefficients are replaced by their approximate values. Small coefficients are eliminated in this step, i.e. are equal zero after quantization. The strength of the quantization is controlled by a parameter (usually denoted by q) representing the number of quantization levels or the distance between these levels (quantization step)

— **Binary encoding:** symbol sequences are replaced by bit sequences. The Huffman coding or arithmetic coding are most often used

The encoding bit-rate R and distortion D are expressed in terms of quantization parameter q in a conventional R-D analysis. The knowledge of $R(q)$ and $D(q)$ functions, called R-D model, is necessary in all rate control algorithms. The exact, analytical formula for R-D functions can be found only for data sources with simple statistical model. In practical applications like image or video coding approximate R-D model derived from the empirical data must be used. He and Mitra in [10] proposed a new R-D model in which fraction of zeros among quantized transform coefficients, denoted by ρ, is used instead of quantization parameter q. It has been shown [10] that in standard video coding systems the bit-rate R is a linear function of ρ:

$$R(\rho) = \theta \cdot (1 - \rho) \tag{1}$$

The context in which ρ is computed depends on the data source encoding options. It can be defined for frames or basic units of type I, P and B in one dimension or in color components Y, C_b, C_r correspondingly. In presented method such context was defined for P frames and color component.

The slope θ is modeled on the basis of the previous context and given by the formula:

$$\theta = \frac{r_{prev}}{1 - \rho_{prev}} \tag{2}$$

Parameters r_{prev} and ρ_{prev} denote the bit-rate and zero fraction in the previous context, respectively.

Such a modeling scheme makes application of ρ- domain methodology impractical for I type frames as time interval between them is large. Thus the scene view can change drastically during this period and the slope θ calculated for the previous frame of this type can be inadequate for the current frame encoding.

The mapping from ρ to quantization index q is straightforward, having lookup table build on the basis of histogram for zero quantized coefficients obtained for all possible indices q. While model parameter θ depends strongly on the local data, the relationship between ρ and q is less dependent on the data prediction errors.

The experimental results for the MPEG-4 AVC/H.264 encoder confirming the above linear R-D model have been presented in [13]. The linear R-D model in ρ-domain has also been used for statistical multiplexing of compressed video bitstreams [14] and low bit rate video streaming [15].

2. ROI ENABLED BITRATE CONTROL

ROI in the encoded sequence can be defined as one connected area or a set of connected components [16]. It is composed of macroblocks for which at least one pixel intersects with ROI (Fig. 2). Let us denote all such macroblocks by L_1. Then

we can define level sets L_i (for $i>1$) as sets of macroblocks which are 8-neighbors of macroblocks in L_{i-1} and are not included in L_j for all $j<i$. These level sets are further characterized by $N_i = |L_i|$ — number of macroblocks on the given level set, ρ_i — zero fraction on L_i and r_i — bit-rate for L_i. The number of level sets will be denoted by i_{max}, we used the fixed value of $i_{max}=4$ in all our experiments.

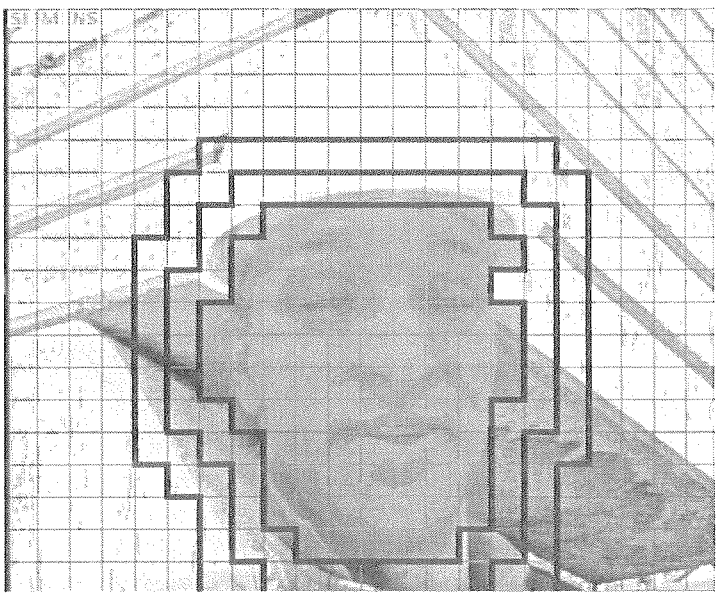

Fig. 2. Level sets in the first frame of the *Foreman* sequence

In order to distribute bit budget allocated for the frame by ρ -domain algorithm, we decided to increase the fraction of zeros ρ_i in consecutive level sets L_i by $\Delta\rho \cdot \gamma_i$ such that:

$$\rho_i = \rho_{i-1} + \Delta\rho \cdot \gamma_i \quad i = 2...i_{\max} \tag{3}$$

where

$$\gamma_i = \begin{cases} \sqrt{1 + \dfrac{\mathrm{var}_a - \mathrm{var}_i}{\mathrm{var}_a}} & \text{if } \mathrm{var}_1 > \mathrm{var}_a \\ 1.0 & \text{if } \mathrm{var}_1 \leqslant \mathrm{var}_a \end{cases} \tag{4}$$

In the equation (4) var_i denotes the image signal variance on the level set L_i and var_a is the whole frame variance. The variance is calculated on motion compensated image and gives us information about image complexity on consecutive level sets.

Assuming that global frame bit-rate is distributed to the level sets L_i proportionally to their sizes we have:

$$r = \sum_{i}^{i_{\max}} w_i r_i \tag{5}$$

$$\rho_1 = 1 - \frac{r}{\theta} - \Delta\rho \sum_{i=2}^{i_{\max}} \left(w_i \sum_{j=1}^{i} \gamma_j \right) \tag{6}$$

where $w_i = \frac{N_i}{N}$, N is the number of all macroblocks in a frame and r denotes the bit-rate (in bits per pixel) for the frame.

Hence for the fixed $\Delta\rho$ we compute ρ_1 by the formula (6) and next ρ_i for all $i > 1$ using (3). Having ρ_i for $i = 1..i_{max}$ we can execute further steps of ρ-domein algorithm which include extraction of the quantization index q_i from look-up table $\rho[q]$, establishing the encoding mode for all macroblocks and model updating.

Value of ρ_i on all level sets except ROI is modified by γ_i, which is equal to 1.0 when the variance of ROI signal is below or equal to the variance of the whole frame and is greater then 1.0 in other cases. Such formulation causes that quantization index q_i on a level set L_i ($i > 1$) increases more if the ROI is more complex than rest of the image. We can cut bits from background area and allocate more to ROI as not very complex signal generates lower error in PSNR sense during reconstruction.

Value of $\Delta\rho$ in all our initial tests was treated as the input parameter of ROI encoding algorithm. It was usually arbitrary chosen from the range [0.0125, 0.025]. In this paper we propose a methodology of automatic generation of $\Delta\rho$ value.

For this purpose histograms of zero quantized coefficients obtained for all possible indices q on all level sets are needed. Let's denote them as $H_1, ..., H_{i_{\max}}$. At the initial stage of our algorithm we look for a quantization index q_F for the whole frame, not considering ROI bit budget allocation at all, using only equations (1), (2). Then we select among all level sets one with the lowest ($L_{i_{vl}}$) and one with the highest variance ($L_{i_{vh}}$). Having quantization index q_F for the frame we find on histograms $H_{i_{vl}}$ and $H_{i_{vh}}$ values of ρ_{vl} and ρ_{vh} corresponding to it. Parameter $\Delta\rho$ can be set as $\Delta\rho = |\rho_{vl} - \rho_{vh}|$. However, in order to limit too drastic changes in PSNR between ROI level sets we additionally limit $\Delta\rho$:

$$\Delta\rho = \max\left(\min\left(|\rho_{vl} - \rho_{vh}|, 1 - \rho_F\right), 0.025\right) \tag{7}$$

where ρ_F is the estimated percentage of insignificant transform coefficients for the current frame.

The proposed ROI bit allocation scheme works well on P frames. For I frames similar technique as in JVT-G012 [17] proposal was applied. On each level set L_i we calculate a sum S^i_{pq} of quantization indices q_i for all P frames in a group of pictures (GOP). Then quantization indices for ROI level sets on I frame in a given GOP were calculated using formula:

$$q_i = \frac{S^i_{pq}}{N_p} - \min\left(2, \frac{N_{gop}}{15}\right) \tag{8}$$

where N_p denotes the number of P frames in the previous GOP and N_{gop} is the size of GOP. Also the change between the current I type frame quantization index and the previous one on the appropriate level set should not be greater then 2.

The same methodology as for P frames can be applied to B type frames. However, conducted experiments showed drawbacks of such approach. In the B type frames vast amount of macroblocks is encoded using motion vectors where resulting coefficients are all equal to zero after DCT transform and quantization. Sometimes, B frames occur with all coefficients equal to zero, and these extreme results cause ρ-model inconsistency. Therefore for B frames the solution inspired by the JVT-G012 algorithm is proposed in this work. For consecutive B frames in a sequence level sets L_i are defined in a similar way as for P frames. Values of quantization indices on ROI level sets L_i are then determined on the basis of corresponding quantization indices for level sets on surrounding P frames. One of the surrounding frames could be of type I at the GOP start, so in such case quantization indices from level sets on this frame are used instead.

The formula for determining quantization indices values on B frames is given below:

$$q_{B,i}^{k} = \begin{cases} \frac{1}{2}\left(q_i^{k_{prev}} + q_i^{k_{next}} + 2\right) & if\, q_i^{k_{prev}} \neq q_i^{k_{next}} \\ q_i^{k_{prev}} & otherwise \end{cases} \tag{9}$$

where k is the B frame index, k_{prev}, k_{next} are indices of the closest two P/I frames and i is the level set number.

In the proposed scheme there is no direct allocation of bits for B frames. Bit-rate control algorithm is based mainly on P frames complexity and estimations on the supposed bit budget for the following B frames.

The described ROI bit budged allocation scheme based on consecutive increase of zero fraction by $\Delta\rho \cdot \gamma_i$ takes into account image complexity. This complexity is measured as frame pixels variance after motion compensation. The scheme gives better results for images in which ROI is more complex than the rest of the image. But in images in which ROI is less complex than background, taking into account the image complexity, caused rather equalization of PSNR on all level sets. So in such case we decided to increase ρ_i by constant $\Delta\rho$ in order to preserve higher quality on ROI and gradually lower quality on level sets with increased distance from the ROI area.

3. EXPERIMENTAL RESULTS

The proposed algorithm was evaluated on several standard test sequences. The ROI definitions were loaded to the encoder from external files. These files were created manually by test sequence browsing. The GOP composed of 30 frames with two B frames between I/P frames were used. The algorithm works correctly on all sequences recorded with CIF and QCIF resolutions and at different bit- rates. The required bit-rate is with very high accuracy preserved for all GOPs in test videos while at the same time quality of ROI region is better with respect to the original JVT-G012 implementation in JM 8.2 [12]. Figure 3 presents PSNR measures for the *Foreman* sequence encoded with the proposed bit allocation algorithm. The results for the JM 8.2 with JVT-G012

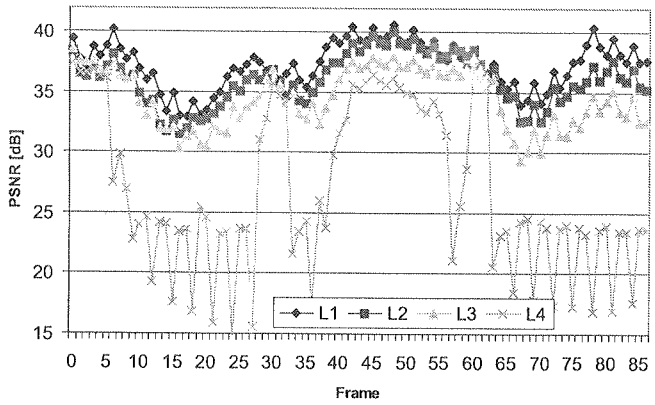

Fig. 3. Experimental results for the proposed algorithm with automatic $\Delta\rho$ calculation; test sequence — *Foreman CIF*, bitrate 312 kbit/s

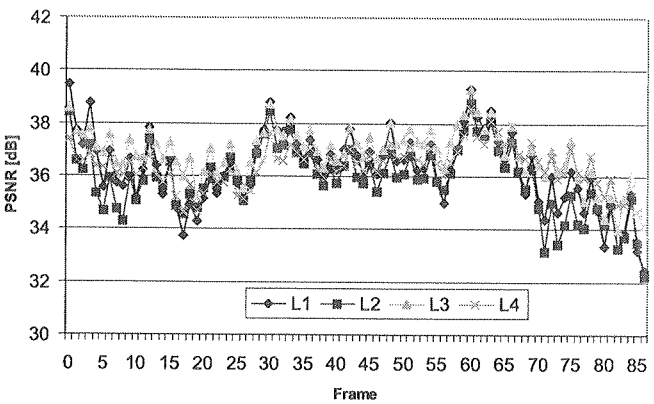

Fig. 4. Experimental results for the original JM 8.2; test sequence — *Foreman CIF*, bitrate 312 kbit/s. The PSNR values were calculated for macroblock collections $L_1, ..., L_4$ used as level sets in the proposed ρ-domain algorithm

algorithm are presented in Fig. 4. The PSNR values for the JM 8.2 were calculated in the same macroblock sets as level sets defined for the proposed ρ-domain algorithm. Comparing two diagrams, we can observe, that PSNR measure on ROI region is more stable for bit allocation method working in ρ- domain. Also quality of ROI region is better for almost all frames by more than 1.5 dB.

Quality on level sets L_1 and L_2 is comparable in both implementations. Only on the last level set quality in JM 8.2 is better than in ROI ρ-domain algorithm, where more bits were allocated to the area of interest. We proposed to divide all macroblocks into level sets in our bit allocation algorithm to avoid strong quality change on the border between interest region and rest of the image. Such solution allows gradually decreasing quality on consecutive level sets lying farther from ROI. It's clearly visible

that quality on L_2 is almost always slightly below that on L_1 for *Foreman* sequence (Fig. 3) and quality on consecutive level sets is lower than on previous ones. This allows smooth transition from ROI with highest quality to the background.

The above observation is even more evident if we look at the *News* test sequence, for which encoding results are presented on Fig. 5.

In comparison to the results of original JM 8.2 algorithm (Fig. 6) PSNR measure on ROI (Fig. 7) was increased by almost 5 dB.

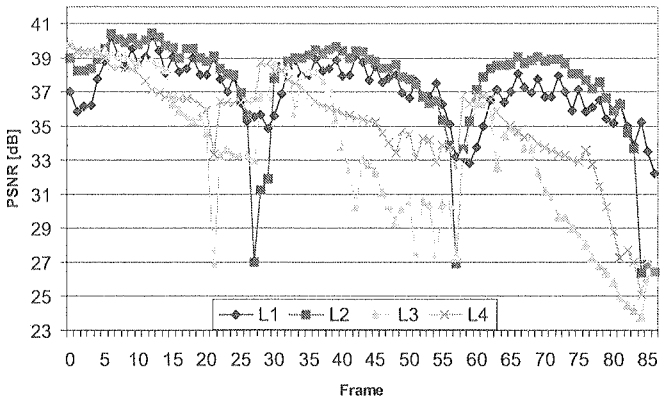

Fig. 5. Experimental results for the proposed algorithm with automatic $\Delta\rho$ calculation; test sequence — *News CIF*, bitrate 192 kbit/s

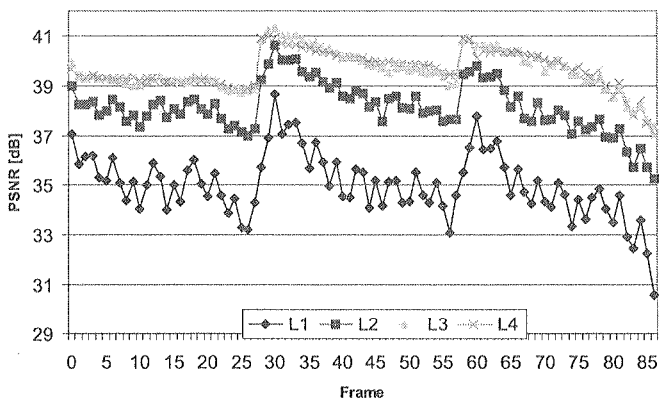

Fig. 6. Experimental results for the original JM 8.2; test sequence — *News CIF*, bitrate 192 kbit/s. The PSNR values were calculated for macroblock collections $L_1, \ldots, L_4$ used as level sets in the proposed ρ-domain algorithm

On the *Mobile & Calendar* sequence quality difference between proposed method and the original JVT implementation is most visible in the defined ROI if we encoded it at low bit-rate (Fig. 8, 9).

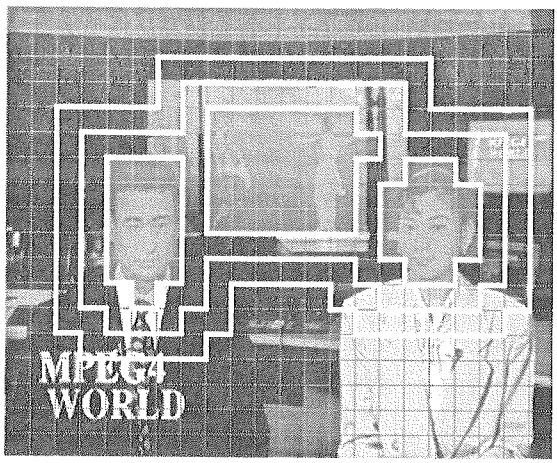

Fig. 7. ROI definition in the first frame of the *News* sequence

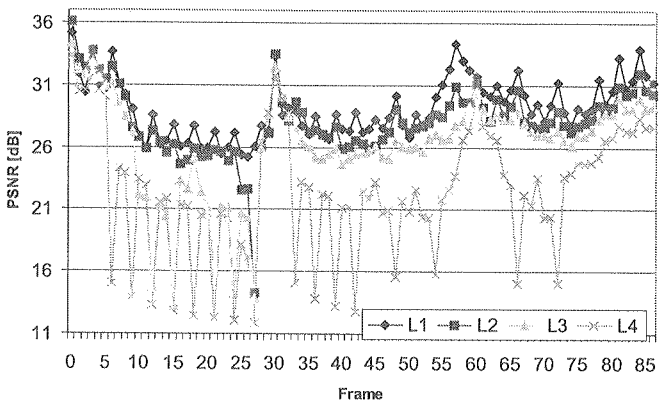

Fig. 8. Experimental results for the proposed algorithm with automatic $\Delta\rho$ calculation; test sequence — *Mobile & Calendar CIF*, bit-rate 356 kbit/s

The ROI which was defined on a calendar (Fig. 10) remains readable even with the bit-rate of 80 kbit/s what is not possible to achieve for the whole frame encoding implemented in JM 8.2. Average bit-rate for all GOPs (309.30 kbit/s) is below the desired value (312 kbit/s) in the ρ-domain method, while it is slightly above (313.87 kbit/s) in the case of the JM 8.2.

Table 1 compares the performance of the proposed algorithm with the performance of the original JM 8.2. It contains PSNR values on level sets averaged over the whole test sequences. Results for *Foreman, News* and *Mobile & Calendar* are presented. Each sequence contained 90 frames. For all sequences the quality on ROI (level set L_1), is better by more then 1 dB in relation to the original JM 8.2/JVT-G012 proposal. This quality improvement in ROI is controlled by the value of the $\Delta\rho$ parameter. Greater

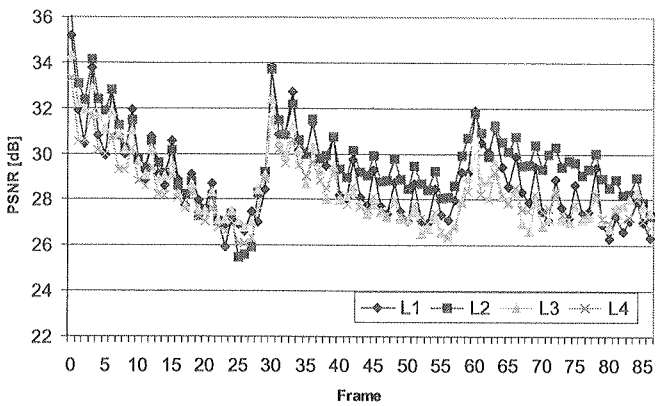

Fig. 9. Experimental results for the original JM 8.2; test sequence — *Mobile & Calendar CIF*, bit-rate 356 kbit/s. The PSNR values were calculated for macroblock collections $L_1, ..., L_4$ used as level sets in the proposed ρ-domain algorithm

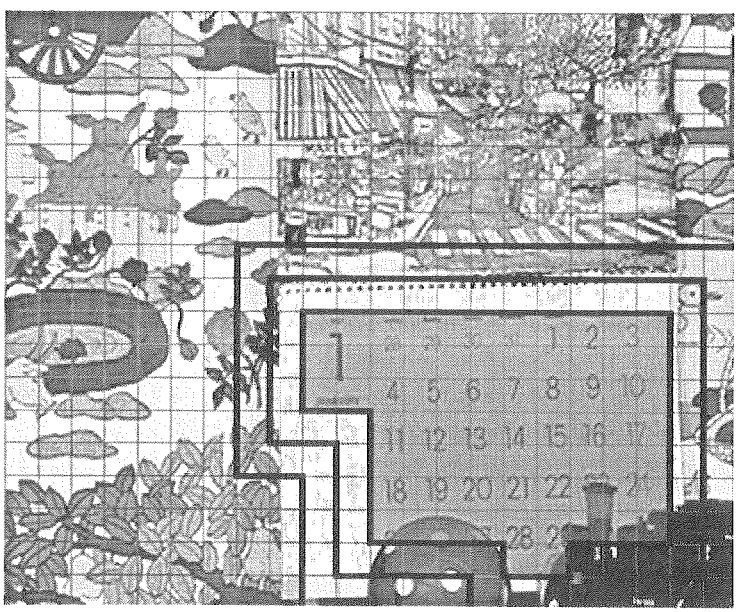

Fig. 10. ROI definition in the first frame of the *Mobile & Calendar* sequence

$\Delta\rho$ values give better quality in ROI, which decreases smoothly on macroblocks laying farther from the defined area of interest.

Table 1

Averaged PSNR (in dB) on level sets in the proposed ρ-domain algorithm and the original JM 8.2

Sequence	Level set	JM-8	ρ-domain	ρ-domain with automatic $\Delta\rho$ calculation)
Foreman 312 kb/s IBBP	L_1	36.28	37.33	37.31
	L_2	35.89	36.26	36.06
	L_3	36.89	34.95	34.52
	L_4	36.38	29.23	26.94
News 192 kb/s IBBP	L_1	35.02	36.49	37.05
	L_2	38.15	37.64	37.46
	L_3	39.64	34.12	33.34
	L_4	39.66	35.46	35.15
Mobile & Calendar 356 kb/s IBBP	L_1	28.93	28.96	29.18
	L_2	29.66	27.89	28.10
	L_3	28.54	25.76	26.20
	L_4	28.24	22.70	22.45

The algorithm described in this paper also outperforms the algorithm presented in our previous paper [18]. By taking into consideration the local image complexity we have improved the increase of the PSNR in the ROI for the *News* video sequence by approximately 0.7 dB.

4. CONCLUSIONS

The algorithm presented in this paper guarantees higher quality of the reconstructed video in the ROI and gradual video quality degradation outside the ROI. The available bit budget was distributed among level sets in the consecutive frames by increasing the fraction of zero quantized coefficients by a constant value multiplied by the factor depending on the local image complexity. Taking into consideration the image complexity in the bit budget distribution allowed to improve the algorithm performance when the complexity of ROI is higher than the complexity of the background.

5. ACKNOWLEDGEMENT

The work presented was developed within VISNET, a European Network of Excellence (http://www.visnet-noe.org), funded under the European Commission IST FP6 programme.

6. REFERENCES

1. ISO/IEC 14496-2:2004: *Information Technology — Coding of Audio-Visual Objects — Part 2: Visual*, 3rd Edition, 2004.
2. F. Pereira, T. Ebrahimi, eds.: *The MPEG-4 Book*, Prentice Hall, 2002.
3. Ch-W. Lin, Y-Ch. Chen, M-T. Sun: Dynamic Region of Interest Transcoding for Multipoint Video Conferencing, *IEEE Transaction on Circuits and Systems for Video Technology*, pp. 982-992, Vol. 13, No. 10, October 2003.
4. N. Doulamis, A. Doulamis, D. Kalogeras, S. Kollias: Low Bit-Rate Coding of Image Sequences Using Adaptive Regions of Interest, *IEEE Transaction on Circuits and Systems for Video Technology*, pp. 928-934, Vol. 8, No. 8, December 1998.
5. D. Chai, K.N. Ngan, A. Bouzerdoum: "Foreground/Background Bit Allocation for Region-of-Interest Coding," *Int. Conf on Image Processing 2000 (ICIP 2000)*, 10-13 September, 2000, Vancouver, Canada.
6. A. Ch.-W. Wong, Y.K. Kwok: "On a Region-of-Interest Based Approach to Robust Wireless Video Transmission", *Proc. of the 7th Int. Symp. on Parallel Architectures, Algorithms and Networks (ISPAN'04)*, May 10-12, 2004, Hong-Kong, China.
7. M.-Ch. Chi, M.-J. Che, Ch.-T. Hsu: "Region-of- Interest Video Coding by Fuzzy Control for H.263+ Standard", *2004 IEEE Int. Symp. on Circuits and Systems (ISCAS 2004)*, May 23-26, 2004, Vancouver, Canada.
8. W-H. Peng: "Adding Selective Enhancement Functionality to Scalable Video Coding", *Joint Video Team of ISO/IEC MPEG & ITU-T VCEG*, JVT-O020, Busan, Korea, April 2005.
9. J.Reichel, H.Schwarz, M.Wien: "Working draft 1.0 of 14496-10:200x/AMD1 scalable video coding", *ISO/IEC JTC1/SC29/WG11*, N6901, Hong Kong, China, 2005.
10. Z. He, S.K. Mitra: "A Unified Rate-Distortion Analysis Framework for Transform Coding", *IEEE Transaction on Circuits and Systems for Video Technology*, pp. 1221-1236, Vol. 11, No. 12, December 2001.
11. ISO/IEC, *Generic Coding of Audiovisual Objects — Part 10: Advanced Video Coding (MPEG-4 AVC)*, ISO/IEC 14496-10, October 2003.
12. *H.264/AVC Software Coordination*, http://iphome.hhi.de/ suehring/tml/
13. P. Bobinski, W. Skarbek: "Analysis of RD Models for Coding Efficiency in H.264 Standard", *5th International Workshop on Image Analysis for Multimedia Interactive Services WIAMIS 2004*, Lisboa, Portugal, April 2001.
14. Z. He, D. Wu: "Linear rate control and optimum statistical multiplexing for JVT encoders," *IEEE Transaction on Broadcast*, submitted in October 2004.
15. J. Cai, Z. He, C. W. Chen: "A novel frame-level bit allocation based on two-pass video encoding for low bit rate video streaming applications", accepted by *Journal of Visual Communications and Image Representation*.
16. W. Skarbek, A.Buchowicz, A.Pietrowcew, F. Pereira: "Bit-rate Control for Compression of Video with ROI", *International Conference on Computer Vision and Graphics ICCVG 2004*, Warszawa, Poland, September 2004.

17. Z. Li, F. Pan, K. P. Lim, G. Feng, X. Lin, S. Rahardja: "Adaptive Basic Unit Layer Rate Control for JVT", *Joint Video Team of ISO/IEC MPEG ITU-T VCEG*, JVT-G012-r1, Pattaya, Thailand, March 2003.
18. A. Pietrowcew, A. Buchowicz, W. Skarbek: "Bit-rate Control for Video Coding with ROI", *International Workshop on Image Analysis for Multimedia Interactive Services WIAMIS 2005*, Montreux, Switzerland, April, 2005.

A. PIETROWCEW, A. BUCHOWICZ, W. SKARBEK

ALGORYTM KONTROLI PRZEPŁYWALNOŚCI DLA KODOWANIA WIDEO Z REGIONAMI ZAINTERESOWANIA

Streszczenie

W artykule przedstawiono algorytm kontroli przepływności umożliwiający kodowanie regionów zainteresowania w sekwencjach wideo. Algorytm rozdziela dostępny budżet bitowy pomiędzy warstwy na które dzielone są poszczególne ramki sekwencji - pierwsza z tych warstw jest regionem zainteresowania, kolejne warstwy otaczają poprzednie warstwy. Przy podziale budżetu bitowego brana jest pod uwagę zarówno odległość danej warstwy od regionu zainteresowania jak i złożoność obrazu w tej warstwie. Algorytm zapewnia poprawę jakości obrazu w regionie zainteresowania kosztem pogorszenia jakości obrazu poza tym regionem, przy zachowaniu wymagań odnośnie całkowitej przepływności strumienia bitowego. Algorytm zapewnia także stopniową degradację jakości obrazu na granicy pomiędzy regionem zainteresowania i pozostałymi obszarami w kolejnych ramkach sekwencji.

Słowa kluczowe: kodowanie wideo, kontrola przepływności, standard H.264/AVC

KWARTALNIK ELEKTRONIKI I TELEKOMUNIKACJI, 2005, 51, ZESZYT SPECJALNY, ss. 173–188

Viseme recognition

W. SKARBEK, M. LESZCZYŃSKI, S. BADURA

Warsaw University of Technology,
Faculty of Electronics and Information Technology,
ul. Nowowiejska 15/19, 00-665 Warszawa, Poland
{W.Skarbek, M.Leszczyński, S.Badura}@ire.pw.edu.pl

Three classification algorithms for visual mouth appearances (visemes) which correspond to phonemes and their speech contexts, were compared w.r.t. recognition rate, time complexity, and ROC performance. Two feature extraction procedures were verified. The first one is based on the normalized triangle MESH covering mouth area and the color image texture vector indexed by barycentric coordinates. The second procedure performs DFT on the image rectangle including mouth w.r.t. small blocks of DFT coefficients.
The classifiers has been designed by PCA approach and by the optimized LDA method which uses two singular subspaces approach. It appears that DFT+LDA exhibits higher recognition rate than MESH+LDA and MESH+PCA methods — 97.6% versus 94.4 and 90.2%, respectively. It is also much faster than MESH+PCA (5ms per one video frame versus 26ms on Pentium IV, 3.2GHz) and slower than MESH+LDA (5ms versus 1ms).

Keywords: viseme, viseme dassification, LDA, PCA, diphone modeling

1. INTRODUCTION

This research refers to a development of software tools supporting animation of human face models integrated with Polish speech generator. With a gradual performance progress of computer systems w.r.t. computing and transmission speed the talking head applications show higher realism in speech and dynamic visual face appearance (viseme).

An animated talking head attracts immediately the attention of a user. Seeing a face makes many people feel more comfortable while interacting with computer. Generating animated talking heads that look like real people is a difficult task. To be considered natural, a face has to be not just realistic in appearance, but it must also exhibit proper plastic deformations of the lips synchronized with speech, realistic head movements and emotional expressions.

In computer graphics, many significant and different techniques exist for modeling talking head, achieving various degrees of realism and flexibility (cf.[3,4,5]). All synthesized heads are still far from reaching a perfect animation of lip synchronized with speech.

One of the main goal of our efforts is generating in real time realistic animated face synchronized with synthesized or real speech. To achieve it, we need de- termine accurate correspondence between visemes and phonemes. In this paper we especially focus on automatic viseme classification methods based on PCA and LDA.

2. DIPHONE MODELING

The speech synthesis system used in our talking head application requires definition of a set of basic speech units to be used for concatenative synthesis. Although the Polish phonetic notation provides only a few dozens of symbols (e.g. 36 in the SAMPA notation), the influence of one phoneme on the next at transitions between them requires to take into account the context of each phoneme. Similarly, this context influences the mouth shape. The set of basic speech units may be extended to cover all possible contexts. But including both the left and right context extends the set to about 60000 basic units. However, not all transitions are used in a real language.

Because the number of phoneme contexts is too large, we have used a set of diphones, i.e. transitions between pairs of phones. A diphone covers time interval from the middle point of the first phoneme to the middle of the second one. The set of diphones contains about 1000 elements to cover all transitions.

The set of recorded sentences has been chosen to be equal to a set used in the Corpora speech database (cf.[6]). All recordings have been automatically labeled in time domain using tools from the HTK toolkit (cf.[7]). The process of labeling requires a definition of a set of phonemes, a dictionary of words and their phonetical transcription. As a result, a sequence of labels in time domain is obtained. Fig. 1 shows an example of such a result – automatically labeled recording. Labels are later used in visemes selection and concatenative speech synthesis.

A concatenative speech synthesizer creates an utterance concatenating basic speech units — in this case diphones. This approach does not always give satisfactory results. Without further processing, no prosody is simulated. There are also differences in the base tone frequency (F_0). The reasons are:

— no synchronization of diphone boundaries with fundamental tone periods is attempted
— differences in F_0 among recorded utterances,
— different length of basic speech units.

In order to improve the quality of the synthesized speech, the following approaches have been considered: shifting of samples in speech domain, normalization of samples in frequency domain, involving of prosody. The synthesis consists of the following stages:

— splitting of a sentence, given in ortographical transcription, to tokens (words, punctuation characters, numerals, acronyms),
— expansion of acronyms and numerals,
— phonetical transcription,
— concatenative synthesis.

About 1000 diphones are automatically chosen from a larger (about 10 times) set of diphones. Selection is based on the tone frequency and amplitude — they are compared with the average value for the whole set of diphones and diphones with closest values are chosen. In case of a missing diphone, it is synthesized from existing half-diphones, which decreases the quality of the synthesized speech.

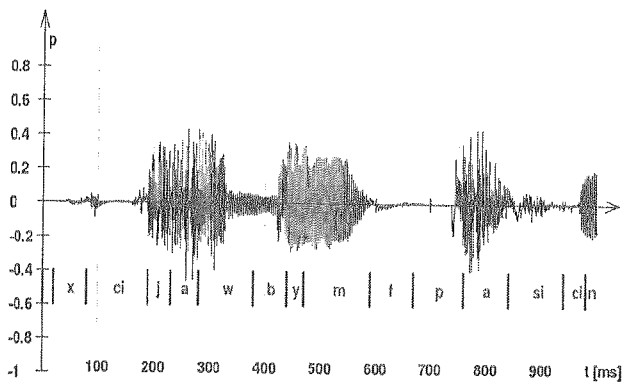

Fig. 1. Example of automatically assigned labels in time domain

3. CTVP TABLE

Based on phonetic time sections we could observe any viseme as visual equivalent of phonemes. Each viseme has multiple instances, but not all of them can be clear-cut classified. Therefore for the modeling viseme sets of instances were selected manually. This selection allows creating good models, but it still requires quite a lot of selected instances.

Shape of mouth for some different phonemes look similarly, so visemes are grouped into class of visemes. Previous classification distinguishes classes of visemes by grouping images for similar uttering phonemes. We are proposing new classification method.

Firstly we distinguish six classes of shape and ap-pearance of mouth (cf. Fig. 2):

1. opened mouth with upper teeth, lower teeth, and tongue visible;
2. opened mouth with upper teeth, and lower teeth visible, and tongue invisible;
3. opened mouth with upper teeth, and tongue visible, lower teeth invisible;
4. opened mouth with upper teeth visible, tongue and lower teeth invisible;

5. opened mouth visible, upper teeth, tongue, and lower teeth invisible;
6. closed mouth.

First 5 of the above classes with opened mouth has three subclasses referring to the degree of mouth openness: wide, medium, narrow.

Each pronounced phoneme is classified to one of the above classes depending on the uttering context in the uttered word.

Fig. 2. Representative images for six major viseme classes – the 16 minor classes are obtained by discrimination between small, medium, and high degree of mouth opening within the first five major classes

4. VISEME CLASSIFICATION

Below we explain how the viseme classifier had been designed to support the creation of CTVP table. To this goal the classification performance of 80% could be sufficient. However, we are going to use our viseme classifier to animate the human head model on the basis of live video. Therefore the real time and high performance of the classifier are the also main objectives of our research.

4.1. IMAGE NORMALIZATION

The realistic visual speech can be achieved by integrating the person specific face model with mouth model optionally augmented with the model of chin and cheeks. Using a triangle mesh (cf. Fig. 3), we can cover those speech sensitive areas and try to get the model for at least two goals: viseme classification and mouth animation.

Alternatively we can approximate the mouth area by a least rectangle touching lips from outside (cf. the upper part of Fig. 4).

Obviously, the triangle mesh approximation of mouth area is more exact than rectangular one and therefore a texture vector built from the rectangle includes compo-

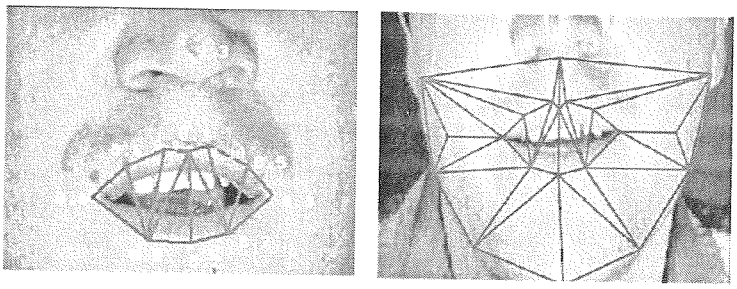

Fig. 3. Triangle mesh for mouth with MPEG-4 FAP points depicted (left), and its neighbourhood (right)

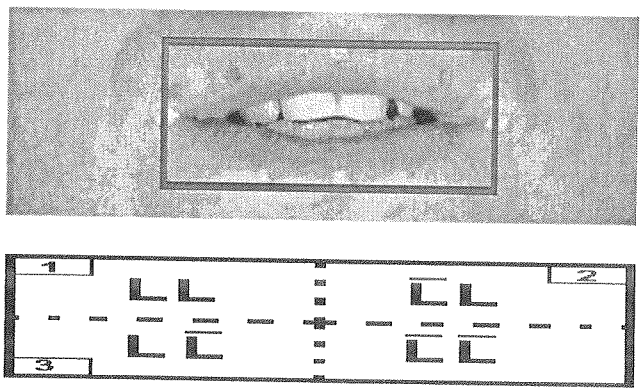

Fig. 4. The rectangle including mouth area (upper), and channel subdivision for 2D DFT (lower)

nents hard for matching. In this case change to 2D Discrete Fourier Transform (DFT) domain enables correct matching of mouth images normalized to reference mouth rectangle. As the vertical variability of the mouth image dominates the horizontal one we expect that out of three corner blocks (cf. the lower part of Fig.4) in DFT domain (usually considered at DFT based feature extraction) only the one corresponding to the least frequencies (without conjugated part) will be important for classification. Our expectation has been confirmed by the experiments.

In mesh approach we deal with variations of the mesh shape and of the mesh texture (appearance). In order to make comparable two meshes we have to normalize them with respect to a reference mesh.

We perform the nonlinear normalization of the mesh by mapping each triangle in the current image onto the corresponding triangle in the reference image. Each local mapping is affine, but globally we obtain the mapping which is piecewise affine.

Let the *i*-th triangle $\Delta_i(P_0, P_1, P_2)$ in the reference mesh M be mapped by the affine mapping $A_i(P) = B_iP + t_i$ onto the triangle $\Delta'_i(P'_0, P'_1, P'_2)$ in the current mesh M', where B_i is the square matrix, t_i is the vector, $P \in \Delta_i$, $P' \in \Delta'_i$, $i = 1, ..., K$. Then we have the following properties:

1. The piecewise affine mappings $A_1, \ldots, A_K$ are *continuous mappings* of M onto M' in geometric space
2. If $P = \alpha_0 P_0 + \alpha_1 P_1 + \alpha_2 P_2$ has the barycentric coordinates α_0, α_1, α_2 w.r.t. the triangle $\Delta_i(P_0,P_1,P_2)$ then the point $A_i(P) = \alpha_0 P'_0 + \alpha_1 P'_1 + \alpha_2 P'_2$, i.e. it has *the same barycentric coordinates* with respect to the triangle $\Delta'_i(P'_0, P'_1, P'_2)$:

$$A_i(P) = B_i P + t_i$$

$$= B_i(\alpha_0 P_0 + \alpha_1 P_1 + \alpha_2 P_2) + (\alpha_0 P_0 + \alpha_1 P_1 + \alpha_2) t_1 = \alpha_0(B_i P_0 + t_i) + \alpha_1(B_i P_1 + t) +$$

$$\alpha_2(B_i P_2 + t_i)$$

$$= \alpha_0 P'_0 + \alpha_1 P'_1 + \alpha_2 P'_2$$

3. If $f' : \Delta_P i'(P'_0, P'_1, P_2') \rightarrow C_{RGB}$ is the texture mapping in the current mesh then the mapping
$f : \Delta_i(P_0, P_1, P_2) \rightarrow C_{RGB}$ is defined by the barycentric coordinates for i=1,...,K as follows:

$$\begin{aligned} f(P) &= f(\alpha_0 P_0 + \alpha_1 P_1 + \alpha_2 P_2) \\ &= f'(\alpha_0 P'_0 + \alpha_1 P'_1 + \alpha_2 P_2) \end{aligned} \tag{1}$$

The above substitution transfers the texture from the current mesh onto the reference mesh with possible deformation of linear segments which intersect at least two triangles in the mesh.

We have used the texture mapping as described in point 3 above and despite the negative conclusion of the property 3 we observe no special visual degradation in the mapped texture on visemes (cf. Fig. 5).

Fig. 5. Comparison of original mouth views with the normalized images with respect to the reference mouth (the leftmost image)

4.2. SUBSPACE METHOD FOR MOUTH CLASSIFICATION

Due to the robust normalization, all mouth classes can be now represented in one texture space of high dimensionality $N \approx 10^3$. Applying the Principal Component Analysis (PCA — cf. [8]) reduces this dimensionality significantly. However, the variability within the class using one PCA subspace for all classes is too high. Therefore we model each class with its own separate PCA subspace. This leads to the known subspace method of pattern recognition (cf. [9]).

In Fig. 6 we show the dependence of subspace dimension $K_i(e)$ on percentage of signal energy e represented by PCA subspaces obtained for six mouth appearance classes, i=1,...,6.

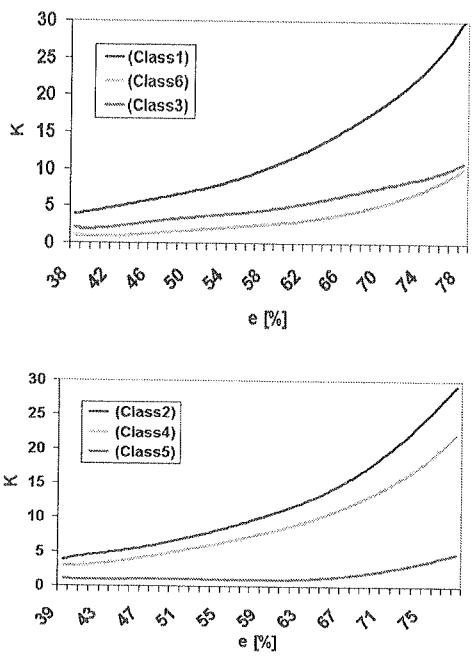

Fig. 6. Dependence of subspace dimension $K_i(e)$ on percentage of signal energy e included in the i-th subspace, i=1,...,6

Having PCA eigenvalues $\lambda_i^{(k)}$ for i=1,...,6, and k=1,...,N, we compute e_i as follows:

$$e_i(K) = \frac{\sum_{k=1}^{K} \lambda_i^{(k)}}{\sum_{k=1}^{N} \lambda_i^{(k)}} \cdot 100\% \tag{2}$$

The classification of mouth texture $M \in R^N$ by subspace method requires computing of reconstruction $M_i \in R^N$ against each subspace $(\overline{M}_i, W_i)$, $\overline{M}_i \in R^N$, $W_i \in R^{NxKi}$:

$$M_i = \overline{M}_i + W_i(W_i^t(M - \overline{M}_i)), \quad i, ..., 6 \tag{3}$$

Having reconstructions M_i of mouth texture M, the subspace method selects the mouth class with minimum reconstruction error:

$$i_{opt} = \arg \min_{1 \leqslant i \leqslant 6} \|M - M_i\|^2 \tag{4}$$

The time complexity for the subspace classification for C classes, can be estimated from the above formulas to $O(NK+NC+N^2)=O(N^2)$.

The subspace method does not require to have all classes modelled in one space. However, having classes in one space means that we avoid C-1 additional normalizations which take significant part of the algorithm's time.

4.3. LDA FOR MOUTH CLASSIFICATION

The advantage of having all texture classes (in mesh case) or DFT coefficients classes (in rectangular case) in common space R^N allows us to use the Linear Discriminant Analysis (LDA) to design the extremely fast classifier of linear complexity O(N).

Before we reached LDA feature vector of dimension five, the general Fisher LDA criterium (cf.[10,11,12]) had been used for K dimensional training feature vector $y_i = W^t x_i, x_i \in R^N, i = 1, ..., L, y \in R^K, W \in R^{NxK}$:

$$W_{opt} = \arg \max \frac{\text{between class variance for } \{ y_i \}}{\text{within class variance for } \{ y_i \}} = \frac{tr(W^t S_b W)}{tr(W^t S_w W)} \tag{5}$$

where Sb, Sw are the between and within class scatter matrices. The above criterium has points of singularity if W is arbitrary. Therefore Fisher imposed the following constraints on the domain of W :

$$W^t S w W = I, W \perp \ker(Sw) \tag{6}$$

This leads us to the following steps to obtain the optimal
W described in details as two singular subspace method in [1] with tuning parameters q equal to the dimension of the intra-class singular subspace (cf. [13]):

1. Class mean shifting of the training sequence: $X = [x_1, \ldots, x_L]$;
2. Grand mean shifting for class means: $M = [m_1, \ldots, m_C]$;
3. Singular Value Approximation for X with subspace dimension equal to q :

$$[U_q \ \Sigma_q] := sva(X, q); A_q = U_q \Sigma_q^{-1};$$

4. Whitening of columns in M : $M = A_q^t M$;
5. Singular Value Approximation for M with subspace dimension equal to r :

$$V_r := \mathrm{sva}(M, q); W = A_q V_r;$$

6. Return W;

The vector LDA features with maximum possible value $r = C - 1 = 5$ gives in our case the best results. The LDA feature $y = W^t x$ for the texture vector x is classified by the distance to LDA features $y_i = W^t x_i$ representing the mouth appearance classes $i = 1, \ldots, 6$:

$$i_{opt} = \arg \min_{1 \leqslant i \leqslant 6} \|y - y_i\|^2 \tag{7}$$

4.4. EXPERIMENTAL RESULTS

For the training of models for feature extraction 488 mouth image were selected with unbalanced distribution in the classes what corresponds to the distribution in the whole recorded video sequence:

$$L1 = 123, L2 = 122, L3 = 42, LA = 88, L5 = 36, L6 = 77$$

For the testing another 500 frames were selected independent of training frames. measure e:

$$e = e_i(K_i), \quad i = 1, ..., 6$$

Dimensions, K_i of PCA subspaces were established using a common which specifies what fraction of signal energy (energy cover) included in the training set can be attributed to the given subspace. The Fig. 7 (the upper graph) shows how the recognition rate depends on this measure. The performance graphs show that the best results are obtained for lower resolution of training and testing frames. The time performance in Figure 7 (the lower graph) is referred to our algorithm implementation on PC Pentium IV, 3.2GHz.

In mesh texture case of LDA, the best result (94.4% — cf. Fig. 8) is achieved for higher resolution image with subsequcnt subsampling of texture vector. However slightly worse result 94.0% is obtained for lower resolution image.

Since in case of LDA, the extraction time is independent of q we accept higher values of q giving higher generalization of the classifier even if the recognition rate is slightly higher for lower values of q.

In DFT+LDA case the best result (97.6% — cf. Fig. 9) is achieved for various combinations of parameters. In rectangular DFT case the best recognition result equal to 97.6% are achieved for the following setup of parameters:

1. DFT blocks LL, $\overline{L}L$ for horizontal frequencies 0 — 4 and vertical frequencies 0 — 14 (cf. Fig. 4 lower part and graphs of Fig. 9 upper part)
2. DC component is skipped

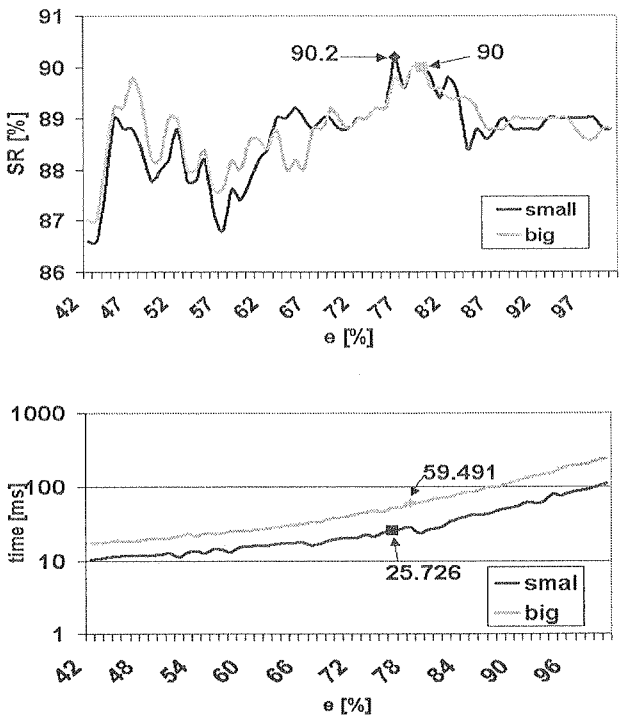

Fig. 7. Recognition rate (upper graph) and time (lower graph)for PCA classifier as a function of energy percentage e included in each class subspace at big and small training images resolution

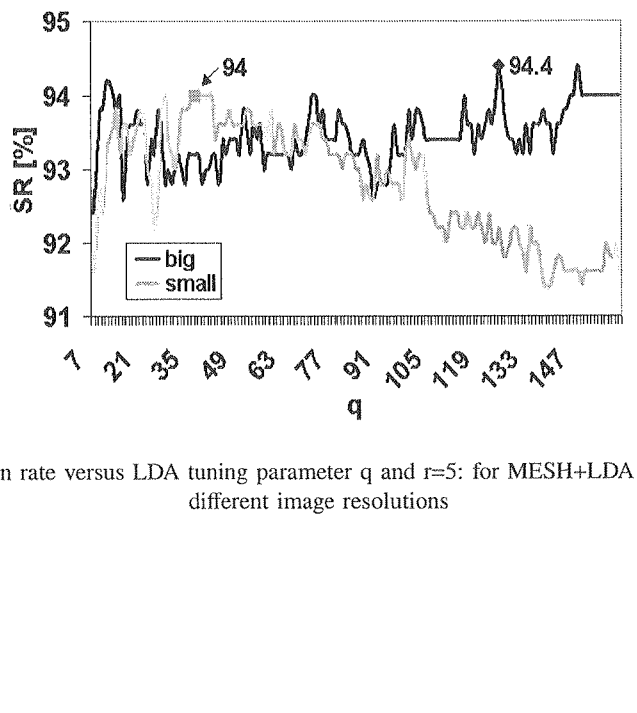

Fig. 8. Recognition rate versus LDA tuning parameter q and r=5: for MESH+LDA classifier and two different image resolutions

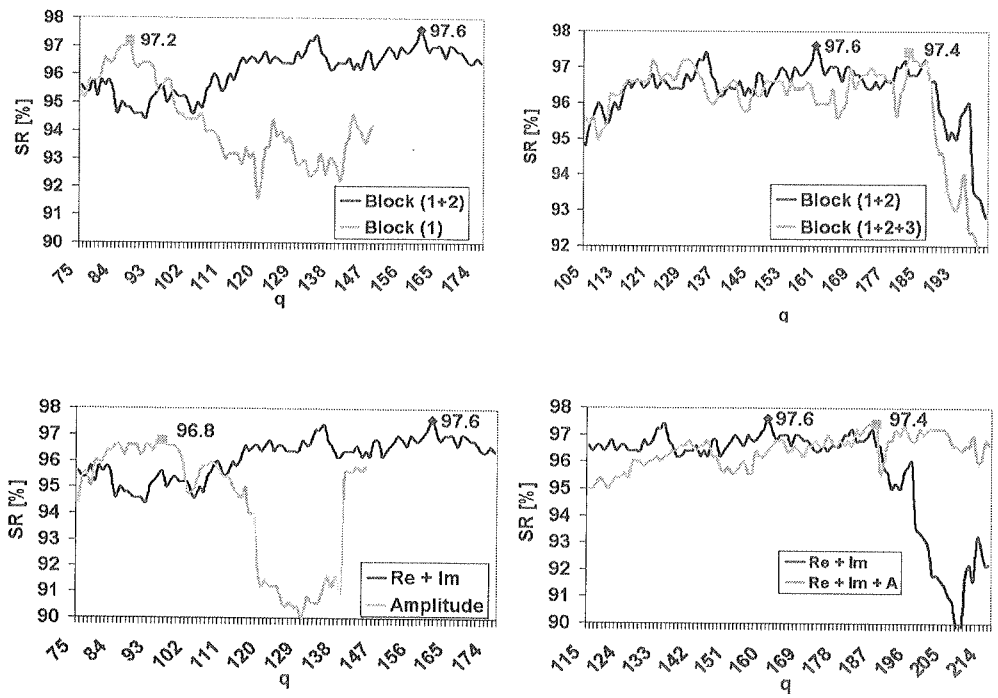

Fig. 9. Recognition rate versus LDA tuning parameter q and r=5: for different choice of DFT channels (in upper graphs block 1 contains coefficients of LL frequencies, 2 -$\overline{LL}$, 3 – L$\overline{L}$) and different combinations of real, imaginary and amplitude parts in DFT (lower graphs)

3. imaginary and real parts of all coefficients in blok LL and $\overline{L}$L are stacked in one vector of size 296 (contrary to the face classifier used in our system, the amplitude of DFT coefficients for mouth classifier has appeared to be insignificant — cf. graphs of Fig. 9 lower part)
4. intra-class singular subspace dimension equal to 160 (cf. Fig. 9)
5. inter-class singular subspace dimension equal to 5

It appears that mouth images which were wrongly classified are only from the class of slightly opened mouth with visible upper teeth, without visible tongue. They were confused with opened mouth, visible upper teeth and visible tongue. However, by eye view (the important measure in talking head application) the difference between such two images is not annoying while watching the mouth animation.

The very interesting comparison of the classifiers identification power delivers ROC analysis. The receiver operating characteristic curves are shown in Fig.10. It appears that minimum Equal Error Rate when false detection rate occurs for DFT+LDA and it is slightly less than for MESH+LDA (3.4% versus 3.6%), but it is significantly smaller than EER for MESH+PCA (3.4% versus 16.4%).

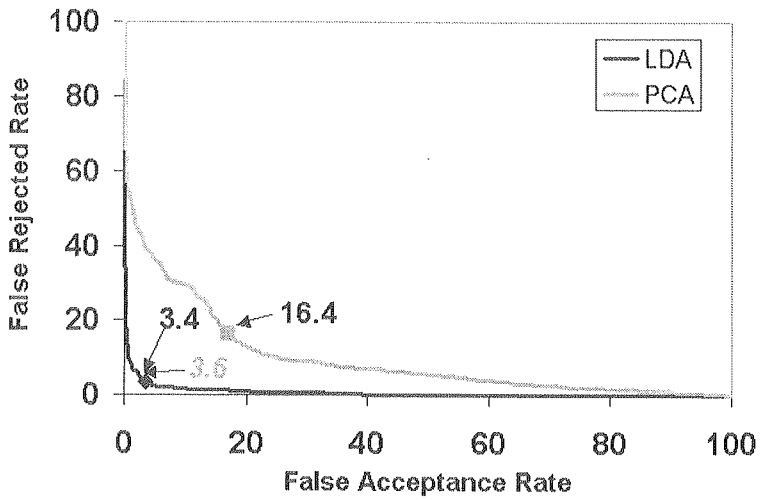

Fig. 10. Receiver operating characteristic curves (ROC) for MESH+PCA (EER = 16.4%), and overlapping curves for MESH+LDA and DFT+LDA with EER = 3.6% and EER = 3.4%, respectively

5. SYNTHESIS AND ANIMATION

The main goal of our efforts is the real-time generating animated face synchronized with synthesized or real speech. In case when the input of the synthesis and animation is only text, the text has to be preprocessed in order to expand numerals, abbreviations and acronyms to the full text form. To get a list of diphones, the text after preprocessing undergoes phonetic and prosodic transcriptions. Now the system has all information to select essential diphones from the diphones database for speech synthesizer and essential visemes from visemes database for mouth animation. Consecutive diphones are concatenated to form words and accent is added by the synthesizer for every generated word. At the end of speech synthesis generated sound is scaled in time depending on given speed of speech which is the parameter of the application.

The animation is created in parallel to the speech synthesis. The animation relies on results of phonetic and prosodic transcriptions, which is necessary for selecting appropriate visemes from database.

In the next step, the consecutive visemes are processed to animate given 3D head model.

In case when we have speech as sound track the system needs make an analysis to get a list of consecutive phonemes. The phoneme which are context sensitive transcoded into viseme symbols.

In the animation process the selected visemes are integrated with face model. For transition between visemes we used a shape morphing methods. In the intermediate frames we took advantage of textures from subclasses of currently animated consecutive visemes. At the end the system applies smoothing filters to remove any distortion arisen.

6. CONCLUSION

Three real time algorithms MESH+PCA, MESH+LDA and DFT+LDA for visemes classification were compared w.r.t. recognition rate, time complexity and ROC performance. Two feature extraction procedures were verified.

It was experimentally proved that DFT+LDA exhibits higher recognition rate than MESH+LDA and MESH+PCA methods — 97.6% versus 94.4% and 90.2%, respectively. It is also much faster than MESH+PCA (5ms per one video frame versus 26ms on Pentium IV, 3.2GHz) and slower than MESH+LDA (5ms versus 1ms).

Both LDA algorithms benefit of optimization stage when the optimal first singular subspace dimension is selected in our LDA design. LDA matrix in mesh has about 30 times more elements than LDA matrix in DFT case. However this advantage at matrix computation is absorbed by dominating DFT computational time.

Preliminary feature extraction for MESH+LDA is slightly faster but less robust in case of automatic mesh identification. Therefore for *talking head* applications, DFT+LDA technique is recommended as a tool for visemes classification.

Correct viseme recognition is very important to provide a realistic correspondence between visual face appearance and phonemes. High speed and low error rate of some methods allow us to realize assumed scenarios.

7. ACKNOWLEDGEMENT

The work presented was developed within VISNET, a European Network of Excelence (http://www.visnet-noe.org), funded under the European Commision IST FP6 programme.

8. BIBLIOGRAPHY

1. M. Bober, K. Kucharski, W. Skarbek: *Face Recognition by Fisher and Scatter Linear Discriminant Analysis, in Computer Analysis of Images and Patterns*, eds.Petkov N., Westenberg M., Springer LNCS 2756, 2003, pp. 638-645.
2. W. Skarbek, K. Kucharski, M. Bober: *Dual LDA for face recognition, in Fundamenta Informaticae*, Volume 61 , Issue 3,4 (July 2004) pp. 303-334.
3. V. Blanz, C. Basso, T. Poggio, T. Vetter: *Reanimating Faces in Images and Video*, Eurographics 2003.
4. T. Ezzat, T. Pioggio: *Visual Speech Synthesis by Morphing Visemes*, A.I. Memo No. 1658, C.B.C.L. Paper No. 173, May 1999.
5. CH. Bregler, M. Covell, M. Slaney: Video Rewrite: Visual Speech Synthesis from Video. Proceedings of the AVSP'97 Workshop, Rhodes (Greece), September 26-27, 1997.
6. S. Grocholewski: *CORPORA — Speech Database for Polish Diphones*, 5th European Conference on Speech Communication and Technology EUROSPEECH '97 Rhodes, Greece, September 22-25, 1997.
7. The Hidden Markov Model Toolkit (HTK), http://htk.eng.cam.ac.uk/, 2003.

8. I. T. Jolliffe: *Principal Component Analysis*. Springer, New York, 2002.
9. E. Oja: *Subspace Methods of Pattern Recognition*, Research Studies Press, England, 1983.
10. K. Fukunaga: *Introduction to statistical pattern recognition (2nd ed)*. Academic Press, Boston, 1990.
11. B. D. Ripley: *Pattern Recognition and Neural Networks*. Cambridge University Press, 1996.
12. D. L. Swets, J. Weng: *Using Discriminant Eigenfeatures for Image Retrieval*, IEEE Trans. on PAMI, 18(8):831-837, August 1996.
13. G. Golub, C. Van Loan: *Matrix Computations*. Baltimore: Johns Hopkins University Press, 1996.
14. S. Badura, M. Leszczyński, W. Skarbek: *Mouth Modeling by Local PCA for Audio Visual Synchronization*, April 2005.
15. T. Ezzat, T. Poggio: "Miketalk: A talking facial display based on morphing visemes," Proceedings of IEEE Computer Animation, Philadelphia PA, USA, 8-10 June, 1998, pp. 96-102.
16. L. R. Bahl, P. F. Brown, P. V. de Souza, R. L. Mercer: "Speech Recognition with continuous parameter hidden markov models," Proceedings ICASSP-88, New York, May 1988, pp. 40-43.
17. R. E. Donovan, E. M. Eide: "The IBM Trainable Speech Synthesis System," Proceedings International Conference on Speech and Language Processing, 1998.
18. P. Duchnowski, U. Meier, A. Waibel: "See me, hear me: Integrating automatic speech recognition and lip-reading", Proc. Int. Conf. Spoken Lang. Process., pp. 547-550, 1994.
19. M. E. Hennecke, D. G. Stork, K. V. Prasad: "Visionary speech: Looking ahead to practical speechreading systems," in Speechreading by Humans and Machines, D.G. Stork and M.E. Hennecke, Eds. Berlin: Springer, pp. 331–349, 1996.
20. L. R. Rabiner: "A tutorial on hidden Markov models and selected applications in speech recognition", Proc. IEEE, 77(2):257-285, 1989.
21. R. Campbell, B. Dodd, D. Burnham: Eds., Hearing by Eye II. Psychology Press Ltd. Pub., 1998.
22. C. Bregler, Y. Konig: "Eigenlips' for robust speech recognition," Proc. IEEE Int. Conf. Acous. Speech Sig. Process., pp. 669-672, 1994.
23. Odisio and Bailly (2004). "Shape and appearance models of talking faces for model-based tracking." Speech Communication: 44: 63-82.
24. Bailly, Bérar, Elisei and Odisio (2003). "Audiovisual speech synthesis." International Journal of Speech Technology 6: 331-346.
25. H. McGurk, J. W. MacDonald: "Hearing lips and seeing voices," Nature, vol. 264, pp. 746-748, 1976.
26. Q. Summerfield: "Use of visual information for phonetic perception," Phonetica, vol. 36, pp. 314-331, 1979.
27. L. Rabiner, B.-H. Juang: *Fundamentals of Speech Recognition*. Prentice Hall, Englewood Cliffs, 1993.
28. T. F. Cootes, G. J. Edwards, T. J. Taylor: "Active appearance models", Proc. Europ. Conf. Comp. Vision, pp. 484-498, 1998.
29. T. Chen, R. R. Rao: -Visual Integration in Multimodal Communication, Proc. IEEE, Vol. 86, pp. 837-852, 1998.
30. D. G. Stork, M. E. Hennecke, editors. *Speechreading by Humans and Machines: Models, Systems and Applications*, volume 150 of NATO ASI Series F: Computer and Systems Sciences. Springer-Verlag, Berlin, 1996.
31. E. Vatikiotis-Bateson, K. G. Munhall, M. Hirayama: *The dynamics of audiovisual behavior in speech*. In Stork and Hennecke [7], pages 221-232.
32. S. Young, D. Kershaw, J. Odell, D. Ollason, V. Valtchev, P. Woodland: The HTK Book. Entropic Ltd., Cambridge, 1999.

33. N. Brooke: *Talking heads and speech recognizers that can see: The computer processing of visual speech signals.* In Stork and Hennecke [91], pages 351-371.
34. N. M. Brooke, S. D. Scott: *PCA image coding schemes and visual speech intelligibility.* Proc. Institute of Acoustics, 16(5):123{129, 1994.
35. G. Chiou, J.-N. Hwang: Lipreading from color video. IEEE Transactions on Image Processing, 6(8):1192-1195, 1997.
36. T. F. Cootes, C. J. Taylor, D. H. Cooper, J. Graham: *Training models of shape from sets of examples.* In D. Hogg and R. Boyle, editors, Proc. British Machine Vision Conference, pages 9-18. BMVA Press, 1992.
37. M. Kass, A. Witkin, D. Terzopoulos: *Snakes: Active contour models.* International Journal of Computer Vision, 1(4):321-331, 1988.
38. T. Kuratate, H. Yehia, E. Vatiokotis-Bateson: *Kinematics based synthesis of realistic talking faces.* In Proc. Workshop on Audio Visual Speech Processing, Terrigal, 1998.
39. R. Lippmann: *Speech recognition by machines and humans.* Speech Communication, 22(1), 1997.
40. J. Luettin, N. A. Thacker: *Speechreading using probabilistic models.* Computer Vision and Image Understanding, 65(2):163-178, 1997.
41. J. Luettin, N. A. Thacker, S. W. Beet: *Active shape models for visual feature extraction.* In Stork and Hennecke [91], pages 383{390.
42. J. Luettin: *Towards speaker independent continuous speechreading.* In Proc. of the European Conference on Speech Communication and Technology, pages 1991-1994, Rhodes, 1997.
43. R. R. Rao, R. M. Mesereau: *Lip modeling for visual speech recognition.* In 28th Annual Asilomar Conference on Signals, Systems, and Computers, volume 1, pages 587-590, 1994.
44. J. J. Williams, J. C. Rutledge, D. C. Garstecki, A. K. Katsaggelos: *Frame rate and viseme analysis for multimedia applications.* In Proc. IEEE 1st Workshop on Multimedia Signal Processing, pages 13{18, Princeton, 1997.
45. T. Chen: "udiovisual speech processing. Lip reading and lip synchronization," IEEE Signal Processing Mag., 18(1):9-21, 2001.
46. M. M. Cohen, D. W. Massaro: "What can visual speech synthesis tell visual speech recognition?" in Proc. Asilomar Conf. Signals, Systems, Computers, Pacific Grove, CA, 1994.
47. E. Cosatto, G. Potamianos, H. P. Graf: "Audio-visual unit selection for the synthesis of photo-realistic talking-heads", in Proc. Int. Conf. Multimedia Expo, New York, NY, July 30–Aug. 2, 2000, pp. 1097- 1100.
48. E. Cosatto, H. P. Graf: "Photo-realistic talking-heads from image samples", IEEE Trans. Multimedia, vol. 2, pp. 152-163, Sept. 2000.
49. E. G. Keller, A. I. C. Bailly, J. Monaghan, J. Terken, M. Huckvale: (2002). *Improvements in Speech Synthesis.* Chichester, England, J. Wiley & Sons, Ltd.
50. M. Odisio, G. Bailly (2004): "Shape and appearance models of talking faces for model-based tracking." Speech Communication: 44: 63-82.

W. SKARBEK, M. LESZCZYŃSKI, S. BADURA

ROZPOZNAWANIE WIZEMÓW

Streszczenie

W artykule przedstawiono trzy algorytmy klasyfikacji wizemów (kształtu i wyglądu ust) jako odpowiedników fonemów i ich kontekstów. Kryterium porównawczym był stopień poprawnego rozpoznania, złożoność obliczeniowa i krzywa ROC. W badaniach wykorzystano dwa sposoby ekstrakcji wizemów. Pierwszy oparty na normalizacji siatką trójkątów i współrzędnych barycentrycznych (MESH). Drugi na znalezieniu prostokąta obejmującego usta i obliczeniu współczynników DFT. Zaproponowane klasyfikatory oparte były na metodzie PCA i zoptymalizowanej metodzie LDA. Wyniki eksperymentów pokazały, że algorytm oparty na DFT+LDA wykazuje wyższy stopień poprawnej klasyfikacji w stosunku do MESH+LDA i MESH+PCA — odpowiednio 97,6%, 94,4% i 90,2%. Jest on jednocześnie dużo szybszy od MESH+PCA (5ms vs 26ms) oraz wolniejszy od MESH+LDA (5ms vs 1ms). Eksperymenty przeprowadzano na komputerze klasy PC Pentium IV 3,2 GHz.

Słowa kluczowe: wizem, klasyfikacja wizemów, LDA, PCA, modelowanie difonów

INFORMACJE DLA AUTORÓW

Redakcja przyjmuje do publikowania prace oryginalne, przeglądowe i monograficzne wchodzące w zakres szeroko pojętej elektroniki. Ponieważ KWARTALNIK ELEKTRONIKI I TELEKOMUNIKACJI jest czasopismem Komitetu Elektroniki i Telekomunikacji Polskiej Akademii Nauk, w związku z tym na jego łamach znajdują się prace naukowe dotyczące podstaw teoretycznych i zastosowań z zakresu elektroniki, telekomunikacji, mikroelektroniki, optoelektroniki, radiotechniki i elektroniki medycznej.
Artykuły powinno charakteryzować oryginalne ujęcie zagadnienia, własna klasyfikacja, krytyczna ocena (teorii lub metod), omówienie aktualnego stanu, lub postępu danej gałęzi techniki oraz omówienie perspektyw rozwojowych. Artykuły publikowane w innych czasopismach nie mogą być kierowane do druku w Kwartalniku Elektroniki i Telekomunikacji w drugiej kolejności zgłoszenia.
Objętość artykułu nie powinna przekraczać 30 stron po około 1800 znaków na stronie, w tym rysunki i tabele.

Wymagania podstawowe.
Artykuły należy nadsyłać na wyraźnym, jednostronnym, czarno-białym wydruku komputerowym. Wydruk w formacie A4 powinien mieć znormalizowaną liczbę wierszy i znaków w wierszu (30 wierszy po 60 znaków w wierszu), w dwóch egzemplarzach, w języku polskim lub angielskim wybranym przez autora. Do wydruku powinna być dołączona dyskietka z elektronicznym tekstem artykułu. Preferowane edytory to WORD 6 lub 8.
Układ artykułu (w wersji podstawowej) musi być następujący:
- Tytuł.
- Autor (imię i nazwisko autora/ów).
- Miejsce pracy (nazwa instytucji, miejscowość, adres. + ew. adres elektroniczny (e-mail).
- Zwięzłe streszczenie powinno być w języku takim, w jakim jest pisany artykuł (wraz ze słowami kluczowymi).
- Tekst podstawowy powinien mieć następujący układ:
  1. WPROWADZENIE
  2. np. TEORIA
  3. np. WYNIKI NUMERYCZNE
  3.1. .....
  3.2. .....
  4. .....
  5. .....
  6. PODSUMOWANIE
  7. ew. PODZIĘKOWANIA
  8. BIBLIIOGRAFIA
- Układ streszczenia w dodatkowej wersji językowej powinien być następujący:
  AUTOR (inicjał imienia i nazwisko).
  TYTUŁ (w języku angielskim – o ile artykuł pisany jest w języku polskim i na odrwót).

Obszerne do 3600 znaków streszczenia (wraz z słowami kluczowymi) w języku:
  a. angielskim, gdy artykuł pisany jest w języku polskim.
  b. polskim, gdy artykuł pisany jest w języku angielskim.

Streszczenie to powinno pozwolić czytelnikowi na uzyskanie istotnych informacji zawartych w pracy. Z tego względu w streszczeniu tym mogą być cytowane numery istotnych wzorów, rysunków i tabel zawartych w podstawowej wersji językowej.
- Wszystkie strony muszą mieć numerację ciągłą.

Sposób pisania tekstu.
Tekst powinien być pisany bez używania wyróżnień, a w szczególności nie dopuszcza się spacjowania, podkreślania i pisania tekstu dużymi literami z wyjątkiem wyrazów, które umownie pisze się dużymi literami (np. FORTRAN). Proponowane wyróżnienia Autor może zaznaczyć w maszynopisie zwykłym ołówkiem za pomocą przyjętych znaków adjustacyjnych, np. podkreślenie linią przerywaną oznacza spacjowanie (rozstrzelenie), podkreślenie linią ciągłą – pogrubienie, podkreślenie wężykiem — kursywa.

Tekst powinien być napisany z podwójnym odstępem między wierszami, tytuły i podtytuły małymi literami. Marginesy z każdej strony powinny mieć około 35 mm. Wielkość czcionki wydruku powinna być zbliżona co najmniej co wielkości czcionki maszyny do pisania (minimum 12 punktów). Przy podziale pracy na rozdziały i podrozdziały cyfrowe ich oznaczenia nie powinny być większe niż II stopnia (np. 4.1.1.).

Sposób pisania tabel.
Tabele powinny być pisane na oddzielnych stronach. Tytuły rubryk pionowych i poziomych powinny być napisane małymi literami z podwójnym odstępem między wierszami. Przypisy (notki) dotyczące tabel należy pisać bezpośrednio pod tabelami. Tabele należy numerować kolejno liczbami arabskimi, u góry każdej tabeli podać tytuł dwujęzyczny. W pierwszej kolejności w podstawowej wersji językowej, a później w dodatkowej wersji językowej. Tabele umieścić na końcu maszynopisu. Przyjmowane są tabele algorytmów i programy na wydrukach komputerowych. W tym przypadku zachowany jest ich oryginalny układ. Tabele powinny być cytowane w tekście.

Sposób pisania wzorów matematycznych.
Rozmieszczenie znaków, cyfr, liter i odstępów powinno być zbliżone do rozmieszczenia elementów druku. Wskaźniki i wykładniki potęg powinny być napisane wyraźnie i być prawidłowo obniżone lub podwyższone w stosunku do linii wiersza podstawowego. Znaki nad literami i cyfram, całkami i in. symbolami (strzałki, linie, kropki, daszki) powinny być umieszczone dokładnie nad tymi elementami, do których się odnoszą. Numery wzorów cyframi arabskimi powinny być kolejne i umieszczone w nawiasach okrągłych z prawej strony. Nazwy jednotek, symbole literowe i graficzne powinny być zgodne z wytycznymi IEE (International Electronical Commision) oraz ISO (International Organization of Standarization).

Powołania.
Powołania na publikacje powinny być umieszczone na ostatnich stronach tekstu pod tytułem „Bibliografia", opatrzone numeracją kolejną bez nawiasów. Numeracja ta powinna być zgodna z odnośnikami w tekście artykułu. Przykłady opisu publikacji:

- periodycznej — 1. F. Valdoni: A new milimetre wave satelite. E.T.T. 1990, vol. 2, no 5, pp. 141–148
- nieperiodyczne — 2. K. Andersen: A resource allocation framework. XVI International Symposium, Stockholm (Sweden), may 1991, paper A 2,4
- książki — 3. Y.P. Tvidis: Operation and modeling of the MOS transistors. New York, McGraw-Hill, 1987, p. 553

Materiały ilustracyjne.
Rysunki powinny być wykonane wyraźnie, na papierze gładkim lub milimetrowym w formaci ni mnijszym niż 9×12 cm. Mogą być także w postaci wydruku komputerowego (preferowany edytor Corel Draw). Fotografie lub diapozytywy przyjmowane są raczej czarno-białe w formacie nie przekraczającym 10×15 cm. Na marginesie każdego rysunku i na odwrocie fotografii powinno być napisane ołówkiem imię i nazwisko Autora oraz skrót tytułu artykułu, do którego są przeznaczone oraz numer rysunku. Spis podpisów pod rysunki i fotografie powinien być umieszczony na oddzielnej stronie. Podpisy pod rysunkami (fotografiami) powinny być dwujęzyczne: w pierwszej kolejności w podstawowej wersji językowej, a później w dodatkowej wersji językowej. Rysunki powinny być cytowane w tekście.

Uwagi końcowe.
Na odrębnej stronie powinny być podane następujące informacje:
- adres do korespondencji z kodem pocztowym (domowy lub do miejsca pracy),
- telefon domowy i/lub do miejsca pracy,
- adres e-mailowy (jeśli autor posiada).

Autorowi przysługuje bezpłatnie 20 odbitek artykułu. Dodatkowe egzemplarze odbitek, lub cały zeszyt Autor może zamówić u wydawcy na własny koszt.

Autora obowiązują korekta autorska, którą powinien wykonać w ciągu 3 dni od daty otrzymania tekstu z Redakcji oraz zwrócić osobiście lub listownie pod adres Redakcji. Korekta powinna być naniesiona na przekazanych Autorowi szpaltach na marginesach ew. na osobnym arkuszu w przypadku uzupełnień tekstu większych niż dwa wiersze. W przypadku nie zwrócenia korekty w terminie, korektę przeprowadza Redakcja Techniczna Wydawcy. Redakcja prosi Autorów o powiadomienie ją o zmianie miejsca pracy i adresu prywatnego.

INFORMATION FOR AUTHORS OF K.E.T.

The editorial stuff will accept for publishing only original monographic and survey papers concerning widely understood electronics. Because of the fact that KWARTALNIK ELEKTRONIKI I TELEKOMUNIKACJI is a journal of the Committee for Electronics and Telecommunications of Polish Academy of Scince, it presents scientific works concerning theoretical bases and applications from the field of electronics, telecommunications, microelectronics, optoelectronics, radioelectronics and medical electronics.
Articles should be characterised by original depiction of a problem, its own classification, critical opinion (concerning theories or methods), discussion of an actual state or a progress of a given branch of a technique and discussion of development perspectives.
An article published in other magazines can not be submitted for publishing in K.E.T. TThe size of an article can not exceed 30 pages, 1800 character each, including figures and tables.

Basic requirements
The article should be submitted to the editorial stuff as a one side, clear, black and white computer printout in two copies. The article should be prepared in English or Polish. Floppy disc with an electronic version of the article should be enclosed. Preferred wordprocessors: WORD 6 or 8.
Layout of the article.
- Title.
- Author (first name and surname of author/authors).
- Workplace (institution, adress and e-mail).
- Concise summary in a language article is prepared in (with keywords).
- Main text with following layout:
  - Introduction
  - Theory (if applicable)
  - Numerical results (if applicable)
  - Paragraph 1
  - Paragraph 2
  - .....
  - .....
  - Conclusions
  - Acknowledgements (if applicable)
  - References
- Summary in additional language:
  - Author (firs name initials and surname)
  - Title (in Polish, if article was prepared in English and vice versa)
  - Extenstive summary, hawever not exceeching 3600 characters (along with keywords) in Polish, if artide wos prepared in English and vice versa). The summary should be prepared in a way allowing a reader to obtaoin essential information contained in the artide. For that reason in the summary author can place numbers of essential formulas, figures and tables from the article.

Pages should have continues numbering.

Main text
Main text can not contain formatting such as spacing, underlining, words written in capital letters (except words that are commonly written in capital letters). Author can mark suggested formatting with pencil on the margin of the article using commonly accepted adjusting marks.
Text should be written with double line spacing with 35 mro left and right margin. Titles and subtitles should be written with small letters. Titles and subtitles should be numberd using no mor than 3 levels (i.e. 4.1.1.).

Tables
Tables with their titles should be places on separate page at the end of the article. Titles of rows and columns should be written in small letters with double line spacing. Annotations concerning tables

should be placed directly below the table. Tables should be numbered with Arabic numbers on the top of each table. Table can consist algorithm and program listings. In such cases original layout of the table will be preserved. Table should be cited in the text.

Mathematical formulas

Characters, numbers, letters and spacing of the formula should be adequate to layout of main text. Indexes should be properly lowered or raised above the basic line and clearly written. Special characters such as lines, arrows, dots should be placed exactly over symbols which they ar attributed to. Formulas should be numbered with Arabic numbers place in brackets on the right side of the page. Units of measure, letter and graphic symbols should be printed according to requirements of IEE (International Electronical Commission) and ISO (International Organisation of Standardisation).

References

References should be placed at the and of the main text with th subtitle „References". Refrences should be numbered (without brackets) adequately to references placed in the text. Examples of periodical [@], non-periodical [2] and book [3] references:

1. F. Valdoni: A new milimetre wave satelite. E.T.T. 1990, vol. 2, no 5, pp. 141–148
2. K. Anderson: A resource allocation framework. XVI International Symposium (Sweden). May 1991. paper A 2.4
3. Y.P. Tvidis: Operation and modeling of the MOS transistors. Nw York. McGraw-Hill. 1987. p. 553

Figures

Figures should be clearly drawn on plain or milimetre paper in the format not smaller than 9 × 12 cm. Figures can be also printed (preferred editor – CorelDRAW). Photos or diapositives will be accepted in black and whit format not gratd than 10 × 15 cm. On th margin of each drawing and on th back side of each ohoto authorp name and abbreviation of the title of article should be placed. Figure's captures should be given in two longuaqes (first in the language the article is writtes in and then in additional language). Figure's captures should be also listed on separate page. Figures should be cited in the text.

Additional information

On the separate page following information should be placed:

- mailing address (home or office),
- phone (home or/and office),
- e-mail.

Author is entiled to free of charg 20 copies of articl. Additional copies or the whole magazine can be ordered at publisher at th one's expense.

Author is obliges to perform the author's correction, which should be accomplished within 3 days starting from the date of receiving of the text from the ditorial stuff. Corrected text should be return to the editorial stuff personally or by mail. Correction marks should bc placcd on th margin of copies received from the editorial stuff or if needed on separate pages. In the case when the correction is not returned in said time limit, correction will be performed by technical editorial stuff of the publisher.

In case of changing of workplace or home address Authors are asked to inform the editorial stuff.